The Abdus Salam International Centre for Theoretical Physics

United Nations Educational, Scientific and Cultural Organization

The International Union of Geodesy and Geophysics

IAEA International Atomic Energy Agency

2373-8

Workshop on Geophysical Data Analysis and Assimilation

29 October - 3 November, 2012

An introduction to data assimilation in Geomagnetism

Alexandre Fournier
Institut de Physique du Globe de Paris
France

An introduction to data assimilation in Geomagnetism

Alexandre Fournier

Équipe de Géomagnétisme
Institut de Physique du Globe de Paris
Sorbonne Paris Cité, Université Paris Diderot,
INSU/CNRS (UMR 7154), F-75005 Paris, France
fournier@ipgp.fr
www.ipgp.fr/~fournier

This document has been assembled for the students who will attend the workshop on Geophysical Data Analysis and Assimilation in the Abdus Salam International Center for Theoretical Physics in Trieste (Italy).

It comprises several components, most notably

1. a general part on the fundamentals of data assimilation,
2. a copy of the slides that I (at the time of writing) intend to show during the workshop on the topic of Geomagnetic Data assimilation
3. a review paper entitled An introduction to data assimilation and predictability in Geomagnetism,
4. the text describing two computer-based labs dealing with Lorenz's 1963 model

Acknowledgements

Most of the notes on the fundamentals of data assimilation (chapters 1 to 3) were made possible thanks to the generous input of my friend and colleague Emmanuel Cosme. Emmanuel is a physical oceanographer working at the Université of Grenoble, www-meom.hmg.inpg.fr/Web/pages-perso/Cosme/. On his webpage you will find much more material related to the foundations and applications of data assimilation.

I am grateful to Chris Finlay for sharing a series of slides and data which allowed me to thicken the part on geomagnetic observations and their connection with the geodynamo.

Last, but not least, Matthias Morzfeld's codes and suggestions were very much appreciated when designing the two computer labs on Lorenz's 1963 model. They can be run using the `matlab` software, as well as its open-source clone, `octave`.

I deserve full credit for any mistake in the notes, labs, codes, ...

October 15, 2012,
AF

Contents

I Notes on the fundamentals of data assimilation 5

1 Introduction 7

1.1 What is data assimilation? . . . 7

1.2 A scalar example . . . 7

1.3 Notations . . . 10

1.4 Useful references . . . 12

2 Stochastic estimation 15

2.1 Basics of probability and statistics . . . 15

2.2 The two pillars of estimation theory . . . 17

2.3 Optimal estimates . . . 18

2.4 The BLUE . . . 19

2.5 The Gaussian case . . . 20

3 The Kalman filter 22

3.1 Introduction . . . 22

3.2 The Kalman filter algorithm . . . 22

3.3 Implementation issues . . . 25

4 Variational assimilation 29

II Slides 36

III Review article 66

1 An introduction to data assimilation and predictability in geomagnetism 67

IV Computer labs 113

1 Lorenz's (1963) model: forward modelling 114

1.1 Introduction 114
1.2 Forward integration 115
1.3 Sensitivity to initial conditions 116

2 Application of the ensemble Kalman filter (EnKF) to Lorenz's 1963 model 117
2.1 Statistical ingredients 117
2.2 Algorithm 118
2.3 Application of the EnKF 119

V Appendix 124

A Derivation of the discrete adjoint equation 125

B Lorenz 1963 127

C Bibliography on geomagnetic data assimilation 140

Part I

Notes on the fundamentals of data assimilation

Chapter 1

Introduction

1.1 What is data assimilation?

The basic purpose of data assimilation is to combine different sources of information in order to produce the best possible estimate of the state of a system. These sources generally consist of observations of the system and of physical laws describing its behaviour, often represented in the form of a numerical model. Why not simply use observations? First because observations are often too sparse or partial in geophysics. Some extra information is needed to interpolate the information contained in the observations to unobserved regions or quantities. A numerical model naturally performs this task. Second, because observations are contaminated by errors (they are noised). Combining (by means of the model) several noised data can be an efficient way of to filter out at least part of the noise and to provide a more accurate estimate ("accuracies are added", see below).

The problem of data assimilation can be tackled using different mathematical approaches: signal processing, control theory, estimation theory, ... Stochastic methods, such as the popular Kalman filter, are based on estimation theory. On the other hand, variational methods (3D-Var, 4D-Var...) are rooted in control theory.

The historical development of data assimilation for geophysical systems can hardly be disconnected from meteorology. Data assimilation is indeed a mandatory step if one wishes to provide a weather prediction system with a good initialization (an initial condition), and until the early nineteen-nineties data assimilation was mostly used for this purpose. Today, its application is generalized to many other fields (atmospheric chemistry, oceanic biochermistry, glaciology, physical oceanography, geomagnetism, stellar magnetism, seismology...), and for a variety of purposes :

- the estimation of the trajectory of a system to study its variability (reanalyses)
- the identification of systematic errors in numerical models
- the estimation of unobserved field variables (e.g. the magnetic field inside Earth's core)
- the estimation of parameters (e.g. a structural Earth model in seismology)
- the optimization of observation networks

1.2 A scalar example

Following for instance Ghil and Malanotte-Rizzoli (1991), assume we have two distinct measurements, $y_1 = 1$ and $y_2 = 2$, of the same unknown quantity x. What estimation of its true value can

we make ?

1.2.1 First approach

We seek x which minimizes $(x-1)^2+(x-2)^2$, and we find the estimate $\widehat{x}=3/2=1.5$ (this is the least-squares solution). This solution has the following problems:

- it is sensitive to any change of units. If $y_1=1$ is a measurement of x and $y_2=4$ is a measurement of $2x$, then minimizing $(x-1)^2+(2x-4)^2$ leads to $\widehat{x}=9/5=1.8$.
- it does not reflect the quality of the various measurements.

1.2.2 Reformulation in a statistical framework

We define

$$Y_i = x+\epsilon_i, \tag{1.1}$$

where the observation errors ϵ_i satisfy the following hypotheses

- $\mathrm{E}(\epsilon_i)=0$ (unbiased measurements)
- $\mathrm{Var}(\epsilon_i)=\sigma_i^2$ (accuracy is known)
- $\mathrm{Covar}(\epsilon_1,\epsilon_2)=0$, i.e. $\mathrm{E}(\epsilon_1\epsilon_2)=0$, errors are independent.

We next seek an estimator (i.e. a random variable) $\widehat{X}$ which is

- linear: $\widehat{X}=\alpha_1 Y_1+\alpha_2 Y_2$
- unbiased: $\mathrm{E}\left(\widehat{X}\right)=x$
- of minimum variance: $\mathrm{Var}\left(\widehat{X}\right)$ minimal (optimal accuracy)

This estimator is called the **BLUE**: Best Linear Unbiased Estimator. To compute the α_i we use the unbiased hypothesis

$$\mathrm{E}\left(\widehat{X}\right)=x=(\alpha_1+\alpha_2)x+\alpha_1\mathrm{E}(\epsilon_1)+\alpha_2\mathrm{E}(\epsilon_2)=(\alpha_1+\alpha_2)x, \tag{1.2}$$

so that $\alpha_1+\alpha_2=1$, or $\alpha_2=1-\alpha_1$. Next we compute the variance of $\widehat{X}$.

$$\begin{aligned}\mathrm{Var}\left(\widehat{X}\right) &= \mathrm{E}\left[\left(\widehat{X}-x\right)^2\right]=\mathrm{E}\left[\left(\alpha_1\epsilon_1+\alpha_2\epsilon_2\right)^2\right]\\ &= \alpha_1^2\mathrm{E}\left(\epsilon_1^2\right)+2\alpha_1\alpha_2\mathrm{E}\left(\epsilon_1\epsilon_2\right)+\alpha_2^2\mathrm{E}\left(\epsilon_2^2\right)\\ &= \alpha_1^2\sigma_1^2+\alpha_2^2\sigma_2^2\\ &= \alpha_1^2\sigma_1^2+(1-\alpha_1)^2\sigma_2^2.\end{aligned}$$

Our estimator $\widehat{X}$ has to minimize this quantity. Computing α_1 such that

$$\frac{\mathrm{d}}{\mathrm{d}\alpha_1}\mathrm{Var}\left(\widehat{X}\right)=0 \tag{1.3}$$

yields

$$\alpha_1 = \frac{\sigma_2^2}{\sigma_2^2 + \sigma_1^2}. \tag{1.4}$$

It follows that

$$\widehat{X} = \frac{\sigma_2^2}{\sigma_1^2 + \sigma_2^2} y_1 + \frac{\sigma_1^2}{\sigma_1^2 + \sigma_2^2} y_2. \tag{1.5}$$

Note that we get the same result if we try to minimize the functional

$$\mathcal{J}(x) = \frac{1}{2}\left[\frac{(x - y_1)^2}{\sigma_1^2} + \frac{(x - y_2)^2}{\sigma_2^2}\right]. \tag{1.6}$$

Comments:

- This statistical approach solves the problem of sensitivity to units and it incorporates measurement accuracies.
- The accuracy of the estimator is given by the second derivative of $\mathcal{J}$

  $$\left.\frac{\mathrm{d}^2\mathcal{J}}{\mathrm{d}x^2}\right|_{x=\widehat{X}} = \frac{1}{\mathrm{Var}\left(\widehat{X}\right)} = \frac{1}{\sigma_1^2} + \frac{1}{\sigma_2^2}, \tag{1.7}$$

  so that "accuracies are added".
- If we consider that $y_1 = x^b$ is a first guess of x (with standard deviation $\sigma_b = \sigma_1$) and $y_2 = y$ is an additional observation (with std dev $\sigma = \sigma_2$), then we can rearrange Eq. (1.5) as

  $$\widehat{X} = x^b + \frac{\sigma_b^2}{\sigma^2 + \sigma_b^2}\left(y - x^b\right). \tag{1.8}$$

  The quantity $y - x^b$ is called the **innovation**. It contains the additional information provided by y with respect to x^b.

1.2.3 Data assimilation methods

There are two classes of methods

- statistical methods: direct computation of the BLUE thanks to algebraic computations (the Kalman filter);
- variational mehods: minimization of the functional J (4DVar).

Shared properties:

- they provide the same result (in the linear case);
- their optimality can only be demonstrated in the linear case;

Shared difficulties:

- accounting for non-linearities

- dealing with large problems
- error statistics are required but sometimes only poorly known

Courtier (1997) provides a concise and elegant discussion of the two classes of methods and discusses their equivalence.

1.3 Notations

There exists some sort of standard notations, summarized by Ide et al. (1997).

- $\mathbf{x}$ state vector
- $\mathbf{x}^t$ true state
- $\mathbf{x}^b$ background state
- $\mathbf{x}^a$ analyzed state

Superscripts denote vector types, subscripts refer to space or time. In the following: unless otherwise noted, all vectors will be column vectors. If $\mathbf{a}$ and $\mathbf{b}$ are two column vectors of equal size n, with the superscript T denoting transposition, then

$$\mathbf{a}^T\mathbf{b} \quad \text{is their scalar product } = \sum a_i b_i, \tag{1.9}$$

$$\mathbf{a}\mathbf{b}^T \quad \text{is a matrix of coefficients } a_i b_j, (i,j) \in \{1,\ldots,n\}^2 . \tag{1.10}$$

1.3.1 Discretization and true state

Most of the time, our goal will be to estimate as accurately as possible a geophysical field that varies continuously in space and time. This real, continuous (and possibly multivariate) field is denoted by ɔ.

Numerical models are often used for the estimation. Numerical models operate in a discrete world and only handle discrete representations of physical fields. Therefore we will try to estimate a projection of the real state ɔ onto a discrete space. Let $\mathbf{\Pi}$ denote the associated projector, and $\mathbf{x}^t$ be the projection of ɔ

$$\mathbf{x}^t = \mathbf{\Pi}(\text{ɔ}). \tag{1.11}$$

$\mathbf{x}^t$ is called the true state (see above); this is the state we wish to estimate in practice.

In a data assimilation problem, one deals with **dynamical** models that compute the time evolution of the simulated state. Let ɔ_i and ɔ_{i+1} be the real (continuous) states at two consecutive observation times, i being a time index. These two states are related by a causal link (the physical model)

$$\text{ɔ}_{i+1} = g\left(\text{ɔ}_i\right). \tag{1.12}$$

Projecting this equality into the discrete world, we get

$$\mathbf{x}^t_{i+1} = \mathbf{\Pi}\left[g\left(\text{ɔ}_i\right)\right]. \tag{1.13}$$

The dynamical model g is not strictly known, even though we hopefully know most of the physics involved in it (in our vibrating string problem, our model will be exactly known). This physics

is represented in the discrete world by our numerical model $\mathcal{M}$, which operates on discrete states such as $\mathbf{x}^t$. Introducing this model into Eq. (1.13), we get

$$\mathbf{x}_{i+1}^t = \mathcal{M}_{i,i+1}\left(\mathbf{x}_i^t\right) + \boldsymbol{\eta}_{i,i+1}, \tag{1.14}$$

in which

$$\boldsymbol{\eta}_{i+1} = \mathbf{\Pi}\left[g\left(\text{x}_i\right)\right] - \mathcal{M}_{i,i+1}\left(\mathbf{x}_i^t\right). \tag{1.15}$$

The **model error** $\boldsymbol{\eta}_{i+1}$ term accounts for the errors in the numerical models (e.g. misrepresentation of some physical processes) and for the errors due to the discretization. The covariance matrix $\mathbf{Q}_{i+1}$ of the model error is given by

$$\mathbf{Q}_{i+1} = \text{Covar}\left(\boldsymbol{\eta}_{i+1}\right) = \text{E}\left[\left(\boldsymbol{\eta}_{i+1} - \langle\boldsymbol{\eta}_{i+1}\rangle\right)\left(\boldsymbol{\eta}_{i+1} - \langle\boldsymbol{\eta}_{i+1}\rangle\right)^T\right], \tag{1.16}$$

where $\langle\boldsymbol{\eta}_{i+1}\rangle = \text{E}\left(\boldsymbol{\eta}_{i+1}\right)$ is the average error.

1.3.2 Observations

The real, continous field x results in a signal $\mathcal{y}$ in the space of observations. This involves a mapping $\mathcal{h}$

$$\mathcal{y} = \mathcal{h}\left(\text{x}\right). \tag{1.17}$$

Despite its simplicity, this equation can not be used in practice. First, we do not have access to the real $\mathcal{y}$: the observed field $\mathbf{y}^o$ is contaminated with measurement errors, denoted by $\boldsymbol{\epsilon}^\mu$. Accordingly,

$$\mathbf{y}^o = \mathcal{h}\left(\text{x}\right) + \boldsymbol{\epsilon}^\mu. \tag{1.18}$$

Second, $\mathcal{h}$, which represents the physics of the measurement process (which might be exactly known), is a continuous mapping. In practice, this physics is represented by a numerical operator $\mathcal{H}$, which is applied to the discrete state we wish to estimate, $\mathbf{x}^t$. Incorporating $\mathcal{H}$ and $\mathbf{\Pi}$ in Eq. (1.18) yields

$$\mathbf{y}^o = \mathcal{H}(\mathbf{x}^t) + \underbrace{\mathcal{h}\left(\text{x}\right) - \mathcal{H}\left[\mathbf{\Pi}(\text{x})\right]}_{\boldsymbol{\epsilon}^r} + \boldsymbol{\epsilon}^\mu, \tag{1.19}$$

where $\boldsymbol{\epsilon}^r$ is often termed the error of representativeness (Lorenc, 1986), which includes the errors related to the representation of the physics in $\mathcal{H}$ and those errors due to the projection $\mathbf{\Pi}$ of the real state x onto the discrete state space (due for instance to numerical interpolation). The sum of the measurement error and the error of representativeness is the **observation error**

$$\boldsymbol{\epsilon}^o = \boldsymbol{\epsilon}^\mu + \boldsymbol{\epsilon}^r. \tag{1.20}$$

This allows us to write the final form of the equation relating the discrete true state $\mathbf{x}^t$ and the observations

$$\mathbf{y}^o = \mathcal{H}\left(\mathbf{x}^t\right) + \boldsymbol{\epsilon}^o. \tag{1.21}$$

The covariance matrix of the observation error $\boldsymbol{\epsilon}^o$ is defined by

$$\mathbf{R} = \text{Covar}\left(\boldsymbol{\epsilon}^o\right) = \text{E}\left[\left(\boldsymbol{\epsilon}^o - \langle\boldsymbol{\epsilon}^o\rangle\right)\left(\boldsymbol{\epsilon}^o - \langle\boldsymbol{\epsilon}^o\rangle\right)^T\right]. \tag{1.22}$$

In our labs, we will be dealing with synthetic data and we will artificially introduce observation errors $\boldsymbol{\epsilon}^o$ (the statistics of which we will assume to be Gaussian).

1.3.3 A priori (background) information

It can be that we have some a priori knowledge of the state $\mathbf{x}^t$, under the form of a vector $\mathbf{x}^b$ having the same dimension as $\mathbf{x}^t$. This is the **background state**. Following a similar logic, the background error is defined as

$$\boldsymbol{\epsilon}^b = \mathbf{x}^b - \mathbf{x}^t. \tag{1.23}$$

Often the estimate of the background state comes from a model simulation. In this case, the background is a **forecast** and is rather denoted by $\mathbf{x}^f$, with forecast error $\boldsymbol{\epsilon}^f$.

The covariance $\mathbf{P}^b$ of the background error is given by

$$\mathbf{P}^b = \text{Covar}\left(\boldsymbol{\epsilon}^b\right) = \text{E}\left[\left(\boldsymbol{\epsilon}^b - \langle\boldsymbol{\epsilon}^b\rangle\right)\left(\boldsymbol{\epsilon}^b - \langle\boldsymbol{\epsilon}^b\rangle\right)^T\right]. \tag{1.24}$$

1.3.4 Analysis

The result of the assimilation process is often called the analysis, and is denoted by $\mathbf{x}^a$. The analysis error is defined by

$$\boldsymbol{\epsilon}^a = \mathbf{x}^a - \mathbf{x}^t, \tag{1.25}$$

while the covariance matrix of the analysis error $\boldsymbol{\epsilon}^a$ is defined by

$$\mathbf{P}^a = \text{Covar}\left(\boldsymbol{\epsilon}^a\right) = \text{E}\left[\left(\boldsymbol{\epsilon}^a - \langle\boldsymbol{\epsilon}^a\rangle\right)\left(\boldsymbol{\epsilon}^a - \langle\boldsymbol{\epsilon}^a\rangle\right)^T\right]. \tag{1.26}$$

An important comment: the problem is entirely set-up once the physical model and the observations have been chosen, and the covariances (and possibly the background) defined. All the physics has been introduced at this stage. The remaining part (the production of the analysis) is technical.

1.4 Useful references

At this stage it might be timely to provide the reader with general references on data assimilation. My favorite book on the topic is "Discrete Inverse and State Estimation Problems", by Wunsch (2006), which provides a very personal and powerful account of adjoint methods and their application in geophysical fluid dynamics (oceanography). In her book entitled "Atmospheric Modelling, Data Assimilation and Predictability ", E. Kalnay (2003) has two comprehensive and very well-written chapters on the basics and applications of data assimilation techniques to atmospheric dynamics. Last, but not least, Evensen (2009) provides a very complete treatment of data assimilation techniques, with a strong and useful emphasis on the basics and applications of the ensemble Kalman filter he invented (we will briefly touch on this in Sect. 3.3.4.2).

For a start, I would highly recommend the review paper by Talagrand (1997), "Assimilation of observations, an introduction" which provides an extremely concise and well-written overview of the topic.

In addition, if you are looking for references related to the geophysical inverse problem in general, Parker (1994) and Tarantola (2005) provide two very personal, insightful, and sometimes contradictory views on how we should go about making inference on the Earth based on a finite number of noisy observations and on physical laws governing its behaviour.

Chapter 2

Stochastic estimation

2.1 Basics of probability and statistics

2.1.1 Probability

2.1.1.1 Random experiment

A random experiment is mathematically described by

- the set Ω of all possible outcomes of an experiment, the result of which can not be perfectly anticipated;
- the subsets of Ω, called events;
- a probability function, P: a numerical expression of a state of knowledge. P is such that, for any disjoint events A and B,

$$\begin{aligned} 0 \leq P(A) &\leq 1, && (2.1)\\ P(\Omega) &= 1, && (2.2)\\ P(A \cup B) &= P(A) + P(B). && (2.3) \end{aligned}$$

Here, $\cup$ means `.OR.` In the next paragraph, $\cap$ will mean `.AND.`

2.1.1.2 Conditional probability

When two events A and B are not independent, knowing that B has occurred changes our state of knowledge on A. This writes

$$P(A|B) = \frac{P(A \cap B)}{P(B)}. \quad (2.4)$$

2.1.2 Real random variables

The outcome of a random experiment is called a random variable. A random variable can be an integer (the number of tries scored by the French rugby team, whose games often ressemble random experiments), or a real number (e.g. the lifetime of a Buzz Lightyear action figure).

2.1.2.1 Probability density function

For a real random variable x, being equal to a given number is not strictly speaking an event. Only the inclusion into an interval is an event. This defines the **probability density function**, also known as pdf

$$P(a \leq x \leq b) = \int_a^b p(x)\mathrm{d}x. \tag{2.5}$$

2.1.2.2 Joint and conditional pdf

If x and y are two real random variables, $p(x, y)$ is the joint pdf of x and y. The conditional pdf $p(x|y)$ writes

$$p(x|y) = \frac{p(x, y)}{p(y)}. \tag{2.6}$$

2.1.2.3 Expectation and variance

A pdf is seldom known completely. In most instances, only some of its properties are determined and handled. The two main properties are the expectation and the variance. The expectation of a random variable x, characterized by a pdf p is given by

$$\mathrm{E}\,(x) = \langle x \rangle = \int_{-\infty}^{+\infty} xp(x)\mathrm{d}x. \tag{2.7}$$

The variance is given by

$$\mathrm{Var}\,(x) = \mathrm{E}\left[(x - \langle x \rangle)^2\right] = \int_{-\infty}^{+\infty} (x - \langle x \rangle)^2 p(x)\mathrm{d}x. \tag{2.8}$$

The standard deviation σ is **the square root of the variance**.

2.1.2.4 The Gaussian distribution

The random variable x has a Gaussian (or normal) distribution with parameters μ and σ^2, denoted by $x \sim \mathcal{N}(\mu, \sigma^2)$ when

$$p(x) = \frac{1}{\sqrt{2\pi\sigma^2}} \exp\left[-\frac{(x-\mu)^2}{2\sigma^2}\right]. \tag{2.9}$$

This Gaussian pdf has the following properties

- the parameters μ and σ^2 are its expectation and variance, respectively;
- If $x_1 \sim \mathcal{N}(\mu_1, \sigma_1^2)$ and $x_2 \sim \mathcal{N}(\mu_2, \sigma_2^2)$ are two independent variables, then $x_1 + x_2$ is also Gaussian and $x_1 + x_2 \sim \mathcal{N}(\mu_1 + \mu_2, \sigma_1^2 + \sigma_2^2)$;
- if $a \in \mathbb{R}$ and $x \sim \mathcal{N}(\mu, \sigma^2)$, then $ax \sim \mathcal{N}(a\mu, a^2\sigma^2)$.

2.1.3 Real random vectors

Real random vectors are vectors whose components are real random variables. The pdf of a vector is the joint pdf of its components.

2.1.3.1 Expectation and variance

The expectation vector is the vector of the expected values of the components. The second moment of the distribution is the covariance matrix. If $\mathbf{x}$ denotes the random vector, the covariance matrix is defined by

$$\mathbf{P} = \mathrm{E}\left[(\mathbf{x} - \langle\mathbf{x}\rangle)(\mathbf{x} - \langle\mathbf{x}\rangle)^T\right]. \tag{2.10}$$

A covariance matrix is symmetric positive definite. The terms appearing on its diagonal are the variances of the vector components. The off-diagonal terms are covariances. If x_i and x_j denote two different components of $\mathbf{x}$, their covariance is

$$P_{ij} = \mathrm{Covar}(x_i, x_j) = \mathrm{E}\left[(x_i - \langle x_i\rangle)(x_j - \langle x_j\rangle)^T\right] \tag{2.11}$$

and their correlation is

$$\rho(x_i, x_j) = \frac{\mathrm{Covar}(x_i, x_j)}{\sqrt{\mathrm{Var}(x_i)\,\mathrm{Var}(x_j)}}. \tag{2.12}$$

2.1.3.2 The multivariate Gaussian distribution

The random vector $\mathbf{x}$ of size n has a Gaussian (or normal) distribution with parameters $\boldsymbol{\mu}$ and $\mathbf{P}$, denoted by $\mathbf{x} \sim \mathcal{N}(\boldsymbol{\mu}, \mathbf{P})$, if

$$p(\mathbf{x}) = \frac{1}{(2\pi)^{n/2}(\det\mathbf{P})^{1/2}} \exp\left\{-\frac{1}{2}\left[(\mathbf{x} - \boldsymbol{\mu})^T \mathbf{P}^{-1}(\mathbf{x} - \boldsymbol{\mu})\right]\right\}. \tag{2.13}$$

Here $\boldsymbol{\mu}$ and $\mathbf{P}$ are the expectation and the covariance matrix of $\mathbf{x}$, respectively; $\det\mathbf{P}$ is the determinant of $\mathbf{P}$. The components of $\mathbf{x}$ are said to be jointly Gaussian.

2.2 The two pillars of estimation theory

If one has to remember only two formulas from this section, these are

1. Bayes' theorem

$$p(\mathbf{x}|\mathbf{y}) = \frac{p(\mathbf{y}|\mathbf{x})p(\mathbf{x})}{p(\mathbf{y})}. \tag{2.14}$$

2. The marginalization rule

$$p(\mathbf{y}) = \int p(\mathbf{x}, \mathbf{y})\mathrm{d}\mathbf{x} = \int p(\mathbf{y}|\mathbf{x})p(\mathbf{x})\mathrm{d}\mathbf{x}. \tag{2.15}$$

where

- $p(\mathbf{y}|\mathbf{x})$ is the measurement model (or likelihood);
- $p(\mathbf{x})$ is the prior distribution;
- $p(\mathbf{y})$ is the marginal distribution (or evidence).

2.3 Optimal estimates

The optimal estimate of the random vector $\mathbf{x}$ given the observation $\mathbf{y}$ is the vector of values which best reflects what a realisation of $\mathbf{x}$ can be, having $\mathbf{y}$ at hand. Optimality is subjective, and several criteria can be proposed in order to define it. For the sake of illustration we present three such estimators below (although the rest of the material discussed this week will only have to do with the minimum variance estimator).

2.3.1 Minimum variance estimation

The estimate we seek is such that the spread around it is minimal. The measure of the spread is the variance. If $p(\mathbf{x}|\mathbf{y})$ is the pdf of $\mathbf{x}$, having $\mathbf{y}^o$ at hand, the minimum variance estimate $\widehat{\mathbf{x}}_{mv}$ is the solution of

$$\boldsymbol{\nabla}_{\widehat{\mathbf{x}}} \mathcal{J}\left(\widehat{\mathbf{x}}\right) = \mathbf{0}, \tag{2.16}$$

where

$$\mathcal{J}(\widehat{\mathbf{x}}) = \int \left(\mathbf{x} - \widehat{\mathbf{x}}\right)^T \left(\mathbf{x} - \widehat{\mathbf{x}}\right) p(\mathbf{x}|\mathbf{y}) \mathrm{d}\mathbf{x} \tag{2.17}$$

and the gradient is defined as

$$\boldsymbol{\nabla}_{\widehat{\mathbf{x}}} = [\partial_{\widehat{x}_1}, \ldots, \partial_{\widehat{x}_i}, \ldots, \partial_{\widehat{x}_n}] \tag{2.18}$$

(This is a row vector.) We can show that the solution is the expectation of the pdf, that is

$$\widehat{\mathbf{x}}_{mv} = \mathrm{E}\left[\mathbf{x}|\mathbf{y}\right]. \tag{2.19}$$

2.3.2 Maximum a posteriori estimation

The estimate is defined at the most probable vector of $\mathbf{x}$ given $\mathbf{y}$, i.e., the vector that maximizes the conditional pdf $p(\mathbf{x}|\mathbf{y})$. $\widehat{\mathbf{x}}_{map}$ is such that

$$\left.\frac{\partial p(\mathbf{x}|\mathbf{y})}{\partial \mathbf{x}}\right|_{\mathbf{x}=\widehat{\mathbf{x}}_{map}} = \mathbf{0}. \tag{2.20}$$

With a Gaussian pdf, the minimum variance and the maximum a posteriori estimators are the same.

2.3.3 Maximum likelihood estimation

The estimate is defined as the most probable vector of $\mathbf{y}$ given $\mathbf{x}$, i.e., the vector which maximizes the conditional pdf $p(\mathbf{y}|\mathbf{x})$. $\widehat{\mathbf{x}}_{ml}$ is such that

$$\left.\frac{\partial p(\mathbf{y}|\mathbf{x})}{\partial \mathbf{x}}\right|_{\mathbf{x}=\widehat{\mathbf{x}}_{ml}} = \mathbf{0}. \tag{2.21}$$

The ML estimator can be interpreted as the MAP estimator without any prior information $p(\mathbf{x})$.

2.4 The best linear unbiased estimate (BLUE)

We now return to the BLUE, which we already introduced based on the simple scalar example of Sect. 1.2. We aim at estimating the true state $\mathbf{x}^t$ of a system, assuming that a background estimate $\mathbf{x}^b$ and partial observations $\mathbf{y}^o$ are given. We assume that these two pieces of information are unbiased and that their uncertainties are known in the form of covariance matrices $\mathbf{P}^b$ and $\mathbf{R}$, respectively (recall paragraphs 1.3.3 and 1.3.2). The observation operator $\mathcal{H}$ is assumed linear (denoted by $\mathbf{H}$). All together we have the following pieces of information

$$\begin{aligned}
\mathbf{H}, \text{such that } \mathbf{y}^o &= \mathbf{H}\mathbf{x}^t + \boldsymbol{\epsilon}^o, && (2.22)\\
\mathbf{x}^b &= \langle \mathbf{x}^t \rangle, && (2.23)\\
\mathbf{P}^b &= \langle \boldsymbol{\epsilon}^b \boldsymbol{\epsilon}^{b\,T} \rangle, && (2.24)\\
\langle \boldsymbol{\epsilon}^o \rangle &= \mathbf{0}, && (2.25)\\
\mathbf{R} &= \langle \boldsymbol{\epsilon}^o \boldsymbol{\epsilon}^{o\,T} \rangle. && (2.26)
\end{aligned}$$

The best estimate (or analysis) $\mathbf{x}^a$ is sought as a linear combination of the background estimate and the observation

$$\mathbf{x}^a = \mathbf{A}\mathbf{x}^b + \mathbf{K}\mathbf{y}^o, \tag{2.27}$$

where $\mathbf{A}$ and $\mathbf{K}$ are to be determined in order to make the estimation optimal (you can think of them as the generalization of the coefficients α_1 and α_2 in the simple scalar example of Sect. 1.2). How do we define optimality? Given the information at hand, a wise choice is to seek an unbiased estimate, with minimum variance. Reintroducing $\boldsymbol{\epsilon}^a = \mathbf{x}^a - \mathbf{x}^t$ we seek $(\mathbf{A}, \mathbf{K})$ such that

$$\begin{aligned}
&\mathrm{E}\left(\boldsymbol{\epsilon}^a\right) = \mathbf{0}, && (2.28)\\
&\mathrm{Tr}\left(\mathbf{P}^a\right) \text{minimum}, && (2.29)
\end{aligned}$$

where $\mathrm{Tr}\left(\cdot\right)$ denotes the trace (sum of the diagonal elements, here the variance of each component of $\mathbf{x}^a$). One can show that

$$\begin{aligned}
\mathbf{A} &= \mathbf{I} - \mathbf{K}\mathbf{H},\\
\mathbf{K} &= \mathbf{P}^b\mathbf{H}^T\left(\mathbf{H}\mathbf{P}^b\mathbf{H}^T + \mathbf{R}\right)^{-1},
\end{aligned}$$

in which $\mathbf{K}$ is called the Kalman gain matrix [1].

The a posteriori error covariance matrix $\mathbf{P}^a$ can also be computed. The final form of the update equations writes

$$\begin{aligned}
\mathbf{K} &= \mathbf{P}^b\mathbf{H}^T\left(\mathbf{H}\mathbf{P}^b\mathbf{H}^T + \mathbf{R}\right)^{-1}, && (2.30)\\
\mathbf{x}^a &= \mathbf{x}^b + \mathbf{K}\left(\mathbf{y}^o - \mathbf{H}\mathbf{x}^b\right), && (2.31)\\
\mathbf{P}^a &= (\mathbf{I} - \mathbf{K}\mathbf{H})\mathbf{P}^b, && (2.32)
\end{aligned}$$

where $\mathbf{I}$ is the identity matrix.

These equations constitute the best linear unbiased estimate (BLUE) equations, under the constraint of minimum variance. They are the backbone of sequential data assimilation methods (soon to come).

[1] We have assumed so far that we were dealing with real-valued variables. When dealing with complex-valued fields, everything holds, provided one replaces the transpose operator T by a transpose conjugate operator, often denoted by a dagger †.

2.5 The Gaussian case

If we know that both the prior and observation pieces of information are adequately represented by Gaussian pdfs, we may apply Bayes' theorem to compute the a posteriori pdf. With

$$\begin{aligned} \mathbf{x}^t &\sim \mathcal{N}(\mathbf{x}^b, \mathbf{P}^b), \\ p(\mathbf{x}^t) &= \frac{1}{(2\pi)^{n/2} \det \mathbf{P}^{b\,1/2}} \exp\left\{-\frac{1}{2}\left[\left(\mathbf{x}^t - \mathbf{x}^b\right)^T \mathbf{P}^{b^{-1}} \left(\mathbf{x}^t - \mathbf{x}^b\right)\right]\right\}, \qquad (2.33) \\ \mathbf{y}^o &\sim \mathcal{N}(\mathbf{H}\mathbf{x}^b, \mathbf{R}), \\ p(\mathbf{y}^o|\mathbf{x}^t) &= \frac{1}{(2\pi)^{n/2} \det \mathbf{R}^{1/2}} \exp\left\{-\frac{1}{2}\left[\left(\mathbf{y}^o - \mathbf{H}\mathbf{x}^t\right)^T \mathbf{R}^{-1} \left(\mathbf{y}^o - \mathbf{H}\mathbf{x}^t\right)\right]\right\}. \qquad (2.34) \end{aligned}$$

Bayes' theorem provides us with the a posteriori pdf

$$p(\mathbf{x}^t|\mathbf{y}^o) \propto \exp(-\mathcal{J}), \qquad (2.35)$$

with

$$\mathcal{J}(\mathbf{x}^t) = \frac{1}{2}\left[\left(\mathbf{x}^t - \mathbf{x}^b\right)^T \mathbf{P}^{b^{-1}} \left(\mathbf{x}^t - \mathbf{x}^b\right) + \left(\mathbf{y}^o - \mathbf{H}\mathbf{x}^t\right)^T \mathbf{R}^{-1} \left(\mathbf{y}^o - \mathbf{H}\mathbf{x}^t\right)\right]. \qquad (2.36)$$

We can show that this last equation can be rewritten as

$$\mathcal{J}(\mathbf{x}^t) = \frac{1}{2}\left[\left(\mathbf{x}^t - \mathbf{x}^a\right)^T \mathbf{P}^{a^{-1}} \left(\mathbf{x}^t - \mathbf{x}^a\right)\right] + \boldsymbol{\beta}, \qquad (2.37)$$

with

$$\begin{aligned} \mathbf{P}^a &= \left[\mathbf{P}^{b^{-1}} + \mathbf{H}^T\mathbf{R}^{-1}\mathbf{H}\right]^{-1}, \qquad (2.38) \\ \mathbf{x}^a &= \mathbf{P}^a\left[\mathbf{P}^{b^{-1}}\mathbf{x}^b + \mathbf{H}^T\mathbf{R}^{-1}\mathbf{y}^o\right], \qquad (2.39) \end{aligned}$$

and $\boldsymbol{\beta}$ a vector independent of $\mathbf{x}^t$. With the help of the Sherman-Morrison formula (aka the matrix inversion lemma according to Wunsch (2006), page 29)

$$[\mathbf{A} + \mathbf{UDV}]^{-1} = \mathbf{A}^{-1} - \mathbf{A}^{-1}\mathbf{U}\left[\mathbf{D}^{-1} + \mathbf{VA}^{-1}\mathbf{U}\right]^{-1}\mathbf{VA}^{-1}, \qquad (2.40)$$

we can show that these are the BLUE equations (2.30-2.32). The a posteriori pdf defined by Eq. (2.35) is thus Gaussian, with parameters given by the BLUE equations. Since the BLUE provides the same result as the application of Bayes' theorem, it is the best estimator (in the case of Gaussian pdfs and of a linear observation operator, though). In passing we can recognize in Eq. (2.36) the cost function used in the static variational method termed 3D-Var. When it minimizes this cost function, the 3D-Var algorithm computes the Maximum A Posteriori estimate of the Gaussian pdf, which is identical to the Minimum Variance estimate found by the BLUE. We can take from this that when statistics are Gaussian and the observation operator is linear, every method, whatever its name, will yield the same optimal solution, which, depending on the philosophy followed, will be given different interpretations.

Chapter 3

The Kalman filter

3.1 Introduction

The system is now dynamical. Instead of a unique estimation, we set out to estimate a series of states $\mathbf{x}_i^t$ (a sequence of real random vectors), where the index i refers to a discrete time index (when observations are made). The situation is summarized in Fig 3.1.

We assume the following a priori knowledge:

- the initial condition $\mathbf{x}_0^t$ is Gaussian-distributed with mean $\mathbf{x}_0^b$ and covariance $\mathbf{P}_0^b$;
- a linear dynamical model $\mathbf{M}$ describes the evolution of the state of the system we are interested in;
- the model errors (recall Sect. 1.3.1) $\boldsymbol{\eta}_i$ are Gaussian with zero mean (they are unbiased) and covariance $\mathbf{Q}_i$;
- the model errors are white (i.e. uncorrelated) in time $\mathrm{E}\left(\boldsymbol{\eta}_i \boldsymbol{\eta}_j^T\right) = \mathbf{0}$ if $i \neq j$;
- Observation errors $\boldsymbol{\epsilon}_i^o$ are Gaussian, with zero mean and covariance matrix $\mathbf{R}_i$;
- observation errors are white in time $\mathrm{E}\left(\boldsymbol{\epsilon}_i^o \boldsymbol{\epsilon}_j^{oT}\right) = \mathbf{0}$ if $i \neq j$;
- Errors of different kinds are independent

$$\mathrm{E}\left(\boldsymbol{\eta}_i \boldsymbol{\epsilon}_j^{oT}\right) = \mathrm{E}\left(\boldsymbol{\eta}_i \boldsymbol{\epsilon}_0^{bT}\right) = \mathrm{E}\left(\boldsymbol{\epsilon}_i \boldsymbol{\epsilon}_0^{bT}\right) = \mathbf{0}.$$

Under these many conditions, the Kalman filter provides the estimate of the states $\mathbf{x}_i^t$, conditioned by the past and present observations $\mathbf{y}_1^o, \ldots, \mathbf{y}_i^o$; in terms of pdf, this amounts to considering

$$p(\mathbf{x}_i | \mathbf{y}_{1:i}^o),$$

where $\mathbf{y}_{1:i}^o = \{\mathbf{y}_1^o, \ldots, \mathbf{y}_i^o\}$.

3.2 The Kalman filter algorithm

The Kalman filter algorithm is sequential and decomposed into two steps:

1. A **forecast**
2. An **analysis** (or observational update)

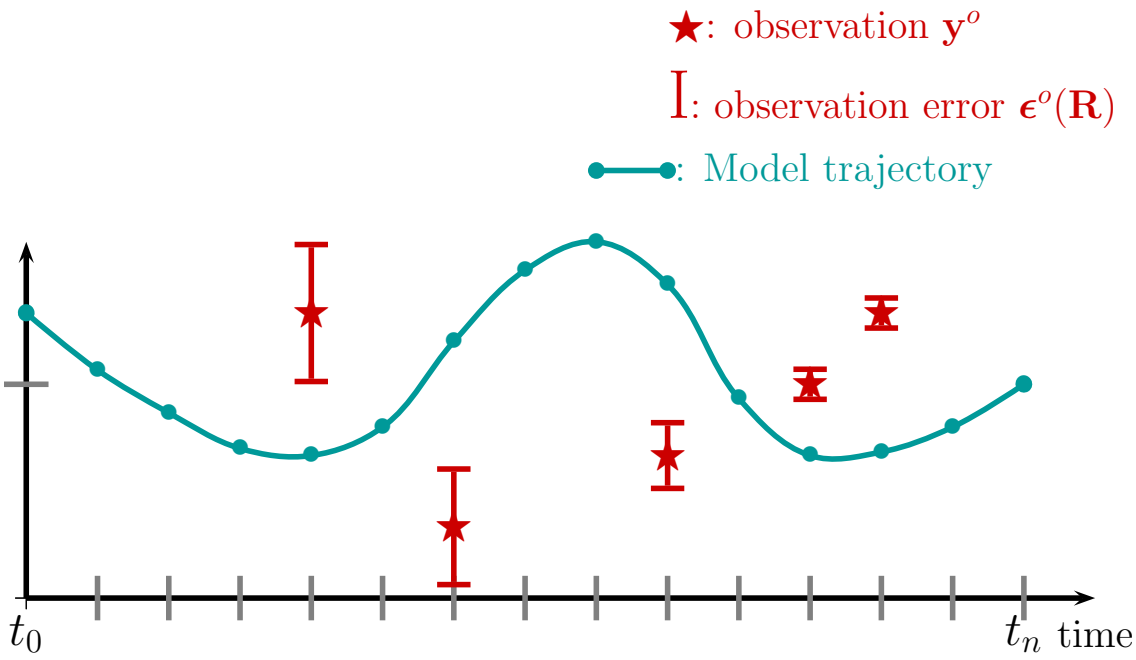

Figure 3.1: Assimilation starts with an unconstrained model trajectory over the time window of interest. It aims at correcting this initial model trajectory in order to provide an optimal fit to the available observations (the stars), given their error bars.

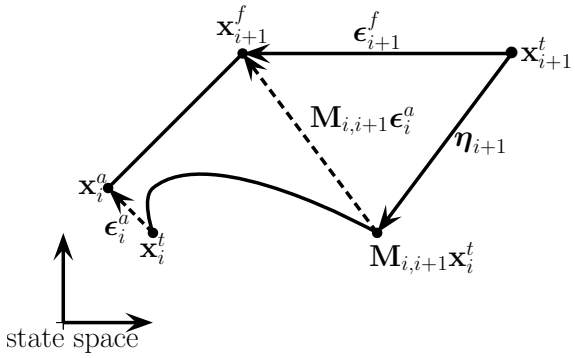

Figure 3.2: The forecast error $\boldsymbol{\epsilon}^f_{i+1}$ has two sources: One is related to the propagation of the a priori error by the model (dashed arrow), and the other is related to the model itself: $\boldsymbol{\eta}_{i+1}$ quanties the physics which the model does not account for properly. After Brasseur (2006).

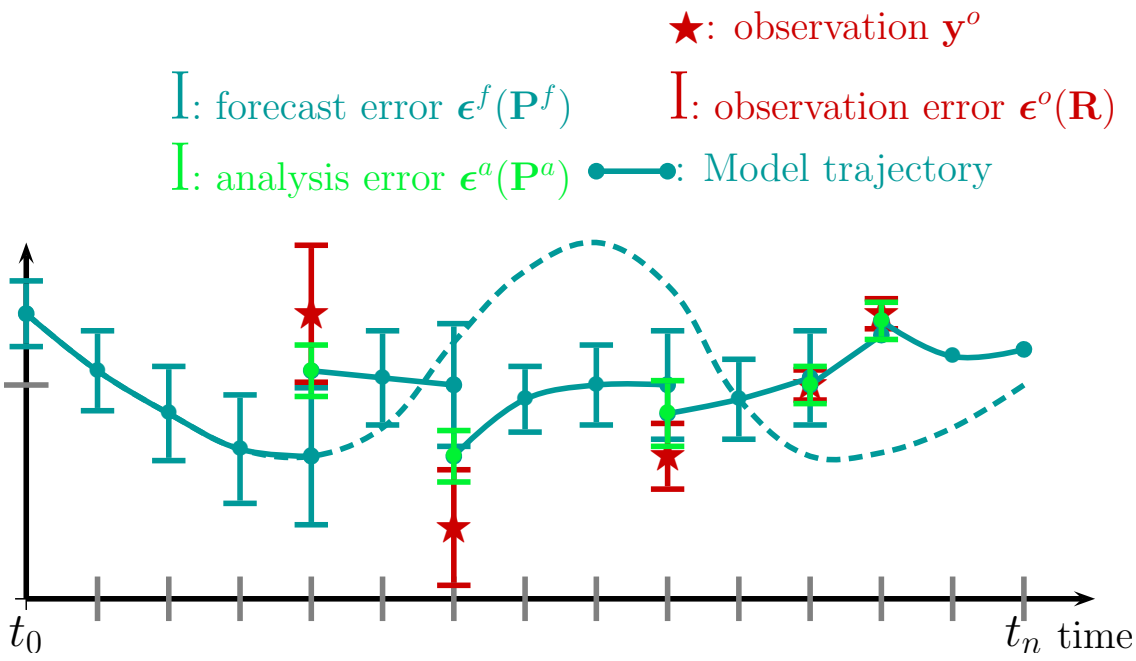

Figure 3.3: The sequential approach to data assimilation. Starting from the initial time, the model trajectory follows the initial forecast, and is characterized by a growth of the forecast error. As soon as the first observation is available, the analysis is performed (green bullet), and the associated error decreases (green error bar). The same cycle is repeated anytime an observation is available, with the assimilated trajectory deviating from the initial guess (the dashed line).

3.2.1 The forecast step

We start from some previously analyzed state $\mathbf{x}_i^a$ (or from the initial condition $\mathbf{x}_0$ if $i = 0$), characterized by the Gaussian pdf $p\left(\mathbf{x}_i^a|\mathbf{y}_{1:i}^o\right)$ of mean $\mathbf{x}_i^a$ and covariance matrix $\mathbf{P}_i^a$.

An estimate of $\mathbf{x}_{i+1}^t$ is provided by the dynamical model. This defines the **forecast**. As seen in Sect. 1.3.1, we have

$$\mathbf{x}_{i+1}^f = \mathbf{M}_{i,i+1}\mathbf{x}_i^a, \text{ and} \tag{3.1}$$

$$\mathbf{P}_{i+1}^f = \mathbf{M}_{i,i+1}\mathbf{P}_i^a\mathbf{M}_{i,i+1}^T + \mathbf{Q}_{i+1}. \tag{3.2}$$

The forecast error $\boldsymbol{\epsilon}_{i+1}^f$ results from the addition of two contributions (see Fig. 3.2): the propagation of the a priori error by the model, and the model error itself.

3.2.2 Analysis step

At time t_{i+1}, $p(\mathbf{x}_{i+1}|\mathbf{y}_{1:i}^o)$ is known through the mean $\mathbf{x}_{i+1}^f$ and covariance matrix $\mathbf{P}_{i+1}^f$, and, again, the assumption of a Gaussian distribution. The analysis step consists of updating this pdf using the observation available at time t_{i+1} and to find $p(\mathbf{x}_{i+1}|\mathbf{y}_{1:i+1}^o)$. This comes down to re-deriving the BLUE equations of paragraph 2.4, this time in a dynamical context. Therefore "all" we have

to do is compute

$$\mathbf{K}_{i+1} = \mathbf{P}^f_{i+1}\mathbf{H}^T_{i+1}\left(\mathbf{H}_{i+1}\mathbf{P}^f_{i+1}\mathbf{H}^T_{i+1} + \mathbf{R}_{i+1}\right)^{-1}, \tag{3.3}$$

$$\mathbf{x}^a_{i+1} = \mathbf{x}^f_{i+1} + \mathbf{K}_{i+1}\left(\mathbf{y}^o_{i+1} - \mathbf{H}_{i+1}\mathbf{x}^f_{i+1}\right), \tag{3.4}$$

$$\mathbf{P}^a_{i+1} = (\mathbf{I} - \mathbf{K}_{i+1}\mathbf{H}_{i+1})\mathbf{P}^f_{i+1}, \tag{3.5}$$

The principle of the Kalman filter is illustrated in Fig. 3.3.

3.3 Implementation issues

3.3.1 Definition of covariance matrices and filter divergence

In case the input statistical information is mis-specified, the filter might end up underestimating the variances of the state errors, $\boldsymbol{\epsilon}^a_i$. Too much confidence is put on the state estimation and too little confidence is put on the information contained in the observations. The effects of the analysis is minimized, and the gain happens to be too small. In the most extreme case, observations are simply rejected. This is a **filter divergence**. We will see how we can get such a behaviour when we consider our vibrating string toy problem.

Very often filter divergence is easy to diagnose: state error variances are small, and the time sequence of innovations is biased. The fix is not as easy to make as the diagnostic. The main rule to follow is not to underestimate model errors. If possible, it is better to use an adaptive scheme to tune them on-the-fly.

3.3.2 Size / Optimal interpolation

The first limitation to the straightforward application of the Kalman filter is related to the size of the problem. If n denotes the size of the state vector, the state covariance matrix is $n \times n$. Since its propagation by means of the model is n times for expensive than a model step, it becomes rapidly out of reach when n increases (not to mention its storage).

If the storage is not an issue, but the computational cost of propagating $\mathbf{P}^a$ is one, a possibility is to resort to a frozen covariance matrix

$$\mathbf{P}^a_i = \mathbf{P}^b \quad \forall t_i.$$

This defines the class of methods known as Optimal Interpolation (OI)[1].

Under this simplifying hypothesis, the two-step assimilation cycles defined above becomes:

1. Forecast:

$$\mathbf{x}^f_{i+1} = \mathbf{M}_{i,i+1}\mathbf{x}^a_i, \tag{3.6}$$

$$\mathbf{P}^f_{i+1} = \mathbf{P}^b. \tag{3.7}$$

2. Analysis:

$$\mathbf{x}^a_{i+1} = \mathbf{x}^f_{i+1} + \mathbf{K}_{i+1}\left(\mathbf{y}^o_{i+1} - \mathbf{H}\mathbf{x}^f_{i+1}\right), \tag{3.8}$$

$$\mathbf{P}^a_{i+1} = \mathbf{P}^b. \tag{3.9}$$

with $\mathbf{K}_{i+1} = \mathbf{P}^b\mathbf{H}^T_{i+1}\left(\mathbf{H}_{i+1}\mathbf{P}^b\mathbf{H}^T_{i+1} + \mathbf{R}_{i+1}\right)^{-1}$.

[1] Although the method is not really optimal, see e.g. Brasseur (2006)

There are at least two approaches to form the static covariance matrix $\mathbf{P}^b$.

1. The analytical formulation: The covariance matrix is formed from a vector of variances and a correlation matrix $\mathbf{C}$

$$\mathbf{P}^b = \mathbf{D}^{1/2}\mathbf{C}\mathbf{D}^{1/2}, \tag{3.10}$$

where $\mathbf{D}$ is a diagonal matrix holding the variances and $\mathbf{C}$ is a correlation matrix to be defined. One example is (Brasseur, 2006, and references therein)

$$C_{mn} = \left(1 + al + \frac{1}{3}a^2l^2\right)\exp(-al), \tag{3.11}$$

where a is a tunable parameter and l is the distance between the grid points m and n. We should make it clear that such an approach is mostly relevant to multi-dimensional problems, as it allows information to be spread from points where observations are made to points where they are missing (think of satellite observation of sea surface height, for instance).

2. The second approach consists of taking an ensemble of N_e snapshots of the state vector from a model free run, and to build the first and second statistical moments, $\mathbf{x}^b$ and $\mathbf{P}^b$, from this collection of snapshots. In practice we compute

$$\mathbf{x}^b = \frac{1}{N_e}\sum_{e=1}^{N_e}\mathbf{x}_e, \tag{3.12}$$

$$\mathbf{P}^b = \frac{1}{N_e-1}\sum_{e=1}^{N_e}\left(\mathbf{x}_e - \mathbf{x}^b\right)\left(\mathbf{x}_e - \mathbf{x}^b\right)^T. \tag{3.13}$$

The static approach suffers from the fact that if a correction is applied along a certain direction in state space during an update, the error statistics are not modified accordingly (by virtue of Eq.(3.9) above). During the next update, the same level of correction might be applied along the very same direction, whereas it might not be needed. The static approach is therefore more suitable if two successive assimilation cycles are separated by a long enough time, so that the corresponding dynamical states are decorrelated enough.

3.3.3 Evolution of the state error covariance matrix

In principle, Eq. (3.2) generates a symmetric matrix. Its practical implementation may not. Numerical truncation errors my lead to an asymmetric covariance matrix and a subsequent collapse of the filter. A remedy is to add an extra step to enforce symmetry, such as

$$\mathbf{P}^f_{i+1} = \frac{1}{2}\left(\mathbf{P}^f_{i+1} + \mathbf{P}^f_{i+1}{}^T\right).$$

Another possibility is to use the square root decomposition of the covariance matrix. Since $\mathbf{P}^a$ is symmetric positive definite, it can be written as

$$\mathbf{P}^a = \mathbf{S}^a\mathbf{S}^{aT},$$

where $\mathbf{S}^a$ is a $n \times n$ matrix. This decomposition is not unique. For instance, in Lab 3, we will use a Cholesky factorization which will provide us with a lower triangular matrix $\mathbf{S}^a$. The propagation of the covariance matrix is performed by first computing $\mathbf{M}_{i,i+1}\mathbf{S}^a_i$, and then by assembling $\mathbf{P}^f_{i+1} = (\mathbf{M}_{i,i+1}\mathbf{S}^a_i)(\mathbf{M}_{i,i+1}\mathbf{S}^a_i)^T + \mathbf{Q}_{i+1}$.

3.3.4 Nonlinearities

Nonlinearities are ubiquitous in geophysical fluid dynamics, and the cause of a great deal of concern for the data assimilation practitioner. Nonlinearities are likely to spoil the Gaussianity of statistics. In addition, the model can no longer be represented by a matrix, and its transpose is no longer defined. This statement also applies to a nonlinear observation operator. A way to proceed with nonlinearities is provided by the Extended Kalman Filter (EKF), which relies on a local linearization about the current model trajectory. This linearization is of course valid only in the case of a weakly nonlinear system.

3.3.4.1 The extended Kalman filter (EKF)

When the dynamical model $\mathcal{M}$ and/or the observation operator $\mathcal{H}$ are (weakly) nonlinear, the Kalman filter can be extended by resorting to the **tangent linear** approximation of $\mathcal{M}$ and $\mathcal{H}$, denoted by $\mathbf{M}$ and $\mathbf{H}$, respectively. The two-step filter assimilation cycle now writes :

1. Forecast:

$$\mathbf{x}^f_{i+1} = \mathcal{M}_{i,i+1}(\mathbf{x}^a_i), \text{ (nonlinear forecast)} \tag{3.14}$$

$$\mathbf{P}^f_{i+1} = \mathbf{M}_{i,i+1}\mathbf{P}^a_i\mathbf{M}^T_{i,i+1} + \mathbf{Q}_{i+1}. \text{ (linear forecast)} \tag{3.15}$$

2. Analysis:

$$\mathbf{x}^a_{i+1} = \mathbf{x}^f_{i+1} + \mathbf{K}_{i+1}\left[\mathbf{y}^o_{i+1} - \mathcal{H}_{i+1}\left(\mathbf{x}^f_{i+1}\right)\right], \tag{3.16}$$

$$\mathbf{P}^a_{i+1} = \left(\mathbf{I} - \mathbf{K}_{i+1}\mathbf{H}_{i+1}\right)\mathbf{P}^f_{i+1}. \tag{3.17}$$

with $\mathbf{K}_{i+1} = \mathbf{P}^f_{i+1}\mathbf{H}^T_{i+1}\left(\mathbf{H}_{i+1}\mathbf{P}^f_{i+1}\mathbf{H}^T_{i+1} + \mathbf{R}_{i+1}\right)^{-1}$.

3.3.4.2 The ensemble Kalman filter (EnKF)

The Kalman filter is only optimal in the case of Gaussian statistics and linear operators, in which case the first two moments (the mean and the covariances) suffice to describe the pdf entering the estimation problem. Practitioners report that its linearized extension to nonlinear problems, the EKF, only works for moderate deviations from linearity and Gaussianity (e.g. Miller et al., 1994). The ensemble Kalman filter (Evensen, 1994, 2009) is a method which has been designed to deal with strong nonlinearities and non-Gaussian statistics, whereby the pdf is described by an ensemble of N_e time-dependent states, $\mathbf{x}_{i,e}$.

A given cycle still consists of a forecast followed by an analysis, which relies on the good old BLUE. The statistical information needed by the BLUE (see below) is provided by the ensemble, at the exception of the observation errors in Eq. 3.24 below, which are random drawings from the Gaussian distribution $\mathcal{N}(\mathbf{0}, \mathbf{R}_i)$. This is necessary for consistency with the observation error covariance matrix.

1. Forecast:

$$\mathbf{x}^f_{i,e} = \mathcal{M}_{i-1,i}(\mathbf{x}^a_{i-1,e}) + \boldsymbol{\eta}_{i,e}, \quad e = \{1, \ldots, N_e\}. \tag{3.18}$$

2. Analysis:

$$\langle \mathbf{x}^f_i \rangle = \frac{1}{N_e} \sum_{e=1}^{N_e} \mathbf{x}^f_{i,e}, \tag{3.19}$$

$$\mathbf{P}^f_i = \frac{1}{N_e - 1} \sum_{e=1}^{N_e} \left(\mathbf{x}^f_{i,e} - \langle \mathbf{x}^f_i \rangle \right) \left(\mathbf{x}^f_{i,e} - \langle \mathbf{x}^f_i \rangle \right)^T, \tag{3.20}$$

$$\mathbf{H}_i \mathbf{P}^f_i = \frac{1}{N_e - 1} \sum_{e=1}^{N_e} \left[\mathcal{H}_i \left(\mathbf{x}^f_{i,e} \right) - \mathcal{H}_i \left(\langle \mathbf{x}^f_i \rangle \right) \right] \left[\mathbf{x}^f_{i,e} - \langle \mathbf{x}^f_i \rangle \right]^T \tag{3.21}$$

$$\mathbf{H}_i \mathbf{P}^f_i \mathbf{H}^T_i = \frac{1}{N_e - 1} \sum_{e=1}^{N_e} \left[\mathcal{H}_i \left(\mathbf{x}^f_{i,e} \right) - \mathcal{H}_i \left(\langle \mathbf{x}^f_i \rangle \right) \right] \left[\mathcal{H}_i \left(\mathbf{x}^f_{i,e} \right) - \mathcal{H}_i \left(\langle \mathbf{x}^f_i \rangle \right) \right]^T \tag{3.22}$$

$$\mathbf{K}_i = \left(\mathbf{H}_i \mathbf{P}^f_i \right)^T \left[\mathbf{H}_i \mathbf{P}^f_i \mathbf{H}^T_i + \mathbf{R}_i \right]^{-1}, \tag{3.23}$$

$$\mathbf{y}^o_{i,e} = \mathbf{y}^o_i + \boldsymbol{\epsilon}^o_e, \quad e = \{1, \ldots, N_e\}, \tag{3.24}$$

$$\mathbf{x}^a_{i,e} = \mathbf{x}^f_{i,e} + \mathbf{K}_i \left[\mathbf{y}^o_{i,e} - \mathcal{H}_i \left(\mathbf{x}^f_{i,e} \right) \right], \quad e = \{1, \ldots, N_e\}. \tag{3.25}$$

The problem of storing the state covariance matrix $\mathbf{P}^a$ is solved, since "only" N_e state vectors need be stored.

A detailed description of the implementation of the EnKF can be found in the book written by its inventor, Geir Evensen, along with a comprehensive list of related publications (appendix B of the book). We will apply the EnKF to Lorenz's 1963 model in our computer-based lab 2.

A note of caution: the update phase (3.25) is still linear, as the Kalmain gain matrix is produced using Eq. (3.23).

Chapter 4

Variational assimilation

Here is a slightly modified excerpt taken from our review paper (Fournier et al., 2010).

Unlike sequential assimilation (which emanates from estimation theory), variational assimilation is rooted in optimal control theory. The analyzed state is not defined as the one maximizing a certain pdf, but as the one minimizing a functional $\mathcal{J}$ of the form

$$\mathcal{J}(\mathbf{x}) = \frac{1}{2}\left\{\sum_{i=0}^{n}\left[\mathcal{H}_i\mathbf{x}_i - \mathbf{y}_i^o\right]^T \mathbf{R}_i^{-1}\left[\mathcal{H}_i\mathbf{x}_i - \mathbf{y}_i^o\right] + \left[\mathbf{x}-\mathbf{x}^b\right]^T \mathbf{P}^{b^{-1}}\left[\mathbf{x}-\mathbf{x}^b\right]\right\}, \tag{4.1}$$

in which $\mathbf{x}_i = \mathcal{M}_{i,i-1}\cdots\mathcal{M}_{1,0}\mathbf{x}$, the sought $\mathbf{x}$ being the best estimate of the initial state of the core, $\mathbf{x}_0$. This objective function is defined over the entire time window of interest. It is the sum of two terms. The first one measures the distance between the observations and the predictions of the model. It is weighted by the confidence we have in the observations. The second term is analogous to the various norms which are added when solving the kinematic core flow problem; it evaluates the distance between the initial condition and an a priori background state $\mathbf{x}^b$. That stabilizing term is weighted by the confidence we have in the definition of the background state, described by the background error covariance matrix $\mathbf{P}^b$[1]. Defining a background state for the core is no trivial matter. But one may substitute (or supplement) the corresponding term in equation 4.1 by (with) another stabilizing term, typically a norm, as was done by Talagrand and Courtier (1987) and Courtier and Talagrand (1987) in their early numerical experiments with the vorticity equation on the sphere.

The goal of variational data assimilation is to minimize $\mathcal{J}$ by adjusting its control variables (or parameters), usually the initial condition $\mathbf{x}_0$ (if everything else is held fixed, see Fig. 4.1), as implied by our formulation in equation 4.1. Iterative minimization requires the computation of the sensitivity (gradient) of $\mathcal{J}$ with respect to its control vector, which writes $\left(\boldsymbol{\nabla}_{\mathbf{x}_0}\mathcal{J}\right)^T$ (the transpose is needed since $\boldsymbol{\nabla}_{\mathbf{x}_0}\mathcal{J}$ is by definition a row vector, recall Eq. 2.18). The size of the problem (the size of the state vector n) precludes a brute force calculation of the gradient (which would imply n realizations of the forward model over $[t_0, t_n]$). Fortunately, as pointed out early on by Le Dimet and Talagrand (1986) and Talagrand and Courtier (1987), a much more affordable method exists: The so-called adjoint method, which is based on the integration of the so-called adjoint equation backward in time

$$\mathbf{a}_{i-1} = \mathbf{M}_{i-1,i}^T\mathbf{a}_i + \mathbf{H}_{i-1}^T\mathbf{R}_{i-1}^{-1}(\mathcal{H}_{i-1}\mathbf{x}_{i-1} - \mathbf{y}_{i-1}^o) + \delta_{i1}\mathbf{P}^{b^{-1}}\left(\mathbf{x}_{i-1}-\mathbf{x}^b\right), \quad n \geq i \geq 1, \tag{4.2}$$

starting from $\mathbf{a}_{n+1} = \mathbf{0}$, where $\mathbf{a}$ is the adjoint field, and δ is the Kronecker symbol. The initial value of the adjoint field provides the sensitivity we seek: $\left(\boldsymbol{\nabla}_{\mathbf{x}_0}\mathcal{J}\right)^T = \mathbf{a}_0$ (e.g. Fournier et al.,

[1] Ide et al. (1997), and many others, use $\mathbf{B}$ to denote that matrix, a notation which is preempted in our case by the magnetic induction.

2007); a derivation of Eq. (4.2) is provided in Appendix A. Note that when writing equation 4.2, we assumed for simplicity that observations were available at every model time-step.

Equation 4.2 indicates that over the course of the backward integration, the adjoint field is fed with innovation vectors. Those vectors have an observational component ($\mathcal{H}_{i-1}\mathbf{x}_{i-1} - \mathbf{y}^o_{i-1}$), and a departure-to-background component $\left(\mathbf{x}_0 - \mathbf{x}^b\right)$ for the initial condition, these two contributions being weighted by the statistics introduced above. The adjoint model $\mathbf{M}^T$ in equation 4.2 is the adjoint of the tangent linear model $\mathbf{M}$ introduced previously in the context of the extended Kalman filter (Sec. 3.3.4.1). The adjoint model has a computational cost similar to that of the forward model, and makes it possible to use an iterative minimization algorithm suitable for large-scale problems.

A few comments on the adjoint method are in order:

- It demands the implementation of the adjoint model $\mathbf{M}^T$: the rules to follow for deriving (and validating) the tangent linear and adjoint codes from an existing forward code are well documented in the literature (e.g. Talagrand, 1991; Giering and Kaminski, 1998), and leave no room for improvisation. Still, this process is rather convoluted. It requires expertise and deep knowledge of the forward code to begin with. The best situation occurs when the forward code is written in a modular fashion, bearing in mind that its adjoint will be needed in the future, and by casting as many operations as possible in terms of matrix-matrix or matrix-vector products (for a one-dimensional illustration with a spectral-element, non-linear magnetohydrodynamic model, see Fournier et al., 2007). The task of coding an adjoint by hand can still become beyond human reach in the case of a very large model. One might then be tempted to resort to an automated differentiation algorithm. Automated differentiation (AD) is a very active field of research[2]: several operational tools are now available, some of which have been tested on geophysical problems by Sambridge et al. (2007).

- The discrete adjoint equation 4.2 is based on the already discretized model of core dynamics. An alternative exists, which consists first in deriving the adjoint equation at the continuous level, and second in discretizing it, using the same machinery as the one used to discretize the forward model. In most instances, both approaches to the adjoint problem yield the same discrete operators. When in doubt, though, in the case of a minimization problem, one should take the safe road and derive the adjoint of the already discretized problem: This guarantees that the gradient injected in the minimization algorithm is exactly the one corresponding to the discrete cost function (equation 4.1), up to numerical roundoff error. Since the efficiency of a minimization algorithm grows in proportion to its sensitivity to errors in the gradient, any error in the gradient could otherwise result in a suboptimal solution.

- The adjoint approach is versatile. Aside from the initial state $\mathbf{x}_0$, one can declare static model parameters (static fields, material properties) adjustable, and add them to the control vector.

- In the case of a non-linear problem, the forward trajectory $\mathbf{x}_i$, $i \in \{0, \ldots, n\}$, is needed to integrate the adjoint equation. The storage of the complete trajectory may cause memory issues (even on parallel computers), which are traditionally resolved using a so-called checkpointing strategy. The state of the system is stored at a limited number of discrete times, termed checkpoints. Over the course of the backward integration of the adjoint model, these checkpoints are then used to recompute local portions of the forward trajectory on-the-fly, whenever those portions are needed (e.g. Hersbach, 1998).

- On a more general note, adjoint methods have gained some popularity in solid Earth geophysics over the past few years, a joint consequence (again) of the increase in computational power and the availability of high-quality satellite, or ground-based, data. Adjoint methods are now applied to problems related to the structure and evolution of the deep Earth: Electromagnetic induction (Kelbert et al., 2008; Kuvshinov et al., 2010), mantle convection

[2] www.autodiff.org

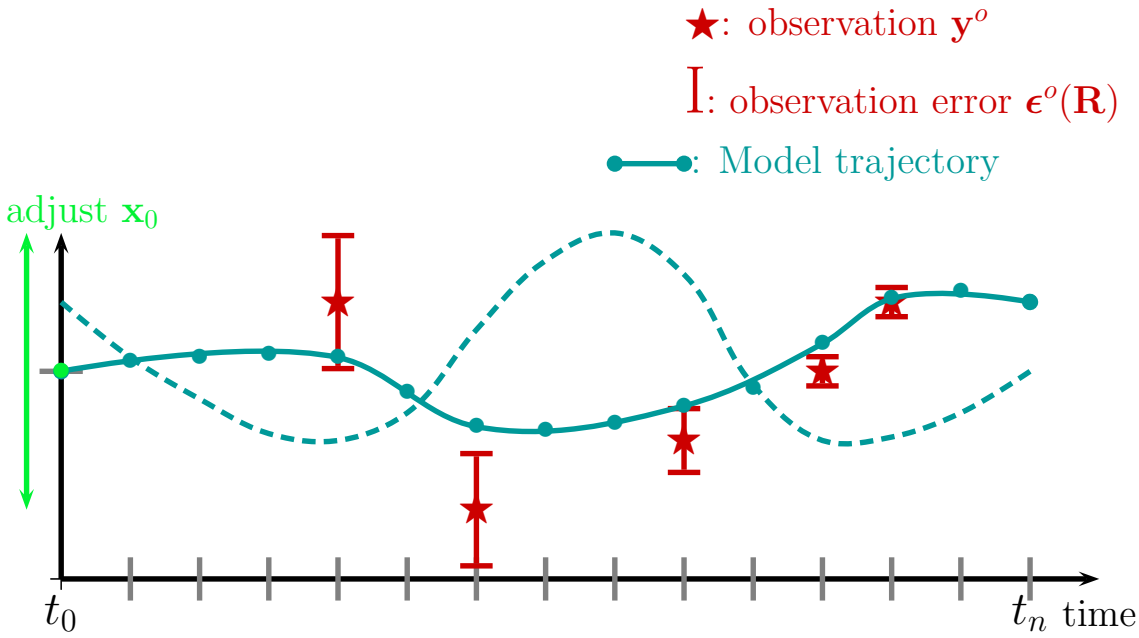

Figure 4.1: The variational approach to data assimilation. After adjustment of the initial condition $\mathbf{x}_0$ (the green bullet on the $t = t_0$ axis) by means of an iterative minimization algorithm, the model trajectory is corrected over the entire time window, in order to provide an optimal fit to the data (in a generalized least squares sense). The dashed line corresponds to the initial (unconstrained) guess of the model trajectory introduced in Fig. 3.1.

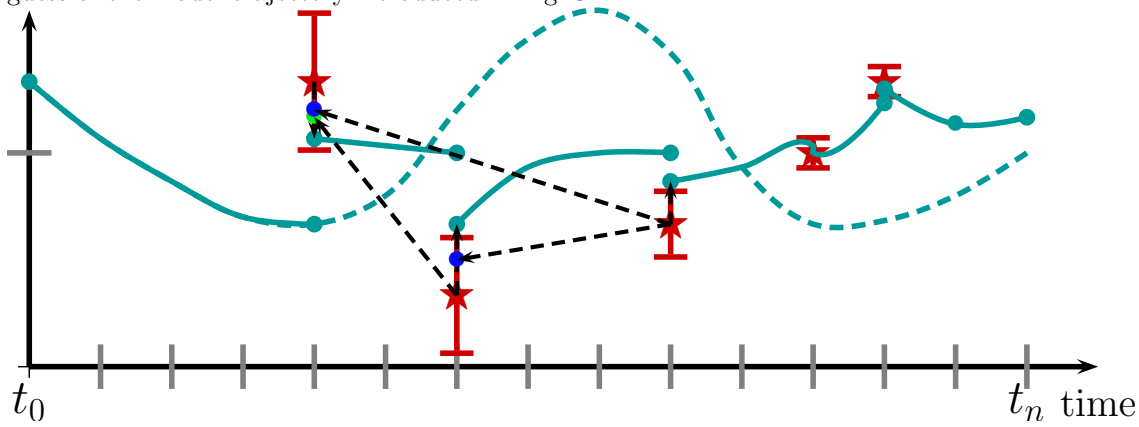

Figure 4.2: Principle of sequential smoothing. The state to observation difference (the innovation) at analysis time can be used to retrospectively correct the past products of analysis.

(Bunge et al., 2003; Liu and Gurnis, 2008; Liu et al., 2008), and seismic wave propagation (Tromp et al., 2005; Fichtner et al., 2006; Tromp et al., 2008), building in that last case on the theoretical work of Tarantola (1984, 1988).

The application of a variational approach to time-dependent problems has been generically labeled as the 4D-Var approach to data assimilation (e.g. Courtier, 1997), and is commonly referred to as 4D-Var. As such, the standard 4D-Var suffers from two drawbacks: It assumes that the model is perfect ($\boldsymbol{\eta} = \mathbf{0}$), and it does not provide direct access to the statistics of the analysis error - notice its absence in Fig. 4.1. An alternative approach to the "strong constraint" assumption ($\boldsymbol{\eta} = \mathbf{0}$) consists in adding a term quantifiying the model error in the definition of the cost function, a term whose weight is controlled by an a priori forecast error covariance. This more general "weak constraint" approach (Sasaki, 1970) has been successfully introduced and implemented (under the name "method of representers") in physical oceanography during the past fifteen years (Egbert et al., 1994; Bennett, 2002, and references therein).

From a general perspective, the advantages of a variational approach are its flexibility regarding the definition and identification of control variables, and its natural ability to handle time-dependent observation operators (and possibly time-correlated errors). It is also well-suited for the reanalysis of past data records (hindcasting), since the state at a given time is estimated using the past and future observations available over the entire time window (see Fig. 4.1). Note, however, that hindcasting is also possible if one resorts to sequential smoothers (see Fig. 4.2), of the kind described by e.g. Cohn et al. (1994), and applied in an oceanic context by e.g. Cosme et al. (2010).

Bibliography

Bennett, A., 2002: *Inverse modeling of the Ocean and Atmosphere*. Cambridge University Press, Cambridge.

Brasseur, P., 2006: Ocean data assimilation using sequential methods based on the Kalman filter. *Ocean Weather Forecasting: An Integrated View of Oceanography*, E. Chassignet and J. Verron, Eds., Springer, 271–316.

Bunge, H.-P., C. Hagelberg, and B. Travis, 2003: Mantle circulation models with variational data assimilation: inferring past mantle flow and structure from plate motion histories and seismic tomography. *Geophysical Journal International*, **152 (2)**, 280–301, doi:10.1046/j.1365-246X.2003.01823.x.

Cohn, S., N. Sivakumaran, and R. Todling, 1994: A Fixed-Lag Kalman Smoother for Retrospective Data Assimilation. *Monthly Weather Review*, **122 (12)**, 2838–2867, doi:10.1175/1520-0493(1994)122$\langle$2838:AFLKSF$\rangle$2.0.CO;2.

Cosme, E., J.-M. Brankart, J. Verron, P. Brasseur, and M. Krysta, 2010: Implementation of a reduced-rank, square-root smoother for high resolution ocean data assimilation. *Ocean modelling*, **33**, 87–100, doi:10.1016/j.ocemod.2009.12.004.

Courtier, P., 1997: Variational Methods. *Journal of the Meteorological Society of Japan*, **75 (1B)**, 211–218.

Courtier, P. and O. Talagrand, 1987: Variational assimilation of meteorological observations with the adjoint vorticity equation. II: Numerical results. *Quarterly Journal of the Royal Meteorological Society*, **113 (478)**, 1329–1347, doi:10.1002/gj.49711347813.

Egbert, G. D., A. F. Bennett, and M. G. G. Foreman, 1994: TOPEX/POSEIDON tides estimated using a global inverse model. *Journal of Geophysical Research*, **99 (C12)**, 24 821–24 852, doi:10.1029/94JC01894.

Evensen, G., 1994: Sequential data assimilation with a nonlinear quasi-geostrophic model using Monte Carlo methods to forecast error statistics. *Journal of Geophysical Research*, **99 (C5)**, 10 143–10 162, doi:10.1029/94JC00572.

Evensen, G., 2009: *Data assimilation: The ensemble Kalman filter*. 2d ed., Springer, Berlin, doi:10.1007/978-3-642-03711-5.

Fichtner, A., H. P. Bunge, and H. Igel, 2006: The adjoint method in seismology I. Theory. *Physics of the Earth and Planetary Interiors*, **157 (1-2)**, 86–104, doi:10.1016/j.pepi.2006.03.016.

Fournier, A., C. Eymin, and T. Alboussière, 2007: A case for variational geomagnetic data assimilation: insights from a one-dimensional, nonlinear, and sparsely observed MHD system. *Nonlinear Processes in Geophysics*, **14**, 163–180, doi:10.5194/npg-14-163-2007.

Fournier, A., et al., 2010: An introduction to data assimilation and predictability in geomagnetism. *Space Science Reviews*, 1–45, 10.1007/s11214-010-9669-4.

Ghil, M. and P. Malanotte-Rizzoli, 1991: Data assimilation in meteorology and oceanography. *Advances in geophysics*, **33**, 141–266.

Giering, R. and T. Kaminski, 1998: Recipes for adjoint code construction. *ACM Transactions on Mathematical Software*, **24 (4)**, 437–474.

Hersbach, H., 1998: Application of the adjoint of the WAM model to inverse wave modeling. *Journal of geophysical research*, **103 (C 5)**, 10 469–10 487, doi:10.1029/97JC03554.

Ide, K., P. Courtier, M. Ghil, and A. C. Lorenc, 1997: Unified notation for data assimilation: Operational, sequential and variational. *Journal of the meteorological society of Japan*, **75**, 181–189.

Kalnay, E., 2003: *Atmospheric modeling, data assimilation, and predictability*. Cambridge University Press, Cambridge.

Kelbert, A., G. Egbert, and A. Schultz, 2008: Non-linear conjugate gradient inversion for global EM induction: resolution studies. *Geophysical Journal International*, **173 (2)**, 365–381, doi:10.1111/j.1365-246X.2008.03717.x.

Kuvshinov, A., et al., 2010: Level 2 products and performances for mantle studies with swarm. Tech. rep., ESA. URL http://esamultimedia.esa.int/docs/EarthObservation/Induction_Study_150110.pdf.

Le Dimet, F.-X. and O. Talagrand, 1986: Variational algorithms for analysis and assimilation of meteorological observations: Theoretical aspects. *Tellus*, **38 (2)**, 97–110.

Liu, L. and M. Gurnis, 2008: Simultaneous inversion of mantle properties and initial conditions using an adjoint of mantle convection. *Journal of Geophysical Research*, **113 (B8405)**, doi:10.1029/2008JB005594.

Liu, L., S. Spasojevic, and M. Gurnis, 2008: Reconstructing Farallon Plate Subduction Beneath North America Back to the Late Cretaceous. *Science*, **322 (5903)**, 934–938, doi:10.1126/science.1162921.

Lorenc, A. C., 1986: Analysis methods for numerical weather prediction. *Quarterly Journal of the Royal Meteorological Society*, **112 (474)**, 1177–1194, doi:10.1002/qj.49711247414.

Miller, R. N., M. Ghil, and F. Gauthiez, 1994: Advanced data assimilation in strongly nonlinear dynamical systems. *Journal of the Atmospheric Sciences*, **51 (8)**, 1037–1056, doi:10.1175/1520-0469(1994)051$\langle$$1037:ADAISN$\rangle$$2.0.CO;2.

Parker, R. L., 1994: *Geophysical inverse theory*. Princeton University Press, Princeton, NJ.

Sambridge, M., P. Rickwood, N. Rawlinson, and S. Sommacal, 2007: Automatic differentiation in geophysical inverse problems. *Geophysical Journal International*, **170 (1)**, 1–8, doi:10.1111/j.1365-246X.2007.03400.x.

Sasaki, Y., 1970: Some basic formalisms in numerical variational analysis. *Monthly Weather Review*, **98 (12)**, 875–883, doi:10.1175/1520-0493(1970)098$\langle$$0875:SBFINV$\rangle$$2.3.CO;2.

Talagrand, O., 1991: The use of adjoint equations in numerical modelling of the atmospheric circulation. *Automatic Differentiation of Algorithms: Theory, Implementation, and Application*, A. Griewank and G. G. Corliss, Eds., Society for Industrial and Applied Mathematics, Philadelphia, PA, 169–180.

Talagrand, O., 1997: Assimilation of observations, an introduction. *Journal of the Meteorological Society of Japan*, **75 (1B)**, 191–209.

Talagrand, O. and P. Courtier, 1987: Variational assimilation of meteorological observations with the adjoint vorticity equation. I: Theory. *Quarterly Journal of the Royal Meteorological Society*, **113 (478)**, 1311–1328, doi:10.1002/gj.49711347812.

Tarantola, A., 1984: Inversion of seismic reflection data in the acoustic approximation. *Geophysics*, **49 (8)**, 1259–1266, doi:10.1190/1.1441754.

Tarantola, A., 1988: Theoretical background for the inversion of seismic waveforms including elasticity and attenuation. *Pure and Applied Geophysics*, **128 (1)**, 365–399, doi:10.1007/BF01772605.

Tarantola, A., 2005: *Inverse problem theory and methods for model parameter estimation*. Society for Industrial Mathematics, Philadelphia, PA.

Tromp, J., D. Komatitsch, and Q. Liu, 2008: Spectral-element and adjoint methods in seismology. *Communications in Computational Physics*, **3 (1-32)**.

Tromp, J., C. Tape, and Q. Liu, 2005: Seismic tomography, adjoint methods, time reversal and banana-doughnut kernels. *Geophysical Journal International*, **160 (1)**, 195–216, doi:10.1111/j.1365-246X.2004.02453.x.

Wunsch, C., 2006: *Discrete inverse and state estimation problems*. Cambridge University Press, Cambridge.

Part II

Slides

An introduction to geomagnetic data assimilation

Alexandre Fournier

Institut de Physique du Globe de Paris

ICTP, Trieste, November 1st, 2012

http://avsgeomag.ipgp.fr

Outline

Introduction – data and field modelling

3D sequential assimilation experiments using synthetic data

Outline

Introduction – data and field modelling

3D sequential assimilation experiments using synthetic data

Messages

- Geomagnetic data provided over the last decade by satellites (and used in conjunction with observatory data) have allowed us to get a more accurate description of the rapid variations of the main geomagnetic field (generated inside earth's core)
- This better description is an incentive for constructing and testing physical models of core dynamics able to account for the observed geomagnetic variations (in a data assimilation framework).
- This effort started about 5 years ago, and we are still at the research (non-operational) stage.

Special thanks to Julien Aubert (IPGP) and Chris Finlay (DTU)

The Earth's main magnetic field

$$\begin{aligned}
\mathbf{B} &= -\nabla V \text{ in a current-free region,} \\
V(\mathbf{r},t) &= a\sum_{\ell,m}\left(\frac{a}{r}\right)^{\ell+1}\left[g_\ell^m(t)\cos m\varphi + h_\ell^m(t)\sin m\varphi\right]P_\ell^m(\cos\theta), \\
B_r(\mathbf{r},t) &= \sum_{\ell,m}\left(\frac{a}{r}\right)^{\ell+2}\left[g_\ell^m(t)\cos m\varphi + h_\ell^m(t)\sin m\varphi\right]P_\ell^m(\cos\theta).
\end{aligned}$$

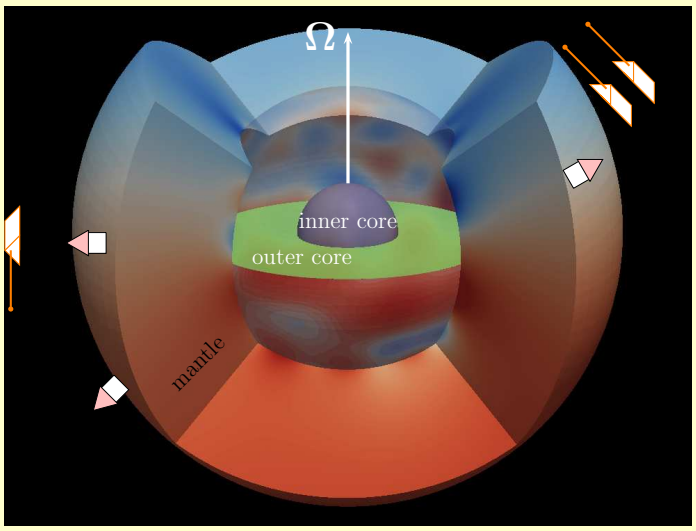

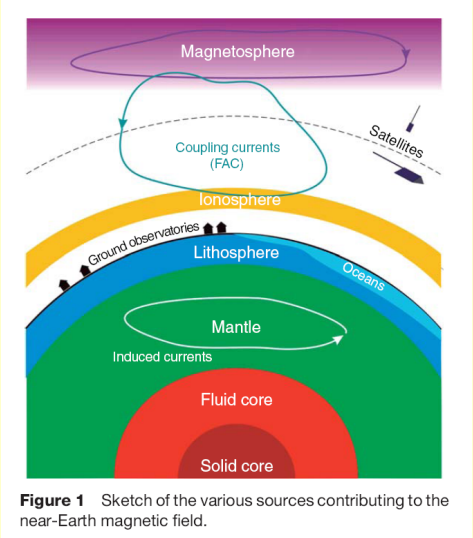

Figure 1 Sketch of the various sources contributing to the near-Earth magnetic field.

Hulot, Sabaka, Olsen TOG 2007

Geomagnetic observations are connected with the (large-scale) radial component of the magnetic induction, B_r, at the core surface (the small scales are screened by the crustal field).

Observed geomagnetic field components

(Courtesy Chris Finlay)

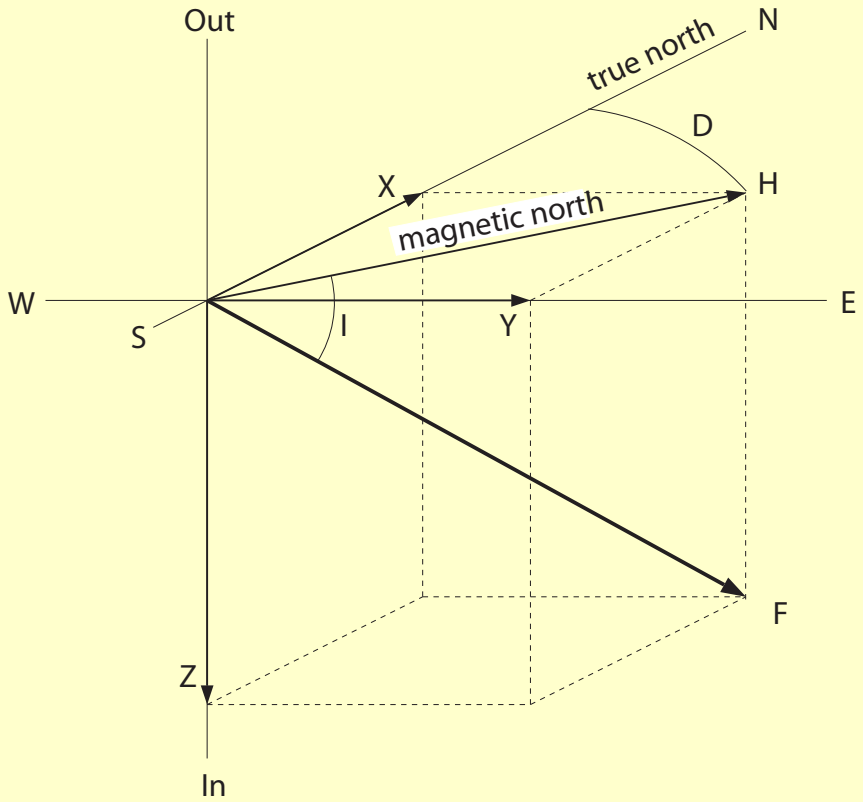

Commonly observed components of the geomagnetic field.

Sensitivity to the core surface magnetic field

(Courtesy Chris Finlay)

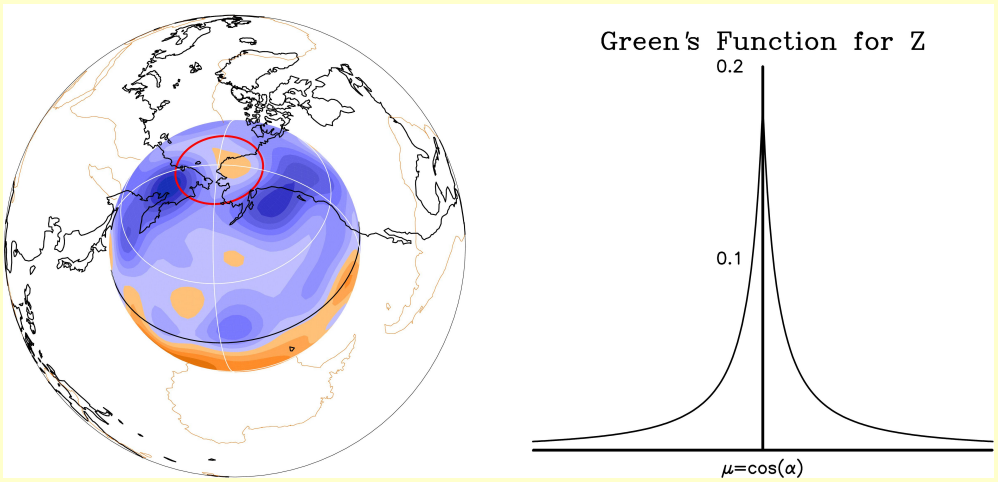

Z at core surface with Earth's surface shown together with the relevant Green's fns.

- Each observation is a weighted average of the core surface field **(Gubbins& Roberts, GJRAS, 1983)**

Sensitivity of D, I, F to B_r at the core surface.

(Courtesy Chris Finlay)

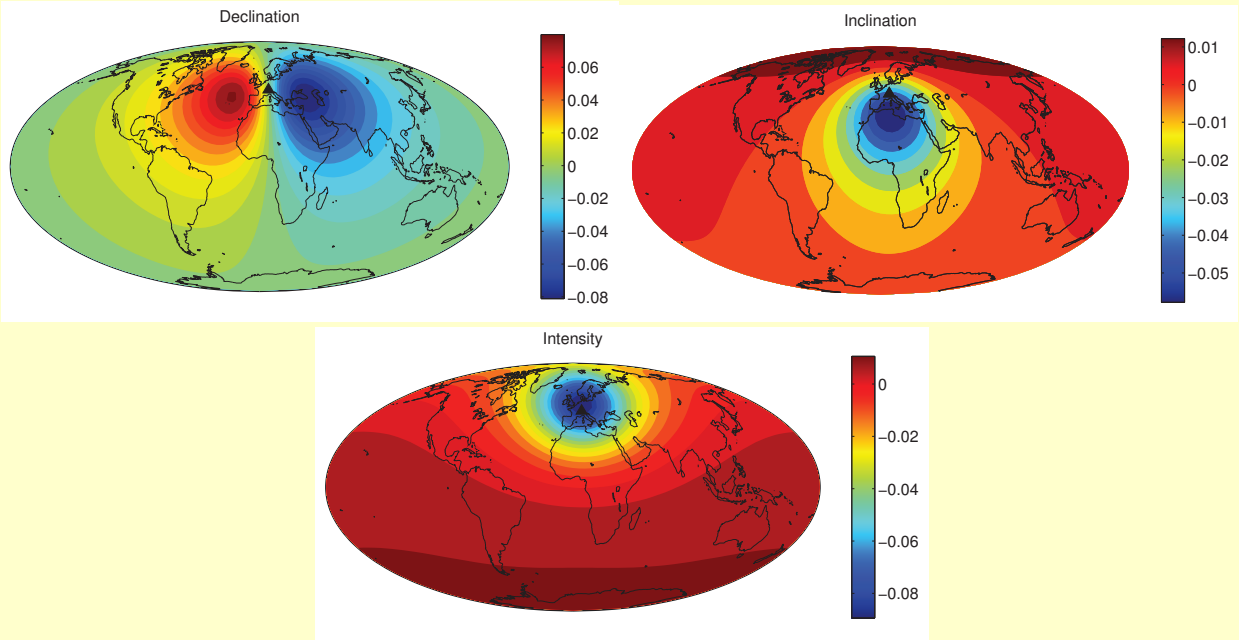

Averaging Kernel's showing sensitivity to B_r at core surface of D, I and F observations in central Europe at Earth's surface. (Plots courtesy of S. Panovska.)

Paleomagnetic observations

(Courtesy Chris Finlay)

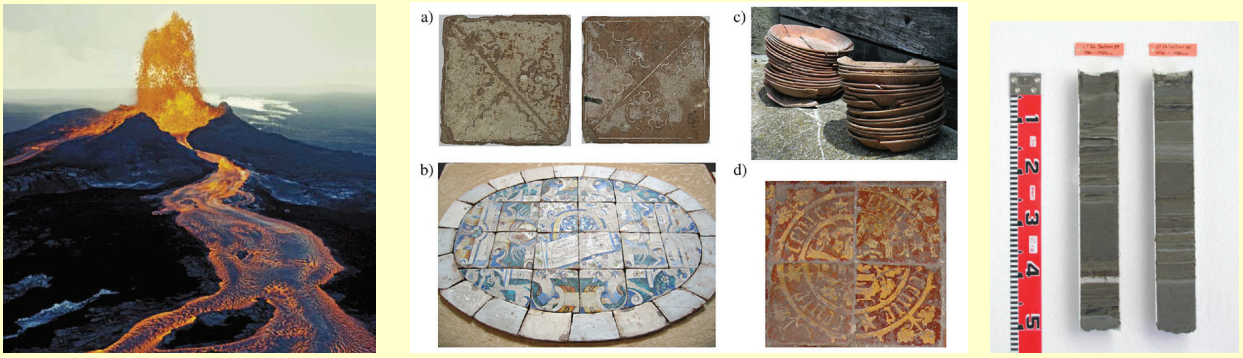

Examples of paleomagnetic data sources: Left: Lavas on Hawaii; Middle: archeological artifacts **(Genevey et al, EPSL, 2009)**; Right: a lake sediment core.

- Magnetization acquired by rocks during formation and artifacts during production records direction and intensity of the ancient field.

Temporal distribution of records in past 10kyrs

(Courtesy Chris Finlay)

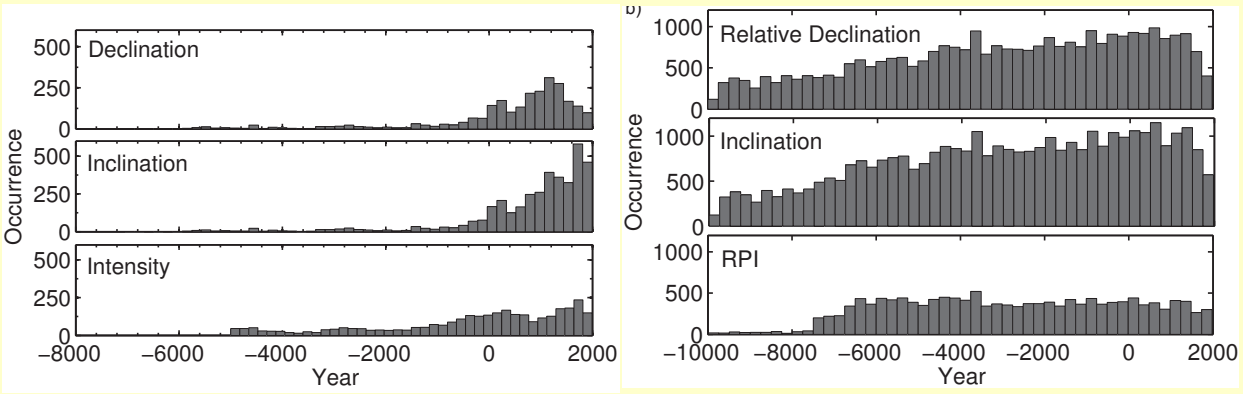

Time distribution of archeomagnetic and (left) and sediment (right) magnetic records during the past 10 kyrs **(Korte et al., EPSL, 2011)**, in 200 yr bins, courtesy of S. Panovska.

Distribution of sediment magnetic data (10 kyrs)

(Courtesy Chris Finlay)

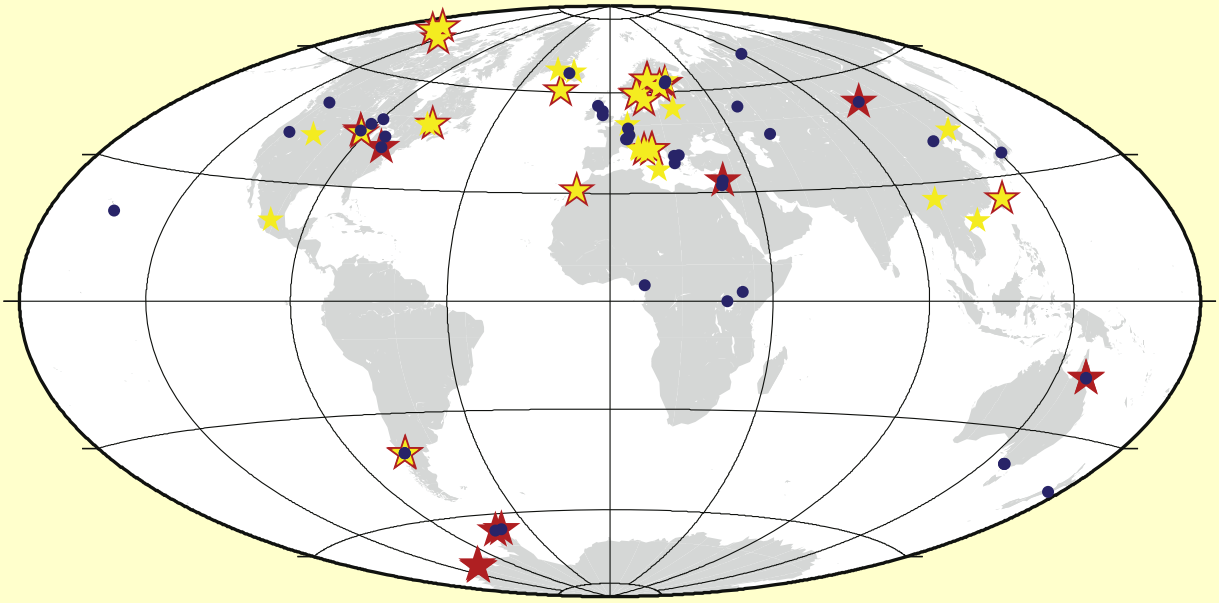

Locations of lake sediment records used to constrain the CALS10K model of **Korte et al. (EPSL, 2011)** spanning the past 10kyrs. Stars show locations of new records: Yellow stars for D/I, red stars or red borders around yellow stars for RPI. Locations of previously used records are blue dots.

Historical observations

(Courtesy Chris Finlay)

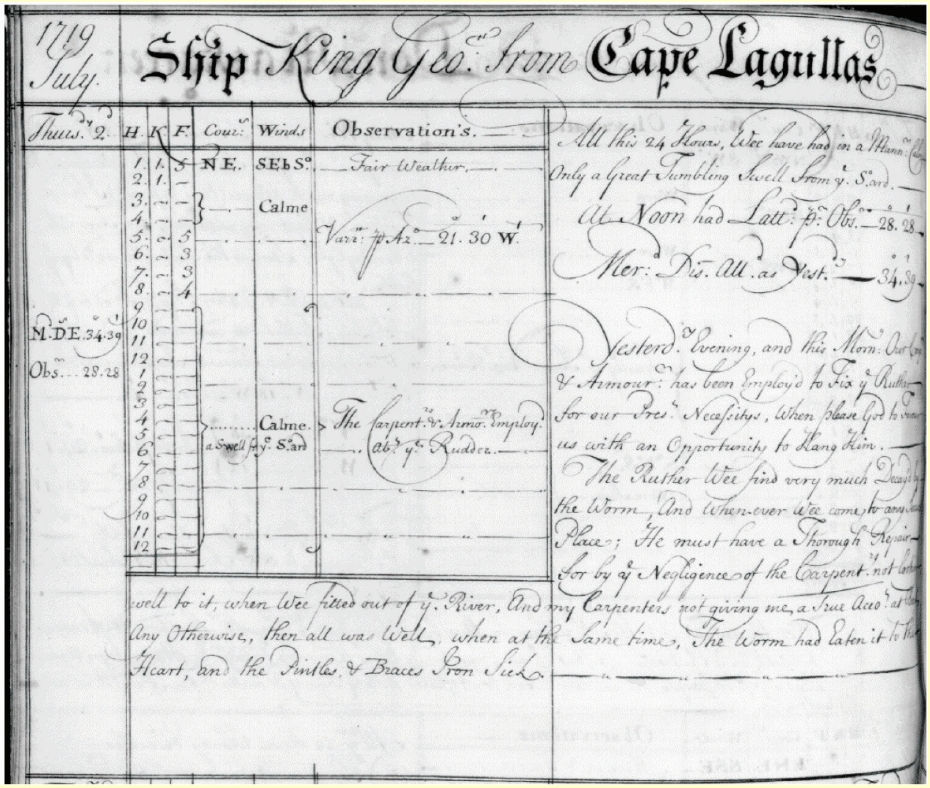

e.g. Extract from logbook of 'King George' from 2nd July 1719 **(Jonkers et al., Rev. Geophys., 2003)**.

Distribution of historical data (1770-1790)

(Courtesy Chris Finlay)

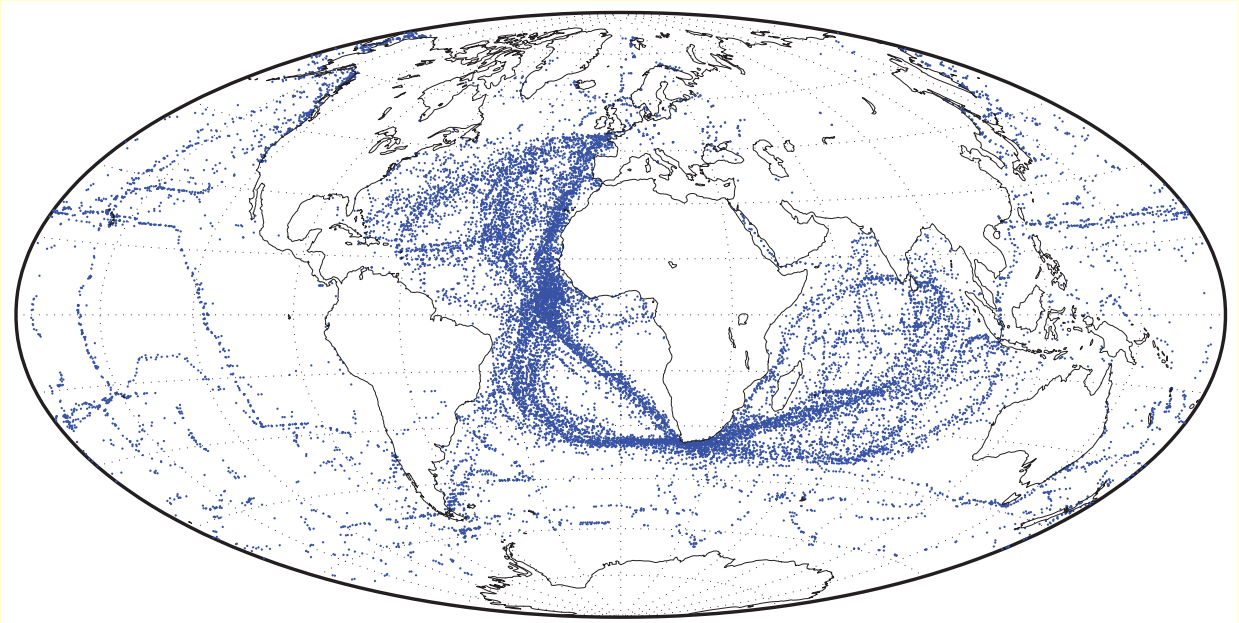

Locations of historical data (all components) between 1770 and 1790 from the **Jonkers et al. (Rev. Geophys., 2003)** database.

Ground magnetic observatories

(Courtesy Chris Finlay)

Magnetic observatories at Eskdalemuir in the UK (top left), Kourou, French Guyana (top right), Qeqertarsuaq/Godhavn in Greenland (bot. left) and Hermanus in S. Africa (bot. right).

Example of instruments in use at observatories

(Courtesy Chris Finlay)

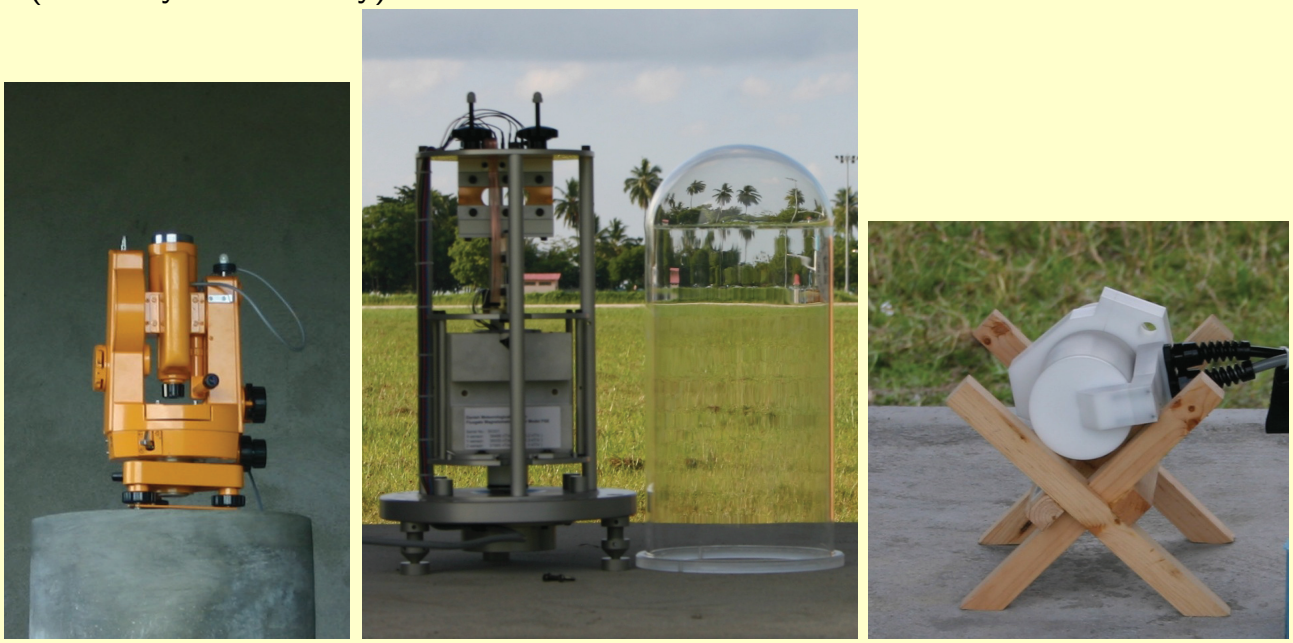

D/I fluxgate theodolite, Danish fluxgate variometer, & Overhauser magnetometer (from ETHZ observatory in development on Gan, Maldives, courtesy of J. Velimsky).

Observatory distribution in 2010

(Courtesy Chris Finlay)

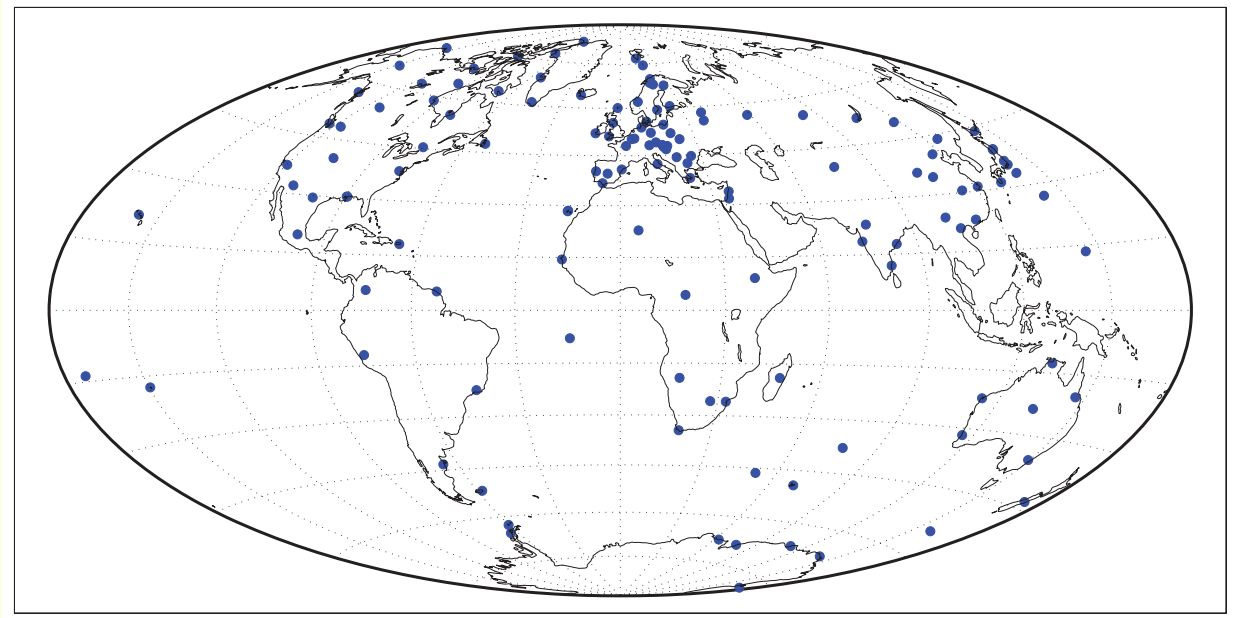

Locations of observatories used in determination of recent internal field models.

An obsy series: 1st dif. annual means from ESK

(Courtesy Chris Finlay)

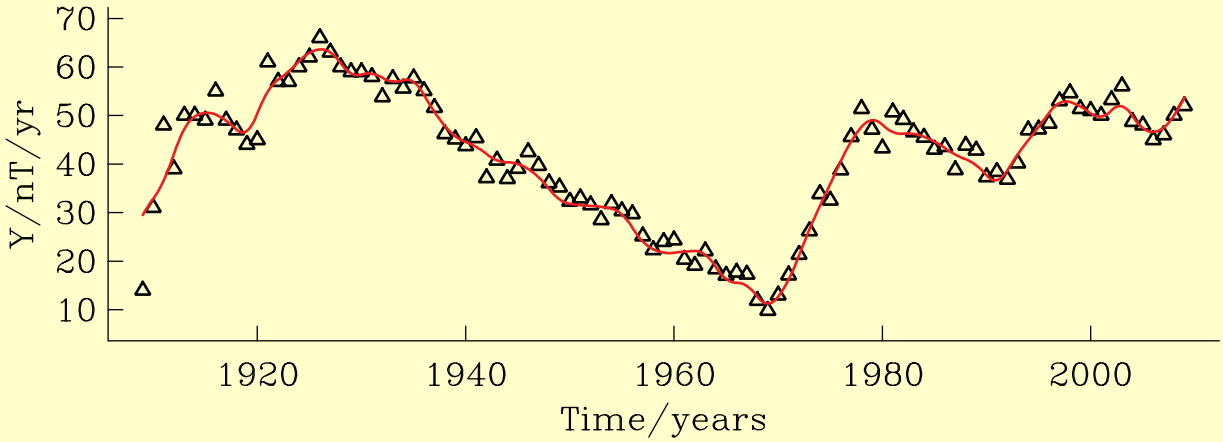

First differences of annual means for Eskdalemuir observatory, Scotland. This is a particularly long and high quality record.

- Note the sharp changes in slope of dY/dt (i.e. discontinuity in second time derivative) known as 'jerks'.

Low Earth orbit satellites

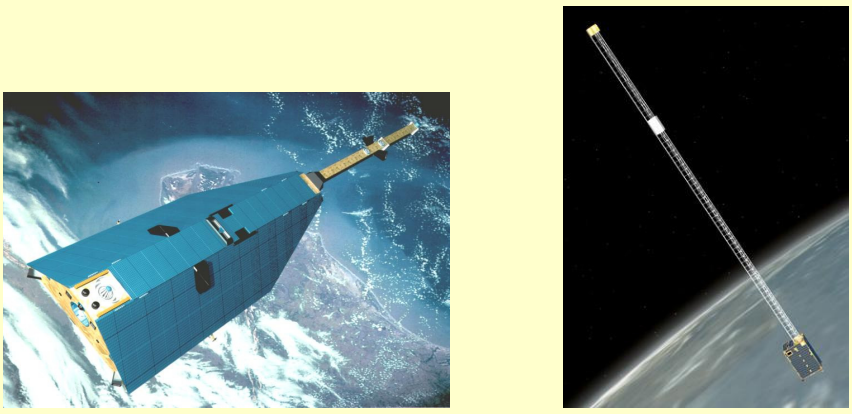

Satellites CHAMP (left) and Ørsted (right) measuring the geomagnetic field.

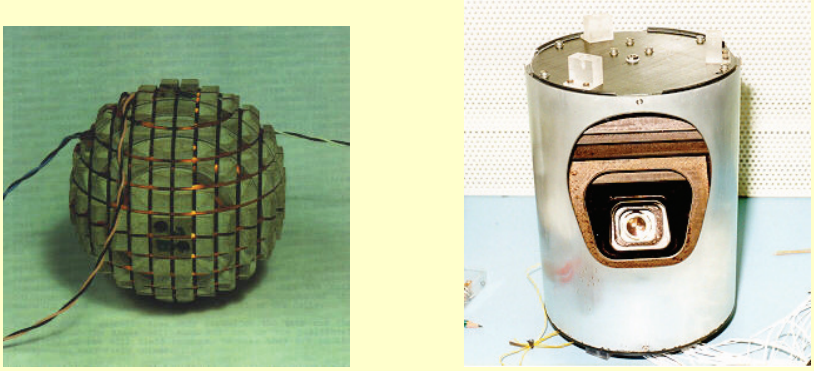

Examples of a satellite fluxgate magnetometer (left) and star cameras (right) for measuring instrument orientation.

Geographical coverage with 3 days of satellite data

(Courtesy Chris Finlay)

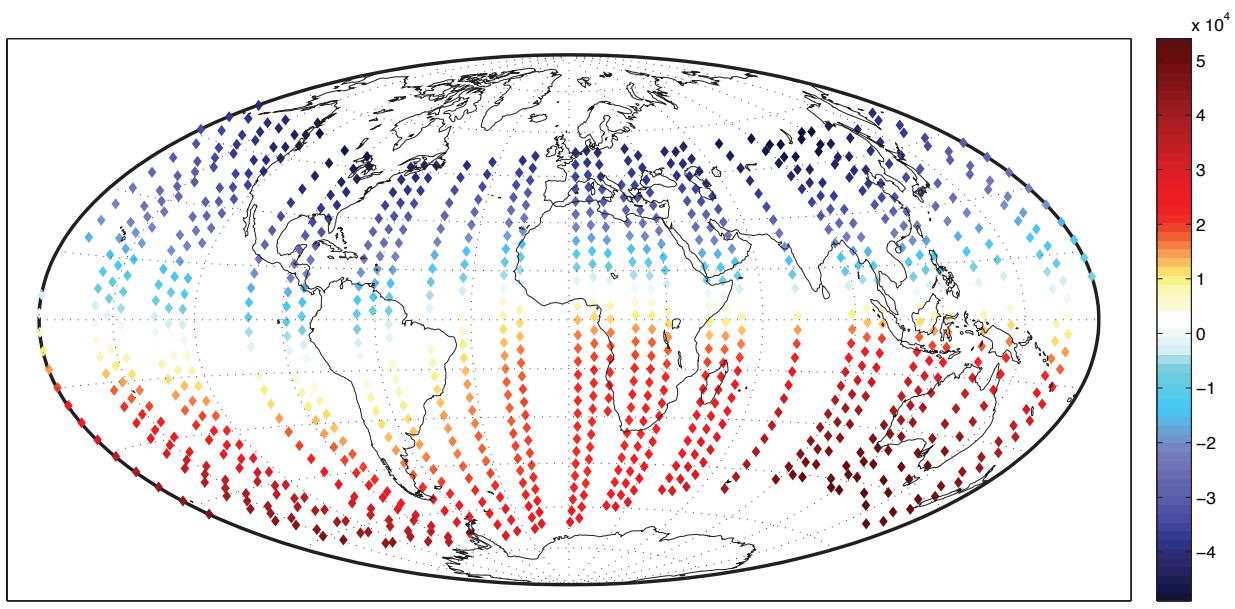

Example showing 3 days of CHAMP vector satellite data from 2009 as used in the construction of the CHAOS-4a model of **Olsen et al.**, http://www.spacecenter.dk/files/magnetic-models/CHAOS-4/.

Constructing global models of core surface field

(Courtesy Chris Finlay)

- Model core field as potential field with purely internal source,

$$\mathbf{B} = -\nabla V \qquad \text{and} \qquad \nabla \cdot \mathbf{B} = 0$$

$$\text{where} \quad V(r,\theta,\phi,t) = a \sum_{\ell=1}^{N} \sum_{m=0}^{\ell} \left(\frac{a}{r}\right)^{\ell+1} g_\ell^m(t) Y_\ell^m(\theta,\phi).$$

- Account for secular variation using a B-spline basis for Gauss coefficients,

$$g_\ell^m(t) = \sum_p g_\ell^{mp} M_p(t).$$

- Solve inverse problem by minimizing a cost function: data misfit & a regularization norm based on core surface field,

$$\Theta = [\mathbf{d} - \mathbf{f}(\mathbf{m})]^T \mathbf{C}_e^{-1} [\mathbf{d} - \mathbf{f}(\mathbf{m})] + \mathcal{R}(\mathbf{m}).$$

$\mathcal{R}(\mathbf{m})$ is a norm measuring spatial & temporal complexity at CMB.

The Earth's main magnetic field

B_r (nT) at Earth's surface in 2007

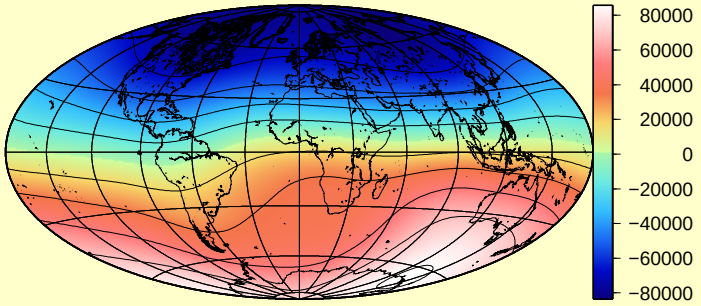

B_r (nT) at the core surface in 2007

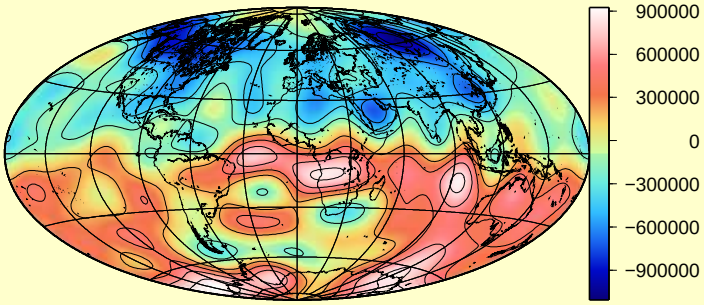

Mauersberger–Lowes spectrum

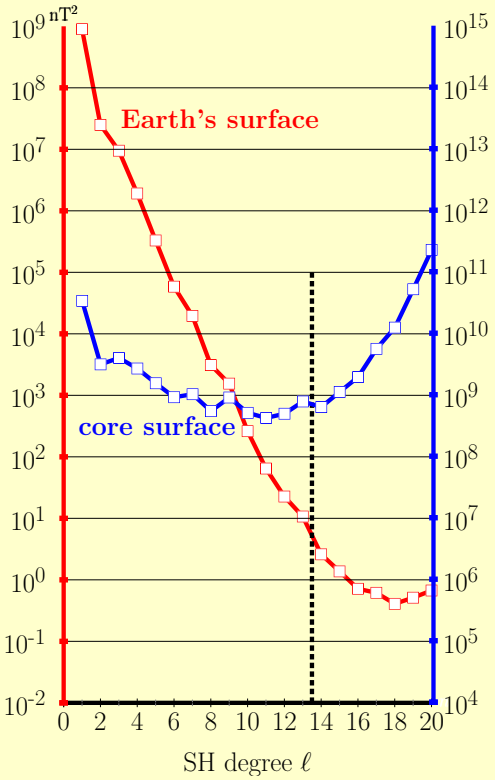

CHAOS2 model (1997-2009), Olsen et al., GJI, 2009

The variations of the main magnetic field

$\dot{B}_r$ (nT/y) at Earth's surface in 2007

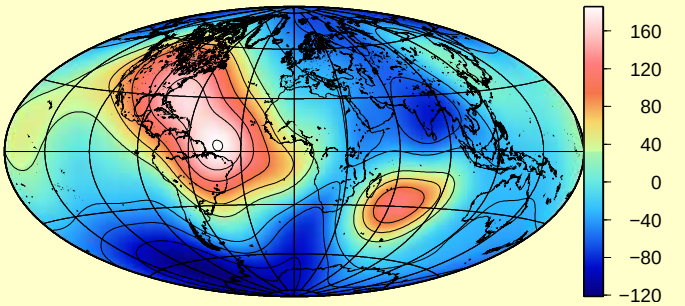

$\dot{B}_r$ (nT/y) at the core surface in 2007

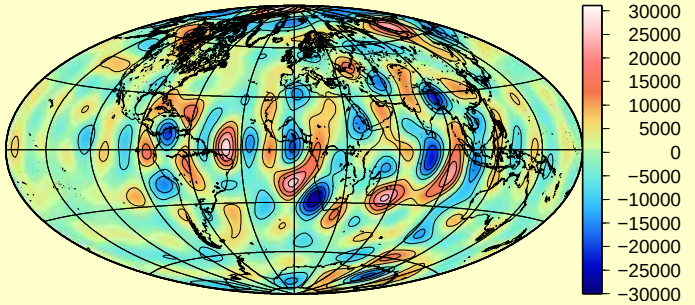

Mauersberger-Lowes spectrum

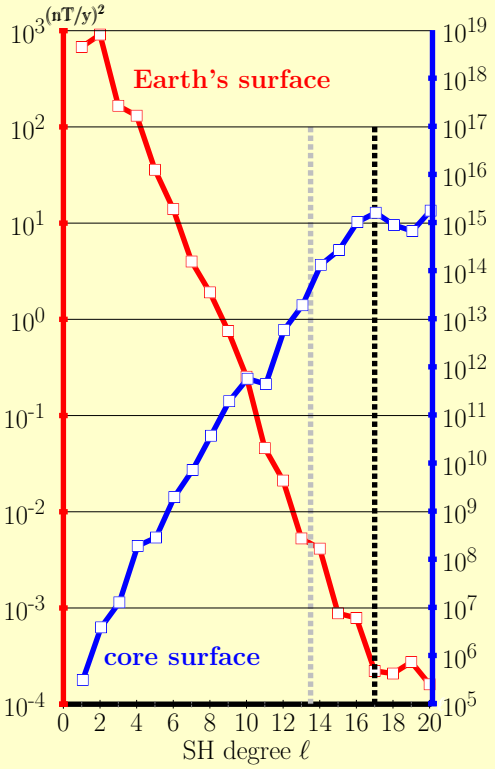

CHAOS2 model (1997-2009), Olsen et al., GJI, 2009

Time scales

Instantaneous correlation times (Hulot & Le Mouël, PEPI, 1994)

$$\tau_\ell(t) = \sqrt{\frac{\sum_{m=0}^{\ell} g_\ell^m(t)^2 + h_\ell^m(t)^2}{\sum_{m=0}^{\ell} \dot{g}_\ell^m(t)^2 + \dot{h}_\ell^m(t)^2}}$$

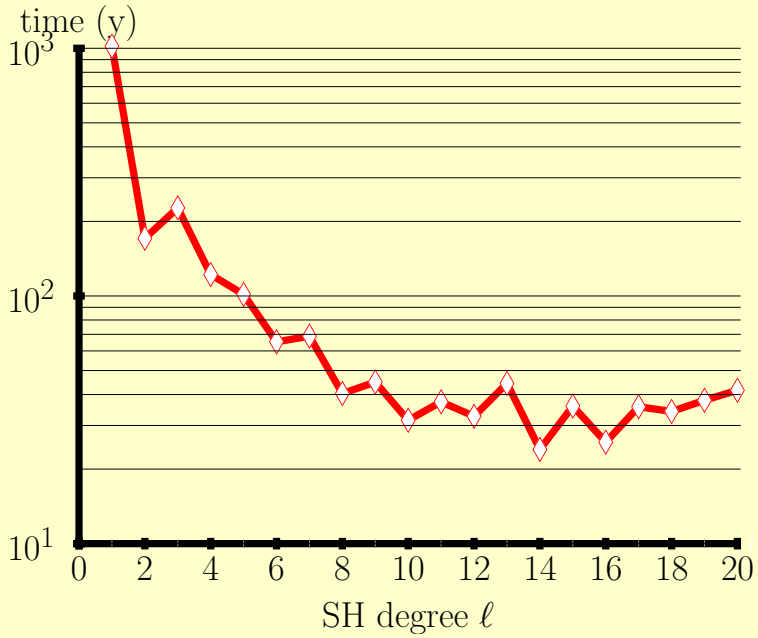

Data distribution vs. time: increase in quantity and accuracy

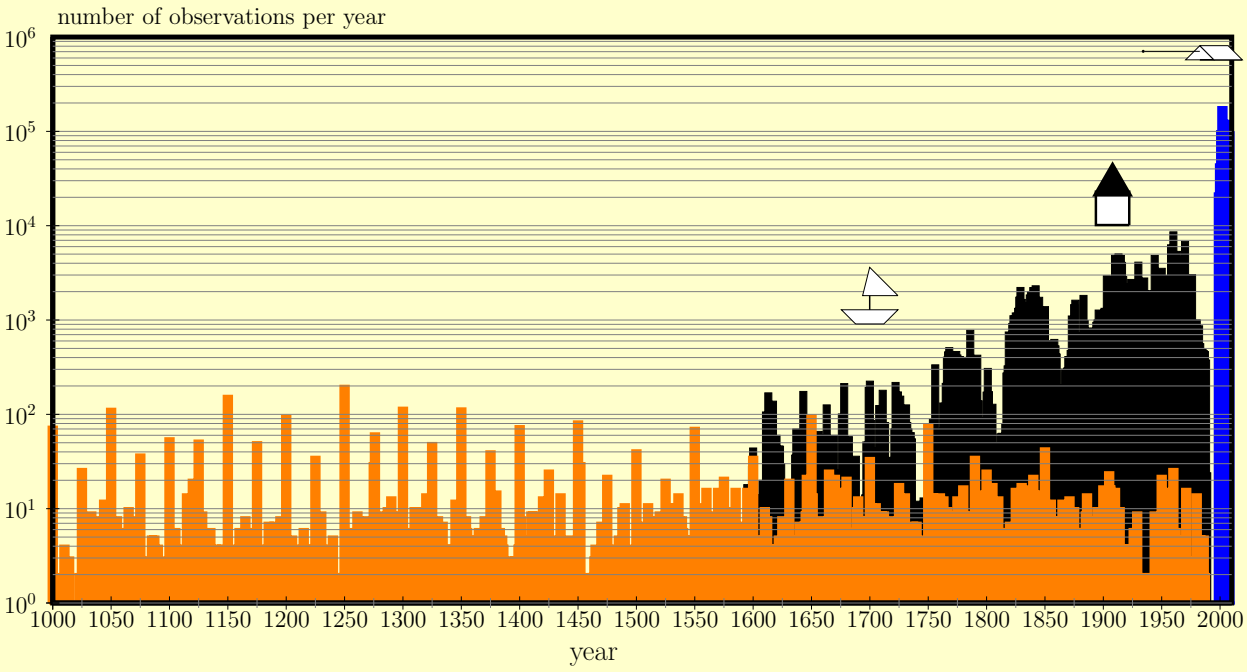

(Fournier et al., Space Sci. Rev., 2010)

archeomagnetic data (orange): geomagia database (Donadini et al., G^3, 2009); historical data (black): *gufm1* (Jackson et al., PhilTrans,2000); satellite data (blue): xCHAOS (Olsen & Mandea, NGEO, 2008).

Satellite data make a difference: error in geomagnetic field models

0.02 $(\mathrm{nT/y})^2$ for CHAOS vs. ~ 30 $(\mathrm{nT/y})^2$ in the 1980ies (Hulot et al., TOG, 2007).

Relationship between observations and dynamics

Kinematic approach : seek the (large scale) core surface flow $\mathbf{u}_h$ such that

$$\partial_t B_r = \dot{B}_r = -\boldsymbol{\nabla}_h \cdot (\mathbf{u}_h B_r)?$$

- Frozen-flux approximation (Roberts & Scott, JGG, 1965),
- Non-uniqueness. Extra hypotheses required: steady flow (Voorhies & Backus, GAFD, 1985), tangencial geostrophy (Le Mouël, Nature, 1984), quasi-geostrophy (Pais & Jault, GJI, 2008; Gillet et al., G^3, 2009), ... + regularization (Holme, TOG, 2007, for a recent review)
- Spatial resolution error $\gg$ observation error.

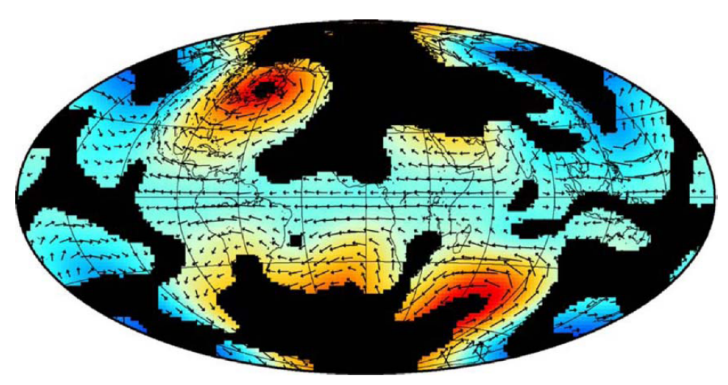

Eymin & Hulot, PEPI, 2005. Peak velocity: 37 km/y. Pressure (color): $\pm$1010 Pa.

Assimilation of geomagnetic observations

A dynamical approach to the inverse problem of estimating the state of the core $\mathbf{x}$ is in order (e.g. Talagrand, JMSJ, 1997, for a review on assimilation).

Ingredients:

1. observations
2. a dynamical model describing the physics of the processes under scrutiny

Goals:

- Probe the physics governing the secular variation: advection, hydromagnetic waves, with an ounce (or more) of diffusion Important because fundamental
- Make inferences on the interior of the core
- Construction of core field and flow models
- Retro-propagate the current quality of observations
- Increase the quality of the geomagnetic forecast, and assess its limits

Specific to the core problem ($\neq$ meteorology, oceanography)

- 'Surface' measurements only
- uncertainties in the knowledge of the background state (the 'climatological' mean)

Which model of core dynamics?

1. Quasi-geostrophic **(Canet et al., JGR, 2009)**

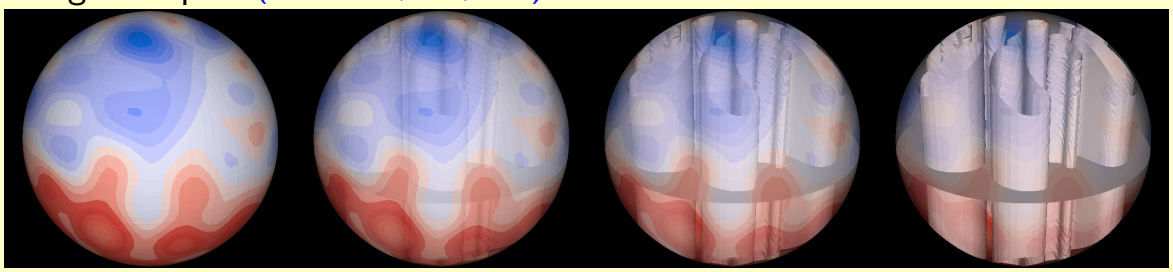

2. Taylor state **(Livermore, Ierley, Jackson., GJI, 2009, PEPI, 2010)**.

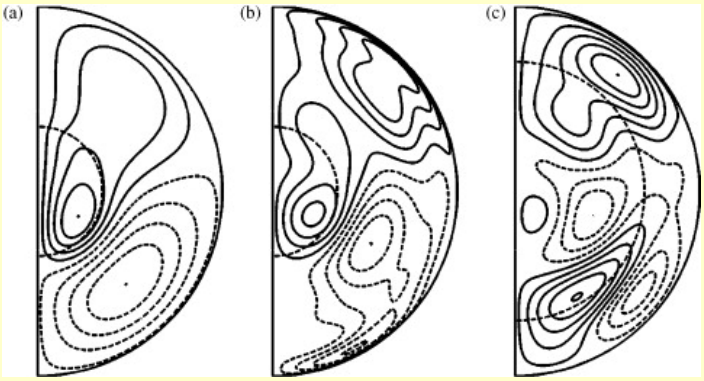

3. Convection-driven geodynamo model **(Liu, Tangborn, Kuang, JGR, 2007; Kuang et al., GJI, 2009)**

Surface and volume

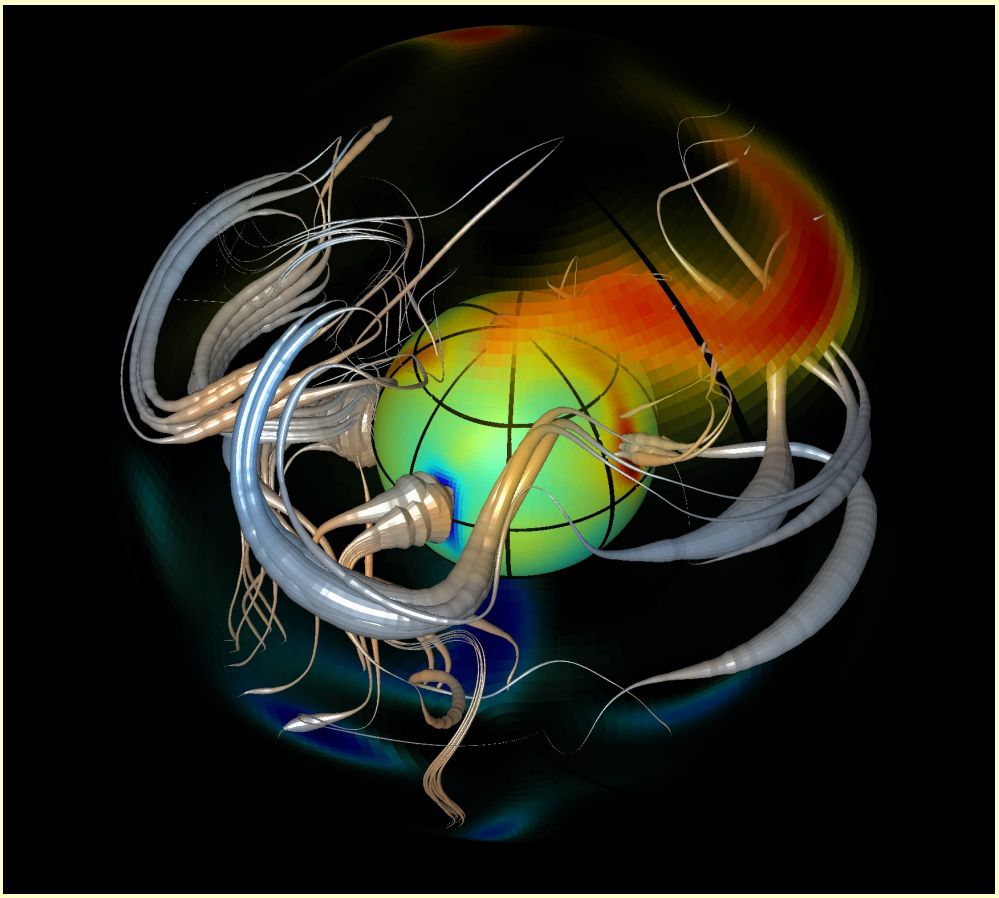

Dynamic Magnetic Field Imaging: Aubert, Aurnou, Wicht (GJI, 2008)

Outline

Introduction – data and field modelling

3D sequential assimilation experiments using synthetic data

Framework in a discrete world

Notations of **Ide et al., J. Met. Soc. Japan, 1997**.

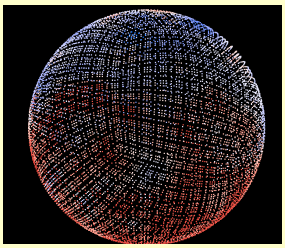

- Forward model (the numerical geodynamo model):

$$\mathbf{x}_{i+1} = M_{i,i+1}[\mathbf{x}_i], \tag{1}$$

  - $\mathbf{x}_i$: modelled core state at discrete time t_i (column vector, size $n_{\mathbf{x}}$).
  - $M_{i,i+1}$: prognostic, nonlinear numerical model of core dynamics (semi-implicit in time).
  - Modeled core state is controlled by $\mathbf{x}_0$ + other control parameters().

- Observations $\mathbf{y}_i^o$:

$$\mathbf{y}_i^o = \mathbf{H}_i[\mathbf{x}_i^t] + \boldsymbol{\epsilon}_i^o, \text{ in which} \tag{2}$$

  - o: o_bservation,
  - $\mathbf{H}_i$: observation operator,
  - t: true,
  - $\boldsymbol{\epsilon}_i^o$: observation error (covariance matrix $\mathbf{R}_i$).

Trajectory in model space

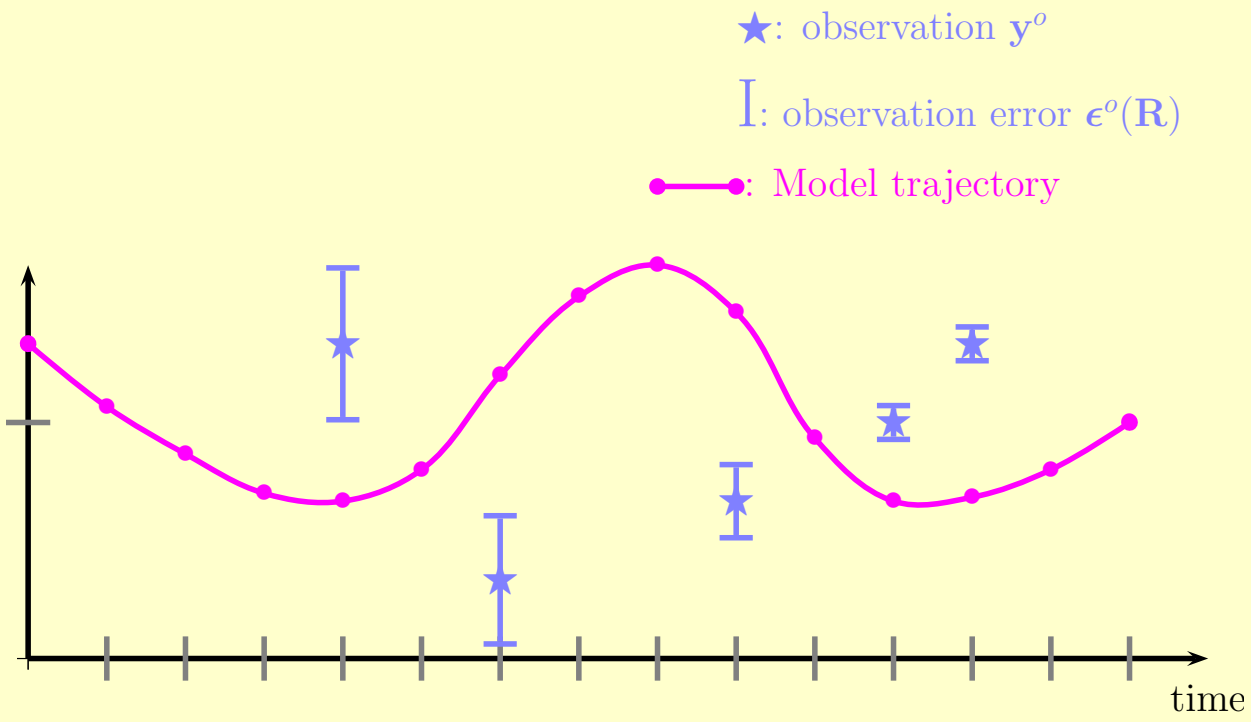

Sequential assimilation

We perform an analysis each time there is some observation available.

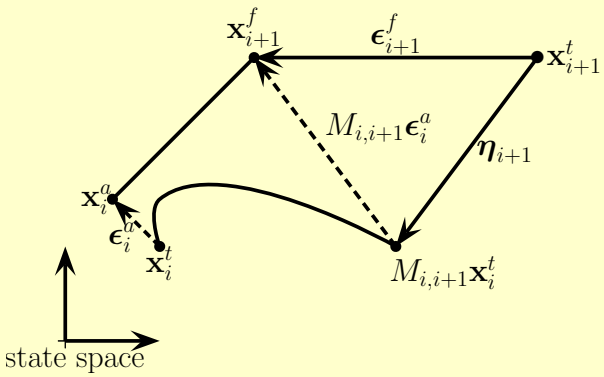

A 2-step procedure: the Kalman filter

1. Forecast:

$$\begin{aligned} \mathbf{x}^f_{i+1} &= M\mathbf{x}^a_i, \\ \mathbf{P}^f_{i+1} &= M\mathbf{P}^a_i M^\dagger + \mathbf{Q}. \end{aligned}$$

2. Analysis:

$$\begin{aligned} \mathbf{x}^a_{i+1} &= \mathbf{x}^f_{i+1} + \mathbf{K}_{i+1}\left(\mathbf{y}^o_{i+1} - \mathbf{H}\mathbf{x}^f_{i+1}\right), \\ \mathbf{P}^a_{i+1} &= \left(I - \mathbf{K}_{i+1}\mathbf{H}\right)\mathbf{P}^f_{i+1}. \end{aligned}$$

with $\mathbf{K}_{i+1} = \mathbf{P}^f_{i+1}\mathbf{H}^\dagger_{i+1}\left(\mathbf{H}_{i+1}\mathbf{P}^f_{i+1}\mathbf{H}^\dagger_{i+1} + \mathbf{R}_{i+1}\right)^{-1}$.

Sequential assimilation

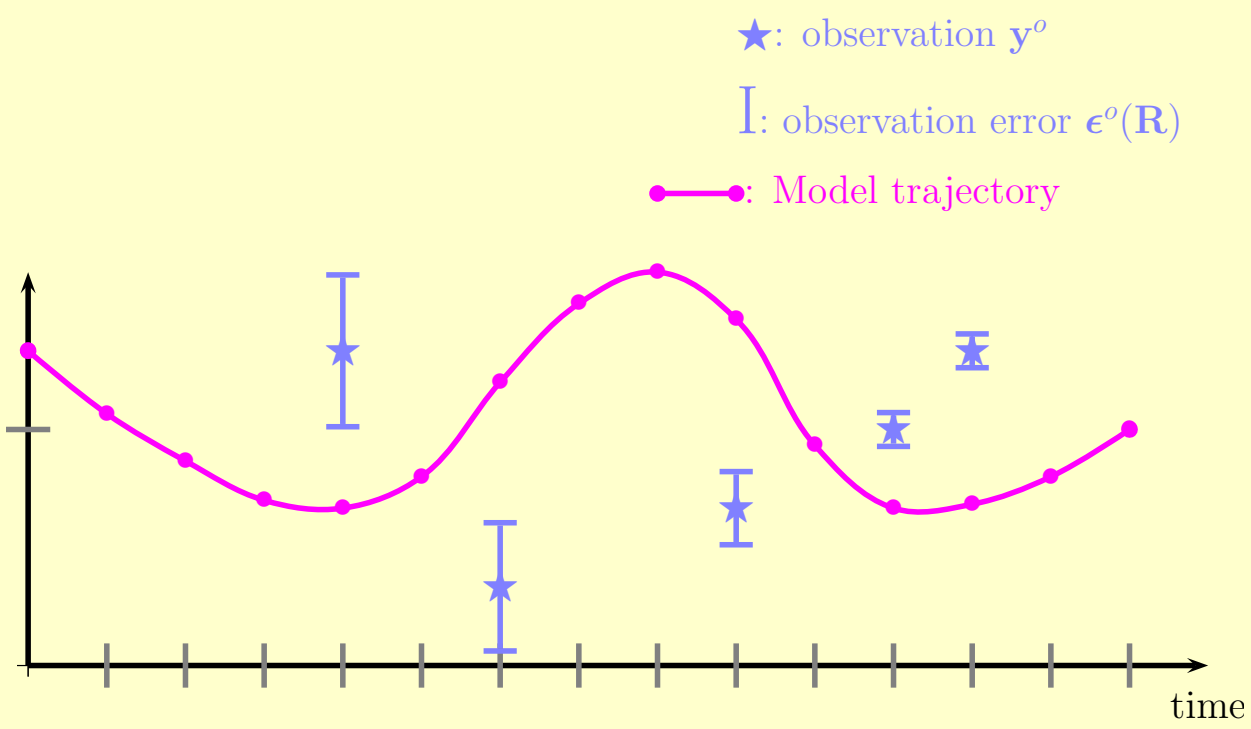

Sequential assimilation

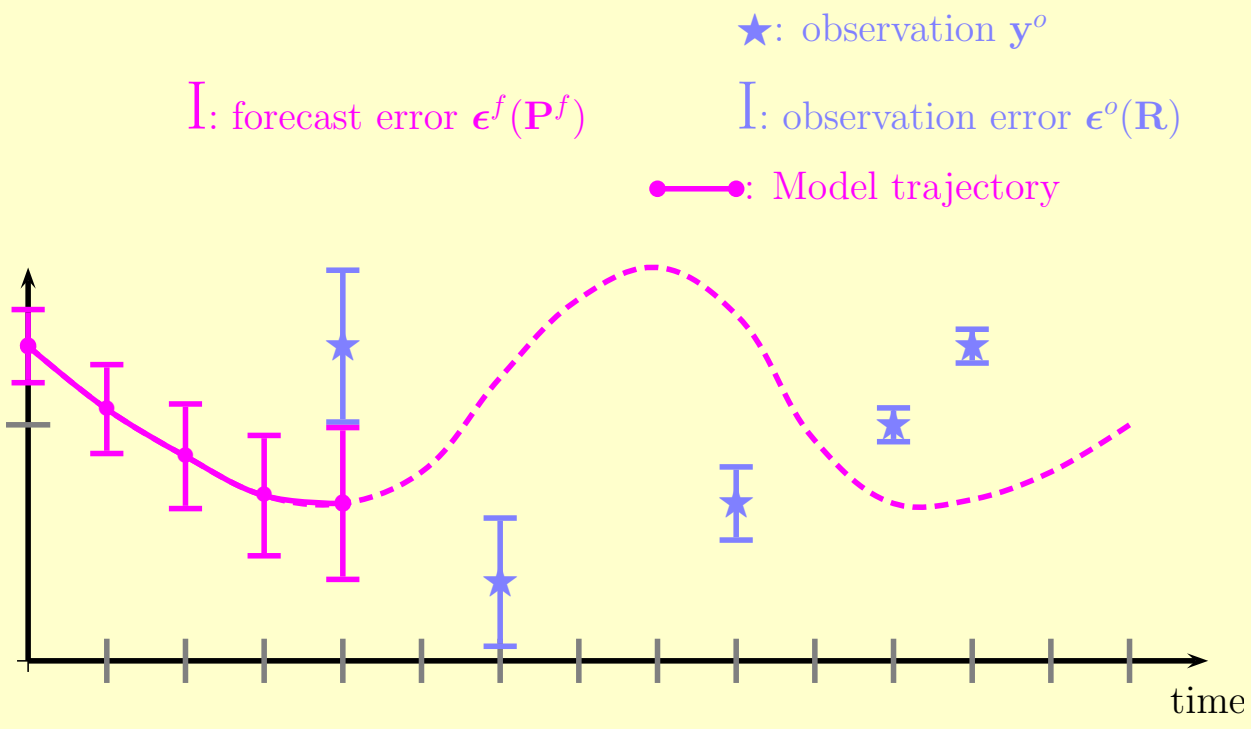

Sequential assimilation

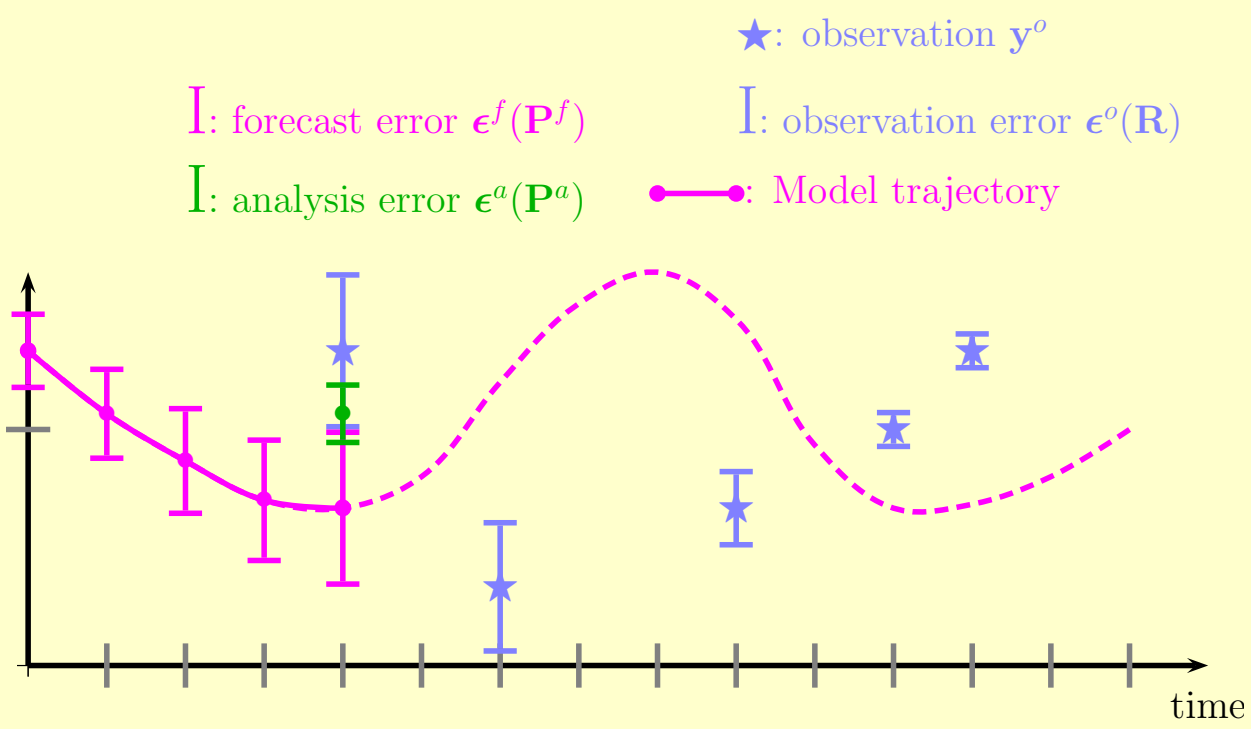

Sequential assimilation

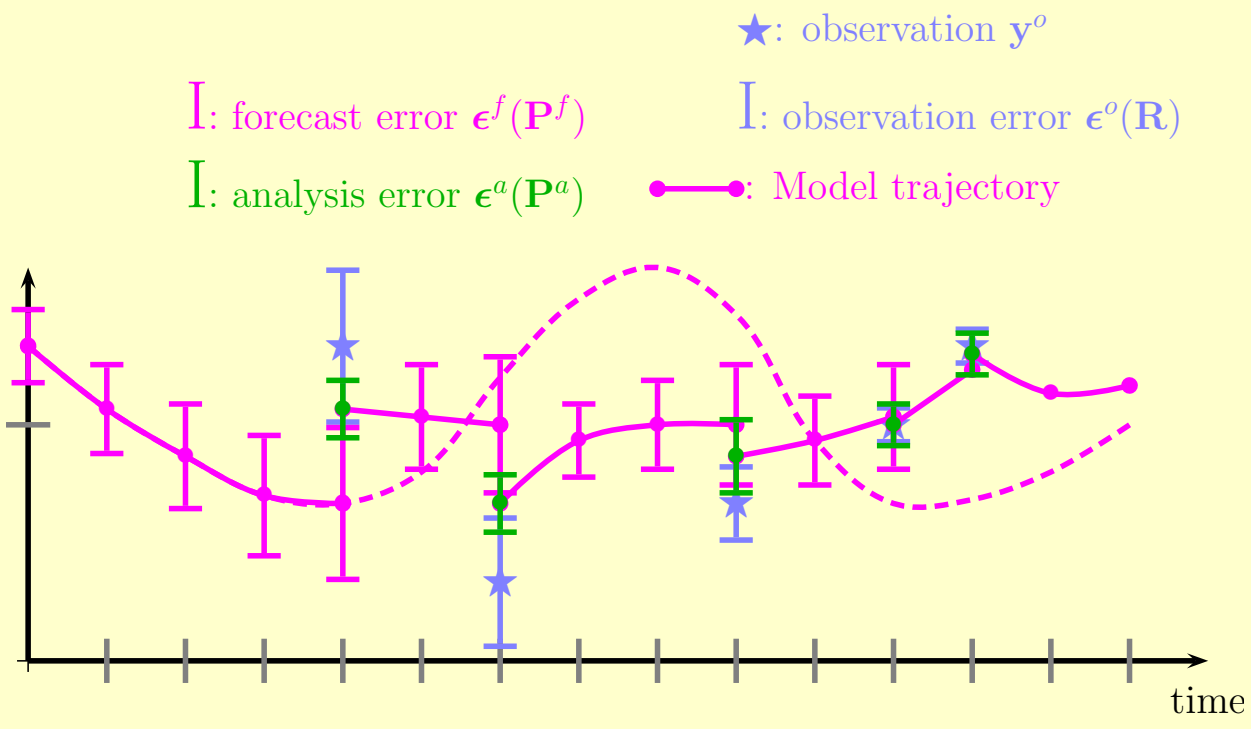

Optimal interpolation

- Size of the covariance matrix: $n_{\mathbf{x}} \times n_{\mathbf{x}}$ ($n_{\mathbf{x}}$ is size of $\mathbf{x}$, typically 10^6).
- Evaluating $M\mathbf{P}_i^a M^\dagger$ requires $\mathcal{O}\left(n_{\mathbf{x}}^4\right)$ operations. ($n_{\mathbf{x}}$ times more expensive than a single model step.)

A 2-step procedure:

1. Forecast:

$$\mathbf{x}_{i+1}^f = M\mathbf{x}_i^a,$$
$$\mathbf{P}_{i+1}^f = M\mathbf{P}_i^a M^\dagger + \mathbf{Q}.$$

2. Analysis:

$$\mathbf{x}_{i+1}^a = \mathbf{x}_{i+1}^f + \mathbf{K}_{i+1}\left(\mathbf{y}_{i+1}^o - H\mathbf{x}_{i+1}^f\right),$$
$$\mathbf{P}_{i+1}^a = \left(I - \mathbf{K}_{i+1}H\right)\mathbf{P}_{i+1}^f.$$

with $\mathbf{K}_{i+1} = \mathbf{P}_{i+1}^f \mathbf{H}_{i+1}^\dagger \left(\mathbf{H}_{i+1}\mathbf{P}_{i+1}^f\mathbf{H}_{i+1}^\dagger + \mathbf{R}_{i+1}\right)^{-1}$.

Optimal interpolation

- Possibility: use a frozen background error covariance matrix $\mathbf{P}^b$.

A 2-step procedure:

1. Forecast:

$$\mathbf{x}_{i+1}^f = M\mathbf{x}_i^a,$$
$$\mathbf{P}_{i+1}^f = \mathbf{P}^b$$

2. Analysis:

$$\mathbf{x}_{i+1}^a = \mathbf{x}_{i+1}^f + \mathbf{K}_{i+1}\left(\mathbf{y}_{i+1}^o - \mathbf{H}\mathbf{x}_{i+1}^f\right),$$
$$\mathbf{P}_{i+1}^a = \mathbf{P}^b$$

with $\mathbf{K}_{i+1} = \mathbf{P}^b\mathbf{H}_{i+1}^\dagger \left(\mathbf{H}_{i+1}\mathbf{P}^b\mathbf{H}_{i+1}^\dagger + \mathbf{R}_{i+1}\right)^{-1}$.

Structure of the background covariance matrix in 3D

Transport of information from the surface downwards:

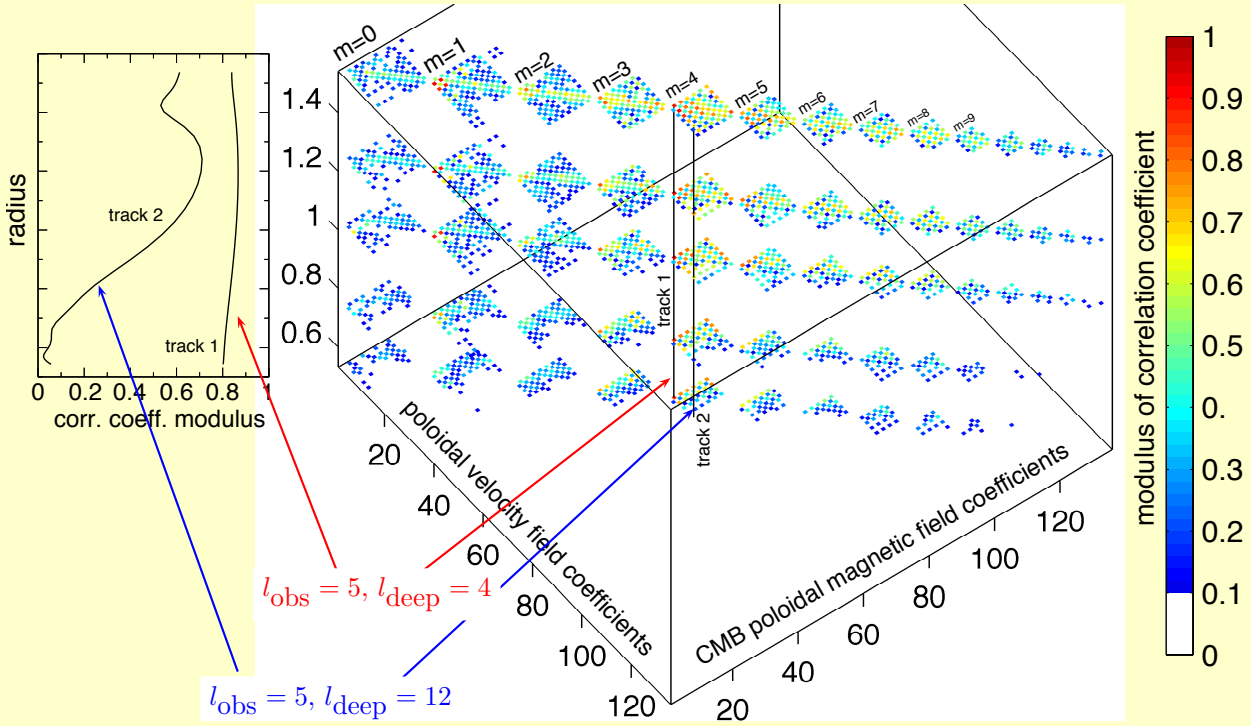

Aubert & Fournier, NPG, 2011

NB: $\mathbf{P}^b$ is 20000×20000

Experiments with synthetic data

Solve a time-dependent assimilation problem:

- Generate synthetic data from model free run over $[t_0, T]$: here maps of B_r at the top of the core (truncated at $\ell = 13$ and assuming perfect observations, $\mathbf{R} = \mathbf{0}$)
- Start from t_0 using wrong initial conditions (for instance the average background state)
- Assimilate synthetic observations and correct model trajectory
- Assess quality of assimilation scheme by comparing the known true dynamo state $\mathbf{x}^t$ and the estimate $\widehat{\mathbf{x}}$
  - Retrieval of internal structure
  - Forecast quality

Synthetic observations

Time between samples: approximately 50 yr. Color scale ± 2 mT.

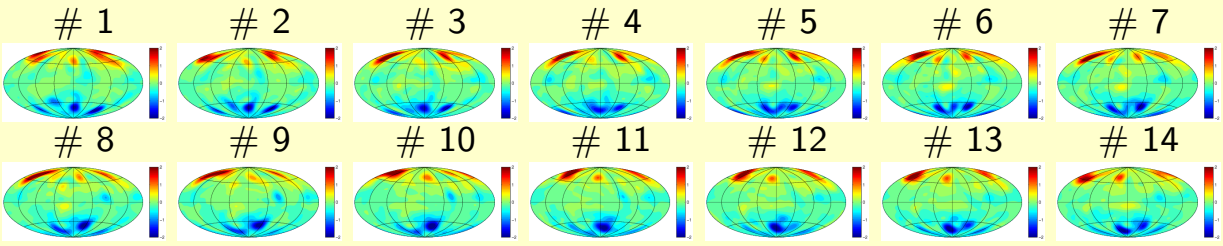

Time span $\sim$ 700 yr.

Retrieval of internal structure

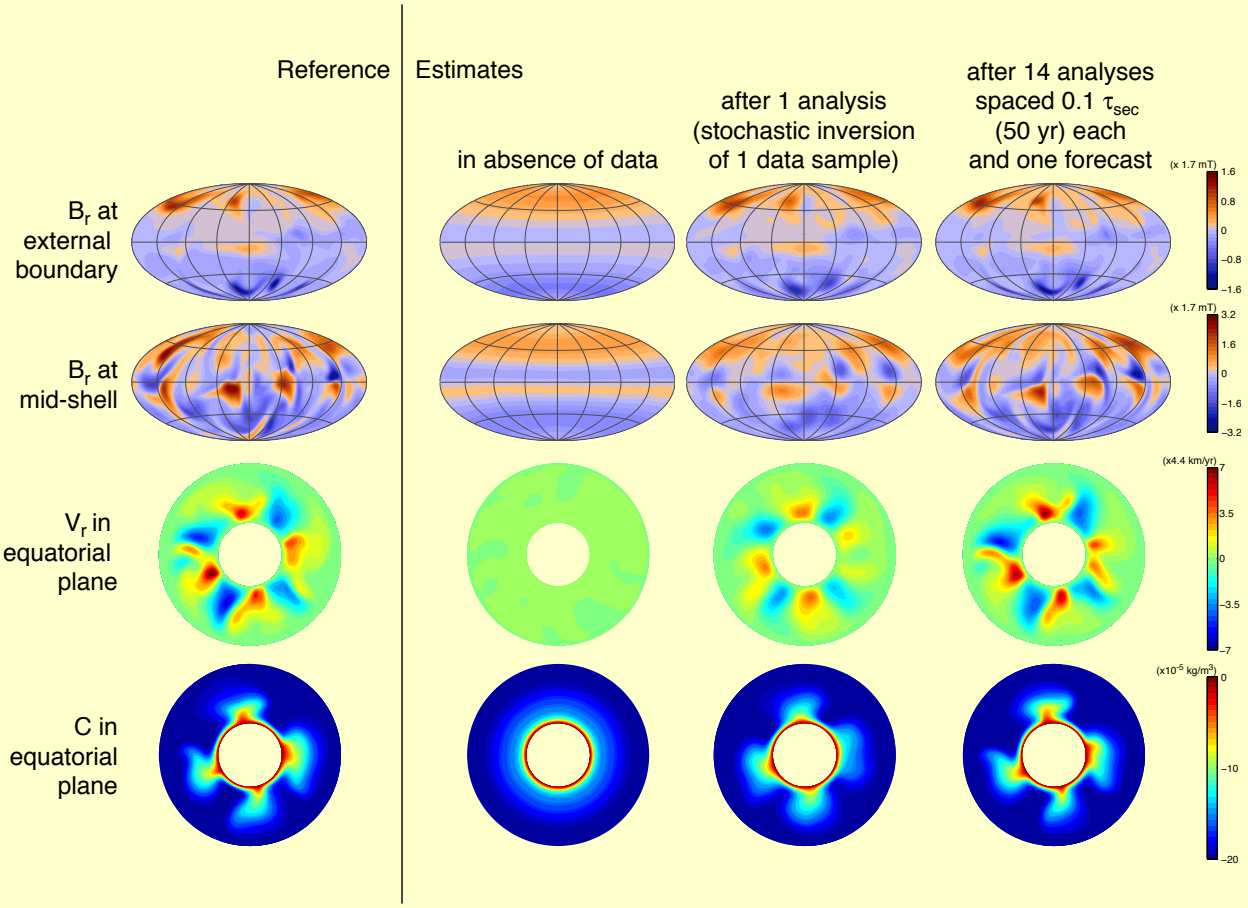

Aubert & Fournier, NPG, 2011

The benefit of using multivariate statistics to construct $\mathbf{P}^b$

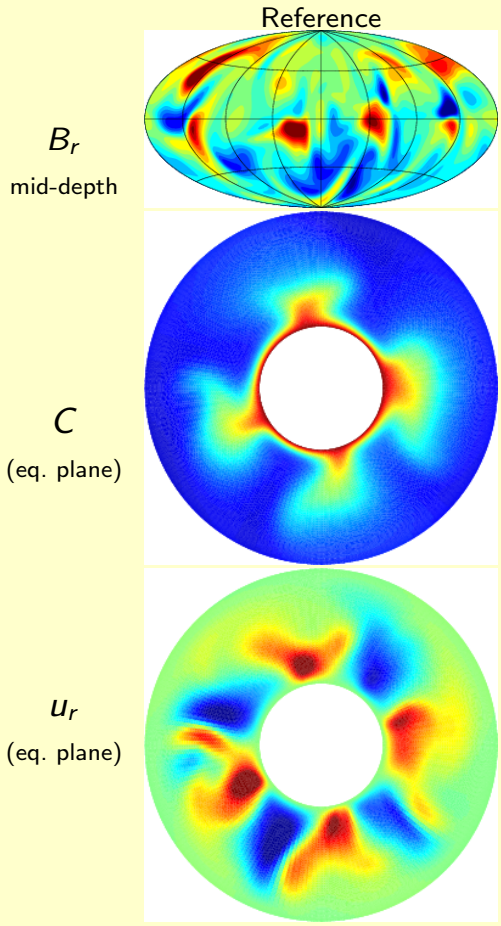

The benefit of using multivariate statistics to construct $\mathbf{P}^b$

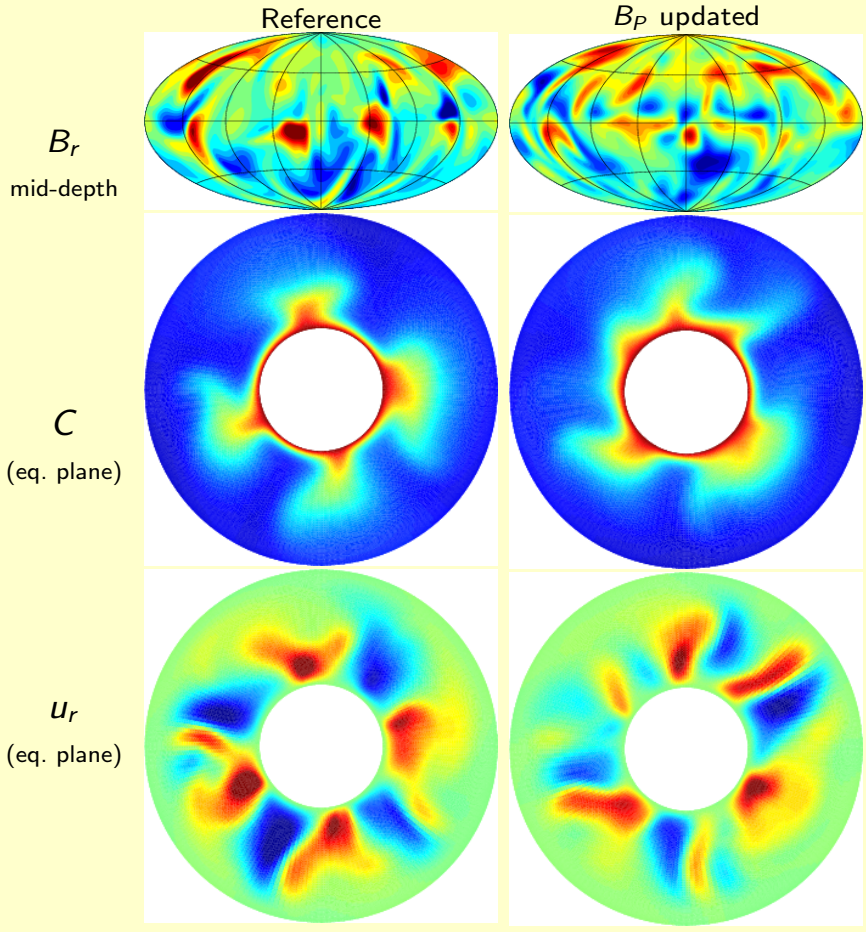

The benefit of using multivariate statistics to construct $\mathbf{P}^b$

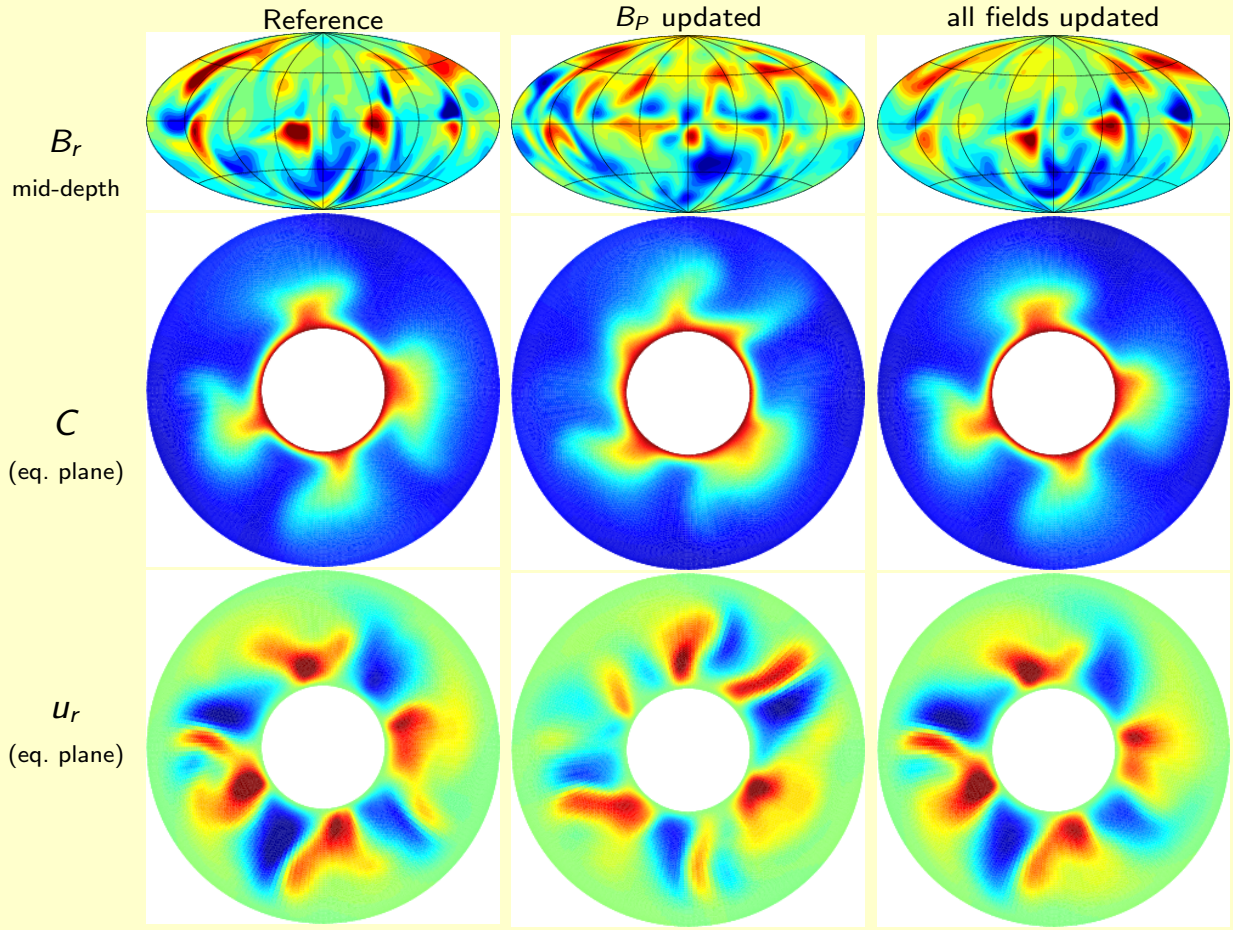

Forecast quality

Define the innovation

$$\mathbf{d}_i = \text{observation} \; - \; \text{forecast} = \mathbf{y}_i^o - \mathbf{H}\mathbf{x}_i^f$$

Involves the first 13 SH degrees of the poloidal field at the core surface.
Forecast quality via the average error

$$\text{error} = \frac{1}{N_{\text{cycles}}} \sum_i \|d_i\|_2 \text{ over 3000 yr}$$

The number of assimilation cycles N_{cycles} is set by the spacing between two successive cycles, Δt_{cycle}. We will take $\Delta t_{\text{cycle}} = 5$, 25, 50 and 100 yr.

Our forecast strategies to define $\mathbf{x}_i^f$ will consist of

1. a no-cast
2. a linear forecast based on the perfectly known SV up to SH degree 8
3. a linear forecast based on the perfectly known SV up to SH degree 13
4. a multivariate OI scheme assimilating B_r maps up to SH degree 13

Forecast results

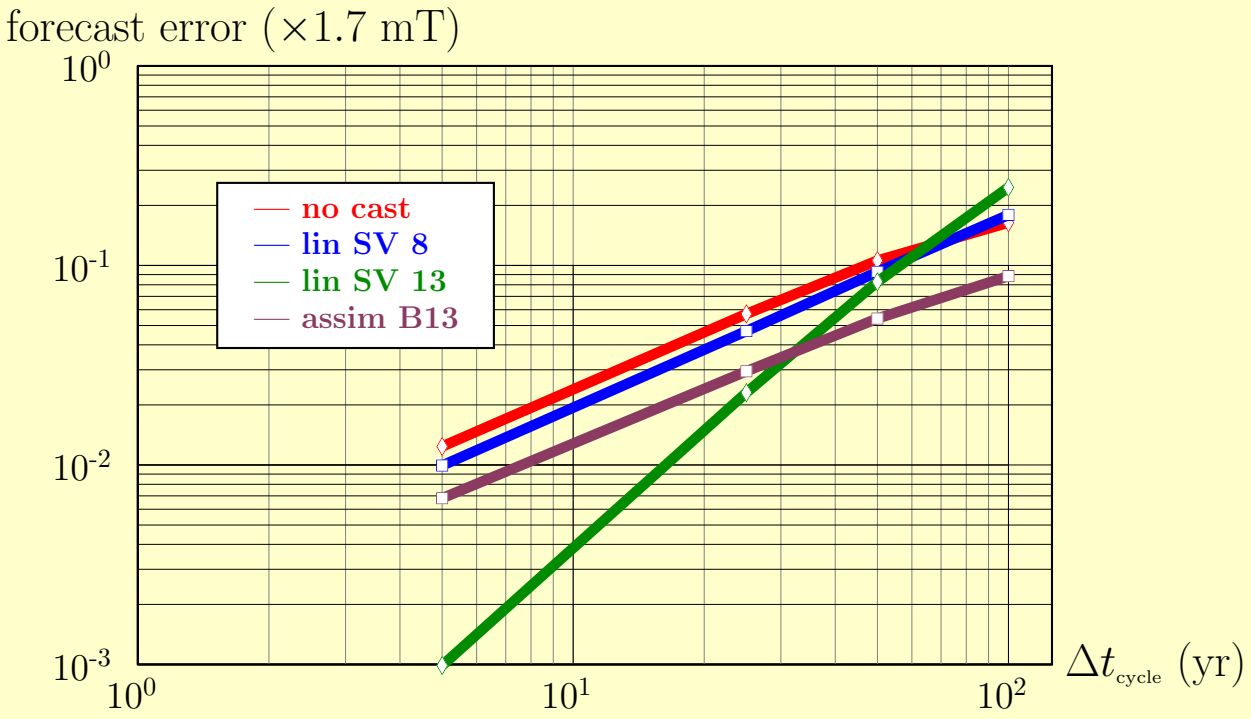

Over long time scales, assimilation provides the best answer.

Terrestrial matters

It is of interest to elucidate the causes (and forecast the evolution) of the South Atlantic Anomaly.

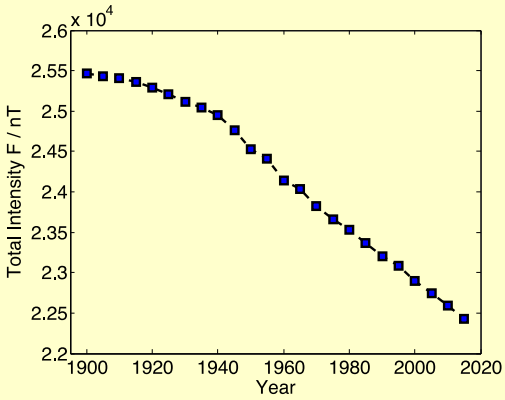

Finlay et al., 11th IGRF, GJI, 2011

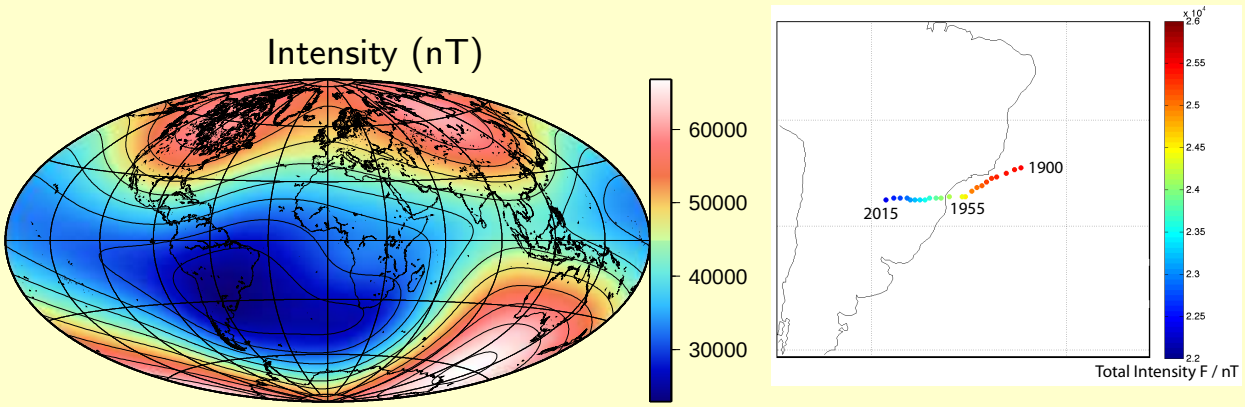

Finlay et al., 11th IGRF, GJI, 2011

Summary of the 3D synthetic section

- Implementation of an optimal interpolation scheme for geomagnetic data assimilation based on 3D dynamo models
- Synthetic experiments:
  - Multivariate statistics help better constrain the internal structure of the core
  - Scheme adapted for long-term predictions of the evolution of the large-scale poloidal field at the top of the core
  - On short time scales: linear prediction based on perfectly well-known large scale SV performs better.

Limit of predictability

Hulot, Lhuillier, Aubert, GRL, 2010; Lhuillier, Aubert, Hulot, GJI, 2011

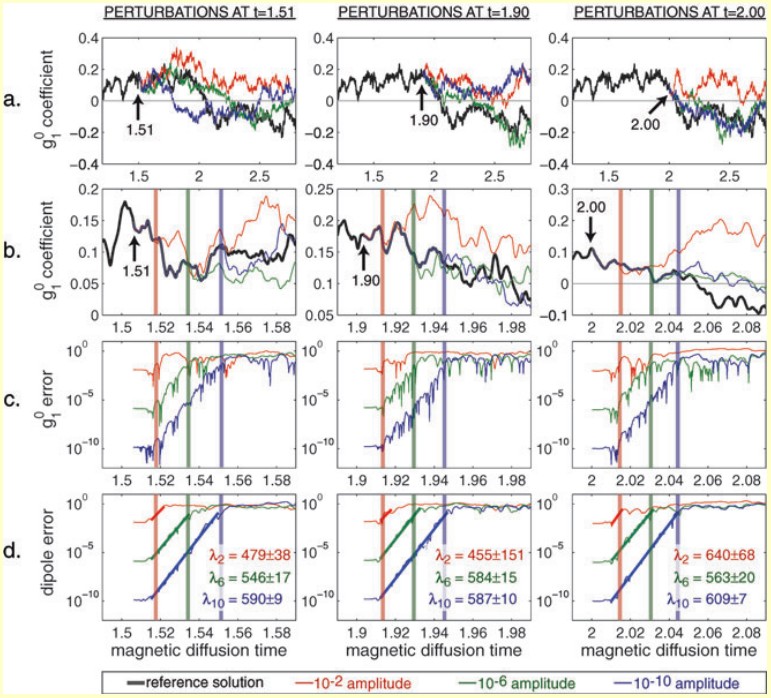

$$\text{error} \propto \exp(\lambda t)$$

$$\lambda^{-1} = \tau_e = 0.18(\pm 0.02)\mathrm{Rm}^{-1}\tau_\eta$$

(with $\tau_\eta = D^2/\eta$, ie 120 kyr for the core)

For the Earth:

- $\tau_e \sim 30$ yr
- limit of predictability: 70 yr

(with optimal model and DA scheme)

Chaotic systems governed by deterministic equations

Lorenz's 1963 model is the canonical example of such a system. Since it is much simpler than the geodynamo, we will study its properties and implement an Ensemble Kalman filter atop it in the computer exercises which follow.

Extra

Supplementary material

Convection-driven model of the geodynamo

Discretization of conservation laws and Maxwell's equations, modified Boussinesq codensity formalism of Braginsky & Roberts (GAFD, 1995).

$$\boldsymbol{\nabla}\cdot\mathbf{u} = 0, \tag{3}$$
$$\rho\left(\partial_t\mathbf{u}+\mathbf{u}\cdot\boldsymbol{\nabla}\mathbf{u}+2\boldsymbol{\Omega}\times\mathbf{u}\right) = -\boldsymbol{\nabla}\Pi+\mathbf{j}\times\mathbf{B}+\rho\nu\nabla^2\mathbf{u}+C\mathbf{g}, \tag{4}$$
$$\partial_t C+\mathbf{u}\cdot\boldsymbol{\nabla}C = \kappa\nabla^2 C+S_{T/\xi}, \tag{5}$$
$$\partial_t\mathbf{B} = \boldsymbol{\nabla}\times(\mathbf{u}\times\mathbf{B})+(1/\mu\sigma)\nabla^2\mathbf{B}, \tag{6}$$

+ no-slip boundary conditions for $\mathbf{u}$, insulating magnetic boundary conditions at the ICB and CMB, prescribed codensity at the ICB and null codensity flux $\boldsymbol{\nabla}C=\mathbf{0}$ at the CMB.

Numerical methods

Numerical scheme based on the pioneering work of Glatzmaier (Journal of Computational Physics, 1984).

- poloidal-toroidal decomposition of $\mathbf{u}$ and $\mathbf{B}$

$$\mathbf{u} = \boldsymbol{\nabla}\times\boldsymbol{\nabla}\times(u_P\mathbf{r})+\boldsymbol{\nabla}\times(u_T\mathbf{r}),$$
$$\mathbf{B} = \boldsymbol{\nabla}\times\boldsymbol{\nabla}\times(B_P\mathbf{r})+\boldsymbol{\nabla}\times(B_T\mathbf{r}).$$

- Spherical harmonic expansion of u_P, u_T, B_P, B_T, and C

$$\begin{bmatrix} u_P \\ u_T \\ B_P \\ B_T \\ C \end{bmatrix}(r,\theta,\phi,t) = \sum_{\ell=0}^{l=L}\sum_{m=-\ell}^{m=\ell}\begin{bmatrix} u_{P\ell m}(r,t) \\ u_{T\ell m}(r,t) \\ B_{P\ell m}(r,t) \\ B_{T\ell m}(r,t) \\ C_{\ell m}(r,t) \end{bmatrix}\mathcal{Y}_\ell^m(\theta,\phi)$$

- Finite differences in radius r
- Computation of nonlinear terms in physical space
- Second order semi-implicit time-differencing

Dormy, Cardin, Jault, EPSL, 1998; Aubert, Aurnou, Wicht, GJI, 2008

Construction of the prior: scaling procedure

1. Assume model and Earth obey the same scaling laws
   (Christensen & Aubert, GJI, 2006; Aubert, Labrosse, Poitou, GJI, 2009)
2. Extrapolate model values to geophysical values

Rescaling

- time:
  correlation times $\tau_\ell = \tau_{\mathrm{SV}}/\ell$
  (Christensen & Tilgner, Nature, 2004; Lhuillier, Fournier, Hulot, Aubert, GRL, 2011); .
  Assume model and Earth share same $\tau_{\mathrm{SV}} = 415$ yr.
- field:
  relate rms field strength B_{rms} and available convective power p

$$B_{\mathrm{rms}} \propto f_{\mathrm{Ohm}}^{1/2} p^{1/3}$$

  Assume $B_{\mathrm{rms}}(\mathrm{Earth}) = 2.4$ mT (Aubert, Labrosse, Poitou, GJI, 2009)

A more quantitative assessment

$$\text{misfit} = \frac{\int_V \left(\mathbf{u}^t - \widehat{\mathbf{u}}\right)^2 \mathrm{d}V}{\int_V \mathbf{u}^{t2} \mathrm{d}V}; \text{correlation} = \frac{\int_V \mathbf{u}^t \cdot \widehat{\mathbf{u}} \mathrm{d}V}{\sqrt{\int_V \mathbf{u}^{t2} \mathrm{d}V} \sqrt{\int_V \widehat{\mathbf{u}}^2 \mathrm{d}V}}$$

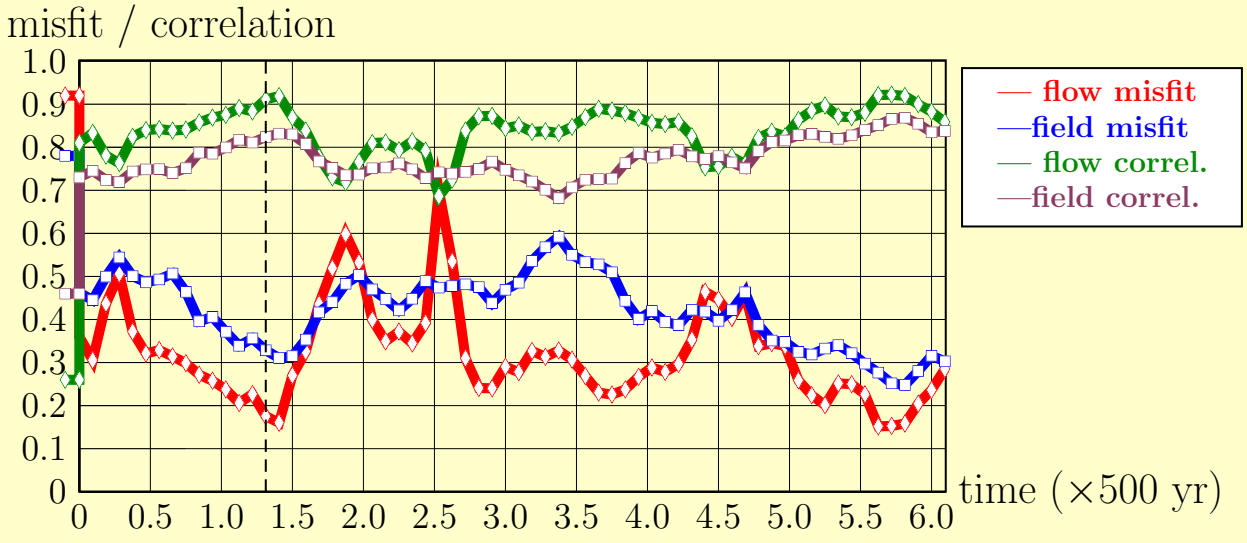

Aubert & Fournier, NPG, 2011

Structure of the background covariance matrix in 3D

The state vector $\mathbf{x}_i$ at discrete time t_i: the complex-valued spectral coefficients at radial levels r_k

$$\mathbf{x}_i = \left[\ldots, u_{P\ell m}^k, \ldots, u_{T\ell m}^k, \ldots, B_{P\ell m}^k, \ldots, B_{T\ell m}^k, \ldots, C_{\ell m}^k, \ldots \right]_i^T$$

Having N_e samples at hand, compute mean

$$\mathbf{x}^b = \frac{1}{N_e} \sum_{i=1}^{N_e} \mathbf{x}_i$$

and variances-covariances

$$\mathbf{P}^b = \frac{1}{N_e - 1} \sum_{i=1}^{N_e} \left(\mathbf{x}_i - \mathbf{x}^b \right) \left(\mathbf{x}_i - \mathbf{x}^b \right)^\dagger$$

Size issues: truncate $L = 15$ and every other radial level.

Structure of the background covariance matrix in 3D

Transport of information from the surface downwards:

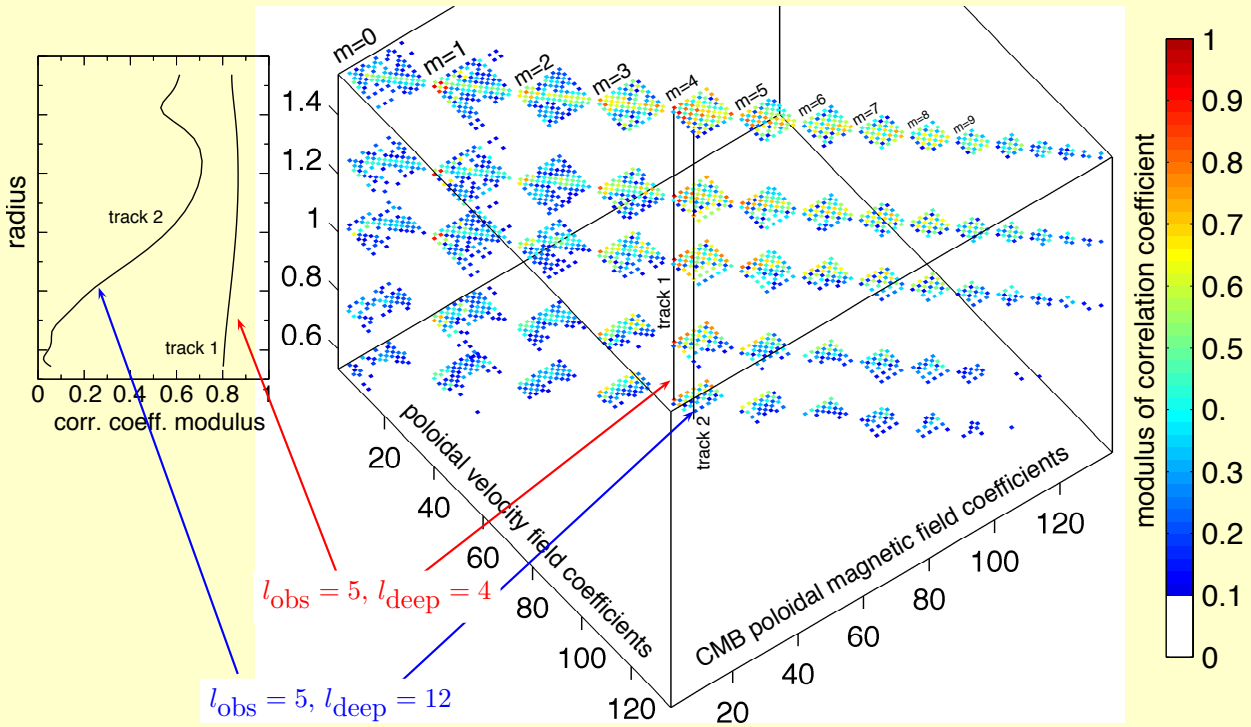

Aubert & Fournier, NPG, 2011

NB: $\mathbf{P}^b$ is 20000 $\times$ 20000

Part III

Review article

Chapter 1

Review article: An introduction to data assimilation and predictability in geomagnetism

Space Sci Rev (2010) 155: 247–291
DOI 10.1007/s11214-010-9669-4

An Introduction to Data Assimilation and Predictability in Geomagnetism

Alexandre Fournier · Gauthier Hulot · Dominique Jault · Weijia Kuang · Andrew Tangborn · Nicolas Gillet · Elisabeth Canet · Julien Aubert · Florian Lhuillier

Received: 14 January 2010 / Accepted: 18 June 2010 / Published online: 17 August 2010

Abstract Data assimilation in geomagnetism designates the set of inverse methods for geomagnetic data analysis which rely on an underlying prognostic numerical model of core dynamics. Within that framework, the time-dependency of the magnetohydrodynamic state of the core need no longer be parameterized: The model trajectory (and the secular variation it generates at the surface of the Earth) is controlled by the initial condition, and possibly some other static control parameters. The primary goal of geomagnetic data assimilation is then to combine in an optimal fashion the information contained in the database of geomagnetic observations and in the dynamical model, by adjusting the model trajectory in order to provide an adequate fit to the data.

A. Fournier (✉) · G. Hulot
Géomagnétisme, Institut de Physique du Globe de Paris, Université Paris Diderot, CNRS, 4 place Jussieu, 75252 Paris cedex 5, France
e-mail: fournier@ipgp.fr

D. Jault · N. Gillet · E. Canet
Laboratoire de Géophysique Interne et Tectonophysique, CNRS, Université Joseph-Fourier, Grenoble, France

W. Kuang
Planetary Geodynamics Laboratory, Goddard Space Flight Center, Greenbelt, MD, USA

A. Tangborn
Joint Center for Earth Systems Technology, University of Maryland Baltimore County, Baltimore, MD, USA

E. Canet
Institut für Geophysik, ETH Zürich, Zürich, Switzerland

J. Aubert
Dynamique des Fluides Géologiques, Institut de Physique du Globe de Paris, Paris, France

F. Lhuillier
Géomagnétisme & Dynamique des Fluides Géologiques, Institut de Physique du Globe de Paris, Paris, France

The recent developments in that emerging field of research are motivated mostly by the increase in data quality and quantity during the last decade, owing to the ongoing era of magnetic observation of the Earth from space, and by the concurrent progress in the numerical description of core dynamics.

In this article we review briefly the current status of our knowledge of core dynamics, and elaborate on the reasons which motivate geomagnetic data assimilation studies, most notably (a) the prospect to propagate the current quality of data backward in time to construct dynamically consistent historical core field and flow models, (b) the possibility to improve the forecast of the secular variation, and (c) on a more fundamental level, the will to identify unambiguously the physical mechanisms governing the secular variation. We then present the fundamentals of data assimilation (in its sequential and variational forms) and summarize the observations at hand for data assimilation practice. We present next two approaches to geomagnetic data assimilation: The first relies on a three-dimensional model of the geodynamo, and the second on a quasi-geostrophic approximation. We also provide an estimate of the limit of the predictability of the geomagnetic secular variation based upon a suite of three-dimensional dynamo models. We finish by discussing possible directions for future research, in particular the assimilation of laboratory observations of liquid metal analogs of Earth's core.

Keywords Geomagnetic secular variation · Dynamo: theories and simulations · Earth's core dynamics · Inverse theory · Data assimilation · Satellite magnetics · Predictability

1 Introduction

1.1 Inference on Core Dynamics from Geomagnetic Observations

We begin with a brief overview of the current status of our knowledge of core dynamics, as deduced from the record of the geomagnetic secular variation. In addition to the various references listed in this section, the interested reader will find a complete account of the theoretical and observational foundations of that knowledge in the reviews by Jackson and Finlay (2007) and Finlay et al. (2010).

Inferences on sub-annual to decadal core dynamics are usually made by assuming that the geomagnetic secular variation at the core-mantle boundary (CMB), as described by the rate-of-change of the radial component of the magnetic induction $\partial_t B_r$, is caused by diffusionless advection by the fluid flow $\boldsymbol{u}_h$:

$$\partial_t B_r = -\nabla_h \cdot (\boldsymbol{u}_h B_r)\,, \tag{1}$$

in which $\nabla_h \cdot$ is the horizontal divergence operator. This so-called frozen-flux hypothesis was originally proposed by Roberts and Scott (1965); it is of central importance for finding estimates of the flow at the top of the core responsible for the observed secular variation. As such, the problem is non-unique (Backus 1968). Consequently, further assumptions on $\boldsymbol{u}_h$ are needed; those are reviewed in detail and discussed by Holme (2007) and Finlay et al. (2010). In addition, the product of the inversion is often regularized: Intermediate—to small-scale features are damped in order to produce a flow of moderate spatial complexity. In the past thirty years, tens of studies based on different approaches have arguably produced a common, large-scale picture of $\boldsymbol{u}_h$ for recent epochs (Holme 2007): it consists in a strong westward flow under the Atlantic ocean, a flow usually weaker under the Pacific hemisphere, and it exhibits large-scale vortices under South Africa and North America, the root

mean square (rms) flow speed being on the order of 15 km/y. Further inspection of various core flow models produced under different working hypotheses reveals features which are far less consensual, and hypotheses-dependent (Holme 2007, and references therein). The large-scale, consensual picture described above evolves slowly over time, as do the large-scale features of the magnetic field (e.g. Hulot and Le Mouël 1994).[1] This can be observed by considering either snapshots of $\boldsymbol{u}_h$ at different epochs (e.g. Hulot et al. 1993), or parameterized, time-dependent core flow models, as computed by Jackson (1997) (recall that time is a parameter, and not a variable, within the kinematic framework we have discussed so far).

In an attempt to relate the dynamics inferred at the top of the core with its deeper origin, the axisymmetric component of time-dependent core surface motions can in turn be interpreted as the signature of torsional oscillations occurring inside the core (Braginsky 1970). The subject of torsional oscillations is reviewed by Finlay et al. (2010). Trying to fit the secular variation (or to explain time-dependent core flow) using that class of wavy motions is of great interest, since it provides in particular constraints on the strength of the cylindrical radial magnetic induction inside the core, B_s. For a recent effort in that direction, consult Buffett et al. (2009).

The path from geomagnetic observations to the description of core dynamics has thus so far mostly consisted in a two-stage, sequential process: First, B_r and $\partial_t B_r$ are estimated at the CMB by downward-continuing surface measurements, using some regularization. Second, the surface flow underneath the CMB is estimated from (1), by imposing one (or several) constraints on the flow, and inevitably some damping. However and regardless of the lack of consistency of that strategy, it now appears that our ability to learn more about core dynamics following this path has almost reached a plateau, even though the quality and density of the recent data keep on improving. This is because spatial resolution errors[2] (the large-scale secular variation due to the interaction of the concealed, small-scale field, with the large-scale flow) now dominate observational errors in the error budget of core flow inversions (Eymin and Hulot 2005).

More recently, sophisticated strategies, such as ensemble approaches, have been used to describe statistically the corresponding unresolved component of the secular variation (Gillet et al. 2009). Modeling strategies bypassing the above two-stage, sequential approach have also been designed to simultaneously invert for the field and the flow at the top of the core (Lesur et al. 2010), in philosophical line with an earlier work by Waddington et al. (1995). Lesur et al. (2010) implement the frozen-flux constraint (equation (1)) in their inversion, thereby introducing a dynamically consistent relationship between B_r and $\boldsymbol{u}_h$ at the top of the core.

These two recent and innovative approaches very much point the way forward to a better understanding and description of core dynamics, by incorporating dynamical constraints (as imposed by the equations governing the secular variation of the geomagnetic field) in the inversion process, and taking spatial resolution errors into account in the most sensible way. Such preoccupations are not limited to the study of the geomagnetic secular variation: During the past decades, they have also been central in the fields of atmospheric dynamics and physical oceanography, and at the heart of the development of data assimilation strategies.

[1] Note, though, that recent field models based on satellite data indicate a reorganization time for the large-scale structures of the secular variation $\partial_t B_r$ itself on the order of 20 y (Olsen et al. 2009).

[2] Also called "errors of representativeness" in the data assimilation literature (e.g. Lorenc 1986; Kalnay 2003; Brasseur 2006).

The terminology "data assimilation" was coined in meteorology to label the set of time-dependent, inverse techniques used for improving the forecast of the state of the atmosphere. In his authoritative article, Talagrand (1997) defines the assimilation of meteorological or oceanographical observations as the process through which all the available information is used in order to estimate as accurately as possible the state of the atmospheric or oceanic flow. Here we complement that definition by explicitly adding that the determination of the associated uncertainty is also desirable.

1.2 A Historical Perspective on Atmospheric Data Assimilation and Numerical Weather Prediction

Precisely because atmospheric data assimilation is so much ahead of geomagnetic data assimilation, it is worth providing the reader first with a brief historical perspective on that area of research (and the related issue of numerical weather prediction). The standards defined by this more mature field will naturally lead us to further argue for the need to develop geomagnetic data assimilation systems.

Data assimilation was initially developed as a means to initialize atmospheric models for use in Numerical Weather Prediction (NWP). Early efforts to predict atmospheric motion through calculation began even before the advent of digital computers. Richardson (1922) developed the first numerical weather prediction system, using a room full of human calculators, and was ultimately unsuccessful. Observations of the atmosphere were hand interpolated to a regular grid in order to initialize an early equations of motion and state system, taking 6 weeks to carry out a 6-hour forecast. The development of early computers led to an effort by Charney et al. (1950), which used numerical interpolation to fit observational data to a regular grid.

The general approach of interpolating a numerical forecast to observation location, calculating the difference between observation and forecast (O − F) (termed the innovation) and interpolating back to the numerical grid, was first developed by Bergthorsson and Döös (1955). This difference was then used to correct the forecast as an initialization of the next segment of the model forecast. Statistical interpolation, a Bayesian approach for giving relative weights to the observations and forecast, was next introduced by Eliassen (1954) and Gandin (1963).

From this time forward the field of numerical weather prediction progressed rapidly, and still continues to do so: the 72-hour forecasts are now as successful (as measured by the average error in the determination of the horizontal pressure gradient over a given area) as the 36-hour forecasts were 10 or 20 years ago (Kalnay 2003). Kalnay (2003) attributes that continuous improvement to the conjunction of four factors:

(F1) the increased power of supercomputers, allowing much finer numerical resolution and fewer approximations in the operational atmospheric models;
(F2) the improved representation of small-scale physical processes (clouds, precipitation, turbulent transfers of heat, moisture, momentum, and radiation) within the models;
(F3) the use of more accurate methods of data assimilation, which results in improved initial conditions for the model; and
(F4) the increased availability of data, especially satellite and aircraft data over the oceans and the Southern hemisphere.

It is striking to see how those factors can equally well be listed as necessary conditions for progress to occur in the field of geomagnetic data analysis and its interpretation in terms of the underlying core dynamics.

1.3 Why Consider Geomagnetic Data Assimilation

It is quite tempting to wonder how the learning curve of atmospheric data assimilation carries over to the subject of geomagnetic data analysis. An intermediate learning curve would actually be that of ocean data assimilation (Ghil and Malanotte-Rizzoli 1991): the interested reader will find in the monograph edited by Chassignet and Verron (2006) an account of its evolution over the past fifteen years, in the wake of the launch of several satellite missions to monitor the state of the world ocean (the Global Ocean Observation System),[3] which led to the international Global Ocean Data Assimilation Experiment program.[4] In geomagnetism, alongside the recent increase in the quantity and quality of observations (factor F4 above, which is described succinctly in Sect. 3 below, and more substantially by Hulot et al. 2007 and Gillet et al. 2010b), there has been considerable improvement in our ability to model numerically the non-linear dynamics of the core since the groundbreaking work of Glatzmaier and Roberts (1995) (e.g. Christensen and Wicht 2007; Sakuraba and Roberts 2009). This improvement essentially follows on from the increase in computational power, and the development of codes able to capitalize on the parallel trend in high-performance computing (factor F1 above). Three-dimensional, convection-driven models of the geodynamo are of particular interest since they are now used to derive scaling laws for its average behavior. Key non-dimensional parameters controlling that behavior can be identified in a database of such models, and for instance used to evaluate, after appropriate extrapolation, the rms strength of the magnetic field inside the core, which is of order 2 mT according to Christensen and Aubert (2006) and Christensen et al. (2009). Despite that indisputable progress, questions remain concerning the applicability of such numerical tools to geomagnetic field modelling, depending on the time scale of interest. Practical numerical considerations make the value of some input diffusive control parameters too large (by several orders of magnitude) compared to what one would expect for the Earth. Part of the dynamics is thus certainly affected (damped) in such numerical simulations (that includes the torsional oscillations). Also, a good modelling of the secular variation on interannual time scales requires a proper separation of the time scales of the relevant physical phenomena, in line with what occurs in the core. These phenomena include inertial waves (which build geostrophy), various types of magnetohydrodynamic waves, advection, and Ohmic dissipation; the corresponding time scales are roughly of order 1 day, 10 yr, 100 yr, and 10,000 yr, respectively (e.g. Gubbins and Roberts 1987; Jault 2008; Finlay et al. 2010). Having those time scales in the right proportion is currently not easily achievable with three-dimensional dynamo models. Their ability to cope with that mismatch will be assessed through their success in analyzing and forecasting short-term geomagnetic changes (in light of the available observations).

Alternatively, one can be tempted to circumvent that overdiffusive behavior by simplifying the model of core dynamics, thereby reducing its dimensionality and making less diffusive simulations, with an appropriate separation of the relevant timescales, possible (at the expense of some physics lost along the way). An example is the quasi-geostrophic approach, which assumes that the flow is invariant along the direction of rotation of the Earth, and effectively considers a two-dimensional flow. The validity of that approach (depending on the time scale and the region under scrutiny) is addressed in Sect. 4.2. In what follows, we actually make a case for geomagnetic data assimilation as a way to test to which extent

[3] www.ioc-goos.org.

[4] www.godae.org.

a given model can be successful in explaining our indirect observations of core dynamics. Bearing in mind the recent evolution in the observation of the geomagnetic field and the modelling of core dynamics, we now list some of the questions which we would like to try and answer using geomagnetic data assimilation:

1. Can the physical mechanisms responsible for the geomagnetic secular variation be identified unambiguously in its record? As an example, are surface measurements the signature of effective material transport of B_r at the CMB, or the signature of hydromagnetic waves (Finlay and Jackson 2003)? Those two effects could very well be combined, and, despite the popularity of the frozen-flux approach, an ounce (or more) of diffusion might also be required (Gubbins 1996; Chulliat and Olsen 2010; Chulliat et al. 2010). Assimilation of geomagnetic measurements into models of core dynamics will first and foremost tell us something about the various models we resort to. As outlined above, a comprehensive model of core dynamics, able to represent all the physics occuring at all time and length scales, is not within reach. Compromises have to be made, and geomagnetic data assimilation appears as the natural framework within which to evaluate the robustness of those compromises, in the light of the data.
2. What is the predictive power of dynamical models of the geomagnetic field? That question is related to the problem of forecasting, a long-standing issue of interest in numerical weather prediction (see Sect. 1.2 above).
3. To which extent is it possible to retro-propagate the current quality of data for the purpose of core field modelling? That question is related to the issue of hindcasting, or reanalysis. Here a reference is the work done on the reanalysis of the state of the atmosphere over the time period 1957–1996, that is supposed to be free of artifacts resulting from changes in the assimilation/analysis techniques used initially in that time interval (Kalnay et al. 1996). This reanalysis has allowed one to recompute more accurately the atmospheric angular momentum over that same time window, and its related contribution to the length-of-day (LOD) time series (Gross et al. 2004).

Regarding that last point, the interest for data assimilation lies in its versatility regarding the type of measurements it can use to obtain some insights on the state of the system under study. Any measurement (even remotely related to the state of system) can be used. The quality and quantity of information contained in those measurements can also vary widely with time, which makes data assimilation particularly well-suited for geomagnetic purposes.

Finally, specific to the core problem is the attractive possibility offered by the joint use of models and observations to probe (indirectly) the deeper dynamics of the core by analyzing its magnetic surficial signature at the core-mantle boundary.

The remainder of this article aims at discussing the possibility of addressing the questions listed above in a foreseeable future with the help of data assimilation. It is organized as follows: The methodological foundations of data assimilation are first presented in Sect. 2. Section 3 summarizes next the observations at hand for geomagnetic data assimilation practice. Section 4 reviews recent studies devoted to the feasibility and application of data assimilation techniques for the purpose of geomagnetic data analysis. Two options have been followed so far:

– One option relies on three-dimensional numerical models of the geodynamo, and is illustrated in Sect. 4.1. Three-dimensional models of the geodynamo have actually also been used to try and estimate the limit of predictability of the secular variation, an account of which is provided in Sect. 4.3.
– Another option is based upon quasi-geostrophic models of the secular variation, and is the subject of Sect. 4.2.

Section 5 concludes this review by providing a tentative summary and by pointing out possible directions for future research.

2 Fundamentals of Data Assimilation

In this section we aim at describing the fundamentals of data assimilation, in its sequential and variational formulations, without providing any proof of the underlying mathematical results. The interested reader will find a much more rigorous and complete treatment of the subject in the recent treatises by Bennett (2002), Kalnay (2003), Wunsch (2006), and Evensen (2009). We will resort as much as possible to the set of notations recommended by Ide et al. (1997); our notations are summarized in Table 1.

2.1 Basic Ingredients

The goal of geomagnetic data assimilation is to solve the time-dependent inverse problem of estimating the state of the core $\mathbf{x}$, with time appearing as an explicit variable. We have at

Table 1 Data assimilation notations used in this paper, which follow for the most part the recommendations made by Ide et al. (1997). With the exception of the objective function J, the quantities listed in this table are time-dependent, and appear in the text with an index i referring to the discrete time t_i at which they come into play

Symbol	Meaning
$\mathbf{x}$	the state vector of the core
$L_{\mathbf{x}}$	size of the state vector
$\mathbf{x}^t$	the true state
M	the forward model of core dynamics
$\boldsymbol{\eta}$	the model error
$\mathbf{Q}$	the model error covariance matrix
$\mathbf{x}^f$	the forecast
$\boldsymbol{\epsilon}^f$	the forecast error
$\mathbf{P}^f$	the forecast error covariance matrix
$\mathbf{x}^a$	the analysis
$\boldsymbol{\epsilon}^a$	the analysis error
$\mathbf{P}^a$	the analysis error covariance matrix
$\mathbf{x}^b$	the background state
$\mathbf{P}^b$	the background error covariance matrix
H	the observation operator
$H' \equiv \mathbf{H}$	the linearized observation operator
$\mathbf{y}^o$	the observations
$L_{\mathbf{y}^o}$	size of the observation vector
$\boldsymbol{\epsilon}^o$	the observational error
$\mathbf{R}$	the observational error covariance matrix
K	the Kalman gain
J	the objective function
$M' \equiv \mathbf{M}$	the tangent linear model
$M'^T \equiv \mathbf{M}^T$	the adjoint model
$\mathbf{d}$	the innovation
$\mathbf{r}$	the residual
$\mathbf{a}$	the adjoint field

our disposal a database of observations of the core and a numerical model of its dynamics. Before proceeding with technicalities, we quote Wunsch (2006): " ... almost all methods in actual use are, beneath the mathematical disguises, nothing but versions of least-square fitting of models to data, but reorganized so as to increase the efficiency of solution, or to minimize storage requirements, or to accommodate continuing data streams."

In the remainder of this section, we shall operate in a discrete world. Assume we have a prognostic, possibly non-linear, numerical model M which describes the dynamical evolution of the core state at any discrete time t_i, $i \in \{0, \ldots, n\}$. If Δt denotes the time-step size, the width of the time window considered here is $T = t_n - t_0 = n\Delta t$, the initial (final) time being t_0 (t_n). In formal assimilation parlance, this is written as

$$\mathbf{x}_{i+1} = M_{i,i+1}\left[\mathbf{x}_i\right], \tag{2}$$

in which $\mathbf{x}_i$ is a column vector (of size $L_{\mathbf{x}_i}$, say), describing the state of the core at discrete time t_i. If M relies for instance on a grid-based discretization of the equations governing the geomagnetic secular variation, then the state vector $\mathbf{x}$ contains the values of all the corresponding field variables at every grid point. The secular variation equations could involve terms with a known, explicit time dependence, hence the dependence of M on time in (2). In the remainder of this paper, we shall omit the model operator time indices for the sake of clarity, unless necessary. Within this framework, the modeled secular variation is controlled by the initial state of the core, $\mathbf{x}_0$, and possibly some other, static, input parameters. The model operator is imperfect: Even if we knew the true state of the core $\mathbf{x}_i^t$ at discrete time t_i, the action of the model would introduce a simulation error $\boldsymbol{\eta}_{i+1}$ at time t_{i+1}, defined as

$$\boldsymbol{\eta}_{i+1} = M\left[\mathbf{x}_i^t\right] - \mathbf{x}_{i+1}^t. \tag{3}$$

In the following, the statistical distribution of that error is assumed to be Gaussian and centered, and we denote the simulation error covariance matrix with $\mathbf{Q}_i$.

Assume now that we have partial and imperfect knowledge of the true dynamical state of the core $\mathbf{x}^t$ through databases of observations $\mathbf{y}^o$ collected at discrete locations in space and time. This formally writes

$$\mathbf{y}_i^o = H_i[\mathbf{x}_i^t] + \boldsymbol{\epsilon}_i^o, \tag{4}$$

in which $\mathbf{y}_i^o$ is a column vector of size $L_{\mathbf{y}_i^o}$, and H_i and $\boldsymbol{\epsilon}_i^o$ are the (possibly time-dependent) discrete observation operator and error, respectively. Modern geomagnetic observations consist of (scalar or vector) measurements of the magnetic field, possibly supplemented by annual to decadal time series of the length-of-day, since these are related to the angular momentum of the core (see Sect. 3). The observation operator is assumed time-dependent: In the context of geomagnetic data assimilation, we can safely anticipate that its dimension will increase dramatically when entering the recent satellite era (1999–present). However, H_i will inevitably connect $\mathbf{x}$ with a space of lower dimensionality than the state space ($L_{\mathbf{y}_i^o} < L_{\mathbf{x}_i}$, see Table 2). The observational error $\boldsymbol{\epsilon}_i^o$ is time-dependent as well. We will assume in the following that it has zero mean and we will denote its covariance matrix at discrete time t_i by $\mathbf{R}_i$. For simplicity and unless otherwise stated, we will also assume that the observation operator is linear, namely that $H = H' \equiv \mathbf{H}$ according to the notations of Table 1.

As illustrated in Fig. 1, we may have a first guess of the model trajectory over the time interval of interest, and some observations (along with their error statistics) available along the way. Our task is to make the best (optimal) use of those available measurements in order to correct the initial trajectory. This can be achieved following either of two strategies, referred to as sequential or variational data assimilation, which we will now introduce.

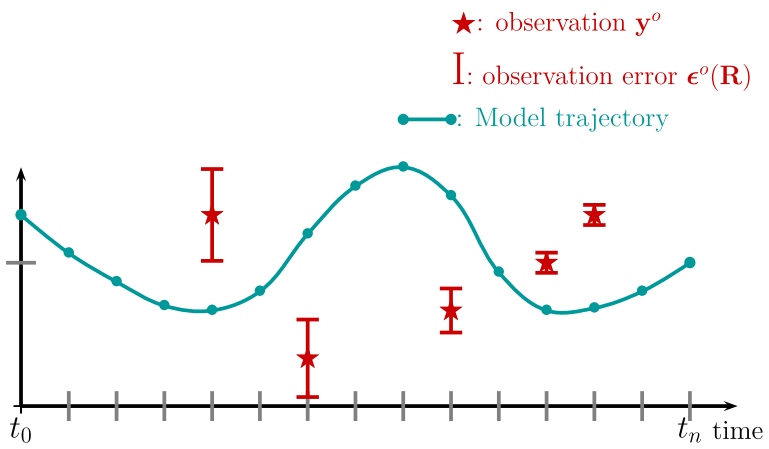

Fig. 1 Assimilation starts with an unconstrained model trajectory over the time window of interest. It aims at correcting this initial model trajectory in order to provide an optimal fit to the available observations (*the stars*), given their *error bars*. In this figure (and also in Figs. 3 and 4), it is assumed for pedagogical simplicity that the state vector and the observation vector belong to the same one-dimensional space

2.2 Methodology: Two Classes of Implementation

2.2.1 Sequential Assimilation

Sequential assimilation is rooted in estimation theory and its two-stage principle is the following: Starting from a previously analyzed core state, we first forecast the evolution of that state, and then correct it (i.e. perform an analysis) as soon as an observation is available. For the sake of simplicity, we shall defer the discussion of the non-linear case and consider for now that M is linear.

1. The forecast: In mathematical terms, the forecast at time t_{i+1}, $\mathbf{x}^f_{i+1}$, is obtained by time-stepping the model, starting from the a priori, analyzed state $\mathbf{x}^a_i$[5] at time t_i:

$$\mathbf{x}^f_{i+1} = M\mathbf{x}^a_i. \tag{5}$$

The forecast error writes accordingly

$$\boldsymbol{\epsilon}^f_{i+1} = \mathbf{x}^f_{i+1} - \mathbf{x}^t_{i+1} = M\left(\mathbf{x}^a_i - \mathbf{x}^t_i\right) + \boldsymbol{\eta}_{i+1}, \tag{6}$$

which shows that it has two components (see Fig. 2):

- The propagated error in the a priori, analyzed estimate of the core state, $M\boldsymbol{\epsilon}^a_i = M(\mathbf{x}^a_i - \mathbf{x}^t_i)$. Even if estimated using previous observations, the estimate $\mathbf{x}^a_i$ is not the true state of the core. The statistics of that component of the error field are described by the time-dependent, a priori error covariance matrix $\mathbf{P}^a_i$. We will assume again that the error has zero mean and that it is distributed as a Gaussian, multivariate random variable.
- The model error $\boldsymbol{\eta}_{i+1} = M\mathbf{x}^t_i - \mathbf{x}_{i+1}$, which was already introduced in the previous paragraph, with covariance matrix $\mathbf{Q}_{i+1}$.

The statistical properties of the forecast error are described by a covariance matrix given by

$$\mathbf{P}^f_{i+1} = E\left(\boldsymbol{\epsilon}^f_{i+1}\boldsymbol{\epsilon}^{f^T}_{i+1}\right) = M\mathbf{P}^a_i M^T + \mathbf{Q}_{i+1}, \tag{7}$$

[5] $\mathbf{x}^a_i$ is either the product of a previous assimilation cycle, or based on the initial guess trajectory in the case of the first encounter with an observation.

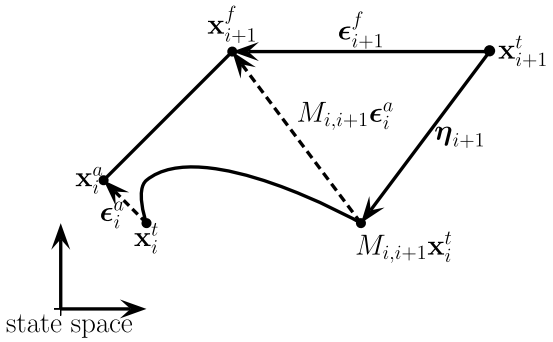

Fig. 2 The forecast error $\boldsymbol{\epsilon}^f_{i+1}$ has two sources: One is related to the propagation of the a priori error by the model (*dashed arrow*), and the other is related to the model itself: $\boldsymbol{\eta}_{i+1}$ quantifies the physics which the model does not account for properly. After Brasseur (2006)

in which $E(\cdot)$ denotes statistical expectation and T means transpose. The error on the initial state is transformed during the forecast state by the model dynamics, and augmented by the model imperfections, both being assumed statistically independent.

2. The analysis: The goal of the analysis is to determine the optimal estimate $\mathbf{x}^a_{i+1}$ of $\mathbf{x}^t_{i+1}$, given the observations $\mathbf{y}^o_{i+1}$. The corresponding conditional probability p is given by Bayes' formula

$$p\left(\mathbf{x}^t_{i+1}|\mathbf{y}^o_{i+1}\right) = \frac{p(\mathbf{y}^o_{i+1}|\mathbf{x}^t_{i+1})\,p(\mathbf{x}^t_{i+1})}{p(\mathbf{y}^o_{i+1})}. \tag{8}$$

The numerator being a simple scaling factor, it can be ignored when trying to maximize that probability density function (pdf). Our hypotheses of Gaussianity imply

$$p\left(\mathbf{x}^t_{i+1}|\mathbf{y}^o_{i+1}\right) \propto \exp\left[-\frac{1}{2}\left(\boldsymbol{\epsilon}^{oT}_{i+1}\mathbf{R}^{-1}_{i+1}\boldsymbol{\epsilon}^o_{i+1} + \boldsymbol{\epsilon}^{fT}_{i+1}\mathbf{P}^{f^{-1}}_{i+1}\boldsymbol{\epsilon}^f_{i+1}\right)\right], \tag{9}$$

and finding the optimal estimation (which maximizes this expression) is equivalent to finding the minimum of the argument of the exponential. Given the expressions of the various error fields, the corresponding functional J writes

$$J(\mathbf{x}) = \left(\mathbf{y}^o_{i+1} - H_{i+1}\mathbf{x}\right)^T \mathbf{R}^{-1}_{i+1}\left(\mathbf{y}^o_{i+1} - H_{i+1}\mathbf{x}\right) + \left(\mathbf{x}^f_{i+1} - \mathbf{x}\right)^T \mathbf{P}^{f^{-1}}_{i+1}\left(\mathbf{x}^f_{i+1} - \mathbf{x}\right). \tag{10}$$

After some algebra, one finds that the optimal estimation for the state vector, $\mathbf{x}^a_{i+1}$, is given by

$$\mathbf{x}^a_{i+1} = \mathbf{x}^f_{i+1} + K_{i+1}\left(\mathbf{y}^o_{i+1} - H_{i+1}\mathbf{x}^f_{i+1}\right), \tag{11}$$

in which

$$K_{i+1} = \mathbf{P}^f_{i+1}H^T_{i+1}\left(H_{i+1}\mathbf{P}^f_{i+1}H^T_{i+1} + \mathbf{R}_{i+1}\right)^{-1} \tag{12}$$

is the so-called Kalman gain matrix. Two limits are of pedagogical interest: First, in the case of perfect observations ($\mathbf{R}_{i+1} \sim \mathbf{0}$) of the entire state ($H_{i+1} \sim \mathbf{I}$), the Kalman gain is the identity $\mathbf{I}$. Second, in the case of an extremely accurate forecast ($\mathbf{P}^f \sim \mathbf{0}$), the correction to the forecast becomes negligible.

The analysis is in turn characterized by an error described by the covariance matrix

$$\mathbf{P}^a_{i+1} = \left[\mathbf{I} - K_{i+1}H_{i+1}\right]\mathbf{P}^f_{i+1}. \tag{13}$$

That last equation shows how the uncertainty in the forecast decreases in proportion to the amount of information added to the system.

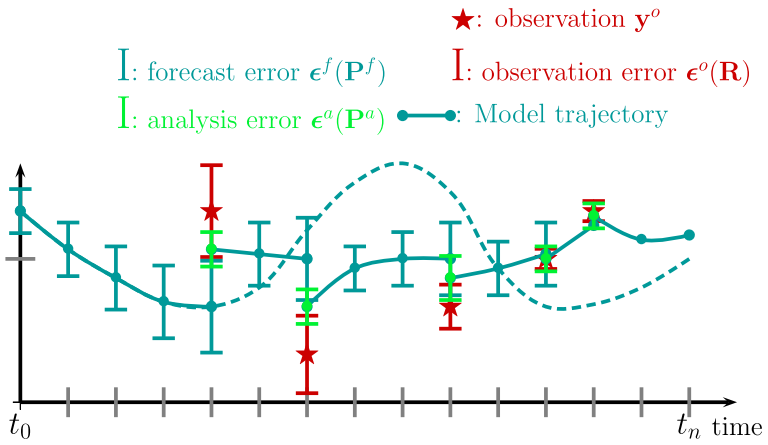

Fig. 3 The sequential approach to data assimilation. Starting from the initial time, the model trajectory follows the initial forecast, and is characterized by a growth of the forecast error. As soon as the first observation is available, the analysis is performed (*green bullet*), and the associated error decreases (*green error bar*). The same cycle is repeated anytime an observation is available, with the assimilated trajectory deviating from the initial guess (*the dashed line*)

The innovation $\mathbf{d}$ then represents the difference between the observations and the forecast

$$\mathbf{d}_{i+1} = \mathbf{y}^o_{i+1} - H_{i+1}\mathbf{x}^f_{i+1}, \tag{14}$$

while the residual $\mathbf{r}$ refers to the difference between the same observations and the analysis

$$\mathbf{r}_{i+1} = \mathbf{y}^o_{i+1} - H_{i+1}\mathbf{x}^a_{i+1}. \tag{15}$$

These two fields are useful for assessing the a posteriori consistency of a data assimilation scheme (see Sect. 2.2.4).

To summarize, sequential assimilation consists first of a forecast stage, where both the forecast and (in principle) its error statistics are computed thanks to the model (see (5) and (7)). During the second stage, the available observations are used to correct the forecast and its error statistics, according to (11) and (13), respectively. That process is repeated sequentially, as illustrated schematically in Fig. 3.

Finally, recall that to get (7), we assumed that the model M was linear. If the assumed dynamics is non-linear, one has to replace M in that equation by the tangent linear model $\mathbf{M}$, obtained by linearizing the model about the current model trajectory. Equations (5), (11), and (13) still hold in the so-called extended Kalman filter (EKF) framework.

2.2.2 *Variational Assimilation*

Unlike sequential assimilation (which emanates from estimation theory), variational assimilation is rooted in optimal control theory. The analyzed state is not defined as the one maximizing a certain pdf, but as the one minimizing a functional J of the form

$$J(\mathbf{x}) = \frac{1}{2}\left\{\sum_{i=0}^{n}\left[H_i\mathbf{x}_i - \mathbf{y}^o_i\right]^T \mathbf{R}_i^{-1}\left[H_i\mathbf{x}_i - \mathbf{y}^o_i\right] + \left[\mathbf{x} - \mathbf{x}^b\right]^T \mathbf{P}^{b\,-1}\left[\mathbf{x} - \mathbf{x}^b\right]\right\}, \tag{16}$$

in which $\mathbf{x}_i = M_{i,i-1}\cdots M_{1,0}\mathbf{x}$, the sought $\mathbf{x}$ being the best estimate of the initial state of the core $\mathbf{x}_0$. This objective function is defined over the entire time window of interest. It is the sum of two terms. The first one measures the distance between the observations and the

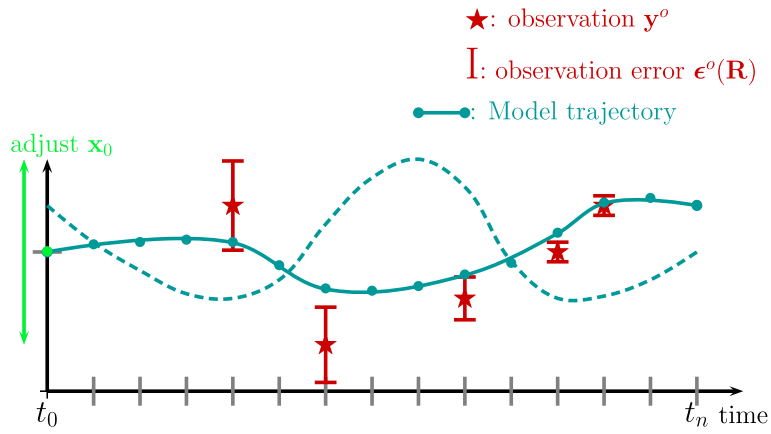

Fig. 4 The variational approach to data assimilation. After adjustment of the initial condition $\mathbf{x}_0$ (*the green bullet* on the $t = t_0$ axis) by means of an iterative minimization algorithm, the model trajectory is corrected over the entire time window, in order to provide an optimal fit to the data (in a generalized least squares sense). The dashed line corresponds to the initial (unconstrained) guess of the model trajectory introduced in Fig. 1

predictions of the model. It is weighted by the confidence we have in the observations. The second term is analogous to the various norms which are added when solving the kinematic core flow problem; it evaluates the distance between the initial condition and an a priori background state $\mathbf{x}^b$. That stabilizing term is weighted by the confidence we have in the definition of the background state, described by the background error covariance matrix $\mathbf{P}^b$.[6] Defining a background state for the core is no trivial matter. But one may substitute (or supplement) the corresponding term in (16) by (with) another stabilizing term, typically a norm, as was done by Talagrand and Courtier (1987) and Courtier and Talagrand (1987) in their early numerical experiments with the vorticity equation on the sphere.

The goal of variational data assimilation is to minimize J by adjusting its control variables (or parameters), usually the initial condition $\mathbf{x}_0$ (if everything else is held fixed, see Fig. 4), as implied by our formulation in (16). Iterative minimization requires the computation of the sensitivity (gradient) of J with respect to its control vector, which writes $(\boldsymbol{\nabla}_{\mathbf{x}_0} J)^T$ (the transpose is needed since $\boldsymbol{\nabla}_{\mathbf{x}_0} J$ is by definition a row vector). The value of $L_{\mathbf{x}}$ precludes a brute force calculation of the gradient (which would imply $L_{\mathbf{x}}$ realizations of the forward model over $[t_0, t_n]$). Fortunately, as pointed out early on by Le Dimet and Talagrand (1986) and Talagrand and Courtier (1987), a much more affordable method exists: The so-called adjoint method, which is based on the integration of the so-called adjoint equation backward in time

$$\mathbf{a}_{i-1} = \mathbf{M}_{i-1,i}^T \mathbf{a}_i + H_{i-1}^T \mathbf{R}_{i-1}^{-1} (H_{i-1}\mathbf{x}_{i-1} - \mathbf{y}_{i-1}^o) + \delta_{i1} \mathbf{P}^{b^{-1}} \left(\mathbf{x}_{i-1} - \mathbf{x}^b\right), \quad n \geq i \geq 1, \quad (17)$$

starting from $\mathbf{a}_{n+1} = \mathbf{0}$, where $\mathbf{a}$ is the adjoint field, and δ is the Kronecker symbol. The initial value of the adjoint field provides the sensitivity we seek: $(\boldsymbol{\nabla}_{\mathbf{x}_0} J)^T = \mathbf{a}_0$ (e.g. Fournier et al. 2007). Note that when writing (17), we assumed for simplicity that observations were available at every model time-step.

Equation (17) indicates that over the course of the backward integration, the adjoint field is fed with innovation vectors. Those vectors have an observational component

[6] Ide et al. (1997), and many others, use $\mathbf{B}$ to denote that matrix, a notation which is preempted in our case by the magnetic induction.

$(H_{i-1}\mathbf{x}_{i-1} - \mathbf{y}^o_{i-1})$, and a departure-to-background component $(\mathbf{x}_0 - \mathbf{x}^b)$, these two contributions being weighted by the statistics introduced above. The adjoint model $\mathbf{M}^T$ in (17) is the adjoint of the tangent linear model $\mathbf{M}$ introduced previously in the context of the extended Kalman filter. The adjoint model has a computational cost similar to that of the forward model, and makes it possible to use an iterative minimization algorithm suitable for large-scale problems.

A few comments on the adjoint method are in order:

- It demands the implementation of the adjoint model $\mathbf{M}^T$: the rules to follow for deriving (and validating) the tangent linear and adjoint codes from an existing forward code are well documented in the literature (e.g. Talagrand 1991; Giering and Kaminski 1998), and leave no room for improvisation. Still, this process is rather convoluted. It requires expertise and deep knowledge of the forward code to begin with. The best situation occurs when the forward code is written in a modular fashion, bearing in mind that its adjoint will be needed in the future, and by casting as many operations as possible in terms of matrix-matrix or matrix-vector products (for a one-dimensional illustration with a spectral-element, non-linear magnetohydrodynamic model, see Fournier et al. 2007). The task of coding an adjoint by hand can still become beyond human reach in the case of a very large model. One might then be tempted to resort to an automated differentiation algorithm. Automated differentiation (AD) is a very active field of research:[7] several operational tools are now available, some of which have been tested on geophysical problems by Sambridge et al. (2007).
- The discrete adjoint equation (17) is based on the already discretized model of core dynamics. An alternative exists, which consists first in deriving the adjoint equation at the continuous level, and second in discretizing it, using the same machinery as the one used to discretize the forward model. In most instances, both approaches to the adjoint problem yield the same discrete operators. When in doubt, though, in the case of a minimization problem, one should take the safe road and derive the adjoint of the already discretized problem: This guarantees that the gradient injected in the minimization algorithm is exactly the one corresponding to the discrete cost function (16), up to numerical roundoff error. Since the efficiency of a minimization algorithm grows in proportion to its sensitivity to errors in the gradient, any error in the gradient could otherwise result in a suboptimal solution.
- The adjoint approach is versatile. Aside from the initial state $\mathbf{x}_0$, one can declare static model parameters (static fields, material properties) adjustable, and consequently part of the control vector. For example, Sect. 4.2 presents the results of twin (synthetic) experiments conducted with a torsional oscillation model, for which the control vector comprises the initial angular velocity and the static profile of the cylindrical radial component of the magnetic induction averaged over geostrophic cylinders.
- In the case of a non-linear problem, the forward trajectory $\mathbf{x}_i$, $i \in \{0, \ldots, n\}$, is needed to integrate the adjoint equation. The storage of the complete trajectory may cause memory issues (even on parallel computers), which are traditionally resolved using a so-called checkpointing strategy. The state of the system is stored at a limited number of discrete times, termed checkpoints. Over the course of the backward integration of the adjoint model, these checkpoints are then used to recompute local portions of the forward trajectory on-the-fly, whenever those portions are needed (e.g. Hersbach 1998).

[7] www.autodiff.org.

– On a more general note, adjoint methods have gained some popularity in solid Earth geophysics over the past few years, a joint consequence (again) of the increase in computational power and the availability of high-quality satellite, or ground-based, data. Adjoint methods are now applied to problems related to the structure and evolution of the deep Earth: Electromagnetic induction (Kelbert et al. 2008; Kushinov et al. 2010), mantle convection (Bunge et al. 2003; Liu and Gurnis 2008; Liu et al. 2008), and seismic wave propagation (Tromp et al. 2005, 2008; Fichtner et al. 2006), building in that last case on the theoretical work of Tarantola (1984, 1988).

The application of a variational approach to time-dependent problems has been generically labeled as the 4D-Var approach to data assimilation (e.g. Courtier 1997), and is commonly referred to as 4D-Var. As such, the standard 4D-Var suffers from two drawbacks: It assumes that the model is perfect ($\boldsymbol{\eta} = \mathbf{0}$), and it does not provide direct access to the statistics of the analysis error—notice its absence in Fig. 4. An alternative approach to the "strong constraint" assumption ($\boldsymbol{\eta} = \mathbf{0}$) consists in adding a term quantifying the model error in the definition of the cost function, a term whose weight is controlled by an a priori forecast error covariance. This more general "weak constraint" approach (Sasaki 1970) has been successfully introduced and implemented (under the name "method of representers") in physical oceanography during the past fifteen years (Egbert et al. 1994; Bennett 2002, and references therein). It allows in particular the derivation of posterior error covariances (see also Uboldi and Kamachi 2000). An interesting discussion on various approaches to "weak constraint" 4D-Var in an operational context is also provided by Trémolet (2006).

From a general perspective, the advantages of a variational approach are its flexibility regarding the definition and identification of control variables, and its natural ability to handle time-dependent observation operators (and possibly time-correlated errors). It is also well-suited for the reanalysis of past data records (hindcasting), since the state at a given time is estimated using the past and future observations available over the entire time window (see Fig. 4). Note, however, that hindcasting is also possible if one resorts to sequential smoothers, of the kind described by e.g. Cohn et al. (1994), and applied in an oceanic context by e.g. Cosme et al. (2010).

2.2.3 Practical Considerations: Non-linearities, Size, Cost

Sequential and variational assimilations share the same goal. As suggested by the definitions of the cost functions in (10) and (16), they are equivalent in the linear Gaussian case (Lorenc 1986). In a weakly non-linear situation (and still assuming Gaussian statistics), the equivalence holds at first order between the EKF and 4D-Var, since both resort to the same tangent linear model $\mathbf{M}$ (Courtier 1997). In a strongly non-linear case, issues arise in both approaches.

From the variational point of view, the cost function can loose its convexity, and several local minima exist. This situation is illustrated in a 1-parameter synthetic situation in Fig. 5. In that example, a reference secular variation is generated using the frozen-flux equation (1). It is initialized by a given map of B_r at the top of the core, and is due to an equatorially symmetric quasi-geostrophic $\boldsymbol{u}_h$. The secular variation is generated over a time window of variable width T, expressed in units of the advective time T_{adv}, defined as the ratio of the outer core radius c to the rms flow speed U (see Table 3). The control vector is reduced to a single scalar, which prescribes the position of a mid-latitude cyclonic vortex (located along the Greenwich meridian in the reference, i.e. 'true', case, see Fig. 5). We generate a collection of guesses of the secular variation by picking the same initial B_r and letting the

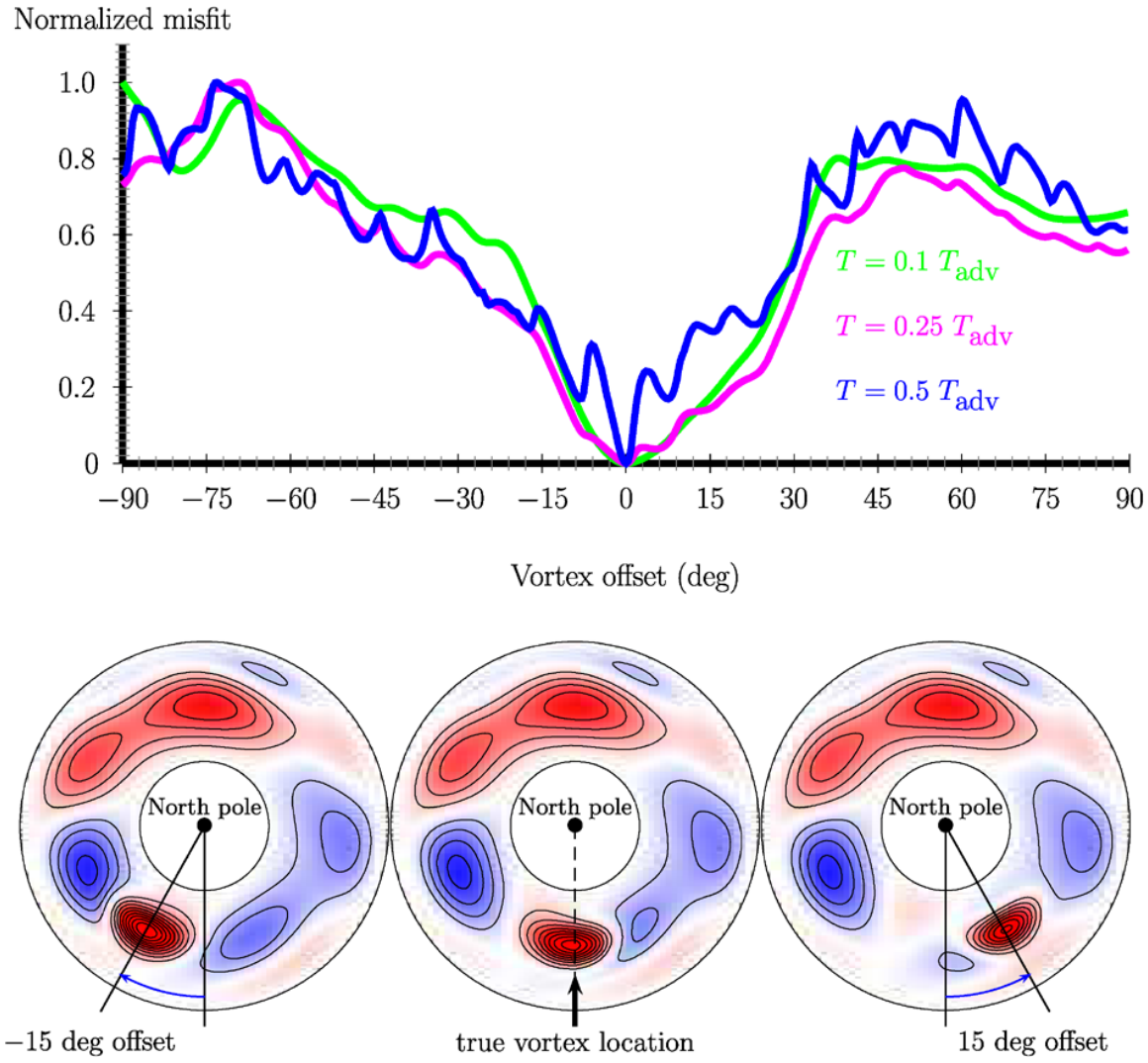

Fig. 5 In the synthetic context of a secular variation generated by a steady quasi-geostrophic core flow $\boldsymbol{u}_h$, the three curves on the top represent the misfit between a reference frozen-flux secular variation, due to a true flow $\boldsymbol{u}_h^t$, and a frozen-flux secular variation due to a guess flow $\boldsymbol{u}_h^g$ (both secular variations are initialized with the same B_r at the top of the core); the only difference between $\boldsymbol{u}_h^t$ and $\boldsymbol{u}_h^g$ is the longitude of the eye of a mid-latitude Gaussian vortex of half-width $c/10$, where c is the radius of the outer core. The streamfunction associated with $\boldsymbol{u}_h^t$ is represented in the *middle of the bottom row* (in the equatorial plane, looking from the North pole). It is based on a solution obtained by Gillet et al. (2009), with a peak-to-peak amplitude on the order of roughly 15,000 y^{-1}, which yields an rms velocity of order 15 km/y. Red and blue correspond to cyclonic and anti-cyclonic motions, respectively. The streamfunctions shown to the *left* and *right* of the true streamfunction are guesses for which the vortex offset is −15 degrees and +15 degrees, respectively (+ means Eastward). In the *top*, the misfit is plotted as a function of the offset longitude in degrees, for three different time window widths T: 0.1, 0.25, and 0.5 advective time T_{adv} (the *green*, *magenta*, and *blue curves*, respectively). The three curves have been normalized to ease cross-comparison. The global minimum (when the guessed flow is the true flow, i.e. the offset is zero) is set in a valley which gets narrower as T is increased, indicating that in an inversion setting, an inaccurate initial guess for the vortex location could result in a solution corresponding to an undesired local minimum

position of this vortex vary (as illustrated on the maps in the bottom of Fig. 5), and estimate the misfit between the reference secular variation and every single guess. Fig. 5 (top) shows the misfit as a function of the vortex offset for three different time window widths T : 0.1, 0.25, and 0.5 advective time T_{adv} (the green, magenta, and blue curves, respectively). The three curves have been normalized to ease cross-comparison. The global minimum (when the guessed flow is the true flow, i.e. the offset is zero) is set in a valley which gets narrower

as T is increased. In addition, the number of local minima (the wiggly character of the misfit) increases substantially with T. This example indicates that in the context of a gradient-based search, an inaccurate initial guess can result in a solution corresponding to a local minimum if the inversion is carried out over a time window of width T representing a substantial portion of the time scale of the dynamics at work (the advective time in our example).

From the sequential point of view, propagating the error statistics via (7) using $\mathbf{M}$ can lead to poor error covariance evolution and even unstable error covariance growth (Miller et al. 1994). This growth is intrinsically related to the chaotic underlying dynamics. In that case, no assimilation should be undertaken over time windows of width larger than the intrinsic predictability time limit for the system, whose value is governed by the combined effects of, first, the amplitude of the error with which the state is estimated from the observations, and, second, the intrinsic error growth rate $\lambda_e = \tau_e^{-1}$ resulting from the chaotic dynamics (Sect. 4.3 discusses further the value of the e-folding time τ_e for the geodynamo).

A remedy to an unstable covariance error growth exists, which relies on a probabilistic description of the non-linear evolution of the model state, and the associated time-dependent pdf based upon a well-chosen ensemble of non-linear forward realizations (Evensen 1994): The so-called ensemble Kalman filter (EnKF) is described in great detail by Evensen (2009), and a first example of a simple application in geomagnetism is that of Beggan and Whaler (2009). Since the time-dependent forecast error covariance matrix is directly derived from the ensemble of forecasts, the EnKF has the extra advantage of making (7) and (13) obsolete: The awfully expensive propagation of error statistics[8] is no longer needed. Actually, the horrendous cost of error statistics propagation often leads data assimilation practitioners to employ a static (frozen) background error covariance matrix, by setting $\mathbf{P}_i^f = \mathbf{P}^b$ for all discrete times: That popular approach is referred to as optimal interpolation (OI), although the convenient approximation upon which it rests makes it suboptimal (e.g. Brasseur 2006). It is, however, a good approximation to begin with, before embarking on more sophisticated strategies such as the EnKF. Section 4.1 presents results obtained in an OI framework by assimilating geomagnetic field models with a three-dimensional model of the geodynamo.

In terms of computer resources, assimilation is very demanding, especially when dealing with non-linear dynamics. For OI and EnKF, the derivation of good error statistics requires an ensemble size of order $\mathcal{O}(10–100)$. Conversely, for 4D-Var, the iterative non-linear minimization might also be achieved in several tens of iterations, bearing in mind that a given iteration relies on a forward and an adjoint calculation. Good preconditioning is therefore almost mandatory. For geomagnetic data analysis, a solution to circumvent the cost problem consists in simplified dynamical models, of reduced dimensionality, and tailored to the study of the secular variation, an example of which is provided in Sect. 4.2.

The computational cost is roughly the same for sequential and variational assimilations.[9] The former is easier to implement than the latter, at the expense of the loss of some flexibility. For an interesting and animated discussion on the relative merits of 4D-Var and the EnKF under their most recent and sophisticated implementations, the reader is referred to Kalnay et al. (2007a, 2007b) and Gustafsson (2007). As far as geomagnetic data assimilation is concerned, and because it is still in its infancy, let us bear in mind for the time being that key to the success of both approaches is a good, trustworthy description of error statistics.

[8] A quick inspection of equations (5) and (7) shows indeed that the propagation of error statistics is $L_{\mathbf{x}}$ times more expensive than a model step, a factor which is prohibitive for almost any practical application, starting from $L_{\mathbf{x}} \gtrsim 1{,}000$, say.

[9] In an operational setting, and at the same computational cost, Buehner (2008) reports that weather forecasts based either on 4D-Var or the EnKF perform equally well.

2.2.4 *A Posteriori Validation, Statistical Consistency and Possible Model Bias*

Once a data assimilation scheme has been implemented, it is possible to perform a posteriori quality and consistency checks to evaluate its performance, and assess the robustness of the hypotheses upon which it relies. These checks are reviewed by Brasseur (2006) in the monograph edited by Chassignet and Verron (2006) and by Talagrand (2003), to which the reader should refer for further detail and references. One intuitive way to assess the efficacy of a given scheme is to compare its predictions with independent measurements of the state of the system. In the oceanographic context, these can consist of measurements of the state of the ocean obtained via a network of buoys. The Earth's core does not lend itself easily to that type of practice, given the sparse database of observations at hand (see Sect. 3 below). Nevertheless, independent and reliable observatory timeseries and the interannual to decadal variation of the length of day (which is related to the angular momentum carried by the core flow, Jault et al. 1988; Jackson et al. 1993) appear as natural candidates for this exercise.

It is also possible to perform internal consistency checks. For instance, in a sequential framework, the first-order moment of the innovation vector (defined in (14)) should vanish over a sufficiently long assimilation sequence

$$E\left(\mathbf{d}_i\right) = E\left(\mathbf{y}_i^o - H_i \mathbf{x}_i^f\right) = E\left[H_i \mathbf{x}_i^t + \boldsymbol{\epsilon}_i^o - H_i\left(\mathbf{x}_i^t + \boldsymbol{\epsilon}_i^f\right)\right] = E\left(\boldsymbol{\epsilon}_i^o\right) - E\left(H_i \boldsymbol{\epsilon}_i^f\right) = \mathbf{0}, \tag{18}$$

in which we have used the definitions of the error fields introduced above, and assumed (as usual) that both were centered. Note that in practice the expectation is computed by taking the time average, i.e. the algebraic mean over all the discrete times t_i at which an assimilation cycle is performed (see the interesting discussion about this practical necessity in Dee and Da Silva 1998). The same property should hold in the variational case, provided the innovation is defined as the difference between the observations and the predictions based upon the estimate of background state $\mathbf{x}^b$ (Talagrand 2003).

A non-zero mean innovation points at a bias, in the observation error or/and in the model error. In case the bias comes from the model, $E\left(\mathbf{d}_i\right)$ provides only the projection of this bias onto the data space, which for the geomagnetic field is restricted to the largest scales of the field at the core-mantle boundary (see Sect. 3 below). Therefore, in the context of geomagnetism, it appears crucial to choose a model that possesses at least some degree of similarity with what we see of the true geomagnetic field. This is necessary if we do not want to deal with a forecast bias, by resorting to a dynamical forecast bias removal strategy such as the one favoured by Dee and Da Silva (1998).

If the model is a three-dimensional model of the geodynamo, we note that in a recent study, Christensen et al. (2010) define a series of quantitative static criteria to help define what would be a good candidate model to represent the geomagnetic field. They consider the ratio of the power in the axial dipole component to that in the rest of the field, the ratios between equatorially symmetric and antisymmetric and between zonal and non-zonal non-dipole components, and a measure for the degree of spatial concentration of magnetic flux at the core surface. Again, these criteria are purely morphological and static; other dynamical properties could be sought, such as the existence of a significant secular variation occuring in the equatorial region, and a tendency for a westward drift of magnetic structures (at least in the Atlantic hemisphere).

The first-order moment of the residual vector (defined in (15)) should also vanish. Should it not, it would hint at the sub-optimality of the system (Talagrand 2003). Many more criteria exist, which involve for instance the second-order moments of the innovation and residual vectors. Here we simply refer the reader to the references listed above for an extensive

coverage of these quality checks (see also Bennett 2002, Sect. 2.3.3). As far as we know, such criteria have not yet been applied to geomagnetic data assimilation schemes, but they should certainly come to the fore when the field becomes more mature, given the insight they can provide (in particular regarding the model bias).

3 Geomagnetic Observations and Their Connection with the State of the Core

Having introduced the basics of data assimilation, let us now try to provide the reader with an overview of the geomagnetic observations $\mathbf{y}^o$ which are in principle amenable to geomagnetic data assimilation practice. We do not aim at discussing here the observation errors (the content of the matrix $\mathbf{R}$), an account of which can be found in the reviews by Hulot et al. (2007), Jackson and Finlay (2007), and Hulot et al. (2010b) for the archeomagnetic database. Rather, we focus on the issue of relating those observations to the state of the core. The keypoint for us is that those measurements are in all cases related to the knowledge of the radial component of the magnetic induction at the top of the core, B_r. We will accordingly discuss the nature of the observation operator H associated with a given measurement.

Modern geomagnetic data consist of appropriately processed time series of the three components of $\boldsymbol{B}$, usually recorded in observatories or by dedicated satellites (see Fig. 6). Those "level-1B"-type data, in space agency parlance, are the observations one would ultimately like to assimilate. At a given location $\boldsymbol{r}^o$, however, the measured field results from the contribution of several internal and external sources (core, crust, ionosphere, magnetosphere, the world ocean), and further time and space filtering is therefore required to isolate the (dominant) signal originating from the core. Various techniques can be used, depending on the type, quantity and quality of data considered. In particular, whereas contributions from non-core sources can only be dealt with as a source of noise when considering early historical data (see e.g. Jackson and Finlay 2007), more advanced techniques have been designed for observatory time series and even more so for satellite data (see e.g. Hulot et al. 2007). In that case, the core field contribution of interest is often directly provided in the form of a so-called geomagnetic field model, which consists in a time-varying spherical harmonic description of the core field. Such models are usually referred to as "level-2" data (products) in space agency parlance.

Practically speaking, and assuming an electrically insulating mantle (a reasonable first-order approximation, see e.g. Alexandrescu et al. 1999), the connection between the state of the core $\mathbf{x}$ (which comprises in some form B_r at the core surface $\mathcal{S}$) and an estimate B_α ($\alpha = 1, 2, 3$) of the core field at $\boldsymbol{r}^o$ is achieved by means of a data kernel K_α

$$B_\alpha(\boldsymbol{r}^o) = \int_{\mathcal{S}} K_\alpha(\boldsymbol{r}^o, \boldsymbol{r}) B_r(\boldsymbol{r}) \, \mathrm{d}^2\boldsymbol{r}, \tag{19}$$

where $\boldsymbol{r}$ denotes a point at the core surface $\mathcal{S}$ (see e.g. Gubbins and Roberts 1983; Bloxham et al. 1989; Jackson 1989, for explicit expressions of these kernels). The exact discrete form of the observation operator H (which is linear in this case) depends ultimately on the quadrature rule used to evaluate the above integral.

Some data (in particular early historical and observatory data) are however sometimes only available in the form of individual inclination and declination measurements. Those are non-linearly related to the components B_α. Directly assimilating such data implies dealing with a non-linear observation operator H. The machinery presented in Sect. 2 remains nevertheless applicable, provided a linearization of H about the current state of the core (or

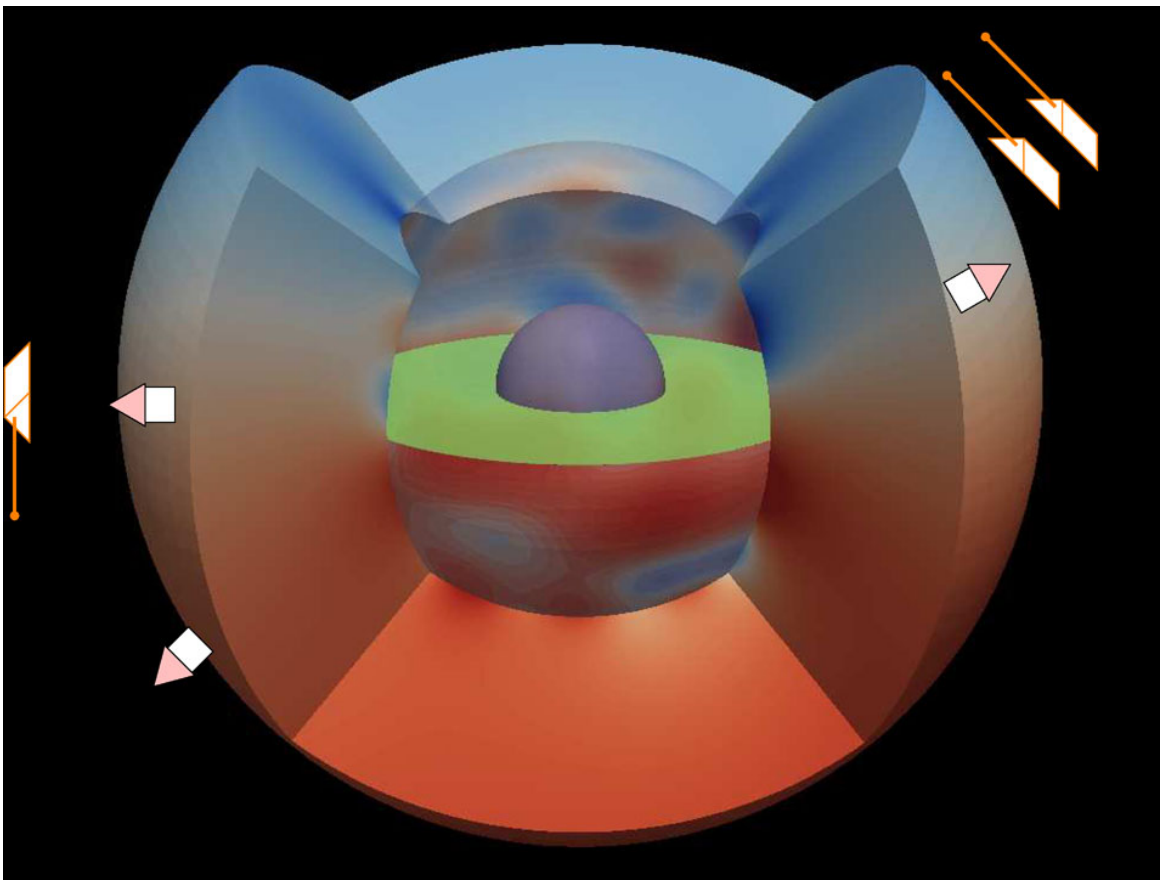

Fig. 6 The magnetic observation of the Earth is made possible by an unevenly distributed network of long-lived magnetic observatories located at its surface. The corresponding database has been supplemented over the past few decades by satellite measurements, most notably during the past ten years for which a continuous satellite database is available. The global coverage provided by the satellites ideally complement the longer observatory time series. In this figure, the innermost sphere is the inner core, which is surrounded by the outer core. The *green plane* is the equatorial plane. The color scale at the core-mantle boundary represents the radial component of the magnetic induction B_r at epoch 2004, according to the CHAOS model of Olsen et al. (2006), with a typical amplitude of ± 1 mT. Going from the surface of the core to the surface of the Earth through the mantle (two thirds of which are represented here), the field decreases. The smaller scales decrease most rapidly, which yields an almost dipolar structure at the surface of the Earth, with the field lines pointing outward in the Southern hemisphere (positive, *red* B_r) and inward in the Northern hemisphere (negative, *blue* B_r). The field amplitude at a given location radius r has been scaled by a factor $(r/c)^3$ for the sake of visibility, c being the radius of the outer core

the background guess, in a weakly non-linear case) is performed, and an iterative solution sought.

On another note, it is also in principle possible to account for the finite electrical conductivity of the mantle σ_m, which introduces a delay between an event occuring at the core surface and its signature at the surface of the Earth. Mantle filter theory (e.g. Backus 1983) requires to replace the kernels in (19) by more general impulse response functions F_α (whose exact form depends on the distribution of σ_m in the mantle), and to convolve these with the history of the evolution of B_r on $\mathcal{S}$

$$B_\alpha(\boldsymbol{r}^o, t) = \int_0^t \int_{\mathcal{S}} F_\alpha(\boldsymbol{r}^o, \boldsymbol{r}, t-\tau) B_r(\boldsymbol{r}, \tau)\, \mathrm{d}^2\boldsymbol{r}\, \mathrm{d}\tau. \tag{20}$$

Implementing such a formalism would be most useful for the investigation of short time scale core dynamics (sub-annual to interannual, say), for which delay and attenuation could

have some importance when trying to interpret the data (e.g. Pinheiro and Jackson 2008). But this calls for substantial novel methodological developments.

Another issue of more immediate concern is the concealing of the smallest spatial scales of the core field by the crustal field. It is related to the formal impossibility of distinguishing the contribution of magnetized sources located within the crust from that of the core. It is well-known that at any given time the core field dominates the largest spatial scales (roughly up to spherical harmonic degree 14, which corresponds to 800 km at the core surface $\mathcal{S}$), whereas the crustal field dominates the smallest spatial scales (e.g. Hulot et al. 2007). This concealing not only affects the field itself but also its time derivative (the secular variation), the smallest scales of which are again expected to be dominated by the crustal secular variation (Hulot et al. 2009). In that case, however, the transition is expected to occur further down the spectrum (near spherical harmonic degree 18, corresponding to a length scale of 600 km on $\mathcal{S}$); this leaves some room for improvement compared to the current situation where the core field secular variation is perhaps recovered up to degree 16 (e.g. Olsen and Mandea 2008). Such an improvement can be expected from the upcoming ESA SWARM mission (Friis-Christensen et al. 2006).[10] The myopia of the geomagnetic observer interested in the core field is a disease which has long been diagnosed. It can be mitigated by resorting to averaging kernels (e.g. Whaler and Gubbins 1981; Jackson 1989; Backus et al. 1996, §4.4.4), and replacing effectively B_r in (19) by an appropriately averaged $\hat{B}_r$ (see also Canet et al. 2009).

Geomagnetic data assimilation is still in its early days and, to our knowledge, a study assimilating "true" geomagnetic observations $\mathbf{y}^o$ remains to be seen. Instead, researchers have so far cautiously dealt with synthetic data (for algorithmic verification), and with published core geomagnetic field models. These models provide parameterized time-dependent maps of B_r at the core surface (through a set of time-dependent Gauss coefficients), and over different time scales, ranging from a decade to several centuries (e.g. Lesur et al. 2008; Olsen et al. 2006; Sabaka et al. 2004; Jackson et al. 2000). Models covering up to several millennia have also been built thanks to the availability of archeomagnetic data (see e.g. Hongre et al. 1998; Korte and Constable 2005; Korte et al. 2009). The accuracy of those models degrades going back in time, as a result of the temporal and spatial sparsity, and greater uncertainty, of the data they rely on. In addition, prior to 1850, historical models are mostly based on directional measurements (Jackson et al. 2000), which makes it possible to recover the field morphology (Hulot et al. 1997), but precludes the determination of the global strength of the field. Still, there is an encouraging ongoing effort to improve on that situation thanks to the construction of archeomagnetic intensity databases (e.g. Genevey et al. 2008). In particular, careful intensity measurements covering the period 1590–1850 could prove useful in complementing the data already extracted from logbooks (Gubbins et al. 2006; Finlay 2008; Genevey et al. 2009).

In Table 2, we have tried to synthesize the information content already available for geomagnetic data assimilation. We computed the average size $L_{\mathbf{y}^o}$ of the data vector that could be fed in an assimilation scheme over different time periods, assuming a model of core dynamics operating with a time-step of 1 week, and relying on the number of data used to construct the field models referenced in the rightmost column. As graphically shown in Fig. 7, the last decade of satellite measurements allows for a dramatic tenfold increase in the size of $\mathbf{y}^o$. In a variational framework aiming at adjusting the initial condition (see Sect. 2.2.2), the size of the control vector (the initial state $\mathbf{x}_0$) for a typical, three-dimensional dynamo

[10] www.esa.int/esaLP/ESA3QZJE43D_LPswarm_0.html.

Table 2 An attempt to summarize the observational content available to geomagnetic data assimilation practitioners. We took the number of data (and corresponding timespan) used in the studies listed in the rightmost column to estimate the average quantity $L_{\mathbf{y}^o}$ of observations that could be fed in an assimilation scheme at every single time-step, assuming a numerical model of core dynamics operating with a time-step $\Delta t = 1$ week

Period	Average $L_{\mathbf{y}^o}$	Type of data	Reference
2000–now	10,000	observatory & satellite	Lesur et al. (2008)
1960–2002	1,000	observatory & satellite	Sabaka et al. (2004)
1900–1960	50	observatory & satellite & survey	Jackson et al. (2000)
1600–1900	10	navigation & observatory	Jackson et al. (2000)
0–1600	0.1	archeomagnetic	Korte and Constable (2005)

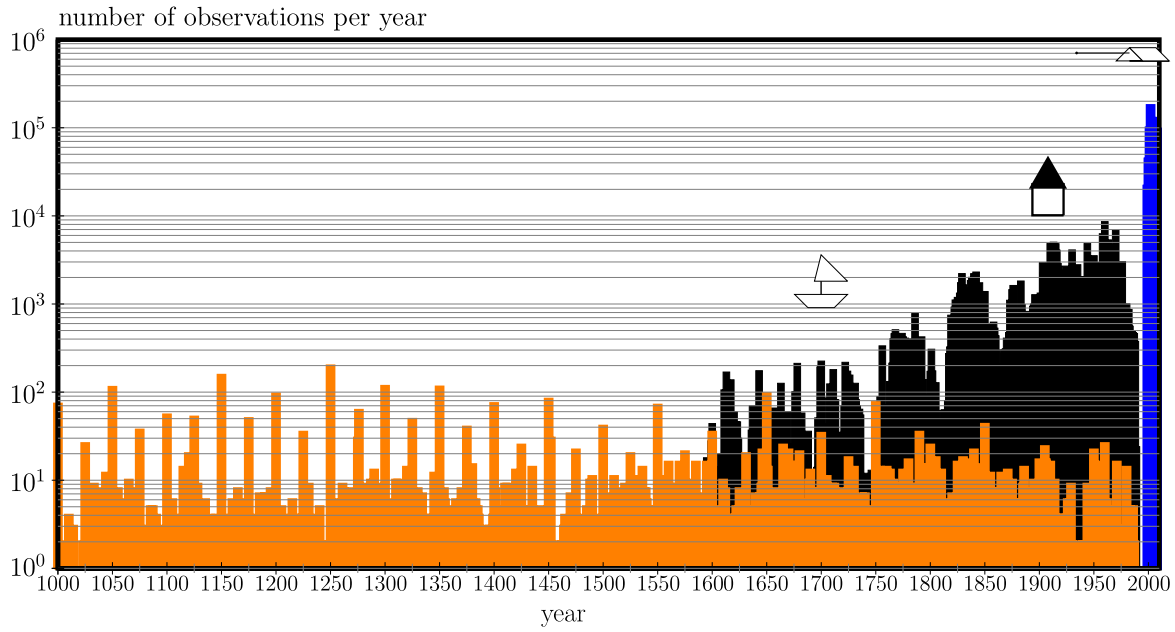

Fig. 7 Amount of geomagnetic measurements available over the last millennium, from archeomagnetic sources (*orange bars*), historical sources (*black bars*), and from the recent satellite era (*blue bars*). The data have been binned in bins of 1 year, and the scale on the y axis is logarithmic. The archeomagnetic curve has been constructed using the Geomagia database, available online at geomagia.ucsd.edu (Korhonen et al. 2008; Donadini et al. 2009). The historical curve is that of the gufm model of Jackson et al. (2000), and the recent satellite curve is based on the xCHAOS model of Olsen and Mandea (2008)

model is of order 1 million:[11] Table 2 encouragingly indicates that two years of satellite data suffice to get a number of observations similar to the size of the control vector. A note of caution is in order, though: At any given time t_i, the number of observations will certainly not exceed the size of the state vector. It is the accumulation of observations over time which is such that their total number will eventually exceed the size of the state vector (and make the minimization problem of variational assimilation "appear" well determined). As seen above, the effective part of the control vector directly sampled by observation involves at

[11] Follow the pseudo-spectral approach of Glatzmaier (1984) and perform the poloidal-toroidal decomposition of flow and magnetic field. The state vector $\mathbf{x}$ then comprises the four corresponding scalar fields, augmented with temperature (or co-density). Operating with 80 Chebyshev polynomials in radius and a spherical harmonic expansion truncated at degree and order 50 to discretize the components of $\mathbf{x}$ yields $L_{\mathbf{x}} \approx 10^6$.

most the first 15 spherical harmonic degrees of the poloidal field at the core-mantle boundary. From the spectral point of view (assuming a horizontal truncation at spherical harmonic degree 50, and 80 points in radius), that amounts to a modest 0.2 per mil of the state vector. However, that static estimate effectively increases by virtue of the dynamics (although that effect is hard to quantify), in the first place through the diffusive and convective transport of information which results from running the forward (or adjoint) model. The correction applied at the top of the dynamo region is communicated to the bulk of the core (through the action of either the Kalman gain or the adjoint model in a 4D-Var framework). This propagation can be made even more effective if multivariate statistics (relating observed and non-observed components of the state vector) are used to construct the background error covariance matrix $\mathbf{P}^b$ (which appears in both the sequential and variational formulations of data assimilation).

Not surprisingly, it is over the historical period, and in particular the twentieth and early twenty-first centuries, that the first data assimilation studies have been attempted. The high quality and quantity of magnetic measurements available over that period imply in turn some confidence in the field models, which can be used as reasonable proxy "observations". From the underlying core dynamics point of view, a century is also long enough to try and understand the fast variability of the geomagnetic secular variation. Dealing with time series of the Gauss coefficients also has a practical advantage: If the model of core dynamics M is discretized by means of spherical harmonics in the horizontal direction, then H very conveniently reduces to a diagonal operator (see e.g. Kuang et al. 2009).

We conclude this section by adding that an extra (geodetic) observation can be included in a geomagnetic data assimilation scheme. The time series of the fluctuation in the length-of-day (ΔLOD) has an annual to decadal component which is usually attributed to fluctuations in the core angular momentum (Jault et al. 1988; Jackson et al. 1993; Pais and Hulot 2000; Gillet et al. 2009). The construction of the component of H which is associated with the ΔLOD signal is straightforward (it is linear).

4 Current Approaches to Geomagnetic Data Assimilation

Different approaches to geomagnetic data assimilation have recently come to the fore in geomagnetism. Early studies have focussed on the feasibility of implementing data assimilation algorithms to the problem of the geomagnetic secular variation, by analyzing the response and behaviour of the assimilating system in a well-controlled environment, using databases of synthetic observations, starting from one-dimensional toy models (Fournier et al. 2007; Sun et al. 2007), and moving on to systems of higher complexity (Liu et al. 2007; Kuang et al. 2008; Canet et al. 2009). Those studies are generically referred to in the literature as "observing system simulations experiments" (OSSEs), or, equivalently, "twin experiments". More recent applications have considered "level-2" observations (see Sect. 3 above), thereby permitting to make some inference on the state of the core $\mathbf{x}$ (Kuang et al. 2009). The approaches followed nowadays differ by the choice of the physical and numerical model M employed to describe core dynamics, and the form of assimilation they resort to (sequential or variational). In this section, we shall give an example of a sequential approach based on a three-dimensional geodynamo model, followed by an example of a variational scheme designed for a two-dimensional quasi-geostrophic model of the secular variation; we will conclude with a discussion of the intrinsic limit of the predictability of the secular variation, as inferred from the results of a suite of three-dimensional dynamo models.

Table 3 Summary of the various core dynamics-related symbols appearing in the text, and the non-dimensional numbers coming into play. Expressions that follow for the Ekman, Roberts, Rossby, and Rayleigh numbers, are obtained using the outer core radius c as the length scale, the magnetic diffusion time $= c^2/\lambda$ as the time scale, $(2\rho\lambda\mu\Omega)^{1/2}$ as the magnetic field scale, and $h_T c$ as the temperature scale

Symbol	Meaning
ρ	core density
σ_e	electrical conductivity
μ	magnetic permeability
λ	magnetic diffusivity $= 1/\mu\sigma_e$
ν	kinematic viscosity
κ	thermal diffusivity
α_T	thermal expansion coefficient
Ω	the angular velocity of the Earth
c	outer core radius
b	inner core radius
d	outer core depth $= c - b$
$\boldsymbol{B}$	the magnetic induction (field)
$\boldsymbol{u}$	the core flow
Θ_0	background temperature profile
Θ	temperature anomaly
h_T	prescribed background temperature gradient $= -\partial_r \Theta_0$ $(r = b)$
g_0	the gravity field at $r = b$
$\boldsymbol{u}_h$	core surface flow
Ψ	geostrophic streamfunction
B_0	magnetic field scale
U	velocity scale
τ	time scale
T_{adv}	advective time scale $\doteq c/U$
V_A	Alfvén wave speed $\doteq B_0/\sqrt{\rho\mu}$
T_A	Alfvén wave period $= c/V_A$
E	Ekman number $\doteq \nu/2\Omega c^2$
q_κ	Roberts number $\doteq \kappa/\lambda$
Ro	Rossby number $\doteq \lambda/2\Omega c^2$
R_{th}	Rayleigh number $\doteq \alpha_T g_0 h_T c^2/2\Omega\lambda$
Rm	magnetic Reynolds number $\doteq Uc/\lambda$
Pm	magnetic Prandtl number $\doteq \nu/\lambda$
Pr	Prandtl number $\doteq \nu/\kappa$
Le	Lehnert number $\doteq B_0/c\Omega\sqrt{\rho\mu}$

A summary of the relevant quantities and notations we shall need is provided in Table 3. The Earth's outer core is considered as a conducting fluid of density ρ, electrical conductivity σ_e, magnetic permeability μ, magnetic diffusivity $\lambda = 1/\mu\sigma_e$, thermal diffusivity κ, and kinematic viscosity ν. Owing to thermal-compositional convection (treated under the Boussinesq approximation) in an ambient gravitational field $\boldsymbol{g}$, the fluid flows at velocity $\boldsymbol{u}$ and sustains a magnetic field (induction) $\boldsymbol{B}$. It is contained in a (to first order) spherical shell of inner radius b and outer radius c, corresponding to the inner-core boundary and core-mantle boundary, respectively. The core rotates about the z-axis (unit vector $\boldsymbol{e}_z$) with an angular velocity Ω. After proper non-dimensionalization, the numerical description of its dynamics is provided by a numerical model M which expects, aside from an initial con-

dition, a set of non-dimensional input parameters, the exact nature of which depends on the scales chosen for length, time, flow, and magnetic field (see Table 3).

4.1 Sequential Assimilation Using Three-dimensional Models of the Geodynamo

Non-linear self consistent numerical dynamo models which are capable of generating an Earth like geomagnetic field have been in existence for a little more than a decade (Glatzmaier and Roberts 1995; Kageyama and Sato 1997; Kuang and Bloxham 1997). While computational limitations do not allow these models to operate in parameter regimes near those of the Earth's core, they are able to produce important physical processes such as dipole dominant poloidal magnetic field, westward drift and occasional field reversals (Christensen and Wicht 2007). However, if we look into the more detailed structures of the geomagnetic field from the dynamo solutions and from the observations, we will find they are very different, as shown in Fig. 8. Obviously, the model outputs are still very far away from those observed at the Earth's surface.

In many ways, these dynamo models are far more successful than the early numerical weather prediction models discussed in Sect. 1.2. But, again, a much bigger difference is

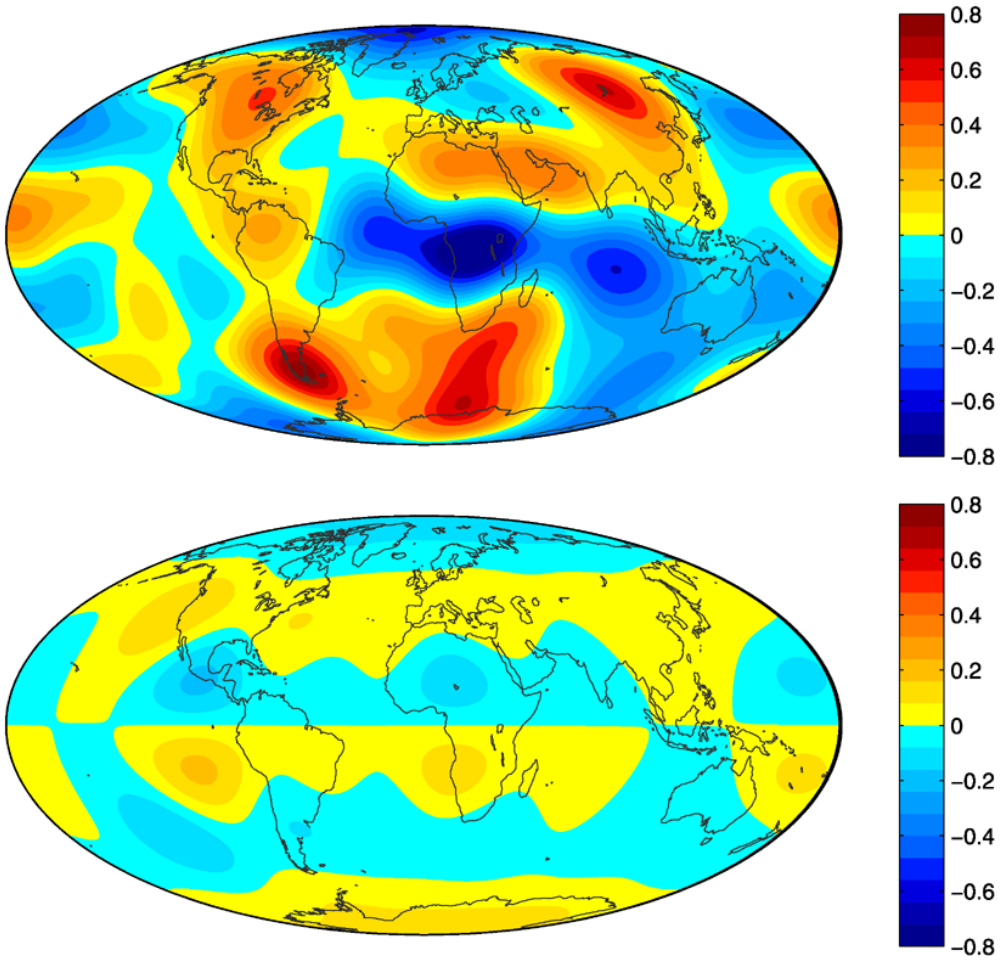

Fig. 8 The non axial dipolar part of the radial component B_r of the magnetic field at the CMB from observation in 2000 according to the CM4 model of Sabaka et al. (2004) (*top*) and from the numerical dynamo simulation (*bottom*). The poloidal scalar (of the magnetic field) is expanded in spherical harmonics, with complex coefficients b_l^m of degree l and order m. Plotted in this figure are the scaled poloidal fields based on the spectral coefficients $\tilde{b}_l^m \equiv b_l^m / b_1^0$, for all $m \le l \le 8$, and without $(l, m) = (1, 0)$. From Kuang et al. (2009)

that in geomagnetic data assimilation, the observations are only made at the surface of the Earth, and even then, only of the poloidal magnetic field. The observation vector $\mathbf{y}^o$ therefore has a far smaller dimension than the state vector $\mathbf{x}$. If we carry out the assimilation in spectral space, and the maximum wave number that can be reliably assimilated is around $l = 13$, the observation operator H essentially acts to project the state space onto the smaller set of observations. State space (or model space) is defined as the magnetic field ($\boldsymbol{B}$), velocity field ($\boldsymbol{u}$) and the temperature perturbation (Θ) within the liquid outer core, with the velocity and magnetic fields further decomposed into poloidal and toroidal components. The only observations of the state are of the poloidal component of the magnetic field at the Earth's surface. The observations can then be downward continued to the dynamo domain boundary (DDB), e.g. the core-mantle boundary (CMB) or the top of the electrically conducting D″-layer (above the CMB). Therefore the observation operator is simply a matrix which projects the complete state space to the poloidal component of the magnetic field at the DDB.

The model M from (2) is in this case the discretization of the momentum, induction and energy equations, which in non-dimensional form are (see Table 3):

$$\mathrm{Ro}\left(\partial_t \boldsymbol{u} + \boldsymbol{u}\cdot\nabla\boldsymbol{u}\right) = -\boldsymbol{e}_z \times \boldsymbol{u} - \nabla p + \boldsymbol{j}\times\boldsymbol{B} + \mathrm{R_{th}}\Theta\boldsymbol{r} + \mathrm{E}\nabla^2\boldsymbol{u}, \tag{21}$$

$$\partial_t \boldsymbol{B} = \nabla\times(\boldsymbol{u}\times\boldsymbol{B}) + \nabla^2\boldsymbol{B}\,, \tag{22}$$

$$\partial_t \Theta = -(\boldsymbol{u}\cdot\nabla)\,\Theta_0 - (\boldsymbol{u}\cdot\nabla)\,\Theta + \mathrm{q}_\kappa\nabla^2\Theta\,. \tag{23}$$

These equations have been solved by both finite difference (Kageyama and Sato 1997), combined spherical harmonics and Chebyshev polynomials (Glatzmaier and Roberts 1995) and combined spherical harmonics and finite differences (Kuang and Bloxham 1997).

A sequential data assimilation system has been built using the Kuang and Bloxham model (Kuang et al. 2008). This system features two possible means to estimate the forecast error covariance, $\mathbf{P}^f$, which are ensemble methods (Sun et al. 2007) and modeling. Ensemble estimation of forecast error covariance has enabled the construction of multivariate error covariances which allow the assimilation of the poloidal magnetic field to directly impact other state variables. Modeled covariances are constructed by choosing functions that result in error covariances that have the required properties of diagonal dominance and positive semi-definiteness (e.g. Gaspari and Cohn 1999). With respect to ensemble methods, they avoid carrying along an ensemble of model runs that generally makes the system too expensive; therefore, they have the advantage of computational efficiency, and can be tuned by adjusting one or more parameters, such as the error correlation length scale. For example, Kuang et al. (2009) use a simple $\mathbf{P}^f$

$$P^f_{ij} = \rho_i \sigma^2 \delta_{ij}, \tag{24}$$

in which

$$\rho_i = \frac{(r_i - r_c)^2}{(r_{do} - r_c)^2}\left[3\,(r_{do} - r_c) - 2\,(r_i - r_c)\right]\left(1 - \frac{r_i - r_{do}}{r_{do}}\right) \quad \text{for } r_i \geq r_c, \tag{25}$$

where r_i denotes the i-th radial grid point, r_{do} is the mean radius of the top of the D″-layer, r_c is the correlation distance from the CMB, and σ is a constant forecast error standard deviation. One could optimize the analysis by changing the correlation length r_c. For the detailed mathematics, we refer the reader to Kuang et al. (2009).

This modelling approach has been incorporated in a series of observing system simulation experiments (OSSEs), in which a model run is used as the true state of the system, $\mathbf{x}^t$ (generally referred to as a nature run) (Liu et al. 2007). From this nature run, observations are generated using the observation operator with added observation error using (4). The assimilation system then uses these synthetic observations with another model run, generally with somewhat different parameter values. OSSEs are used to determine the impact of the assimilation on the unobserved state of a system, which for the geodynamo is nearly the entire state. These experiments therefore have the potential to show whether geomagnetic data assimilation has any potential to really improve our estimates of the dynamics of the Earth's core.

An example of this potential is seen in Fig. 9, which shows the radial component u_r of velocity $\boldsymbol{u}$ at a distance of 35 km below the CMB for three different cases. A nature run with parameter values $\mathrm{R_{th}} = 15000$, $\mathrm{Ro} = 1.25 \times 10^{-6}$ and $\mathrm{E} = 1.25 \times 10^{-6}$ is shown in panel (a). Panel (b) shows u_r from a free model run with the same parameter values except $\mathrm{R_{th}} = 14500$ while panel (c) shows u_r after running the assimilation for a time of 0.892 τ_d, where τ_d is the Earth's magnetic free decay time. Observations of the poloidal magnetic field at the CMB from the nature run with degree $l \leq 8$, are assimilated into the model every 0.01 τ_d. The results show that the assimilation results in a measurable improvement in the radial velocity at this location. In other words, corrections to the poloidal magnetic field will in turn influence the other state variables through the model simulation. Thus, this univariate assimilation of geomagnetic data could be seen to improve the estimation of fluid motion in the Earth's outer core.

Kuang et al. (2009) have applied this system with the surface geomagnetic measurements over the past 100 years. In this application, analysis is made every 5 years. The rms error ϵ is defined as

$$\epsilon = \left\{ \frac{1}{A} \int \left[\left(\tilde{b}_r^f \right) - \left(\tilde{b}_r^o \right) \right]^2 \mathrm{d}A \right\}^{1/2}, \tag{26}$$

where the superscripts f and o have their usual meaning, and $\tilde{b}_r$ is related to the spherical harmonic coefficients b_l^m of the poloidal field at the top of the D″-layer (whose surface is denoted by A) by

$$\tilde{b}_r = \sum_{0 \leq m \leq l}^{8} \frac{l(l+1)}{r^2} \left(\frac{b_l^m}{b_1^0} \right). \tag{27}$$

As shown in Fig. 10, the errors between the assimilated results and surface geomagnetic observations decrease over time, i.e. the model outputs are drawn closer to the observations. The reduction of the errors could be attributed to the changes of the state variables inside the core (Kuang et al. 2009). But since this assimilation is using real observations, there is no known 'true' state with which to compare the changes to the unobserved state variables. However, we can plot the differences in the core state between model runs with and without assimilation. For example, Fig. 11 shows the relative change in the toroidal magnetic field over the one hundred year assimilation run, which reaches as much as 40%. The improved poloidal magnetic field forecast is an indication that these changes have resulted in an improved estimate of the toroidal magnetic field.

In fact, it is worth noting that such geomagnetic data assimilation schemes are already tentatively used in geomagnetic field modeling for short-term forecasting purposes. Indeed, Kuang et al. (2010) utilizes 7,000 years of the field models derived from pale-

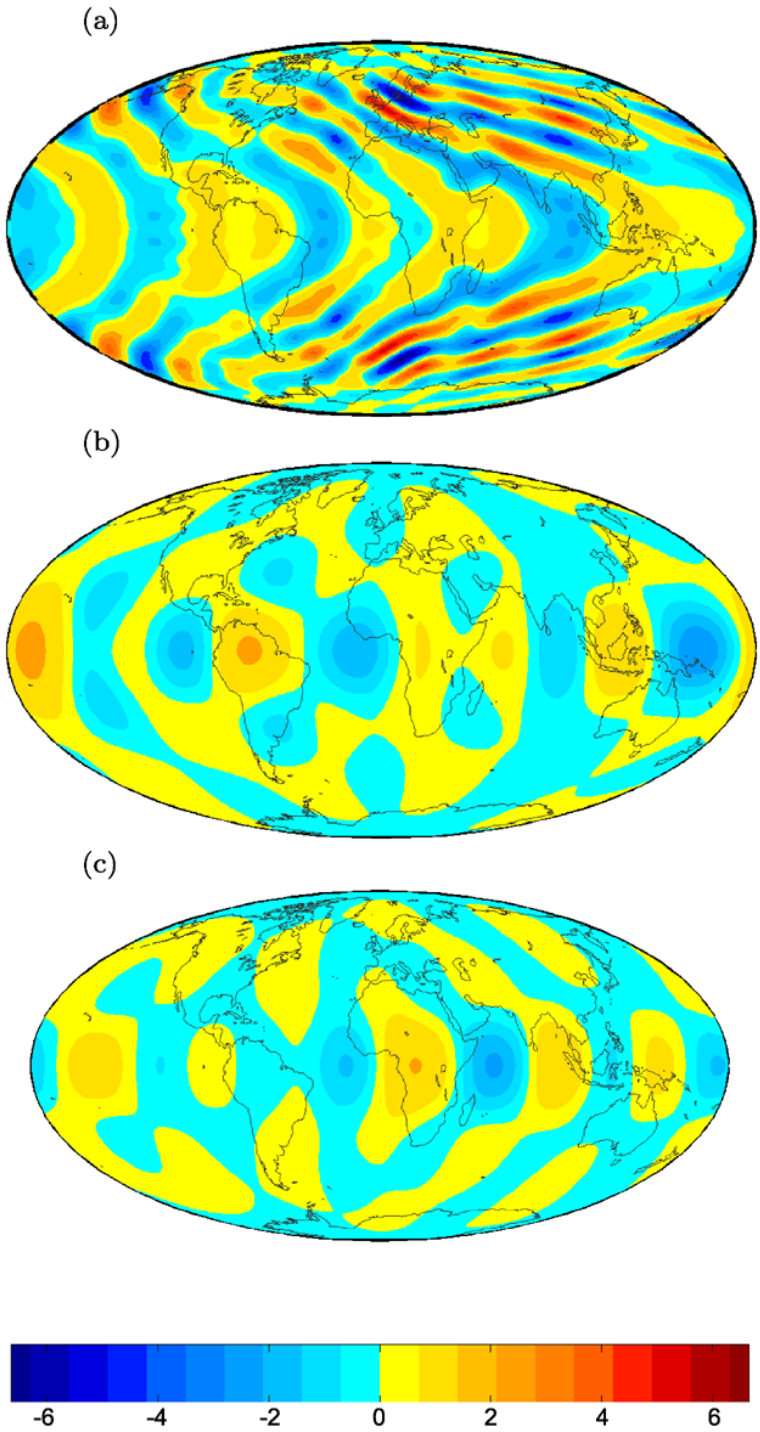

Fig. 9 Radial velocity, u_r, on a spherical shell 35 km below the CMB from a nature run (**a**), a free model run (**b**) and the forecast after assimilating observations from the nature run with $l \leq 8$ (**c**). Assimilation was done every 20 years for 17840 years. The velocities in each panel are non-dimensional (common color scale at the *bottom*). A non-dimensional velocity of unity implies 1.75×10^{-2} km/y

omagnetic, archeomagnetic, historical magnetic, observatory and satellite magnetic data in their geomagnetic data assimilation system (MoSST_DAS). In addition, a prediction-correction algorithm is used to reduce the dynamo system model errors in assimilation output. Their forecasts are benchmarked with earlier forecasts, in particular those of IGRF-8 and IGRF-9. The results demonstrate that, their 5-year field forecasts are comparable to IGRF, and their 5-year SV forecasts are more accurate (with smaller misfit). Using the same system, and the field model output up to 2010, they produced a 5-year SV forecast for the period from 2010–2015. Their forecast is now a component of IGRF-11.

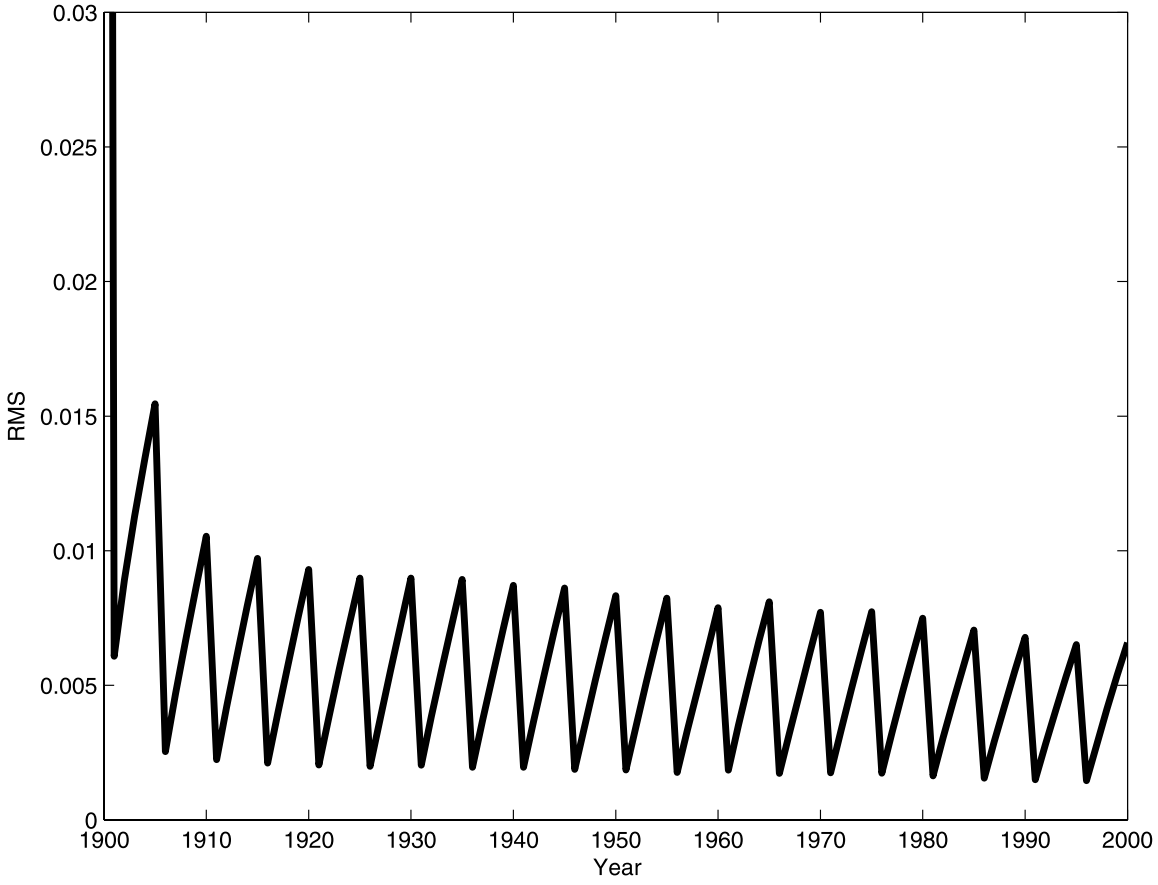

Fig. 10 The difference between the poloidal field at the DDB inverted from surface geomagnetic observations and that from assimilation during the past 100 years. The analysis time, i.e. the time interval between two adjacent analyses, is 5 years

4.2 Variational Assimilation Based on Models Tailored to Account for Observations of the Secular Variation

Following an alternative route, Canet et al. (2009) decided to develop a minimal model of core dynamics M able to account for the observed secular variation. They resort to a quasi-geostrophic approach which aims at describing core processes on short time scales (years to decades). Viscous forces can be readily neglected outside boundary layers and detached shear layers, provided those localized regions do not exert a control on the main body of the fluid. Canet et al. (2009) therefore followed the common practice of defining the core surface flow $\boldsymbol{u}_h$, which appears in (1), as the flow beneath the viscous Ekman layer attached to the core-mantle boundary.

Three-dimensional simulations of the geodynamo (as governed by (21)–(23)), if performed at very low Ekman number ($\mathrm{E} \approx 5 \times 10^{-7}$), require formidable computational power; even if data that can be assimilated are available for no more than a small fraction of a magnetic diffusion time, these simulations are currently out of reach for data assimilation practice in that region of parameter space.[12] Interestingly, though, these recent high-resolution simulations have yielded Earth-like ratios of the magnetic to kinetic energy

[12] An assimilation scheme requires good model error statistics. Even if one resorts to a frozen background error covariance matrix (the optimal interpolation approach to sequential data assimilation), the estimation of that matrix demands to run the model over a significant amount of time (several magnetic diffusion times), which becomes prohibitive in the parameter range recently explored by e.g. Sakuraba and Roberts (2009).

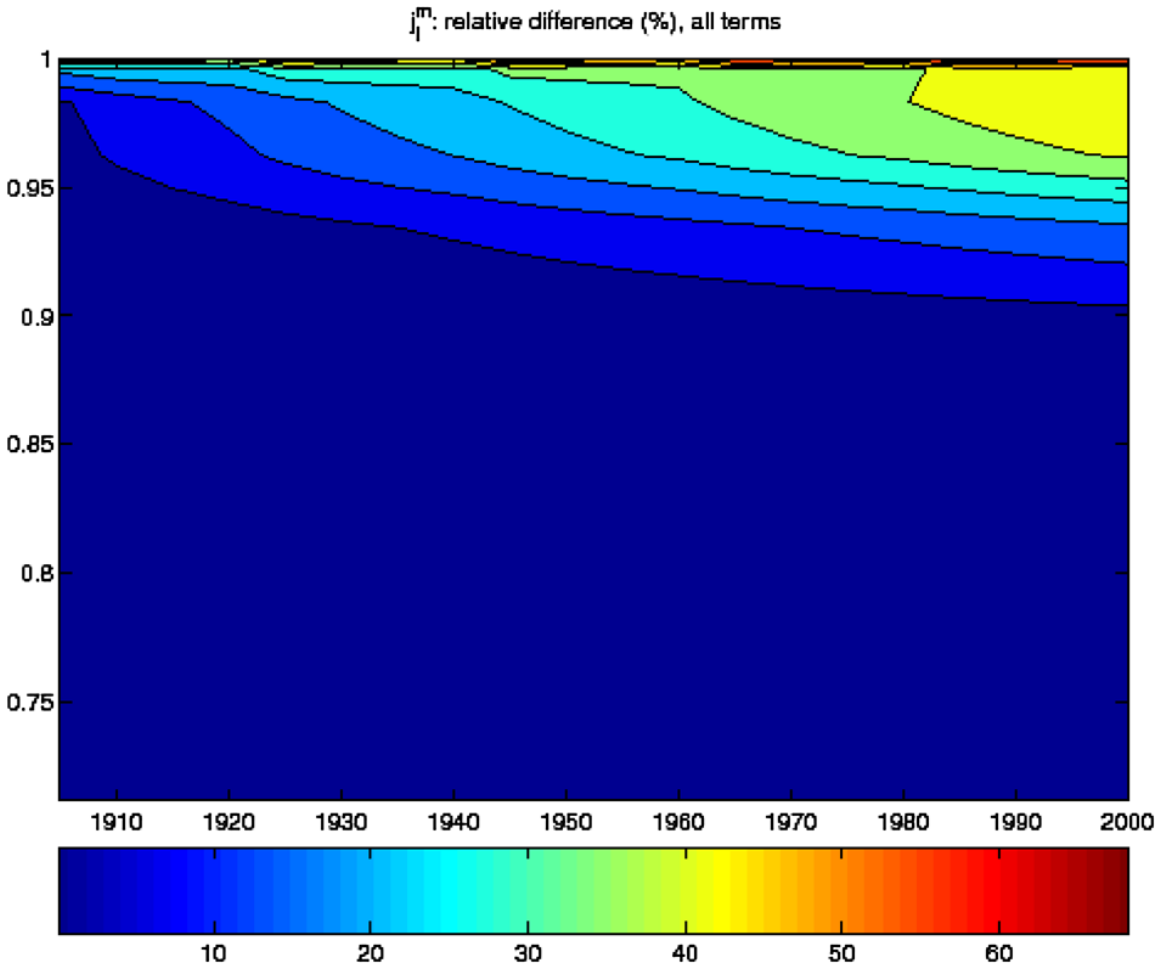

Fig. 11 The relative difference in toroidal magnetic field between the forecast from the assimilation run and the free running model, as a function of time (x-axis) and radial position (y-axis). The analysis is calculated every 20 years (1900, 1920, 1940, 1960 and 1980). The color scale is in percent

for the largest length scales (Takahashi et al. 2008; Sakuraba and Roberts 2009). For a small enough magnetic Prandtl number Pm (typically 0.2), they exhibit smaller scale convection vortices as the Ekman number is decreased towards Earth-like values, while not much variation in the dominant scale of the magnetic field is observed. These simulations thus give hints of dynamo generation taking place at length scales that are kept out of view of the myopic observer at the Earth's surface. That behaviour prompted Canet et al. (2009) to investigate a model which involves only the velocity and magnetic fields, leaving aside the buoyancy forces which power the geodynamo and are responsible for changes in the magnetic field occuring on long (millennial, say) time scales.

On the shorter secular variation time scales, rotation forces are much larger than magnetic forces in the bulk of the fluid. On the basis of theoretical arguments and numerical calculations, Jault (2008) argued that rapidly rotating motions of length scale $\mathcal{L}$ are axially

In addition, ensemble covariances in sequential algorithms increase the assimilation runs at least by one order of magnitude (the size of the ensemble), thus effectively increasing simulation time well beyond a free magnetic decay time. Similar conclusions apply to variational assimilation algorithms: The background error covariance matrix entering the definition of the cost function (16) is the same as the one used in an optimal interpolation framework (its proper determination is therefore as costly). In addition, the minimization of the objective function requires several tens of iterations, since it is not conceivable to come up with a direct estimate of the Hessian.

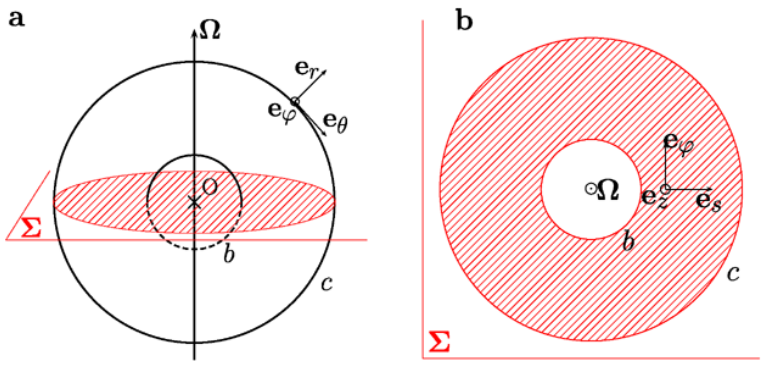

Fig. 12 Geometry of the system and notations used to describe the quasi-geostrophic model of core dynamics. (**a**) Side view. (**b**) Equatorial section. Σ is the equatorial plane, while the CMB corresponds to the outer sphere, located at $r = c$; b is the radius of the inner core. Modified after Canet et al. (2009)

invariant if the relevant non-dimensional Lehnert number, Le, is small enough. That number measures the ratio between the period of inertial waves, $1/\Omega$, and the period of Alfvén waves, $T_A = \mathcal{L}/V_A$ (Lehnert 1954):

$$\mathrm{Le} = \frac{B_0}{\Omega(\mu\rho)^{1/2}\mathcal{L}}. \tag{28}$$

The Alfvén wave speed V_A is classically defined as $V_A = B_0/\sqrt{\rho\mu}$; note that Le is a decreasing function of the length scale $\mathcal{L}$. In the series of calculations carried out by Jault (2008), the flow appears to be invariant in the direction parallel to the rotation axis, provided $\mathrm{Le} \ll 1$. For the Earth's core, a magnetic field strength B_0 on the order of 2 mT (Christensen et al. 2009) and a scale $\mathcal{L}$ of 1,000 km yield $\mathrm{Le} \approx 10^{-4}$, well below unity. Therefore, Canet et al. (2009) assume that the high frequency Earth's core flows, responsible for the observed geomagnetic secular variation, are geostrophic at leading order. Instead of Le, which is based on the magnetic field intensity B_0 and a characteristic length scale $\mathcal{L}$, the appropriate small parameter to characterize the approximation is related to the slopes of the spherical boundaries (e.g. Gillet et al. 2007, and references therein). Indeed, motions with a non zero component in the cylindrical radial direction cannot be fully geostrophic in a spherical shell. Working in the equatorial plane Σ (crosshatched in Fig. 12), a cylindrical set of coordinates (s, φ, z), with $\boldsymbol{e}_z$ parallel to the axis of rotation, is well-suited to study the resulting columnar patterns. The s and φ components of the velocity are independent of z. Outside the cylindrical surface parallel to the rotation axis and tangent to the inner core (the so-called tangent cylinder), the z component of the velocity u_z varies linearly with z, in order for the total flow $\boldsymbol{u}$ to satisfy the no-penetration condition at the outer boundary. Inside the tangent cylinder, one can write $u_z = a(s) + b(s)z$, and choose properly the two functions a and b which guarantee that the total flow satisfies the no-penetration condition at both the ICB and the CMB. Outside the tangent cylinder, the quasi-geostrophic flow is uniquely defined by its streamfunction ψ in the equatorial plane.

The quasi-geostrophic assumption is somehow supported by inversions of tangentially geostrophic core surface flows $\boldsymbol{u}_h$, which do not assume equatorial symmetry. Figure 13 shows the spectrum of the kinetic energy at the core surface as a function of spherical harmonic degree l, after separating $\boldsymbol{u}_h$ into its equatorially symmetric (ES) and equatorially antisymmetric (EA) components (the red and black curves, respectively). The ES component appears to be stronger than the EA component at the largest scales, at least up to $l = 7$.

Using the two-dimensional framework outlined above, the calculation of core surface flows is then incorporated inside a prognostic dynamical model which describes the time evolution of the corresponding streamfunction ψ. Retaining the Lorentz forces for the reasons outlined above implies averaging the magnetic contribution to the vorticity equation along the direction of rotation of the Earth, following a procedure akin to that of Hide

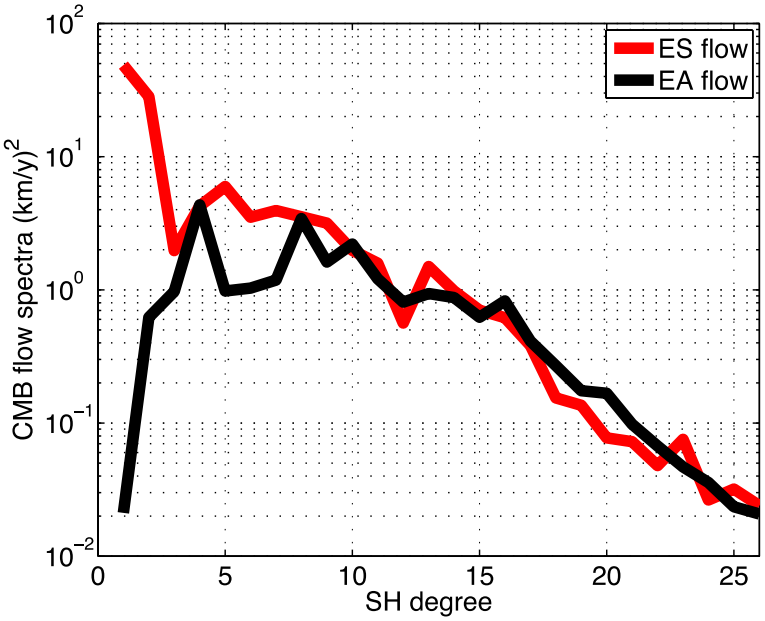

Fig. 13 Spectrum of the energy of the core surface flow inferred from the model xCHAOS of Olsen and Mandea (2008) divided into its equatorially symmetric (ES, *red curve*) and antisymmetric (EA, *black curve*) components. The calculated core flow $\boldsymbol{u}_h$ has been obtained over the time interval [2000–2007] after ensemble averaging 10 different solutions obtained using 10 different realizations of the invisible small-scale magnetic field (spherical harmonic degree $l \geq 13$). Consult Gillet et al. (2009) for further details on the method

(1966), who worked in the β-plane. This yields a term involving only quadratic products of the equatorial components of the magnetic field B_s and B_φ, namely B_s^2, $B_s B_\varphi$ and B_φ^2 (Canet et al. 2009). We shall use the generic notation $\mathcal{B}^2$ to refer to these quantities. The induction equation in the core interior can also be transformed into an equation for the evolution of $\mathcal{B}^2$. Coupling the axial vorticity equation and this modified induction equation, we obtain an extension to non axi-symmetrical core flows of the torsional oscillation model of Braginsky (1970), which involved only

$$\left\{B_s^2\right\}(s) = \frac{1}{2h(s)} \frac{1}{2\pi} \int_0^{2\pi} \int_{-h(s)}^{h(s)} B_s^2(s, \varphi, z) \mathrm{d}z \mathrm{d}\varphi, \tag{29}$$

in which $h(s)$ is the half-height of the geostrophic cylinder of radius s. At the core surface, the flow interacts with the magnetic field, through the radial component of the magnetic induction equation. That part of the model connects the dynamics and the observed secular variation, with the radial component of the magnetic field acting as a passive tracer. In summary, the state of the Earth's core in that approach consists of B_r at the core surface, together with the equatorial streamfunction $\psi(s, \varphi)$ and quadratic quantities $\mathcal{B}^2(s, \varphi)$.

Omission of buoyancy in this model can be challenged. Indeed, Amit et al. (2008) and Aubert et al. (2008) have recently suggested an alternative or complementary model as they have investigated steady core surface flow driven by thermal coupling with the heterogeneous lower mantle. As the mantle and the solid inner core evolve on very long time scales, thermal coupling with heterogeneous solid boundaries can be the source of significant steady flows (Aubert et al. 2007), but not of the rapidly changing flows, of the kind inferred from the recent secular variation observed from satellites (Olsen and Mandea 2008).

From the methodological standpoint, Canet et al. (2009) resort to variational data assimilation to construct formally the relationship between model predictions and observations, following the 4D-Var approach described in Sect. 2.2.2. They have investigated the effect of several factors on the solution (width of the assimilation time window T, amount and quality of data), and they have discussed the potential of the model to deal with real geomagnetic observations. They have illustrated that framework with twin experiments, performed first in the case of the kinematic core flow inverse problem, and then in the case of Alfvén torsional oscillations. In both cases, using the adjoint model enables the estimation of core

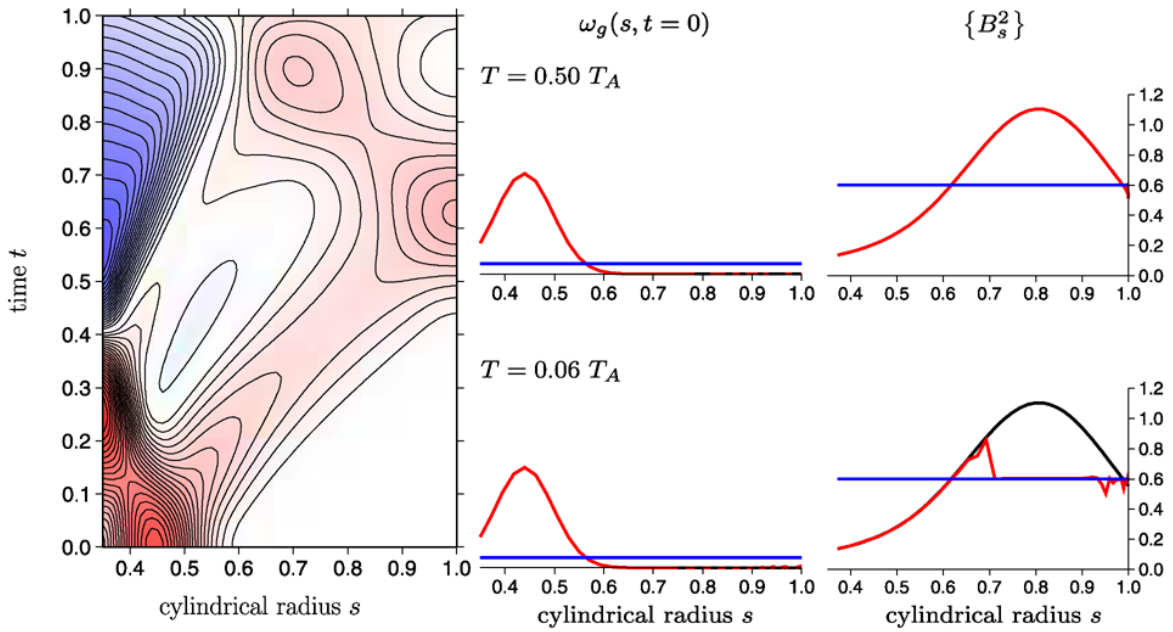

Fig. 14 Torsional oscillations twin experiments in a 4D-Var framework. The control vector for these experiments consists of the initial angular velocity profile in the core, $\omega_g(s, t = 0)$, along with the profile of the static magnetic quantity $\{B_s^2\}(s)$. *Left*: cylindrical radius-time plot of ω_g showing the propagation of a synthetic, reference torsional wave in the region outside the tangent cylinder (cylindrical radius $b < s < c$). *Red* is positive, *blue* is negative (absolute scale is arbitrary). Length and time are scaled by c and T_A, respectively. With our choice of scales, an Alfvén time amounts to 6 y. *Center* and *right panels*: Assimilation results, for two widths of the time interval over which assimilation has been carried out: 0.5 T_A (*top row*) and 0.06 T_A (*bottom row*). *Center panel*: the initial angular velocity profile $\omega_g(s, t = 0)$. In *black*: the true profile. In *blue*: the initial guess. In *red*: the result obtained after assimilation. *Right panel*: same for $\{B_s^2\}(s)$, which is plotted in units of B_0, i.e. 2 mT. Note that in most instances, the *red* and *black curves* are superimposed

state variables which, while taking part in the dynamics, are not directly sampled at the core surface. A pedagogical example of such a behaviour is provided in Fig. 14: The reference (true) case consists of an initial perturbation of the angular velocity (with respect to a solid-body rotation), $\omega_g^t(s, t = 0)$, which propagates in the outer core with a local wavespeed proportional to the rms value of B_s over a geostrophic cylinder (defined in (29)). That progressive torsional wave interacts with B_r at the core surface to generate a synthetic database of secular variation, $\partial_t B_r^t$, over a time interval of width T, assuming an error-free measurement ($\boldsymbol{\epsilon}^o = \mathbf{0}$). Assuming next a wrong initial condition for ω_g and an incorrect profile for $\{B_s^2\}$, the adjoint model can be used in conjunction with the database to correct the guesses for $\omega_g(s, t = 0)$ and $\{B_s^2\}(s)$. In Fig. 14, the results obtained after assimilating the perfect synthetic observations are shown for two values of T, corresponding to a short and a long window (spanning 6% and 50% of an Alfvén time, respectively). In both cases, the retrieval of $\omega_g(s, t = 0)^t$ is perfect in that noise-free context (because the secular variation is directly sensitive to the initial condition), whereas the retrieval of $\{B_s^2\}^t$ is only achieved over the portion of the domain which has been effectively sampled by the wave during its propagation. The short interval case is indeed characterized by a shadow zone which covers the outer third (in radius) of the outer core (see the bottom right panel in Fig. 14); that zone has been illuminated by the passing of the wave in the longer time interval case.

The history of the determination of the magnetic field within the core from the study of torsional oscillations gives us a note of caution about the use of simplified models. It shows that, unfortunately, the choice of the model can dictate the answer. Braginsky (1970, 1984) argued that both LOD variations and magnetic field records show oscillations with periods

about 60 years. If we identify that period with the period of the fundamental eigenmode for torsional oscillations, we obtain an estimate for the rms s-component of the magnetic field within the core $B_s \approx 0.2$ mT. However, the same model can be used to account for variations with periods of about 6 years (Gillet et al. 2010a). Then, we obtain $B_s \approx 2$ mT. In that latter case, we can associate the longer period variations with non-zonal fluctuations which drive the zonal circulation. Both models can nevertheless provide an adequate fit to the data, because the uncertainties on the flow coefficients are very large (Buffett et al. 2009).

From the discussion of this example, we can emphasize two points. First, a good grasp of the different error sources is crucial. As outlined in the introduction, the difficulties arising because of the invisible small scale magnetic field at the core-mantle boundary are now well identified (Eymin and Hulot 2005). They translate into uncertainties in the coefficients of ψ (errors of representativeness) that can be accurately estimated using an ensemble technique (Gillet et al. 2009). Second, the transfer of data assimilation methods to the geomagnetic community has been slowed down by our poor knowledge of the state of the Earth's core prior to the assimilation of geomagnetic data.

That remark calls for an incremental approach whereby our knowledge of the state of the Earth's core $\mathbf{x}$ progressively improves. As noted above (Sect. 1.1), we arguably have a good knowledge of the largest scales of the quasi-geostrophic streamfunction ψ time-averaged over the last ten years during which highly accurate satellite data have been available. On the other hand, time series of ψ inferred from continuous magnetic field models such as CM4 (Sabaka et al. 2004) for the time interval 1960–2002 show artifactual variations. This situation has prompted different groups to forgo sequential approaches and undertake simultaneous predictions of B_r and of the flow (or the streamfunction ψ) at the core surface (Lesur et al. 2010). We can look at these efforts as a step preliminary to the use of the full QG scheme outlined in this section.

4.3 Core Field Forecasting and Earth's Dynamo Limit of Predictability

In parallel to the efforts reported above, which mainly focussed on the ability of data assimilation schemes to recover some information about the hidden components of the state of the geodynamo (such as the magnetic field deep inside the core, recall Figs. 11 and 14), a number of studies have also started looking into the possibility of improving geomagnetic (core) field forecasts. Such forecasts are not only of academic interest. They are very much needed to ensure that an accurate enough global model of the geomagnetic field is permanently available for a large number of practical applications such as navigation, pointing (e.g. for directional drilling), pre-processing of local magnetic surveys for exploration geophysics, and defining the magnetic environment in the near outer space for ionospheric, magnetospheric, and space weather applications (see e.g. Meyers and Davis 1990, for an interesting account of those many, sometimes unexpected, applications). Most of those needs are currently covered by the International Geomagnetic Reference Field (IGRF) models, which are updated, published and widely distributed every five years (see e.g. Maus et al. 2005). Those models are conventionally provided in the form of a set of Gauss coefficients (up to degree 13) defining a spherical harmonic description of the field at a reference epoch (the latest IGRF has just been released for reference epoch 2010.0),[13] together with an additional set of estimates of the first time derivative of those coefficients (up to degree 8), to be used for forecasting the field over the next five years. Thus IGRF forecasts basically rely on a simple linear extrapolation of the field in time.

[13] www.ngdc.noaa.gov/IAGA/vmod/igrf.html.

For most applications, increasing the range of the forecast beyond five years is less an issue than improving the accuracy of the forecast. For other applications, however, increasing the range of the forecast is very much desirable. It is well-known for instance that the global intensity of the field is currently decreasing, especially within a wide region in the South-Atlantic where the field is already much lower than anywhere else, defining a so-called South-Atlantic Anomaly (SAA, see e.g. Hulot et al. 2007). This anomaly evolves very significantly on decadal time scales (e.g. Olsen et al. 2000), through core processes that could lead to a further decrease of the field in this area (Hulot et al. 2002). As the SAA is already an issue to low Earth orbiting space technology (e.g. Heirtzler 2002), which requires significant time for planning and operation, improving our ability to forecast the evolution of the field up to several decades would unquestionably be valuable.

Studies investigating how geomagnetic field forecasting could be improved (compared to the linear IGRF five-year range type of forecasting) have been very few so far. A first series of studies, illustrated by the two recent papers of Maus et al. (2008) and Beggan and Whaler (2009), looked into the possibility of relying on the initial value problem described by (1) to forecast the field. Starting from an initial field B_r at time t_0 and assuming a flow $\boldsymbol{u}_h$ known over the forecasting time window, (1) can be time stepped, and the trajectory of B_r computed, over the same window. Since, as already noted in Sect. 3, knowing B_r at the core surface is equivalent to knowing the field at the Earth's surface and above (where we are interested in predicting the core field), this makes it possible to forecast the field. Note that this forecasting strategy is indeed different from the IGRF strategy: Following the latter would imply to start as well from a known B_r at t_0, but to use a steady right-hand side term (equal to $\partial_t B_r$ at t_0), when time stepping equation (1). In particular, even assuming a forecast based on a stationary flow $\boldsymbol{u}_h$ is different from an IGRF forecast, as the field B_r in the right-hand side term of (1) evolves at each time step, making this term time-dependent.

Using such a core flow based forecasting strategy is a natural first step towards improving on the trivial IGRF forecasting strategy. It nevertheless relies on two fundamental assumptions that need to be spelled out. One is that magnetic diffusion is not expected to play any significant role on the time and length scales of interest. This indeed is widely thought to likely be the case (see e.g. Jackson and Finlay 2007; Holme 2007). The other, far less grounded, is that better a priori information is available with respect to the flow $\boldsymbol{u}_h$ and its time behaviour, than with respect to the field B_r. This is a strong assumption, especially in view of the dynamical interplay between the magnetic field and the flow expected within the quasi-geostrophic conceptual framework discussed in Sect. 4.2. However, and as already pointed out, it may also be that some background quasi-stationary core flows driven by mantle thermal heterogeneities could play a significant role, especially when considering long time scales (Aubert et al. 2007, 2008; Amit et al. 2008). Interestingly, Maus et al. (2008) precisely suggest that using a stationary flow $\boldsymbol{u}_h$ could slightly improve the quality of the forecast when considering predictions up to a decade, beyond the time scale of short term dynamics associated with the so-called geomagnetic jerks. The still unpredictable occurrence of these remains the main limitation to short-term forecasting (see e.g. Thébault et al. 2010). Although such simple core flow based geomagnetic field forecasts are much debated (e.g. Lesur and Wardinski 2009; Maus et al. 2009), further developments, associated with data assimilation techniques, such as initiated by Beggan and Whaler (2009), and with physical models, along the lines discussed in Sects. 4.1 and 4.2, are clearly the way to additional improvements.

An interesting question to be discussed at this point is that of the limit of predictability of the Earth's dynamo. Just as for meteorology, any geomagnetic field forecast is indeed intrinsically limited in time. This is because the geodynamo belongs to the same class of

non-periodic dynamical systems that can exhibit chaotic behaviour. As first pointed out by Edward N. Lorenz in his celebrated 1963 paper (Lorenz 1963), for such systems, unless the initial state is perfectly known, future states are bound to become unpredictable after a finite period of time, even if computed from exactly known deterministic equations. This is because any initial error with respect to the true state of the system $\mathbf{x}^t$, no matter how small, will necessarily grow at some exponential rate and eventually lead to a predicted state $\mathbf{x}^f$ macroscopically different from $\mathbf{x}^t$. In the case of the atmosphere, it is for instance estimated that any initial error will roughly double within 1.5 days (Kalnay 2003), which, given current meteorological data quality and assimilation strategies, translates into the familiar possibility of accurately forecasting the weather up to three days in advance (recall Sect. 1.2), with some confidence up to a week, but hardly beyond. Although some attempts have been made early on to characterize the non-linear behaviour of the Earth's dynamo by using simplified equations (e.g. Jones et al. 1985), it is only very recently that the issue of the associated limit of predictability has begun to be addressed with the help of fully consistent 3D magnetohydrodynamic codes, of the same type as those envisioned for the data assimilation approach described in Sect. 4.1.

The first study of this type has already provided interesting results (Hulot et al. 2010a). It consisted in a systematic study of a series of numerical dynamo simulations, the dynamo being assumed thermally driven with fixed and homogeneous temperatures imposed at both the inner-core and core-mantle boundaries, with the electrically conducting inner core (with the same conductivity as the liquid core) free to rotate axially (along the Earth's rotation axis) with respect to the electrically insulating mantle, and the mechanical boundary conditions assumed rigid at both boundaries. Although such assumptions can be considered as quite restrictive (in particular because internal heat sources, and compositional sources are ignored), they have several advantages. First, they are typical of the type of assumptions currently used for initial attempts of implementation of data assimilation strategies with three-dimensional models of the geodynamo (see Sect. 4.1 above). Second, they make it possible to run a large number of simulations under well-understood physical assumptions, with each simulation characterized by four input dimensionless parameters (the Rayleigh R_{th}, Ekman E, Prandtl Pr, and magnetic Prandtl Pm numbers, see Table 3). Finally, and as precisely suggested by the study of Hulot et al. (2010a), it anyway seems that the issue of the limit of predictability of fully consistent 3D dynamos is less dependent on the details of the way the dynamo is driven, than on the constitutive dimensionless parameters E, Pr, and Pm, the output parameter Rm (the magnetic Reynolds number, see Table 3), or the typical correlation times of the field produced at the core surface, estimates of which can be derived from both contemporary and archeomagnetic observations (Hulot and Le Mouël 1994; Hongre et al. 1998). Thanks to the relatively large number of simulations they ran (37 in total), Hulot et al. (2010a) were thus able to investigate the dependence of the limit of predictability of such dynamos on those various parameters, and propose a relatively simple asymptotic rule that they tentatively applied to the Earth's dynamo.

To both illustrate the origin of this limit of predictability and the method used by Hulot et al. (2010a) in their investigation, Fig. 15 shows the consequence of artificially introducing a slight error in one such simulation. In this figure, we first show the time evolution of the axial dipole field produced at the core surface by the reference simulation (Fig. 15a), which experienced a reversal. This reference simulation was next slightly perturbed by adding an error of relative value ϵ to the axial dipole at a given time t_0 (here close to the reversal). The consequence of introducing this perturbation in the subsequent evolution of the simulation is next shown in Fig. 15b, where a close-up of the initial dipole evolution is plotted, together with the dipole evolution after introducing relative errors of $\epsilon = 10^{-2}$, $\epsilon = 10^{-6}$,

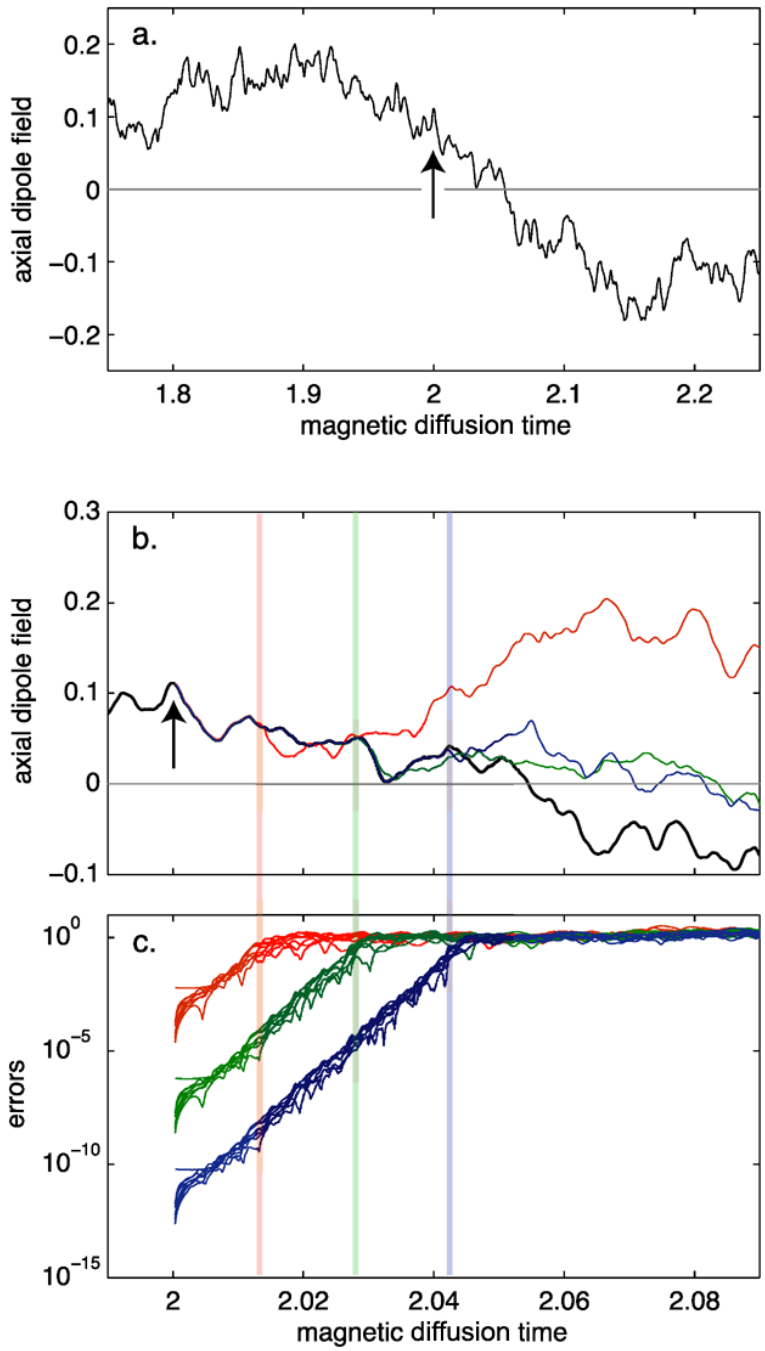

Fig. 15 Error growth in a perturbed fully consistent 3D dynamo simulation, with $\mathrm{E} = 4 \times 10^{-4}$, $\mathrm{Pr} = 1$, $\mathrm{Pm} = 10$ and $\mathrm{Rm} \approx 770$, following the definitions given in Table 3, which are slightly different from those chosen by Hulot et al. (2010a). In (**a**) we first show the evolution of the axial dipole field at the core surface (arbitrary scale) for a reference run as a function of time (scaled in units of magnetic diffusion time $\tau_D = d^2/\lambda$, d being the depth of the core, see Table 3). At time $t_0 = 2.00$ (*arrow*), perturbations with various magnitudes are introduced and the subsequent evolution of the axial dipole field of the perturbed solutions are shown in (**b**) ($\epsilon = 10^{-2}$ *red*, $\epsilon = 10^{-6}$ *green*, and $\epsilon = 10^{-10}$ *blue*), which also shows a close-up of the reference solution (*black*). The detailed way those various perturbed solutions diverge from the reference solution are finally shown in (**c**), which shows semi-logarithmic plots of the relative rms differences for each spherical harmonic degree l (with $1 \leq l \leq 8$, leading to eight overlapping curves) between the core surface poloidal magnetic field produced by the reference simulation and that produced by each perturbed solution (same colour-code as for (**b**)). Colour-coded vertical bars mark the times when the perturbed solutions start behaving in a way totally unrelated to the reference solution (consult Hulot et al. 2010a for more illustrations and details)

and $\epsilon = 10^{-10}$. As can be seen, the perturbed solutions first remain very close to the reference solution, but eventually diverge macroscopically from this solution. The larger the initial error, the sooner the divergence occurs. As shown in Fig. 15c, this is because the difference between the perturbed solution and the reference solution (e.g., the error) gradually increases in an exponential manner with a growth rate independent of the initial error ϵ. The same growth rate is found in the way all quantities defining the state of the dynamo $\mathbf{x}$ diverge from their evolution in the reference simulation (such as the higher degrees of the poloidal magnetic field at the core surface, as plotted in Fig. 15c). As shown by Hulot et al. (2010a) it also is independent of the way and time t_0 (including shortly before a reversal, as is the case here) the perturbation is initially introduced (be it in the magnetic, flow, or temperature fields). Thus, this error growth rate appears to be an intrinsic property of each given dynamo. It can be defined as $\lambda_e = \tau_e^{-1}$, where τ_e is the associated e-folding time. This e-folding time of course depends on the dimensionless parameters governing the dynamo simulation under consideration. But as noted by Hulot et al. (2010a), and at least for the parameter range they investigated, as soon as the magnetic Reynolds number Rm produced by the dynamo is large enough, and even more so when considering E, Pr, and Pm parameter ranges closest (though still very remote, see below) to those thought relevant for the geodynamo, it appears that τ_e only depends on a time scale τ_{sv} that statistically characterizes the time variations of the field produced at the core surface, roughly as

$$\tau_e = 0.05\tau_{\mathrm{sv}}. \tag{30}$$

The time scale τ_{sv} can be recovered from observations by inspection of the spatial power spectra of the field and of its first time derivative (see Hulot and Le Mouël 1994; Christensen and Tilgner 2004; Hulot et al. 2010a, for details). For the geodynamo, τ_{sv} turns out to be of order 535 years (Christensen and Tilgner 2004). Thus, the study of Hulot et al. (2010a) would suggest a value of about 30 years for τ_e, amounting to a doubling time of roughly 20 years, analogue of the 1.5 days doubling time in meteorology.

Assessing how far in the future the core field could then be forecasted (that is, assessing the practical limit of predictability of the Earth's dynamo) also requires some consideration on how well the state of the geodynamo $\mathbf{x}$ could possibly be known at some initial time. This is clearly not a trivial issue. Given the current status of data assimilation schemes, it is fair to say that at present, many of the quantities that define $\mathbf{x}$ are poorly known (particularly those defining the state of the field and flow deep inside the core). As the methods described in Sects. 4.1 and 4.2 improve, it is not unreasonable to expect some significant progress in the coming years. But it also is clear that the basic state of the geodynamo will never be known with better accuracy than the core field that can directly be observed at the Earth's surface. As already noted in Sect. 3, this accuracy is intrinsically limited by the crustal field, which does not make it possible to recover the static component of the core field beyond spherical harmonic degree 14, and its time variations beyond degree 18. In addition, in practice, even those degrees of the core field that can be recovered in principle are only recovered with some uncertainties. Using the order of magnitude of the error associated with current IGRF models (typically of order 10–20 nT at the Earth's surface at the epoch of reference of the model, the average magnitude of the field being of order 40,000 nT), and the fact that current linear IGRF type of forecasts lead to errors typically of order 100 nT after just 5 years, Hulot et al. (2010a) note that the above results would suggest that using an ideal assimilation scheme could possibly lead to a prediction of similar quality after 50 to 70 years, thus leaving some room for significant improvements compared to the current simple IGRF linear forecasts.

Probably the main limitation of the Hulot et al. (2010a) investigation is the parameter regimes in which the simulations operate, which are still very remote from the one thought to be relevant for the geodynamo (with $E = 10^{-3}$–10^{-5}, $Pr = 1$, and $Pm = 0.5$–15, whereas $E = 10^{-9}$–10^{-14}, $Pr = 0.1$–1, and $Pm = 10^{-5}$–10^{-6} are thought to be appropriate for the Earth). In this respect, extrapolating the asymptotic rule given by (30) to the Earth can be considered as a strong move. However there is far less doubt that those results essentially apply to all fully consistent 3D numerical dynamos that could be used in practice for data assimilation. Since those would have to produce a field with the same τ_{sv} time scale as the geodynamo and be fed by the observed field with the same initial error as described above, forecasts based on such 3D dynamos would then indeed be limited by the limit of predictability identified by Hulot et al. (2010a). Unfortunately, additional limitations could then also arise as a result of the fact, already mentioned (see Sect. 1.3), that all such 3D dynamos tend to damp out high frequency magnetohydrodynamic phenomena such as torsional oscillations and geomagnetic jerks (both of which could be related, see e.g. Bloxham et al. 2002). Interestingly however, we also note that such phenomena tend to only mildly affect the medium-term trend of the geomagnetic field. Perhaps the best data assimilation approach in terms of forecasting could be one smartly combining 3D modelling of medium to long-term dynamo processes (along the lines described in Sect. 4.1), with 2D quasi-geostrophic modelling of short-term processes (along the lines described in Sect. 4.2).

One last outcome of the Hulot et al. (2010a) study worth mentioning is that it also implies that the timing of the next geomagnetic reversal is essentially unpredictable. As is indeed illustrated by Fig. 15, as soon as a perturbed solution has started diverging macroscopically from the reference solution, it behaves in a totally unrelated way. In particular, even if the reference solution was about to reverse, with already a fairly low axial dipole component, the perturbed solution may either postpone the reversal, or eventually decide not to reverse. Since it is well-known from examination of past reversals that these can hardly occur within less than a couple of thousand years when starting from dipole field value comparable to the present value (see e.g. Constable and Korte 2006; Hulot et al. 2010b), it is quite unavoidable that given the value of $\tau_e = 30$ y expected for the geodynamo, predicting a reversal several millennia ahead of time would require a knowledge of the present state of the core way beyond our observational capacity.

5 Summary and Outlook

In this paper, we have motivated the development and implementation of data assimilation techniques for the purpose of geomagnetic data analysis. The ongoing era of magnetic observation of the Earth with satellites is a great and exciting incentive for investigating to what extent such techniques could be beneficial for improving both our understanding of core dynamics and our ability to model the core field. Of particular interest are the possibilities, on the one hand, to combine satellite data with observatory data to try and perform a reanalysis of historical field models over the past four hundred years or so, and, on the other hand, to produce better forecasts of the secular variation in the years to come.

We have succinctly introduced the basics of the algorithmic machinery in operational use in the atmospheric and oceanic communities in order to explain how to construct formally the relationship between a numerical model of core dynamics and geomagnetic observations. As we saw, the most critical points for its application to geomagnetism, compared to that in atmospheric or oceanic weather prediction, are

– that the observations directly access a much smaller fraction of the state vector,

– and that we still have to convince ourselves, in a trial-and-error fashion, that the various models that we use are adequate for this task.

Specific to the core problem is the remote, blurred and incomplete observation of its state. Accordingly, we lack a well-defined background state (the equivalent of a "climatological" mean), about which the dynamics of the secular variation is likely to take place, even though we have a fairly good idea of the large to medium length scales of the poloidal field at the top of the core over a 400 year period, and for the largest scales much longer back in time (e.g. Hulot et al. 2010b, and references therein). Also specific and important for geomagnetic data analysis is the need we are in to separate the various sources contributing to the field measured at a given location (in particular at satellite altitude). Our hope is that a better description of the core field by dynamical models could contribute to better recover it, in the same way similar approaches have already improved our understanding of the ionospheric and magnetospheric fields (e.g. Scherliess et al. 2006; Tsyganenko and Sitnov 2007).

The first results described in Sect. 4 indicate that, in the assimilation framework, surface measurements of B_r can provide some information and constraints about the structure of the field and the flow within the core. The propagation of the information (the innovation) from the core-mantle boundary to the bulk of the core is achieved either through the non-linear interactions between the dynamical actors (the various components of the state vector, which include the poloidal field), when operating with a three-dimensional model of the geodynamo, or by some a priori constraint imposed on the nature of the dynamics (under the quasi-geostrophic assumption, the invariance of the flow in the direction of rotation). There is room for improvement with respect to the way surface information is transferred to the bulk of the fluid: An appealing direction for future research in that area would be to resort to multivariate statistics and relate surface dynamical patterns with their roots, using empirical orthogonal functions. In oceanography, their use in conjunction with surficial observations leads to much better estimates of the state of the ocean, at least above the thermocline; see e.g. Penduff et al. (2002) for an illustration in the South Atlantic Ocean.

The issue of the climatological mean (the background state) for the core need also be looked at in detail. That mean could reflect the thermal control exerted on the core by the overlying mantle, which could thereby influence the long-term secular variation (e.g. Aubert et al. 2007). In addition, theoretical arguments favor a geodynamo operating close to a so-called Taylor state (Taylor 1963). It might then prove useful to seek an average core state $\mathbf{x}^b$ satisfying Taylor's constraint, which, following Sasaki (1970), could be enforced using either a weak or a strong formalism. For recent developments in that direction, the reader is referred to Livermore et al. (2009, 2010).

To conclude, let us emphasize that further understanding of the mechanisms controlling the short- and long-term secular variation and the internal structure and dynamics of the core could be gained by assimilating experimental results obtained with liquid metal analogs of the core. Such analogs are in use in several places around the globe (e.g. Cardin and Olson 2007, for a recent review): a container is filled with a liquid metal (sodium is today's favorite working fluid), which is set in motion (most of the time by mechanical forcing), and can eventually support dynamo action in a turbulent environment (Monchaux et al. 2007). When well instrumented, liquid metal experiments have the advantage of providing a detailed mapping of the field at the surface of the container, possibly complemented by in-situ flow and field measurements (Nataf et al. 2006). Surface magnetic time series of the experimental secular variation can exhibit interesting features, which can be in turn interpreted as the signature of hydromagnetic waves (Schmitt et al. 2008). These time series have the advantage of lasting for several magnetic diffusion times (several hundreds of thousands of years when upscaled to the core). This is much more than the few centuries

of well-documented record of observations we have at hand for geomagnetic data assimilation practice. Even if the modest size of experimental analogs of the core ($\approx$1 m) creates a collapse of the various time scales over which the dynamical phenomena at work operate, it is almost certain that assimilating such experimental data could complement well the efforts currently led to better understand and model the physical principles governing the geomagnetic secular variation.

Acknowledgements We thank Ulrich Christensen for his thorough and stimulating review which greatly helped improve the manuscript. We are also grateful to Chris Finlay whose reading of the draft led to a much appreciated list of useful suggestions, and to Fabio Donadini for his assistance with the geomagia database. Alexandre Fournier, Dominique Jault, Elisabeth Canet and Nicolas Gillet have been supported by a grant from the French Agence Nationale de la Recherche, Research program VS-QG (grant number BLAN06-2.155316). Partial support also came from the program "observation de la Terre" of the French agency CNES, and from INSU, through the LEFE ASSIMILATION program. Weijia Kuang and Andrew Tangborn are funded by the NSF Collaborative Mathematical Geophysics (CMG) Program under the grant EAR-0327875, and by the NASA Earth's Surface and Interior Program. The authors thank the International Space Science Institute and André Balogh for organizing the workshop on terrrestrial magnetism held in Bern in March 2009. Alexandre Fournier also thanks gratefully Olivier Talagrand, Pierre Brasseur and Emmanuel Cosme for kindly and pedagogically distilling their knowledge of data assimilation over the past few years. Olivier Talagrand is especially thanked for explaining him, among other things, the subtleties of the "discrete of adjoint vs. adjoint of discrete" issue. Part of the figures were made using the following freely available softwares: the generic mapping tools (Wessel and Smith 1991), paraview (www.paraview.org), and the pstricks-add LaTeX package. This is IPGP contribution 3033.

References

M.M. Alexandrescu, D. Gibert, J.L. Le MouëL, G. Hulot, G. Saracco, An estimate of average lower mantle conductivity by wavelet analysis of geomagnetic jerks. J. Geophys. Res. **104**(B8), 17735–17745 (1999). doi:10.1029/1999JB900135

H. Amit, J. Aubert, G. Hulot, P. Olson, A simple model for mantle-driven flow at the top of Earth's core. Earth Planets Space **60**, 845–854 (2008)

J. Aubert, H. Amit, G. Hulot, Detecting thermal boundary control in surface flows from numerical dynamos. Phys. Earth Planet. Inter. **160**(2), 143–156 (2007). doi:10.1016/j.pepi.2006.11.003

J. Aubert, H. Amit, G. Hulot, P. Olson, Thermochemical flows couple the Earth's inner core growth to mantle heterogeneity. Nature **454**, 758–761 (2008). doi:10.1038/nature07109

G.E. Backus, Kinematics of geomagnetic secular variation in a perfectly conducting core. Philos. Trans. R. Soc. Lond. Ser. A Math. Phys. Sci. **263**(1141), 239–266 (1968)

G.E. Backus, Application of mantle filter theory to the magnetic jerk of 1969. Geophys. J. R. Astron. Soc. **74**(3), 713–746 (1983)

G. Backus, R. Parker, C. Constable, *Foundations of Geomagnetism* (Cambridge University Press, Cambridge, 1996)

C.D. Beggan, K.A. Whaler, Forecasting change of the magnetic field using core surface flows and ensemble Kalman filtering. Geophys. Res. Lett. **36**, L18303 (2009). doi:10.1029/2009GL039927

A. Bennett, *Inverse Modeling of the Ocean and Atmosphere* (Cambridge University Press, Cambridge, 2002)

P. Bergthorsson, B. Döös, Numerical weather map analysis. Tellus **7**(3), 329–340 (1955)

J. Bloxham, D. Gubbins, A. Jackson, Geomagnetic secular variation. Philos. Trans. R. Soc. Lond. Ser. A Math. Phys. Sci., 415–502 (1989)

J. Bloxham, S. Zatman, M. Dumberry, The origin of geomagnetic jerks. Nature **420**(6911), 65–68 (2002). doi:10.1038/nature01134

S.I. Braginsky, Torsional magnetohydrodynamic vibrations of the earth's core and variations in day length. Geomagnet. Aeron. **10**, 1–8 (1970)

S.I. Braginsky, Short period geomagnetic variations. Geophys. Astrophys. Fluid Dyn. **30**, 1–78 (1984)

P. Brasseur, Ocean data assimilation using sequential methods based on the Kalman filter, in *Ocean Weather Forecasting: An Integrated View of Oceanography*, ed. by E. Chassignet, J. Verron. (Springer, Berlin, 2006), pp. 271–316

M. Buehner, Inter-comparison of 4D-Var and EnKF systems for operational deterministic numerical weather prediction, in *WWRP/THORPEX Workshop on 4D-VAR and Ensemble Kalman Filter Intercomparisons*, Buenos Aires, Argentina, 2008

B. Buffett, J. Mound, A. Jackson, Inversion of torsional oscillations for the structure and dynamics of Earth's core. Geophys. J. Int. **177**(3), 878–890 (2009). doi:10.1111/j.1365-246X.2009.04129.x

H.P. Bunge, C. Hagelberg, B. Travis, Mantle circulation models with variational data assimilation: inferring past mantle flow and structure from plate motion histories and seismic tomography. Geophys. J. Int. **152**(2), 280–301 (2003). doi:10.1046/j.1365-246X.2003.01823.x

E. Canet, A. Fournier, D. Jault, Forward and adjoint quasi-geostrophic models of the geomagnetic secular variation. J. Geophys. Res. **114**, B11101 (2009). doi:10.1029/2008JB006189

P. Cardin, P. Olson, Experiments on core dynamics, in *Core Dynamics*, ed. by P. Olson, G. Schubert. Treatise on Geophysics, vol. 8 (Elsevier, Amsterdam, 2007), pp. 319–343, Chap. 11

J.G. Charney, R. Fjortoft, J. Von Neumann, Numerical integration of the barotropic vorticity equation. Tellus **2**(4), 237–254 (1950)

E. Chassignet, J. Verron, *Ocean Weather Forecasting: An Integrated View of Oceanography* (Springer, Berlin, 2006)

U.R. Christensen, J. Aubert, Scaling properties of convection-driven dynamos in rotating spherical shells and application to planetary magnetic fields. Geophys. J. Int. **140**, 97–114 (2006). doi:10.1111/j.1365-246X.2006.03009.x

U.R. Christensen, A. Tilgner, Power requirement of the geodynamo from ohmic losses in numerical and laboratory dynamos. Nature **429**(6988), 169–171 (2004). doi:10.1038/nature02508

U.R. Christensen, J. Wicht, Numerical dynamo simulations, in *Core Dynamics*, ed. by P. Olson, G. Schubert. Treatise on Geophysics, vol. 8 (Elsevier, Oxford, 2007), pp. 245–282, Chap. 8

U.R. Christensen, V. Holzwarth, A. Reiners, Energy flux determines magnetic field strength of planets and stars. Nature **457**(7226), 167–169 (2009). doi:10.1038/nature07626

U.R. Christensen, J. Aubert, G. Hulot, Conditions for Earth-like geodynamo models. Earth Planet. Sci. Lett. (2010). doi:10.1016/j.epsl.2010.06.009

A. Chulliat, N. Olsen, Observation of magnetic diffusion in the Earth's core from Magsat, Oersted and CHAMP data. J. Geophys. Res. **115**, B05105 (2010). doi:10.1029/2009JB006994

A. Chulliat, G. Hulot, L.R. Newitt, Magnetic flux expulsion from the core as a possible cause of the unusually large acceleration of the north magnetic pole during the 1990s. J. Geophys. Res. **115**, B07101 (2010). doi:10.1029/2009JB007143

S. Cohn, N. Sivakumaran, R. Todling, A fixed-lag Kalman smoother for retrospective data assimilation. Mon. Weather Rev. **122**(12), 2838–2867 (1994). doi:10.1175/1520-0493(1994)122<2838:AFLKSF>2.0.CO;2

C. Constable, M. Korte, Is Earth's magnetic field reversing? Earth Planet. Sci. Lett. **246**(1–2), 1–16 (2006). doi:10.1016/j.epsl.2006.03.038

E. Cosme, J.M. Brankart, J. Verron, P. Brasseur, M. Krysta, Implementation of a reduced-rank, square-root smoother for high resolution ocean data assimilation. Ocean Model. **33**(1–2), 87–100 (2010). doi:10.1016/j.ocemod.2009.12.004

P. Courtier, Variational methods. J. Meteorol. Soc. Jpn. **75**(1B), 211–218 (1997)

P. Courtier, O. Talagrand, Variational assimilation of meteorological observations with the adjoint vorticity equation. II: Numerical results. Q. J. R. Meteorol. Soc. **113**(478), 1329–1347 (1987). doi:10.1002/gj.49711347813

D. Dee, A. Da Silva, Data assimilation in the presence of forecast bias. Q. J. R. Meteorol. Soc. **124**(545), 269–295 (1998)

F. Donadini, M. Korte, C. Constable, Geomagnetic field for 0–3 ka: 1. New data sets for global modeling. Geochem. Geophys. Geosyst. **10**, Q06007 (2009). doi:10.1029/2008GC002295

G.D. Egbert, A.F. Bennett, M.G.G. Foreman, TOPEX/POSEIDON tides estimated using a global inverse model. J. Geophys. Res. **99**(C12), 24821–24852 (1994). doi:10.1029/94JC01894

A. Eliassen, Provisional report on calculation of spatial covariance and autocorrelation of the pressure field. Institute of Weather and Climate Research, Academy of Sciences, Oslo, Report 5 (1954)

G. Evensen, Sequential data assimilation with a nonlinear quasi-geostrophic model using Monte Carlo methods to forecast error statistics. J. Geophys. Res. **99**(C5), 10143–10162 (1994). doi:10.1029/94JC00572

G. Evensen, *Data Assimilation: The Ensemble Kalman Filter*, 2nd edn. (Springer, Berlin, 2009). doi:10.1007/978-3-642-03711-5

C. Eymin, G. Hulot, On core surface flows inferred from satellite magnetic data. Phys. Earth Planet. Inter. **152**, 200–220 (2005). doi:10.1016/j.pepi.2005.06.009

A. Fichtner, H.P. Bunge, H. Igel, The adjoint method in seismology I. Theory. Phys. Earth Planet. Inter. **157**(1–2), 86–104 (2006). doi:10.1016/j.pepi.2006.03.016

C.C. Finlay, Historical variation of the geomagnetic axial dipole. Phys. Earth Planet. Inter. **170**(1–2), 1–14 (2008). doi:10.1016/j.pepi.2008.06.029

C.C. Finlay, A. Jackson, Equatorially dominated magnetic field change at the surface of earth's core. Science **300**(5628), 2084–2086 (2003). doi:10.1126/science.1083324

C.C. Finlay, M. Dumberry, A. Chulliat, A. Pais, Short timescale dynamics: Theory and observations. Space Sci. Rev. (2010, in revision)

A. Fournier, C. Eymin, T. Alboussière, A case for variational geomagnetic data assimilation: insights from a one-dimensional, nonlinear, and sparsely observed MHD system. Nonlinear Process. Geophys. **14**, 163–180 (2007)
E. Friis-Christensen, H. Lühr, G. Hulot, Swarm: A constellation to study the Earth's magnetic field. Earth Planets Space **58**, 351–358 (2006)
L.S. Gandin, *Objective Analysis of Meteorological Fields (Objektivnyi Analiz Meteorologicheskikh Polei)* (Gidrometeor. Izd.i, Leningrad, 1963) (in Russian). English translation by Israel program for scientific translations, Jerusalem, 1965
G. Gaspari, S.E. Cohn, Construction of correlation functions in two and three dimensions. Q. J. R. Meteorol. Soc. **125**(554), 723–757 (1999). doi:10.1002/qj.49712555417
A. Genevey, Y. Gallet, C. Constable, M. Korte, G. Hulot, ArcheoInt: An upgraded compilation of geomagnetic field intensity data for the past ten millennia and its application to the recovery of the past dipole moment. Geochem. Geophys. Geosyst. **9**(4), Q04038 (2008). doi:10.1029/2007GC001881
A. Genevey, Y. Gallet, J. Rosen, M. Le Goff, Evidence for rapid geomagnetic field intensity variations in Western Europe over the past 800 years from new French archeointensity data. Earth Planet. Sci. Lett., 132–143 (2009). doi:10.1016/j.epsl.2009.04.024
M. Ghil, P. Malanotte-Rizzoli, Data assimilation in meteorology and oceanography. Adv. Geophys. **33**, 141–266 (1991)
R. Giering, T. Kaminski, Recipes for adjoint code construction. ACM Trans. Math. Softw. **24**(4), 437–474 (1998)
N. Gillet, D. Brito, D. Jault, H.C. Nataf, Experimental and numerical studies of convection in a rapidly rotating spherical shell. J. Fluid Mech. **580**, 83–121 (2007). doi:10.1017/S0022112007005265
N. Gillet, A. Pais, D. Jault, Ensemble inversion of time-dependent core flow models. Geochem. Geophys. Geosyst. **10**, Q06004 (2009). doi:10.1029/2008GC002290
N. Gillet, D. Jault, E. Canet, A. Fournier, Fast torsional waves and strong magnetic field within the Earth's core. Nature **465**, 74–77 (2010a). doi:10.1038/nature09010
N. Gillet, V. Lesur, N. Olsen, Geomagnetic core field secular variation models. Space Sci. Rev. (2010b, in press). doi:10.1007/s11214-009-9586-6
G.A. Glatzmaier, Numerical simulations of stellar convective dynamos. I—The model and method. J. Comput. Phys. **55**(3), 461–484 (1984). doi:10.1016/0021-9991(84)90033-0
G.A. Glatzmaier, P.H. Roberts, A three-dimensional self-consistent computer simulation of a geomagnetic reversal. Nature **377**, 203–209 (1995). doi:10.1038/377203a0
R.S. Gross, I. Fukumori, D. Menemenlis, P. Gegout, Atmospheric and oceanic excitation of length-of-day variations during 1980–2000. J. Geophys. Res. **109**, B01406 (2004). doi:10.1029/2003JB002432
D. Gubbins, A formalism for the inversion of geomagnetic data for core motions with diffusion. Phys. Earth Planet. Inter. **98**(3), 193–206 (1996). doi:10.1016/S0031-9201(96)03187-1
D. Gubbins, N. Roberts, Use of the frozen flux approximation in the interpretation of archeomagnetic and palaeomagnetic data. Geophys. J. R. Astron. Soc. **73**(3), 675–687 (1983). doi:10.1111/j.1365-246X.1983.tb03339.x
D. Gubbins, P.H. Roberts, Magnetohydrodynamics of the Earth's core, in *Geomagnetism*, vol. 2, ed. by J.A. Jacobs (Academic Press, London, 1987)
D. Gubbins, A.L. Jones, C.C. Finlay, Fall in Earth's magnetic field is erratic. Science **312**(5775), 900–902 (2006). doi:10.1126/science.1124855
N. Gustafsson, Discussion on '4D-Var or EnKF?'. Tellus **59A**(5), 774–777 (2007). doi:10.1111/j.1600-0870.2007.00262.x
J.R. Heirtzler, The future of the South Atlantic anomaly and implications for radiation damage in space. J. Atmos. Sol.-Terr. Phys. **64**(16), 1701–1708 (2002). doi:10.1016/S1364-6826(02)00120-7
H. Hersbach, Application of the adjoint of the WAM model to inverse wave modeling. J. Geophys. Res. **103**(C5), 10469–10487 (1998). doi:10.1029/97JC03554
R. Hide, Free hydromagnetic oscillations of the Earth's core and the theory of the geomagnetic secular variation. Philos. Trans. R. Soc. Lond. Ser. A Math. Phys. Sci. **259**, 615–647 (1966)
R. Holme, Large-scale flow in the core, in *Core Dynamics*, ed. by P. Olson, G. Schubert. Treatise on Geophysics, vol. 8 (Elsevier, Amsterdam, 2007), pp. 107–130, Chap. 4
L. Hongre, G. Hulot, A. Khokhlov, An analysis of the geomagnetic field over the past 2000 years. Phys. Earth Planet. Inter. **106**(3), 311–335 (1998). doi:10.1016/S0031-9201(97)00115-5
G. Hulot, J.L. Le Mouël, A statistical approach to the Earth's main magnetic field. Phys. Earth Planet. Inter. **82**(3), 167–183 (1994). doi:10.1016/0031-9201(94)90070-1
G. Hulot, M. Le Huy, J.L. Le Mouël, Secousses (jerks) de la variation séculaire et mouvements dans le noyau terrestre. C. R. Acad. Sci. Sér. 2, Méc. Phys. Chim. Sci. Univers Sci. Terre **317**(3), 333–341 (1993)
G. Hulot, A. Khokhlov, J.L. Le Mouël, Uniqueness of mainly dipolar magnetic fields recovered from directional data. Geophys. J. Int. **129**(2), 347–354 (1997). doi:10.1111/j.1365-246X.1997.tb01587.x

G. Hulot, C. Eymin, B. Langlais, M. Mandea, N. Olsen, Small-scale structure of the geodynamo inferred from Oersted and Magsat satellite data. Nature **416**(6881), 620–623 (2002). doi:10.1038/416620a
G. Hulot, T. Sabaka, N. Olsen, The present field, in *Geomagnetism*, ed. by M. Kono, G. Schubert. Treatise on Geophysics, vol. 5 (Elsevier, Amsterdam, 2007), Chap. 2
G. Hulot, N. Olsen, E. Thebault, K. Hemant, Crustal concealing of small-scale core-field secular variation. Geophys. J. Int. **177**(2), 361–366 (2009). doi:10.1111/j.1365-246X.2009.04119.x
G. Hulot, F. Lhuillier, J. Aubert, Earth's dynamo limit of predictability. Geophys. Res. Lett. **37**, L06305 (2010a). doi:10.1029/2009GL041869
G. Hulot, C.C. Finlay, C.G. Constable, N. Olsen, M. Mandea, The magnetic field of planet Earth. Space Sci. Rev. **152**(1–4), 159–222 (2010b). doi:10.1007/s11214-010-9644-0
K. Ide, P. Courtier, M. Ghil, A.C. Lorenc, Unified notation for data assimilation: Operational, sequential and variational. J. Meteorol. Soc. Jpn. **75**, 181–189 (1997)
A. Jackson, The Earth's magnetic field at the core-mantle boundary. Ph.D. Thesis, Cambridge (1989)
A. Jackson, Time-dependency of tangentially geostrophic core surface motions. Phys. Earth Planet. Inter. **103**, 293–311 (1997). doi:10.1016/S0031-9201(97)00039-3
A. Jackson, C.C. Finlay, Geomagnetic secular variation and its application to the core, in *Geomagnetism*, ed. by P. Olson, G. Schubert. Treatise on Geophysics, vol. 5 (Elsevier, Amsterdam, 2007), pp. 148–193, Chap. 5
A. Jackson, J. Bloxham, D. Gubbins, Time-dependent flow at the core surface and conservation of angular momentum in the coupled core–mantle system, in *Dynamics of Earth's Deep Interior and Earth Rotation*, ed. by J.L. Le Mouël, D.E. Smylie, T. Herring. (American Geophysical Union, Washington, 1993), pp. 97–107
A. Jackson, A. Jonkers, M. Walker, Four centuries of geomagnetic secular variation from historical records. Philos. Trans. R. Soc. Ser. A, Math. Phys. Eng. Sci. **358**(1768), 957–990 (2000)
D. Jault, Axial invariance of rapidly varying diffusionless motions in the Earth's core interior. Phys. Earth Planet. Inter. **166**(1–2), 67–76 (2008). doi:10.1016/j.pepi.2007.11.001
D. Jault, C. Gire, J.L. Le Mouël, Westward drift, core motions and exchanges of angular momentum between core and mantle. Nature **333**(6171), 353–356 (1988). doi:10.1038/333353a0
C. Jones, N. Weiss, F. Cattaneo, Nonlinear dynamos: a complex generalization of the Lorenz equations. Physica D **14**, 161–176 (1985). doi:10.1016/0167-2789(85)90176-9
A. Kageyama, T. Sato, Generation mechanism of a dipole field by a magnetohydrodynamic dynamo. Phys. Rev. E **55**(4), 4617–4626 (1997). doi:10.1103/PhysRevE.55.4617
E. Kalnay, *Atmospheric Modeling, Data Assimilation, and Predictability* (Cambridge University Press, Cambridge, 2003)
E. Kalnay, M. Kanamitsu, R. Kistler, W. Collins, D. Deaven, L. Gandin, M. Iredell, S. Saha, G. White, J. Woollen et al., The NCEP/NCAR 40-year reanalysis project. Bull. Am. Meteorol. Soc. **77**(3), 437–471 (1996). doi:10.1175/1520-0477(1996)077<0437:TNYRP>2.0.CO;2
E. Kalnay, H. Li, T. Miyoshi, S. Yang, J. Ballabrera-Poy, 4-D-Var or ensemble Kalman filter? Tellus **59A**(5), 758–773 (2007a). doi:10.1111/j.1600-0870.2007.00261.x
E. Kalnay, H. Li, T. Miyoshi, S. Yang, J. Ballabrera-Poy, Response to the discussion on "4D-Var or EnKF?" by Nils Gustaffson. Tellus **59A**(5), 778–780 (2007b). doi:10.1111/j.1600-0870.2007.00263.x
A. Kelbert, G. Egbert, A. Schultz, Non-linear conjugate gradient inversion for global EM induction: resolution studies. Geophys. J. Int. **173**(2), 365–381 (2008). doi:10.1111/j.1365-246X.2008.03717.x
K. Korhonen, F. Donadini, P. Riisager, L.J. Pesonen, GEOMAGIA50: An archeointensity database with PHP and MySQL. Geochem. Geophys. Geosyst. **9**, Q04029 (2008). doi:10.1029/2007GC001893
M. Korte, C.G. Constable, Continuous geomagnetic field models for the past 7 millennia: 2. CALS7K. Geochem. Geophys. Geosyst. **6**(2), Q02H16 (2005). doi:10.1029/2004GC000801
M. Korte, F. Donadini, C.G. Constable, Geomagnetic field for 0–3 ka: 2. A new series of time-varying global models. Geochem. Geophys. Geosyst. **10**, Q06008 (2009). doi:10.1029/2008GC002297
W. Kuang, J. Bloxham, An Earth-like numerical dynamo model. Nature **389**(6649), 371–374 (1997). doi:10.1038/38712
W. Kuang, A. Tangborn, W. Jiang, D. Liu, Z. Sun, J. Bloxham, Z. Wei, MoSST-DAS: the first generation geomagnetic data assimilation framework. Commun. Comput. Phys. **3**, 85–108 (2008)
W. Kuang, A. Tangborn, Z. Wei, T. Sabaka, Constraining a numerical geodynamo model with 100-years of geomagnetic observations. Geophys. J. Int. **179**(3), 1458–1468 (2009). doi:10.1111/j.1365-246X.2009.04376.x
W. Kuang, Z. Wei, R. Holme, A. Tangborn, Prediction of geomagnetic field with data assimilation: a candidate secular variation model for IGRF-11. Earth Planets Space (2010, accepted)
A. Kushinov, J. Velímský, P. Tarits, A. Semenov, O. Pankratov, L. Tøffner-Clausen, Z. Martinec, N. Olsen, T.J. Sabaka, A. Jackson, Level 2 products and performances for mantle studies with Swarm. ESA Technical Report (2010)

F.X. Le Dimet, O. Talagrand, Variational algorithms for analysis and assimilation of meteorological observations: Theoretical aspects. Tellus **38**(2), 97–110 (1986)

B. Lehnert, Magnetohydrodynamic waves under the action of the Coriolis force. Astrophys. J. **119**, 647–654 (1954). doi:10.1086/145869

V. Lesur, I. Wardinski, Comment on"Can core-surface flow models be used to improve the forecast of the Earth's main magnetic field?" by Stefan Maus, Luis Silva, and Gauthier Hulot. J. Geophys. Res. **114**, B04104 (2009). doi:10.1029/2008JB006188

V. Lesur, I. Wardinski, M. Rother, M. Mandea, GRIMM: the GFZ reference internal magnetic model based on vector satellite and observatory data. Geophys. J. Int. **173**(2), 382–394 (2008). doi:10.1111/j.1365-246X.2008.03724.x

V. Lesur, I. Wardinski, S. Asari, B. Minchev, M. Mandea, Modelling the Earth's core magnetic field under flow constraints. Earth Planets Space (2010). doi:10.5047/eps.2010.02.010

L. Liu, M. Gurnis, Simultaneous inversion of mantle properties and initial conditions using an adjoint of mantle convection. J. Geophys. Res. **113**, B8405 (2008). doi:10.1029/2008JB005594

D. Liu, A. Tangborn, W. Kuang, Observing system simulation experiments in geomagnetic data assimilation. J. Geophys. Res. **112**, B8 (2007). doi:10.1029/2006JB004691

L. Liu, S. Spasojevic, M. Gurnis, Reconstructing Farallon plate subduction beneath North America back to the late cretaceous. Science **322**(5903), 934–938 (2008). doi:10.1126/science.1162921

P.W. Livermore, G.R. Ierley, A. Jackson, The construction of exact Taylor states. I: The full sphere. Geophys. J. Int. **179**(2), 923–928 (2009). doi:10.1111/j.1365-246X.2009.04340.x

P.W. Livermore, G.R. Ierley, A. Jackson, The construction of exact Taylor states. II: The influence of an inner core. Phys. Earth Planet. Inter. **178**, 16–26 (2010). doi:10.1016/j.pepi.2009.07.015

A.C. Lorenc, Analysis methods for numerical weather prediction. Q. J. R. Meteorol. Soc. **112**(474), 1177–1194 (1986). doi:10.1002/qj.49711247414

E.N. Lorenz, Deterministic nonperiodic flow. J. Atmos. Sci. **20**(2), 130–141 (1963)

S. Maus, S. Macmillan, T. Chernova, S. Choi, D. Dater, V. Golovkov, V. Lesur, F. Lowes, H. Lühr, W. Mai, S. McLean, N. Olsen, M. Rother, T. Sabaka, A. Thomson, T. Zvereva, The 10th-generation international geomagnetic reference field. Geophys. J. Int. **161**, 561–565 (2005). doi:10.1111/j.1365-246X.2005.02641.x

S. Maus, L. Silva, G. Hulot, Can core-surface flow models be used to improve the forecast of the Earth's main magnetic field? J. Geophys. Res. **113**, B08102 (2008). doi:10.1029/2007JB005199

S. Maus, L. Silva, G. Hulot, Reply to comment by V. Lesur et al. on "Can core-surface flow models be used to improve the forecast of the Earth's main magnetic field". J. Geophys. Res. **114**, B04105 (2009). doi:10.1029/2008JB006242

H. Meyers, W.M. Davis, A profile of the geomagnetic model users and abusers. J. Geomagn. Geoelectr. **42**(9), 1079–1085 (1990)

R.N. Miller, M. Ghil, F. Gauthiez, Advanced data assimilation in strongly nonlinear dynamical systems. J. Atmos. Sci. **51**(8), 1037–1056 (1994). doi:10.1175/1520-0469(1994)051<1037:ADAISN>2.0.CO;2

R. Monchaux, M. Berhanu, M. Bourgoin, M. Moulin, P. Odier, J.F. Pinton, R. Volk, S. Fauve, N. Mordant, F. Pétrélis, et al., Generation of a magnetic field by dynamo action in a turbulent flow of liquid sodium. Phys. Rev. Lett. **98**(4), 044502 (2007). doi:10.1103/PhysRevLett.98.044502

H.C. Nataf, T. Alboussière, D. Brito, P. Cardin, N. Gagnière, D. Jault, J.P. Masson, D. Schmitt, Experimental study of super-rotation in a magnetostrophic spherical Couette flow. Geophys. Astrophys. Fluid Dyn. **100**, 281–298 (2006). doi:10.1080/03091920600718426

N. Olsen, M. Mandea, Rapidly changing flows in the earth's core. Nat. Geosci. **1**, 390–394 (2008). doi:10.1038/ngeo203

N. Olsen, R. Holme, G. Hulot, T. Sabaka, T. Neubert, L. Tøffner-Clausen, F. Primdahl, J. Jørgensen, J. Léger, D. Barraclough, J. Bloxham, J. Cain, C. Constable, V. Golovkov, A. Jackson, P. Kotze, B. Langlais, S. Macmillan, M. Mandea, J. Merayo, L. Newitt, M. Purucker, T. Risbo, M. Stampe, A. Thomson, C. Voorhies, Ørsted initial field model. Geophys. Res. Lett. **27**(22), 3607–3610 (2000). doi:10.1029/2000GL011930

N. Olsen, H. Lühr, T.J. Sabaka, M. Mandea, M. Rother, L. Tøffner-Clausen, S. Choi, CHAOS-a model of the Earth's magnetic field derived from CHAMP, Ørsted, and SAC-C magnetic satellite data. Geophys. J. Int. **166**(1), 67–75 (2006). doi:10.1111/j.1365-246X.2006.02959.x

N. Olsen, M. Mandea, T. Sabaka, L. Tøffner-Clausen, CHAOS-2—a geomagnetic field model derived from one decade of continuous satellite data. Geophys. J. Int. **179**(3), 1477–1487 (2009). doi:10.1111/j.1365-246X.2009.04386.x

A. Pais, G. Hulot, Length of day decade variations, torsional oscillations and inner core superrotation: evidence from recovered core surface zonal flows. Phys. Earth Planet. Inter. **118**(3–4), 291–316 (2000). doi:10.1016/S0031-9201(99)00161-2

T. Penduff, P. Brasseur, C. Testut, B. Barnier, J. Verron, A four-year eddy-permitting assimilation of sea-surface temperature and altimetric data in the South Atlantic Ocean. J. Mar. Res. **60**(6), 805–833 (2002). doi:10.1357/002224002321505147

K. Pinheiro, A. Jackson, Can a 1-D mantle electrical conductivity model generate magnetic jerk differential time delays? Geophys. J. Int. **173**(3), 781–792 (2008). doi:10.1111/j.1365-246X.2008.03762.x

L.F. Richardson, *Weather Prediction by Numerical Process* (Cambridge University Press, Cambridge, 1922)

P.H. Roberts, S. Scott, On analysis of the secular variation. J. Geomagn. Geoelectr. **17**(2), 137–151 (1965)

T. Sabaka, N. Olsen, M. Purucker, Extending comprehensive models of the Earth's magnetic field with Ørsted and CHAMP data. Geophys. J. Int. **159**(2), 521–547 (2004). doi:10.1111/j.1365-246X.2004.02421.x

A. Sakuraba, P.H. Roberts, Generation of a strong magnetic field using uniform heat flux at the surface of the core. Nat. Geosci. **2**, 802–805 (2009). doi:10.1038/ngeo643

M. Sambridge, P. Rickwood, N. Rawlinson, S. Sommacal, Automatic differentiation in geophysical inverse problems. Geophys. J. Int. **170**(1), 1–8 (2007). doi:10.1111/j.1365-246X.2007.03400.x

Y. Sasaki, Some basic formalisms in numerical variational analysis. Mon. Weather Rev. **98**(12), 875–883 (1970). doi:10.1175/1520-0493(1970)098<0875:SBFINV>2.3.CO;2

L. Scherliess, R.W. Schunk, J.J. Sojka, D.C. Thompson, L. Zhu, Utah State University Global Assimilation of Ionospheric Measurements Gauss-Markov Kalman filter model of the ionosphere: Model description and validation. J. Geophys. Res. **111**, A11315 (2006). doi:10.1029/2006JA011712

D. Schmitt, T. Alboussière, D. Brito, P. Cardin, N. Gagnière, D. Jault, H.C. Nataf, Rotating spherical Couette flow in a dipolar magnetic field: experimental study of magneto-inertial waves. J. Fluid Mech. **604**, 175–197 (2008). doi:10.1017/S0022112008001298

Z. Sun, A. Tangborn, W. Kuang, Data assimilation in a sparsely observed one-dimensional modeled MHD system. Nonlinear Process. Geophys. **14**(2), 181–192 (2007)

F. Takahashi, M. Matsushima, Y. Honkura, Scale variability in convection-driven mhd dynamos at low Ekman number. Phys. Earth Planet. Inter. **167**, 168–178 (2008). doi:10.1016/j.pepi.2008.03.005

O. Talagrand, The use of adjoint equations in numerical modelling of the atmospheric circulation, in *Automatic Differentiation of Algorithms: Theory, Implementation, and Application*, ed. by A. Griewank, G.G. Corliss. (Society for Industrial and Applied Mathematics, Philadelphia, 1991), pp. 169–180

O. Talagrand, Assimilation of observations, an introduction. J. Meteorol. Soc. Jpn. **75**(1B), 191–209 (1997)

O. Talagrand, A posteriori validation of assimilation algorithms, in *Data Assimilation for the Earth System*, ed. by R. Swinbank, V. Shutyaev, W. Lahoz. (Kluwer Academic, Dordrecht, 2003), pp. 85–95

O. Talagrand, P. Courtier, Variational assimilation of meteorological observations with the adjoint vorticity equation. I: Theory. Q. J. R. Meteorol. Soc. **113**(478), 1311–1328 (1987). doi:10.1002/gj.49711347812

A. Tarantola, Inversion of seismic reflection data in the acoustic approximation. Geophysics **49**(8), 1259–1266 (1984). doi:10.1190/1.1441754

A. Tarantola, Theoretical background for the inversion of seismic waveforms including elasticity and attenuation. Pure Appl. Geophys. **128**(1), 365–399 (1988). doi:10.1007/BF01772605

J.B. Taylor, The magneto-hydrodynamics of a rotating fluid and the earth's dynamo problem. Proc. R. Soc. Lond. Ser. A, Math. Phys. Sci. **274**(1357), 274–283 (1963)

E. Thébault, A. Chulliat, S. Maus, G. Hulot, B. Langlais, A. Chambodut, M. Menvielle, IGRF candidate models at times of rapid changes in core field acceleration. Earth Planets Space (2010). doi:10.5047/eps.2010.05.004

Y. Trémolet, Accounting for an imperfect model in 4D-Var. Q. J. R. Meteorol. Soc. **132**(621), 2483–2504 (2006). doi:10.1256/qj.05.224

J. Tromp, C. Tape, Q. Liu, Seismic tomography, adjoint methods, time reversal and banana-doughnut kernels. Geophys. J. Int. **160**(1), 195–216 (2005). doi:10.1111/j.1365-246X.2004.02453.x

J. Tromp, D. Komatitsch, Q. Liu, Spectral-element and adjoint methods in seismology. Commun. Comput. Phys. **3**, 1–32 (2008)

N.A. Tsyganenko, M.I. Sitnov, Magnetospheric configurations from a high-resolution data-based magnetic field model. J. Geophys. Res. **112**, A06225 (2007). doi:10.1029/2007JA012260

F. Uboldi, M. Kamachi, Time-space weak-constraint data assimilation for nonlinear models. Tellus A **52**(4), 412–421 (2000). doi:10.1034/j.1600-0870.2000.00878.x

R. Waddington, D. Gubbins, N. Barber, Geomagnetic field analysis-V. Determining steady core-surface flows directly from geomagnetic observations. Geophys. J. Int. **122**(1), 326–350 (1995). doi:10.1111/j.1365-246X.1995.tb03556.x

P. Wessel, W.H.F. Smith, Free software helps map and display data. Trans. Am. Geophys. Union **72**, 441–445 (1991). doi:10.1029/90EO00319

K. Whaler, D. Gubbins, Spherical harmonic analysis of the geomagnetic field: an example of a linear inverse problem. Geophys. J. R. Astron. Soc. **65**(3), 645–693 (1981). doi:10.1111/j.1365-246X.1981.tb04877.x

C. Wunsch, *Discrete Inverse and State Estimation Problems* (Cambridge University Press, Cambridge, 2006)

Part IV

Computer labs

Lab 1

Lorenz's (1963) model: forward modelling

Very special thanks to Matthias Morzfeld (math.lbl.gov/~mmo) for making this lab (and the next) possible.

1.1 Introduction

A good understanding of the forward model is mandatory before any practice of data assimilation. The goal of this first lab is to get familiar with the numerical model we will deal with in the practicals. The model we are interested in is the famous model proposed by Edward Lorenz (1963). This model is the canonical example of a set of coupled deterministic, nonlinear, ordinary differential equations (ode) able to exhibit chaotic behaviour. It is an admittedly simplified, 3-variable representation of atmospheric cellular convection, based on the earlier work of Saltzman (1962). The state vector $\mathbf{x}$ has only three components $\mathbf{x} \equiv [X, Y, Z]^T$. Its time evolution is governed by the following set of nondimensional equations

$$\frac{\mathrm{d}X}{\mathrm{d}t} = -\mathrm{Pr}(X - Y), \tag{1.1}$$

$$\frac{\mathrm{d}Y}{\mathrm{d}t} = -XZ + \mathrm{r}X - Y, \tag{1.2}$$

$$\frac{\mathrm{d}Z}{\mathrm{d}t} = XY - bZ, \tag{1.3}$$

which has to be supplemented with a (column) vector of initial conditions

$$\mathbf{x}_0 = [X(t=0), Y(t=0), Z(t=0)]^T .$$

The variable X is connected with the streamfunction describing atmospheric flow, while both variables Y and Z are connected with the temperature deviation responsible for convection (for further details, please consult Lorenz (1963) – a great read, see appendix B). So the state of atmospheric quiescence (no convection) is described by $\mathbf{x} = [0, 0, 0]^T$. Three nondimensional numbers define the parameter space

- Pr, the Prandtl number, which is the ratio of kinematic viscosity to thermal diffusivity
- r, which is the ratio of the Rayleigh number Ra to the critical value of the Rayleigh number Ra_c (in convection parlance, r tells you how many times supercritical the system is).

- b, which is a geometrical factor.

(Note that time had been non-dimensionalized using the thermal diffusion timescale as the timescale of reference.) In what follows, we will first stick to Lorenz's original choice, and pick

$$\mathrm{Pr} = 10, \tag{1.4}$$
$$\mathrm{r} = 28, \tag{1.5}$$
$$b = 8/3. \tag{1.6}$$

1.2 Forward integration

The previous set of equations is integrated numerically using a standard explicit integration scheme, known as the explicit Runge-Kutta scheme of order 4 (aka RK4). This means in practice that the time axis is discretized, being divided into segments of width Δt; 4th order accuracy means that the error characterizing this numerical approximation is proportionnal to Δt^4 [1].

As an initial condition, we will begin by using Lorenz's initial choice

$$\mathbf{x}_0 = [0, 1, 0]^T, \tag{1.7}$$

which is a slight departure from a state of atmospheric rest.

Q1: The matlab code `lab1_runq1.m` reads in a file called `inparam_lab1_q1`,in which the initial condition and time step size Δt are specified. It integrates Lorenz's model for 30 nondimensional time units and plots the variations of X, Y, and Z. Edit the `inparam_lab1_q1.m` file in order to specify the initial condition (1.7), letting Δt equal to its value 0.01. Run the code. Compare what you get for $Y(t)$ with Fig. (1) of Lorenz (1963). Comment.

Q2: Now let us look more precisely on the impact of the value of Δt on the solution obtained. We want to estimate what value of Δt is necessary to ensure stability and, more importantly, convergence. We will proceed in a simple trial and error fashion. The matlab code `lab1_runq2.m` reads in a file called `inparam_lab1_q2.m`, which contains three different values of Δt. It computes the three dynamical trajectories and plots them on top of each other. Figure 1.1 shows a screenshot of the results I obtained (using octave, matlab's opensource cousin). Use this code to determine empirically the largest value of Δt (denoted by $\Delta t_{\max}$), which ensures adequate numerical convergence. Empirically means that over the time window of integration, the trajectories obtained using $\Delta t_{\max}$ and a comparatibely smaller value of Δt look alike when compared on the screen.

Q3: We now want to estimate how $\Delta t_{\max}$ is sensitive to the vigor of convection, which is controlled by the Rayleigh number r. The parameter file `inparam_lab1_q3.m` allows you to set the value of r along with (again) three different values of the $\Delta t_{\max}$. The `lab1_runq3.m` script integrates the model for each value of Δt (using the initial condition (1.7)) and plots the corresponding trajectories. Use this tool to fill the following table

r	28	40	56
$\Delta t_{\max}$			

Is there a scaling law relating $\Delta t_{\max}$ to r? In other words, are the results you found compatible with a law of the form

$$\Delta t_{\max} \propto \mathrm{r}^{\alpha},$$

in which α is a (real) exponent? Try to find α. A caveat here: 3 points is certainly not enough to find a robust estimate, but we do not want to spend to much time on this. I will leave it up to you to perform a more systematic study if you feel so inclined.

[1] A good and concise introduction to time integration can be found in appendix D of Canuto et al. (2006)

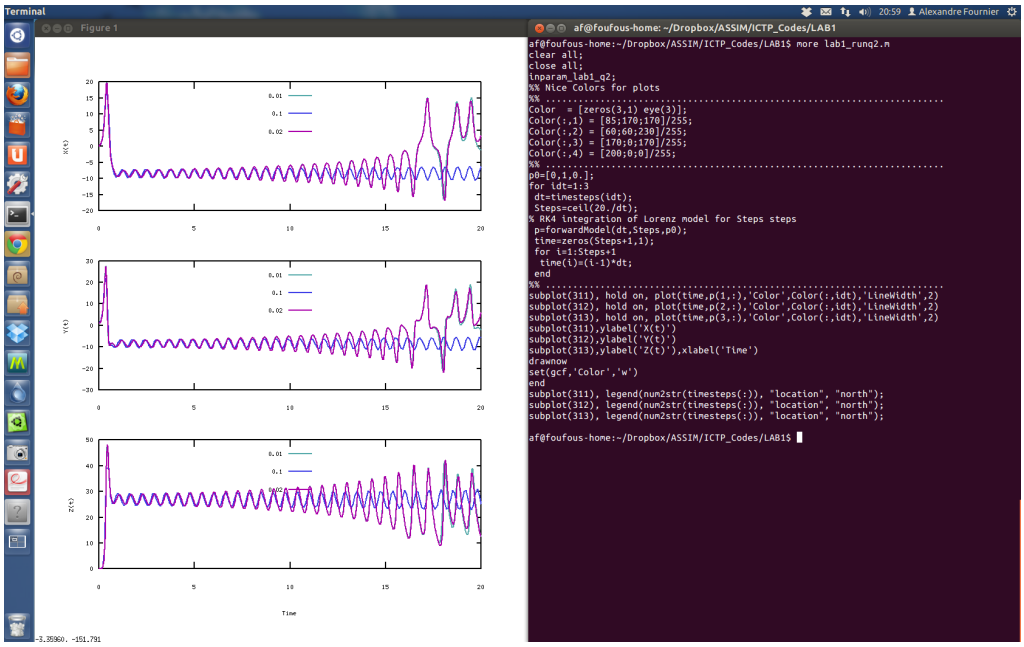

Figure 1.1: A screenshot obtained after using the `lab1_runq2` matlab command.

1.3 Sensitivity to initial conditions

Q4: Let us now consider the sensitivity of the model to the initial conditions, $\mathbf{x}_0$. We use the following parameters

$$\mathrm{Pr} = 10, \tag{1.8}$$
$$\mathrm{r} = 35, \tag{1.9}$$
$$b = 8/3. \tag{1.10}$$

(Following the previous question, Δt is set to an admissible value in the code - you do not have to worry about it.) The `lab1_runq4.m` script reads in the value of two different initial conditions, $\mathbf{x}_0^{(1)}$ and $\mathbf{x}_0^{(2)}$, in the `inparam_lab1_q4.m` file. The two solutions, $\mathbf{x}^{(1)}(t)$ and $\mathbf{x}^{(2)}(t)$, are computed, and superimposed on the left panel of a plot. On the right panel, the difference between the two solutions, is plotted versus time, on a log – log plot, for each component of the state vector. Fix the value of $\mathbf{x}_0^{(1)}$ to Lorenz's choice, and choose $\mathbf{x}_0^{(2)}$ close to $\mathbf{x}_0^{(1)}$ (by close we mean that the difference between the two must be much smaller than 1, which corresponds to a macroscopic difference). Run the `lab1_runq4.m` script and describe what you observe.

The sensitivity to the initial condition has important consequences, since we never have perfect knowledge of the state of the system we are interested in. The uncertainty in the knowledge is what imposes **a limit of predictability** on dynamical systems (similar to the Lorenz's model) governed by equations capable of generating chaotic dynamics, even though those dynamics are deterministic. An example is the Earth's atmosphere: we do not have perfect knowledge of the state of the atmosphere, and we can not make a good weather prediction above a limit which is now on the order of 5 days (for an account of the progress of operational numerical weather prediction over the past few decades, read the first chapter of Kalnay (2003).)

Lab 2

Application of the ensemble Kalman filter (EnKF) to Lorenz's 1963 model

The goal of this lab is to get familiar with the working of a sequential assimilation scheme running a so-called twin experiment: A true, reference model trajectory $\mathbf{x}_i^t$ is generated, and is used to construct a catalog of synthetic observations. These observations are then assimilated in order to correct a second model trajectory, which differs from the first one (the true one). In our case it will differ because we will assume a different initial condition, $\mathbf{x}_0 \neq \mathbf{x}_0^t$.

Twin experiments (also called OSSE, Observing System Assimilation Experiments) are a logical first step when implementing an assimilation scheme, since they allow to develop an understanding for the behaviour of the scheme, without the additional complexity which may arise from the inability of the forward model to represent some of the physics expressed in the observations. Today we will run these twin experiments using Lorenz (1963) model, and we will resort to the ensemble Kalman filter, as described in Sect. 3.3.4.2.

2.1 Statistical ingredients

We need to begin by specifying the statistical bits of information needed by the scheme, in the form of the covariance matrices $\mathbf{P}^b$ and $\mathbf{R}$ of background and observation error, respectively. Since we are dealing with the EnKF here, $\mathbf{P}^b$ is not really explicitly needed, since the knowledge of the ensemble is sufficient to compute the statistical moments of the distribution it aims at representing. The ensemble comprises N_e members.

2.1.1 Model

On the account of our perfect control of both the physics we are interested in and its numerical approximation (thanks to lab1), we will neglect modelling errors (as introduced for the first time in the notes in Eq. 1.15)

$$\boldsymbol{\eta} = \mathbf{0}. \tag{2.1}$$

Again, the knowledge of each ensemble member $\mathbf{x}_{i,e}$, $e \in \{1, \ldots, N_e\}$, at any discrete time t_i suffices to compute the mean and covariances, according to

$$\langle \mathbf{x}_i \rangle = \frac{1}{N_e} \sum_{e=1}^{N_e} \mathbf{x}_{i,e}, \tag{2.2}$$

$$\mathbf{P}_i = \frac{1}{N_e - 1} \sum_{e=1}^{N_e} \left(\mathbf{x}_{i,e} - \langle \mathbf{x}_i \rangle \right) \left(\mathbf{x}_{i,e} - \langle \mathbf{x}_i \rangle \right)^T. \tag{2.3}$$

To initialize our EnKF, we have to choose N_e and specify the Gaussian distribution $\mathcal{N}(\mathbf{x}_0, \mathbf{P}_0)$ that the various members of the ensemble will follow. To keep things simple we will assume a diagonal $\mathbf{P}_0$ having uniform variance σ_{ens}. The initial mean $\mathbf{x}_0$ is not a priori the true initial condition, $\mathbf{x}_0^t$.

2.1.2 Observations

The true (reference) trajectory $\mathbf{x}_i^t$ is used to generate observations. The state vector in the Lorenz's model comprises 3 variables, X, Y, and Z (recall Equations (1.1)–(1.3)). Depending on the questions that you will find below, the observation of the system will be either complete or partial (restricted to one of the variables).

Observations are made every ΔT_{obs} in time. This value (which we will be able to specify) controls the frequency at which observations are made, and information brought into the system. It can imply success or failure of the assimilation process.

2.2 Algorithm

2.2.1 Preparation of data

In this lab, all the parameters are defined in `inparam_lab2.m`.

We set the duration of the experiment (`duration` in matlab) to a value $T = 20$ non-dimensional time units. We use the following parameters

$$\text{Pr} = 10, \tag{2.4}$$

$$\text{r} = 35, \tag{2.5}$$

$$b = 8/3, \tag{2.6}$$

and the following 'true' initial condition

$$\mathbf{x}_0 = [0, 2, 0]^T.$$

The specification of the standard deviation of the observation error σ_{obs} allows us to generate observations on-the-fly, while computing the sequence of $\mathbf{x}_i^t$, by the now well-known formula

$$\mathbf{y}_i^o = \mathbf{H}\mathbf{x}_i^t + \boldsymbol{\epsilon}_i^o, \tag{2.7}$$

in which every component ϵ_i^o of the vector of size $\boldsymbol{\epsilon}_i^o$ is drawn randomly following a normal distribution with zero mean and standard deviation σ_{obs}.

The observation operator $\mathbf{H}$ is a rectangular 3×3 matrix, whose exact shape depends on the components of $\mathbf{x}$ which are effectively observed.

Here is what `inparam_lab2.m` looks like :

```
%% parameters for lab2 (EnKF applied to the Lorenz model)
%% .....................................................................
dtobs = 1; % time between observations
WhichVariablesAreObserved = [1 0 1];
                     % Determines which variables are available to
                     % the EnKF. For example:
                     % WhichVariablesAreObserved = [1 1 1];
                     % means: X, Y, Z are observed
                     % WhichVariablesAreObserved = [1 0 1];
                     % means: X and Z are observed
                     % WhichVariablesAreObserved = [1 0 0];
                    % means: X is observed
sigobs = sqrt(8);  % standard deviation of the observation noise
%Initial mean for the ensemble
x0ens=[0,2,0];
%
sigens = 2;         % standard deviation of the ensemble
M = 50;             % Number of ensemble members
WhatToPlot = [1 1 1]; % Determines what to plot when applying the EnKF
                      % For example:
                      % What to plot = [1 1 1] means:
                      % plot the truth, EnKF
                      % reconstruction and the data.
                      %
                      % What to plot = [1 1 0] means:
                      % plot the truth, EnKF
                      % reconstruction.
%% .....................................................................
```

The last parameters listed have to do with the EnKF itself, but you can already play around with the first parameters, and see how they affect the reference trajectory and the database of synthetic observations that will be generated. To do so, please run the `lab2_demo.m` script. What will be displayed will be the reference dynamical trajectory, and the catalog of synthetic observations. An example of a screenschot is shown in Fig. 2.1.

2.3 Application of the EnKF

In `inparam_lab2.m`, you can edit the value of the initial condition `x0ens`, $\mathbf{x}_0$: this is the mean value about which the N_e members of the ensemble will be generated (drawn for a normal distribution characterized by a diagonal covariance matrix $\mathbf{P}_0$, with diagonal variance equal to $\sigma^2_{\rm obs}$).

The script `lab2_runenkf.m` does everything for you: it uses what is in `inparam_lab2` to generate the true trajectory, the set of observations, the initial ensemble and its evolution with time. Any time observations are present, the analysis step of the EnKF is performed.

A final plot allows you to judge visually of the quality of the job done by the EnKF, the mean of the ensemble $\langle \mathbf{x} \rangle$ being plotted againt the truth, $\mathbf{x}^t$. In addition, once you have run the `lab2_runenkf.m` script, you can also use the `lab2_plotdiff` command which will create a second figure showing the difference

$$\mathbf{x} - \langle \mathbf{x} \rangle (\text{EnKF})$$

as a function of time. Finally, the `lab2_rmsdiff.m` command returns the value of the root mean

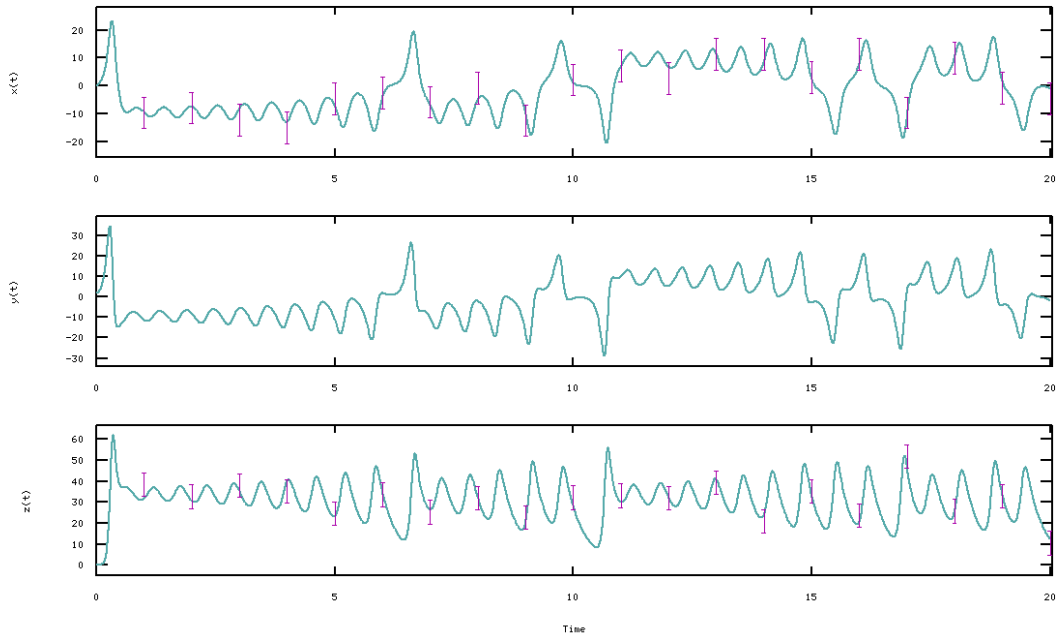

Figure 2.1: A screenshot of what I obtained running the `lab2_demo.m` script with the following parameters: $\Delta T_{\text{obs}} = 1$ nondimensional time unit, $\sigma_{\text{obs}} = \sqrt{8}$ (why not?) and `WhichVariablesAreObserved = [1 0 1]` (meaning that only X and Z are observed). The observations plotted with their error bars are going to be used subsequently by the ensemble Kalman filter.

squared difference between the truth and the EnKF estimate over the $[0, T]$ window, defined as

$$\left\{ \frac{1}{T} \int_0^T \left[\left(X^t - \langle X \rangle_{\text{EnKF}} \right)^2 + \left(Y^t - \langle Y \rangle_{\text{EnKF}} \right)^2 + \left(Z^t - \langle Z \rangle_{\text{EnKF}} \right)^2 \right] \mathrm{d}t \right\}^{1/2}.$$

You may find this indicator useful.

2.3.1 Influence of the quality of observations

In practice observations are always contaminated by errors. We begin by choosing the following parameters

```
dtobs = 0.5;% time between observations
WhichVariablesAreObserved = [1 1 1];
                    % Determines which variables are available to
                    % the EnKF. For example:
                    % WhichVariablesAreObserved = [1 1 1];
                    % means: X, Y, Z are observed
                    % WhichVariablesAreObserved = [1 0 1];
                    % means: X and Z are observed
                    % WhichVariablesAreObserved = [1 0 0];
                   % means: X is observed
sigobs = 5;  % standard deviation of the observation noise
%Initial mean for the ensemble
```

```
x0ens=[0,-5,0];
%
sigens = 2   ;        % standard deviation of the ensemble
M = 20;               % Number of ensemble members
WhatToPlot = [1 1 1]; % Determines what to plot when applying the EnKF
```

in the `inparam_lab2` file. The fact that `x0ens=[0,-5,0]` means in particular that our guess for the initial condition is 'suboptimal'.

Q1: All other parameters remaining constant, find the maximum value of σ_{obs} which leads to an acceptable behaviour of the EnKF (define what you would consider an acceptable behaviour of the EnKF).

2.3.2 Influence of the frequency of observations

Q2: Now with all other parameters remaining constant (σ_{obs} being equal to the value you just found), find the largest value of ΔT_{obs} which leads to an acceptable behaviour of the EnKF.

Q3: Is there a connection between this value and the typical time scale of the dynamics of the model?

2.3.3 Influence of the portion of the state vector observed

Set ΔT_{obs} to half the maximum value you just found. Keeping all the other parameter constant, assume now that only X or Y is observed.

Q4: Comment on the quality of the EnKF estimate based on either option.

Q5: It may be that the quality of the results depend strongly on the variable which is observed (X or Y). Would you have an explanation for this, based on a simple analysis of the equations (1.1)–(1.3) which govern the dynamics of the L63 model?

2.3.4 Influence of the ensemble size

We now define `inparam_lab2.m` as such

```
dtobs = 1.;% time between observations
WhichVariablesAreObserved = [1 1 1];
                    % Determines which variables are available to
                    % the EnKF. For example:
                    % WhichVariablesAreObserved = [1 1 1];
                    % means: X, Y, Z are observed
                    % WhichVariablesAreObserved = [1 0 1];
                    % means: X and Z are observed
                    % WhichVariablesAreObserved = [1 0 0];
                   % means: X is observed
sigobs = 4;  % standard deviation of the observation noise
%Initial mean for the ensemble
x0ens=[0,-5,0];
%
sigens = 4   ;        % standard deviation of the ensemble
M = 15;               % Number of ensemble members
WhatToPlot = [1 1 1]; % Determines what to plot when applying the EnKF
```

Q5: All other parameters remaining constant, find the minimum number of elements of the ensemble which leads to a good behaviour of the EnKF.

Note: One could also use a Monte-Carlo sampling of the initial probability density of the state vector to represent a non-Gaussian density. The sampling converges rather slowly towards the sought pdf, like $N_e^{-1/2}$. This implies that for real problems rather large ensemble are required to avoid too big sampling errors (Evensen, 1994).

Bibliography

Canuto, C., M. Y. Hussaini, A. Quarteroni, and T. A. Zang, 2006: *Spectral methods: Fundamentals in Single Domains*. Scientific Computation, Springer, Berlin Heidelberg.

Evensen, G., 1994: Sequential data assimilation with a nonlinear quasi-geostrophic model using Monte Carlo methods to forecast error statistics. *Journal of Geophysical Research*, **99 (C5)**, 10 143–10 162, doi:10.1029/94JC00572.

Kalnay, E., 2003: *Atmospheric modeling, data assimilation, and predictability*. Cambridge University Press, Cambridge.

Lorenz, E. N., 1963: Deterministic Nonperiodic Flow. *Journal of the Atmospheric Sciences*, **20 (2)**, 130–141.

Saltzman, B., 1962: Finite amplitude free convection as an initial value problem–I. *Journal of the Atmospheric Sciences*, **19 (7)**, 329–341.

Part V

Appendix

Appendix A

Derivation of the discrete adjoint equation

This derivation is rather standard, and can be found in review papers and textbooks (Talagrand, 1997; Bennett, 2002; Wunsch, 2006), as well as in the thesis of Canet (2009), in the specific context of the geomagnetic secular variation. We start with the definition of the misfit function (Eq. (4.1)), expressed directly as a function of the initial condition $\mathbf{x}_0$

$$\mathcal{J}(\mathbf{x}_0) = \frac{1}{2}\left\{\sum_{i=0}^{n}\left[\mathcal{H}_i\mathbf{x}_i - \mathbf{y}_i^o\right]^T\mathbf{R}_i^{-1}\left[\mathcal{H}_i\mathbf{x}_i - \mathbf{y}_i^o\right] + \left[\mathbf{x}_0 - \mathbf{x}^b\right]^T\mathbf{P}^{b^{-1}}\left[\mathbf{x}_0 - \mathbf{x}^b\right]\right\}, \tag{A.1}$$

in which $\mathbf{x}_i = \mathcal{M}_{i,i-1}\cdots\mathcal{M}_{1,0}\mathbf{x}_0$. Any infinitesimal change $\delta\mathbf{x}_0$ in the initial condition $\mathbf{x}_0$ will result in a change in $\mathbf{x}_i$, $\delta\mathbf{x}_i$, which writes to first order

$$\delta\mathbf{x}_i = \mathbf{M}_{i,i-1}\cdots\mathbf{M}_{1,0}\delta\mathbf{x}_0, \tag{A.2}$$

or, in a more compact form,

$$\delta\mathbf{x}_i = \left[\prod_{j=i}^{j=1}\mathbf{M}_{j,j-1}\right]\delta\mathbf{x}_0, \tag{A.3}$$

where $\mathbf{M}_{j,j-1}$ is the tangent linear operator, the Jacobian matrix of local partial derivatives of the components of $\mathbf{x}_j$ with respect to those of $\mathbf{x}_{j-1}$. Introducing in a similar manner the tangent linear approximation $\mathbf{H}_i$ of the observation operator $\mathcal{H}_i$, we find that a change in the initial condition $\delta\mathbf{x}_0$ results in a variation of the objective function $\delta\mathcal{J}$ given by

$$\begin{aligned}\delta\mathcal{J} &= \frac{1}{2}\left\{\sum_{i=0}^{n}\delta\mathbf{x}_i^T\mathbf{H}_i^T\mathbf{R}_i^{-1}\left[\mathcal{H}_i\mathbf{x}_i - \mathbf{y}_i^o\right] + \sum_{i=0}^{n}\left[\mathcal{H}_i\mathbf{x}_i - \mathbf{y}_i^o\right]^T\mathbf{R}_i^{-1}\mathbf{H}_i\delta\mathbf{x}_i\right\} \\ &+ \frac{1}{2}\left\{\delta\mathbf{x}_0^T\mathbf{P}^{b^{-1}}\left[\mathbf{x}_0 - \mathbf{x}^b\right] + \left[\mathbf{x}_0 - \mathbf{x}^b\right]^T\mathbf{P}^{b^{-1}}\delta\mathbf{x}_0\right\}.\end{aligned} \tag{A.4}$$

Because of the symmetry of both $\mathbf{R}$ and $\mathbf{P}^b$, it is easy to show that

$$\delta\mathbf{x}_i^T\mathbf{H}_i^T\mathbf{R}_i^{-1}\left[\mathcal{H}_i\mathbf{x}_i - \mathbf{y}_i^o\right] = \left[\mathcal{H}_i\mathbf{x}_i - \mathbf{y}_i^o\right]^T\mathbf{R}_i^{-1}\mathbf{H}_i\delta\mathbf{x}_i \tag{A.5}$$

and that

$$\delta\mathbf{x}_0^T\mathbf{P}^{b^{-1}}\left[\mathbf{x}_0 - \mathbf{x}^b\right] = \left[\mathbf{x}_0 - \mathbf{x}^b\right]^T\mathbf{P}^{b^{-1}}\delta\mathbf{x}_0. \tag{A.6}$$

Using these two equalities along with the compact notation introduced in Eq. (A.3) yields

$$\delta\mathcal{J} = \left\{ \sum_{i=0}^{n} \left[\mathcal{H}_i \mathbf{x}_i - \mathbf{y}_i^o\right]^T \mathbf{R}_i^{-1} \mathbf{H}_i \prod_{j=i}^{j=1} \mathbf{M}_{j,j-1} \delta\mathbf{x}_0 \right\} + \left[\mathbf{x}_0 - \mathbf{x}^b\right]^T \mathbf{P}^{b^{-1}} \delta\mathbf{x}_0. \tag{A.7}$$

Reminding ourselves that $\boldsymbol{\nabla}_{\mathbf{x}_0}\mathcal{J}$ (a row vector) is defined by $\delta\mathcal{J} = \boldsymbol{\nabla}_{\mathbf{x}_0}\mathcal{J}\mathbf{x}_0$, we see that

$$\boldsymbol{\nabla}_{\mathbf{x}_0}\mathcal{J} = \left\{ \sum_{i=0}^{n} \left[\mathcal{H}_i \mathbf{x}_i - \mathbf{y}_i^o\right]^T \mathbf{R}_i^{-1} \mathbf{H}_i \prod_{j=i}^{j=1} \mathbf{M}_{j,j-1} \right\} + \left[\mathbf{x}_0 - \mathbf{x}^b\right]^T \mathbf{P}^{b^{-1}}. \tag{A.8}$$

A correction (update) of the initial condition will require to take the transpose of this row vector

$$\boldsymbol{\nabla}_{\mathbf{x}_0}\mathcal{J}^T = \left\{ \sum_{i=0}^{n} \prod_{j=1}^{j=i} \mathbf{M}_{j,j-1}^T \mathbf{H}_i^T \mathbf{R}_i^{-1} \left[\mathcal{H}_i \mathbf{x}_i - \mathbf{y}_i^o\right] \right\} + \mathbf{P}^{b^{-1}} \left[\mathbf{x}_0 - \mathbf{x}^b\right]. \tag{A.9}$$

Let us rewrite this equation in the more inductive following form

$$\begin{aligned} \boldsymbol{\nabla}_{\mathbf{x}_0}\mathcal{J}^T &= \mathbf{M}_{0,1}^T \left\{ \mathbf{M}_{1,2}^T \left[\cdots \left[\mathbf{M}_{n-1,n}^T \mathbf{H}_n^T \mathbf{R}_n^{-1} \left[\mathcal{H}_n \mathbf{x}_n - \mathbf{y}_n^o\right] \right] \cdots + \mathbf{H}_1^T \mathbf{R}_1^{-1} \left[\mathcal{H}_1 \mathbf{x}_1 - \mathbf{y}_1^o\right] \right] \right. \\ &+ \left. \mathbf{H}_0^T \mathbf{R}_0^{-1} \left[\mathcal{H}_0 \mathbf{x}_0 - \mathbf{y}_0^o\right] \right\} + \mathbf{P}^{b^{-1}} \left[\mathbf{x}_0 - \mathbf{x}^b\right]. \end{aligned} \tag{A.10}$$

If one introduces the auxiliary adjoint field $\mathbf{a}_i$, subject to the terminal condition $\mathbf{a}_{n+1} = \mathbf{0}$, and whose backward time evolution is governed by

$$\mathbf{a}_{i-1} = \mathbf{M}_{i-1,i}^T \mathbf{a}_i + \mathbf{H}_{i-1}^T \mathbf{R}_{i-1}^{-1} (\mathcal{H}_{i-1}\mathbf{x}_{i-1} - \mathbf{y}_{i-1}^o) + \delta_{i1} \mathbf{P}^{b^{-1}} \left(\mathbf{x}_{i-1} - \mathbf{x}^b\right), \; n \geq i \geq 1, \tag{A.11}$$

the inductive form (A.10) shows why the column vector sought simply writes

$$\boldsymbol{\nabla}_{\mathbf{x}_0}\mathcal{J}^T = \mathbf{a}_0. \tag{A.12}$$

($\delta_{i1} = 1$ if $i = 1$, 0 otherwise.)

Appendix B

Lorenz 1963

Deterministic Nonperiodic Flow[1]

EDWARD N. LORENZ

Massachusetts Institute of Technology

(Manuscript received 18 November 1962, in revised form 7 January 1963)

ABSTRACT

Finite systems of deterministic ordinary nonlinear differential equations may be designed to represent forced dissipative hydrodynamic flow. Solutions of these equations can be identified with trajectories in phase space. For those systems with bounded solutions, it is found that nonperiodic solutions are ordinarily unstable with respect to small modifications, so that slightly differing initial states can evolve into considerably different states. Systems with bounded solutions are shown to possess bounded numerical solutions.

A simple system representing cellular convection is solved numerically. All of the solutions are found to be unstable, and almost all of them are nonperiodic.

The feasibility of very-long-range weather prediction is examined in the light of these results.

1. Introduction

Certain hydrodynamical systems exhibit steady-state flow patterns, while others oscillate in a regular periodic fashion. Still others vary in an irregular, seemingly haphazard manner, and, even when observed for long periods of time, do not appear to repeat their previous history.

These modes of behavior may all be observed in the familiar rotating-basin experiments, described by Fultz, *et al.* (1959) and Hide (1958). In these experiments, a cylindrical vessel containing water is rotated about its axis, and is heated near its rim and cooled near its center in a steady symmetrical fashion. Under certain conditions the resulting flow is as symmetric and steady as the heating which gives rise to it. Under different conditions a system of regularly spaced waves develops, and progresses at a uniform speed without changing its shape. Under still different conditions an irregular flow pattern forms, and moves and changes its shape in an irregular nonperiodic manner.

Lack of periodicity is very common in natural systems, and is one of the distinguishing features of turbulent flow. Because instantaneous turbulent flow patterns are so irregular, attention is often confined to the statistics of turbulence, which, in contrast to the details of turbulence, often behave in a regular well-organized manner. The short-range weather forecaster, however, is forced willy-nilly to predict the details of the large-scale turbulent eddies—the cyclones and anticyclones—which continually arrange themselves into new patterns. Thus there are occasions when more than the statistics of irregular flow are of very real concern.

In this study we shall work with systems of deterministic equations which are idealizations of hydrodynamical systems. We shall be interested principally in nonperiodic solutions, i.e., solutions which never repeat their past history exactly, and where all approximate repetitions are of finite duration. Thus we shall be involved with the ultimate behavior of the solutions, as opposed to the transient behavior associated with arbitrary initial conditions.

A closed hydrodynamical system of finite mass may ostensibly be treated mathematically as a finite collection of molecules—usually a very large finite collection—in which case the governing laws are expressible as a finite set of ordinary differential equations. These equations are generally highly intractable, and the set of molecules is usually approximated by a continuous distribution of mass. The governing laws are then expressed as a set of partial differential equations, containing such quantities as velocity, density, and pressure as dependent variables.

It is sometimes possible to obtain particular solutions of these equations analytically, especially when the solutions are periodic or invariant with time, and, indeed, much work has been devoted to obtaining such solutions by one scheme or another. Ordinarily, however, nonperiodic solutions cannot readily be determined except by numerical procedures. Such procedures involve replacing the continuous variables by a new finite set of functions of time, which may perhaps be the values of the continuous variables at a chosen grid of points, or the coefficients in the expansions of these variables in series of orthogonal functions. The governing laws then become a finite set of ordinary differential

[1] The research reported in this work has been sponsored by the Geophysics Research Directorate of the Air Force Cambridge Research Center, under Contract No. AF 19(604)-4969.

equations again, although a far simpler set than the one which governs individual molecular motions.

In any real hydrodynamical system, viscous dissipation is always occurring, unless the system is moving as a solid, and thermal dissipation is always occurring, unless the system is at constant temperature. For certain purposes many systems may be treated as conservative systems, in which the total energy, or some other quantity, does not vary with time. In seeking the ultimate behavior of a system, the use of conservative equations is unsatisfactory, since the ultimate value of any conservative quantity would then have to equal the arbitrarily chosen initial value. This difficulty may be obviated by including the dissipative processes, thereby making the equations nonconservative, and also including external mechanical or thermal forcing, thus preventing the system from ultimately reaching a state of rest. If the system is to be deterministic, the forcing functions, if not constant with time, must themselves vary according to some deterministic rule.

In this work, then, we shall deal specifically with finite systems of deterministic ordinary differential equations, designed to represent forced dissipative hydrodynamical systems. We shall study the properties of nonperiodic solutions of these equations.

It is not obvious that such solutions can exist at all. Indeed, in dissipative systems governed by finite sets of *linear* equations, a constant forcing leads ultimately to a constant response, while a periodic forcing leads to a periodic response. Hence, nonperiodic flow has sometimes been regarded as the result of nonperiodic or random forcing.

The reasoning leading to these concludions is not applicable when the governing equations are nonlinear. If the equations contain terms representing advection—the transport of some property of a fluid by the motion of the fluid itself—a constant forcing can lead to a variable response. In the rotating-basin experiments already mentioned, both periodic and nonperiodic flow result from thermal forcing which, within the limits of experimental control, is constant. Exact periodic solutions of simplified systems of equations, representing dissipative flow with constant thermal forcing, have been obtained analytically by the writer (1962a). The writer (1962b) has also found nonperiodic solutions of similar systems of equations by numerical means.

2. Phase space

Consider a system whose state may be described by M variables $X_1, \cdots, X_M$. Let the system be governed by the set of equations

$$dX_i/dt = F_i(X_1, \cdots X_M), \quad i = 1, \cdots, M, \tag{1}$$

where time t is the single independent variable, and the functions F_i possess continuous first partial derivatives. Such a system may be studied by means of *phase space*—an M-dimensional Euclidean space Γ whose coordinates are $X_1, \cdots, X_M$. Each *point* in phase space represents a possible instantaneous state of the system. A state which is varying in accordance with (1) is represented by a moving *particle* in phase space, traveling along a *trajectory* in phase space. For completeness, the position of a stationary particle, representing a steady state, is included as a trajectory.

Phase space has been a useful concept in treating finite systems, and has been used by such mathematicians as Gibbs (1902) in his development of statistical mechanics, Poincaré (1881) in his treatment of the solutions of differential equations, and Birkhoff (1927) in his treatise on dynamical systems.

From the theory of differential equations (e,g., Ford 1933, ch. 6), it follows, since the partial derivatives $\partial F_i/\partial X_j$ are continuous, that if t_0 is any time, and if $X_{10}, \cdots X_{M0}$ is any point in Γ, equations (1) possess a unique solution

$$X_i = f_i(X_{10}, \cdots, X_{M0}, t), \quad i = 1, \cdots, M, \tag{2}$$

valid throughout some time interval containing t_0, and satisfying the condition

$$f_i(X_{10}, \cdots, X_{M0}, t_0) = X_{i0}, \quad i = 1, \cdots, M. \tag{3}$$

The functions f_i are continuous in $X_{10}, \cdots, X_{M0}$ and t. Hence there is a unique trajectory through each point of Γ. Two or more trajectories may, however, approach the same point or the same curve asymptotically as $t \to \infty$ or as $t \to -\infty$. Moreover, since the functions f_i are continuous, the passage of time defines a continuous deformation of any region of Γ into another region.

In the familiar case of a conservative system, where some positive definite quantity Q, which may represent some form of energy, is invariant with time, each trajectory is confined to one or another of the surfaces of constant Q. These surfaces may take the form of closed concentric shells.

If, on the other hand, there is dissipation and forcing, and if, whenever Q equals or exceeds some fixed value Q_1, the dissipation acts to diminish Q more rapidly then the forcing can increase Q, then $(-dQ/dt)$ has a positive lower bound where $Q \geqq Q_1$, and each trajectory must ultimately become trapped in the region where $Q < Q_1$. Trajectories representing forced dissipative flow may therefore differ considerably from those representing conservative flow.

Forced dissipative systems of this sort are typified by the system

$$dX_i/dt = \sum_{j,k} a_{ijk} X_j X_k - \sum_j b_{ij} X_j + c_i, \tag{4}$$

where $\sum a_{ijk} X_i X_j X_k$ vanishes identically, $\sum b_{ij} X_i X_j$ is positive definite, and $c_1, \cdots, c_M$ are constants. If

$$Q = \tfrac{1}{2} \sum_i X_i^2, \tag{5}$$

and if $e_1, \cdots, e_M$ are the roots of the equations

$$\sum_j (b_{ij}+b_{ji})e_j = c_i, \tag{6}$$

it follows from (4) that

$$dQ/dt = \sum_{i,j} b_{ij}e_ie_j - \sum_{i,j} b_{ij}(X_i-e_i)(X_j-e_j). \tag{7}$$

The right side of (7) vanishes only on the surface of an ellipsoid E, and is positive only in the interior of E. The surfaces of constant Q are concentric spheres. If S denotes a particular one of these spheres whose interior R contains the ellipsoid E, it is evident that each trajectory eventually becomes trapped within R.

3. The instability of nonperiodic flow

In this section we shall establish one of the most important properties of deterministic nonperiodic flow, namely, its instability with respect to modifications of small amplitude. We shall find it convenient to do this by identifying the solutions of the governing equations with trajectories in phase space. We shall use such symbols as $P(t)$ (variable argument) to denote trajectories, and such symbols as P or $P(t_0)$ (no argument or constant argument) to denote points, the latter symbol denoting the specific point through which $P(t)$ passes at time t_0.

We shall deal with a phase space Γ in which a unique trajectory passes through each point, and where the passage of time defines a continuous deformation of any region of Γ into another region, so that if the points $P_1(t_0)$, $P_2(t_0)$, $\cdots$approach $P_0(t_0)$ as a limit, the points $P_1(t_0+\tau)$, $P_2(t_0+\tau)$, $\cdots$must approach $P_0(t_0+\tau)$ as a limit. We shall furthermore require that the trajectories be uniformly bounded as $t \to \infty$; that is, there must be a bounded region R, such that every trajectory ultimately remains with R. Our procedure is influenced by the work of Birkhoff (1927) on dynamical systems, but differs in that Birkhoff was concerned mainly with conservative systems. A rather detailed treatment of dynamical systems has been given by Nemytskii and Stepanov (1960), and rigorous proofs of some of the theorems which we shall present are to be found in that source.

We shall first classify the trajectories in three different manners, namely, according to the absence or presence of transient properties, according to the stability or instability of the trajectories with respect to small modifications, and according to the presence or absence of periodic behavior.

Since any trajectory $P(t)$ is bounded, it must possess at least one *limit point* P_0, a point which it approaches arbitrarily closely arbitrarily often. More precisely, P_0 is a limit point of $P(t)$ if for any $\epsilon>0$ and any time t_1 there exists a time $t_2(\epsilon,t_1)>t_1$ such that $|P(t_2)-P_0|<\epsilon$. Here absolute-value signs denote distance in phase space. Because Γ is continuously deformed as t varies, every point on the trajectory through P_0 is also a limit point of $P(t)$, and the set of limit points of $P(t)$ forms a trajectory, or a set of trajectories, called the *limiting trajectories* of $P(t)$. A limiting trajectory is obviously contained within R in its entirety.

If a trajectory is contained among its own limiting trajectories, it will be called *central*; otherwise it will be called *noncentral*. A central trajectory passes arbitrarily closely arbitrarily often to any point through which it has previously passed, and, in this sense at least, separate sufficiently long segments of a central trajectory are statistically similar. A noncentral trajectory remains a certain distance away from any point through which it has previously passed. It must approach its entire set of limit points asymptotically, although it need not approach any particular limiting trajectory asymptotically. Its instantaneous distance from its closest limit point is therefore a transient quantity, which becomes arbitrarily small as $t \to \infty$.

A trajectory $P(t)$ will be called *stable at a point* $P(t_1)$ if any other trajectory passing sufficiently close to $P(t_1)$ at time t_1 remains close to $P(t)$ as $t \to \infty$; i.e., $P(t)$ is stable at $P(t_1)$ if for any $\epsilon>0$ there exists a $\delta(\epsilon,t_1)>0$ such that if $|P_1(t_1)-P(t_1)|<\delta$ and $t_2>t_1$, $|P_1(t_2)-P(t_2)|<\epsilon$. Otherwise $P(t)$ will be called *unstable* at $P(t_1)$. Because Γ is continuously deformed as t varies, a trajectory which is stable at one point is stable at every point, and will be called a *stable* trajectory. A trajectory unstable at one point is unstable at every point, and will be called an *unstable* trajectory. In the special case that $P(t)$ is confined to one point, this definition of stability coincides with the familiar concept of stability of steady flow.

A stable trajectory $P(t)$ will be called uniformly stable if the distance within which a neighboring trajectory must approach a point $P(t_1)$, in order to be certain of remaining close to $P(t)$ as $t \to \infty$, itself possesses a positive lower bound as $t_1 \to \infty$; i.e., $P(t)$ is uniformly stable if for any $\epsilon>0$ there exists a $\delta(\epsilon)>0$ and a time $t_0(\epsilon)$ such that if $t_1>t_0$ and $|P_1(t_1)-P(t_1)|<\delta$ and $t_2>t_1$, $|P_1(t_2)-P(t_2)|<\epsilon$. A limiting trajectory $P_0(t)$ of a uniformly stable trajectory $P(t)$ must be uniformly stable itself, since all trajectories passing sufficiently close to $P_0(t)$ must pass arbitrarily close to some point of $P(t)$ and so must remain close to $P(t)$, and hence to $P_0(t)$, as $t \to \infty$.

Since each point lies on a unique trajectory, any trajectory passing through a point through which it has previously passed must continue to repeat its past behavior, and so must be *periodic*. A trajectory $P(t)$ will be called *quasi-periodic* if for some arbitrarily large time interval τ, $P(t+\tau)$ ultimately remains arbitrarily close to $P(t)$, i.e., $P(t)$ is quasi-periodic if for any $\epsilon>0$ and for any time interval τ_0, there exists a $\tau(\epsilon,\tau_0)>\tau_0$ and a time $t_1(\epsilon,\tau_0)$ such that if $t_2>t_1$, $|P(t_2+\tau)-P(t_2)|$

$<\epsilon$. Periodic trajectories are special cases of quasi-periodic trajectories.

A trajectory which is not quasi-periodic will be called *nonperiodic*. If $P(t)$ is nonperiodic, $P(t_1+\tau)$ may be arbitrarily close to $P(t_1)$ for some time t_1 and some arbitrarily large time interval τ, but, if this is so, $P(t+\tau)$ cannot remain arbitrarily close to $P(t)$ as $t \rightarrow \infty$. Nonperiodic trajectories are of course representations of deterministic nonperiodic flow, and form the principal subject of this paper.

Periodic trajectories are obviously central. Quasi-periodic central trajectories include multiple periodic trajectories with incommensurable periods, while quasi-periodic noncentral trajectories include those which approach periodic trajectories asymptotically. Nonperiodic trajectories may be central or noncentral.

We can now establish the theorem that a trajectory with a stable limiting trajectory is quasi-periodic. For if $P_0(t)$ is a limiting trajectory of $P(t)$, two distinct points $P(t_1)$ and $P(t_1+\tau)$, with τ arbitrarily large, may be found arbitrary close to any point $P_0(t_0)$. Since $P_0(t)$ is stable, $P(t)$ and $P(t+\tau)$ must remain arbitrarily close to $P_0(t+t_0-t_1)$, and hence to each other, as $t \rightarrow \infty$, and $P(t)$ is quasi-periodic.

It follows immediately that a stable central trajectory is quasi-periodic, or, equivalently, that a nonperiodic central trajectory is unstable.

The result has far-reaching consequences when the system being considered is an observable nonperiodic system whose future state we may desire to predict. It implies that two states differing by imperceptible amounts may eventually evolve into two considerably different states. If, then, there is any error whatever in observing the present state—and in any real system such errors seem inevitable—an acceptable prediction of an instantaneous state in the distant future may well be impossible.

As for noncentral trajectories, it follows that a uniformly stable noncentral trajectory is quasi-periodic, or, equivalently, a nonperiodic noncentral trajectory is not uniformly stable. The possibility of a nonperiodic noncentral trajectory which is stable but not uniformly stable still exists. To the writer, at least, such trajectories, although possible on paper, do not seem characteristic of real hydrodynamical phenomena. Any claim that atmospheric flow, for example, is represented by a trajectory of this sort would lead to the improbable conclusion that we ought to master long-range forecasting as soon as possible, because, the longer we wait, the more difficult our task will become.

In summary, we have shown that, subject to the conditions of uniqueness, continuity, and boundedness prescribed at the beginning of this section, a central trajectory, which in a certain sense is free of transient properties, is unstable if it is nonperiodic. A noncentral trajectory, which is characterized by transient properties, is not uniformly stable if it is nonperiodic, and, if it is stable at all, its very stability is one of its transient properties, which tends to die out as time progresses. In view of the impossibility of measuring initial conditions precisely, and thereby distinguishing between a central trajectory and a nearby noncentral trajectory, all nonperiodic trajectories are effectively unstable from the point of view of practical prediction.

4. Numerical integration of nonconservative systems

The theorems of the last section can be of importance only if nonperiodic solutions of equations of the type considered actually exist. Since statistically stationary nonperiodic functions of time are not easily described analytically, particular nonperiodic solutions can probably be found most readily by numerical procedures. In this section we shall examine a numerical-integration procedure which is especially applicable to systems of equations of the form (4). In a later section we shall use this procedure to determine a nonperiodic solution of a simple set of equations.

To solve (1) numerically we may choose an initial time t_0 and a time increment Δt, and let

$$X_{i,n}=X_i(t_0+n\Delta t). \tag{8}$$

We then introduce the auxiliary approximations

$$X_{i(n+1)}=X_{i,n}+F_i(P_n)\Delta t, \tag{9}$$

$$X_{i((n+2))}=X_{i(n+1)}+F_i(P_{(n+1)})\Delta t, \tag{10}$$

where P_n and $P_{(n+1)}$ are the points whose coordinates are

$$(X_{1,n},\cdots,X_{M,n}) \quad \text{and} \quad (X_{1(n+1)},\cdots,X_{M(n+1)}).$$

The simplest numerical procedure for obtaining approximate solutions of (1) is the forward-difference procedure,

$$X_{i,n+1}=X_{i(n+1)}. \tag{11}$$

In many instances better approximations to the solutions of (1) may be obtained by a centered-difference procedure

$$X_{i,n+1}=X_{i,n-1}+2F_i(P_n)\Delta t. \tag{12}$$

This procedure is unsuitable, however, when the deterministic nature of (1) is a matter of concern, since the values of $X_{1,n}, \cdots, X_{M,n}$ do not uniquely determine the values of $X_{1,n+1}, \cdots, X_{M,n+1}$.

A procedure which largely overcomes the disadvantages of both the forward-difference and centered-difference procedures is the double-approximation procedure, defined by the relation

$$X_{i,n+1}=X_{i,n}+\tfrac{1}{2}[F_i(P_n)+F_i(P_{(n+1)})]\Delta t. \tag{13}$$

Here the coefficient of Δt is an approximation to the time derivative of X_i at time $t_0+(n+\frac{1}{2})\Delta t$. From (9) and (10), it follows that (13) may be rewritten

$$X_{i,n+1}=\tfrac{1}{2}(X_{i,n}+X_{i((n+2))}). \tag{14}$$

A convenient scheme for automatic computation is the successive evaluation of $X_{i(n+1)}$, $X_{i((n+2))}$, and $X_{i,n+1}$ according to (9), (10) and (14). We have used this procedure in all the computations described in this study.

In phase space a numerical solution of (1) must be represented by a jumping particle rather than a continuously moving particle. Moreover, if a digital computer is instructed to represent each number in its memory by a preassigned fixed number of bits, only certain discrete points in phase space will ever be occupied. If the numerical solution is bounded, repetitions must eventually occur, so that, strictly speaking, every numerical solution is periodic. In practice this consideration may be disregarded, if the number of different possible states is far greater than the number of iterations ever likely to be performed. The necessity for repetition could be avoided altogether by the somewhat uneconomical procedure of letting the precision of computation increase as n increases.

Consider now numerical solutions of equations (4), obtained by the forward-difference procedure (11). For such solutions,

$$Q_{n+1}=Q_n+(dQ/dt)_n\Delta t+\tfrac{1}{2}\sum_i F_i^2(P_n)\Delta t^2. \quad (15)$$

Let S' be any surface of constant Q whose interior R' contains the ellipsoid E where dQ/dt vanishes, and let S be any surface of constant Q whose interior R contains S'.

Since $\sum F_i^2$ and dQ/dt both possess upper bounds in R', we may choose Δt so small that P_{n+1} lies in R if P_n lies in R'. Likewise, since $\sum F_i^2$ possesses an upper bound and dQ/dt possesses a *negative* upper bound in $R-R'$, we may choose Δt so small that $Q_{n+1}<Q_n$ if P_n lies in $R-R'$. Hence Δt may be chosen so small that any jumping particle which has entered R remains trapped within R, and the numerical solution does not blow up. A blow-up may still occur, however, if initially the particle is exterior to R.

Consider now the double-approximation procedure (14). The previous arguments imply not only that $P_{(n+1)}$ lies within R if P_n lies within R, but also that $P_{((n+2))}$ lies within R if $P_{(n+1)}$ lies within R. Since the region R is convex, it follows that P_{n+1}, as given by (14), lies within R if P_n lies within R. Hence if Δt is chosen so small that the forward-difference procedure does not blow up, the double-approximation procedure also does not blow up.

We note in passing that if we apply the forward-difference procedure to a conservative system where $dQ/dt=0$ everywhere,

$$Q_{n+1}=Q_n+\tfrac{1}{2}\sum_i F_i^2(P_n)\Delta t^2. \quad (16)$$

In this case, for any fixed choice of Δt the numerical solution ultimately goes to infinity, unless it is asymptotically approaching a steady state. A similar result holds when the double-approximation procedure (14) is applied to a conservative system.

5. The convection equations of Saltzman

In this section we shall introduce a system of three ordinary differential equations whose solutions afford the simplest example of deterministic nonperiodic flow of which the writer is aware. The system is a simplification of one derived by Saltzman (1962) to study finite-amplitude convection. Although our present interest is in the nonperiodic nature of its solutions, rather than in its contributions to the convection problem, we shall describe its physical background briefly.

Rayleigh (1916) studied the flow occurring in a layer of fluid of uniform depth H, when the temperature difference between the upper and lower surfaces is maintained at a constant value ΔT. Such a system possesses a steady-state solution in which there is no motion, and the temperature varies linearly with depth, If this solution is unstable, convection should develop.

In the case where all motions are parallel to the $x-z$-plane, and no variations in the direction of the y-axis occur, the governing equations may be written (see Saltzman, 1962)

$$\frac{\partial}{\partial t}\nabla^2\psi=-\frac{\partial(\psi,\nabla^2\psi)}{\partial(x,z)}+\nu\nabla^4\psi+g\alpha\frac{\partial\theta}{\partial x}, \quad (17)$$

$$\frac{\partial}{\partial t}\theta=-\frac{\partial(\psi,\theta)}{\partial(x,z)}+\frac{\Delta T}{H}\frac{\partial\psi}{\partial x}+\kappa\nabla^2\theta. \quad (18)$$

Here ψ is a stream function for the two-dimensional motion, θ is the departure of temperature from that occurring in the state of no convection, and the constants g, α, ν, and κ denote, respectively, the acceleration of gravity, the coefficient of thermal expansion, the kinematic viscosity, and the thermal conductivity. The problem is most tractable when both the upper and lower boundaries are taken to be free, in which case ψ and $\nabla^2\psi$ vanish at both boundaries.

Rayleigh found that fields of motion of the form

$$\psi=\psi_0\sin(\pi aH^{-1}x)\sin(\pi H^{-1}z), \quad (19)$$

$$\theta=\theta_0\cos(\pi aH^{-1}x)\sin(\pi H^{-1}z), \quad (20)$$

would develop if the quantity

$$R_a=g\alpha H^3\Delta T\nu^{-1}\kappa^{-1}, \quad (21)$$

now called the *Rayleigh number*, exceeded a critical value

$$R_c=\pi^4a^{-2}(1+a^2)^3. \quad (22)$$

The minimum value of R_c, namely $27\pi^4/4$, occurs when $a^2=\frac{1}{2}$.

Saltzman (1962) derived a set of ordinary differential equations by expanding ψ and θ in double Fourier series in x and z, with functions of t alone for coefficients, and

substituting these series into (17) and (18). He arranged the right-hand sides of the resulting equations in double-Fourier-series form, by replacing products of trigonometric functions of x (or z) by sums of trigonometric functions, and then equated coefficients of similar functions of x and z. He then reduced the resulting infinite system to a finite system by omitting reference to all but a specified finite set of functions of t, in the manner proposed by the writer (1960).

He then obtained time-dependent solutions by numerical integration. In certain cases all except three of the dependent variables eventually tended to zero, and these three variables underwent irregular, apparently nonperiodic fluctuations.

These same solutions would have been obtained if the series had at the start been truncated to include a total of three terms. Accordingly, in this study we shall let

$$a(1+a^2)^{-1}\kappa^{-1}\psi = X\sqrt{2}\sin(\pi a H^{-1}x)\sin(\pi H^{-1}z), \tag{23}$$

$$\pi R_c^{-1}R_a\Delta T^{-1}\theta = Y\sqrt{2}\cos(\pi a H^{-1}x)\sin(\pi H^{-1}z) - Z\sin(2\pi H^{-1}z), \tag{24}$$

where X, Y, and Z are functions of time alone. When expressions (23) and (24) are substituted into (17) and (18), and trigonometric terms other than those occurring in (23) and (24) are omitted, we obtain the equations

$$X^{\cdot} = -\sigma X + \sigma Y, \tag{25}$$

$$Y^{\cdot} = -XZ + rX - Y, \tag{26}$$

$$Z^{\cdot} = XY - bZ. \tag{27}$$

Here a dot denotes a derivative with respect to the dimensionless time $\tau = \pi^2 H^{-2}(1+a^2)\kappa t$, while $\sigma = \kappa^{-1}\nu$ is the *Prandtl number*, $r = R_c^{-1}R_a$, and $b = 4(1+a^2)^{-1}$. Except for multiplicative constants, our variables X, Y, and Z are the same as Saltzman's variables A, D, and G. Equations (25), (26), and (27) are the convection equations whose solutions we shall study.

In these equations X is proportional to the intensity of the convective motion, while Y is proportional to the temperature difference between the ascending and descending currents, similar signs of X and Y denoting that warm fluid is rising and cold fluid is descending. The variable Z is proportional to the distortion of the vertical temperature profile from linearity, a positive value indicating that the strongest gradients occur near the boundaries.

Equations (25)–(27) may give realistic results when the Rayleigh number is slightly supercritical, but their solutions cannot be expected to resemble those of (17) and (18) when strong convection occurs, in view of the extreme truncation.

6. Applications of linear theory

Although equations (25)–(27), as they stand, do not have the form of (4), a number of linear transformations will convert them to this form. One of the simplest of these is the transformation

$$X' = X, \quad Y' = Y, \quad Z' = Z - r - \sigma. \tag{28}$$

Solutions of (25)–(27) therefore remain bounded within a region R as $\tau \to \infty$, and the general results of Sections 2, 3 and 4 apply to these equations.

The stability of a solution $X(\tau)$, $Y(\tau)$, $Z(\tau)$ may be formally investigated by considering the behavior of small superposed perturbations $x_0(\tau)$, $y_0(\tau)$, $z_0(\tau)$. Such perturbations are temporarily governed by the linearized equations

$$\begin{bmatrix} x_0 \\ y_0 \\ z_0 \end{bmatrix}^{\cdot} = \begin{bmatrix} -\sigma & \sigma & 0 \\ (r-Z) & -1 & -X \\ Y & X & -b \end{bmatrix} \begin{bmatrix} x_0 \\ y_0 \\ z_0 \end{bmatrix}. \tag{29}$$

Since the coefficients in (29) vary with time, unless the basic state X, Y, Z is a steady-state solution of (25)–(27), a general solution of (29) is not feasible. However, the variation of the volume V_0 of a small region in phase space, as each point in the region is displaced in accordance with (25)–(27), is determined by the diagonal sum of the matrix of coefficients; specifically

$$V_0^{\cdot} = -(\sigma+b+1)V_0. \tag{30}$$

This is perhaps most readily seen by visualizing the motion in phase space as the flow of a fluid, whose divergence is

$$\frac{\partial X^{\cdot}}{\partial X} + \frac{\partial Y^{\cdot}}{\partial Y} + \frac{\partial Z^{\cdot}}{\partial Z} = -(\sigma+b+1). \tag{31}$$

Hence each small volume shrinks to zero as $\tau \to \infty$, at a rate independent of X, Y, and Z. This does not imply that each small volume shrinks to a point; it may simply become flattened into a surface. It follows that the volume of the region initially enclosed by the surface S shrinks to zero at this same rate, so that all trajectories ultimately become confined to a specific subspace having zero volume. This subspace contains all those trajectories which lie entirely within R, and so contains all central trajectories.

Equations (25)–(27) possess the steady-state solution $X = Y = Z = 0$, representing the state of no convection. With this basic solution, the characteristic equation of the matrix in (29) is

$$[\lambda+b][\lambda^2+(\sigma+1)\lambda+\sigma(1-r)] = 0. \tag{32}$$

This equation has three real roots when $r > 0$; all are negative when $r < 1$, but one is positive when $r > 1$. The criterion for the onset of convection is therefore $r = 1$, or $R_a = R_c$, in agreement with Rayleigh's result.

When $r > 1$, equations (25)–(27) possess two additional steady-state solutions $X = Y = \pm\sqrt{b(r-1)}$, $Z = r-1$.

For either of these solutions, the characteristic equation of the matrix in (29) is

$$\lambda^3+(\sigma+b+1)\lambda^2+(r+\sigma)b\lambda+2\sigma b(r-1)=0. \quad (33)$$

This equation possesses one real negative root and two complex conjugate roots when $r>1$; the complex conjugate roots are pure imaginary if the product of the coefficients of λ^2 and λ equals the constant term, or

$$r=\sigma(\sigma+b+3)(\sigma-b-1)^{-1}. \quad (34)$$

This is the critical value of r for the instability of steady convection. Thus if $\sigma<b+1$, no positive value of r satisfies (34), and steady convection is always stable, but if $\sigma>b+1$, steady convection is unstable for sufficiently high Rayleigh numbers. This result of course applies only to idealized convection governed by (25)–(27), and not to the solutions of the partial differential equations (17) and (18).

The presence of complex roots of (34) shows that if unstable steady convection is disturbed, the motion will oscillate in intensity. What happens when the disturbances become large is not revealed by linear theory. To investigate finite-amplitude convection, and to study the subspace to which trajectories are ultimately confined, we turn to numerical integration.

TABLE 1. Numerical solution of the convection equations. Values of X, Y, Z are given at every fifth iteration N, for the first 160 iterations.

N	X	Y	Z
0000	0000	0010	0000
0005	0004	0012	0000
0010	0009	0020	0000
0015	0016	0036	0002
0020	0030	0066	0007
0025	0054	0115	0024
0030	0093	0192	0074
0035	0150	0268	0201
0040	0195	0234	0397
0045	0174	0055	0483
0050	0097	−0067	0415
0055	0025	−0093	0340
0060	−0020	−0089	0298
0065	−0046	−0084	0275
0070	−0061	−0083	0262
0075	−0070	−0086	0256
0080	−0077	−0091	0255
0085	−0084	−0095	0258
0090	−0089	−0098	0266
0095	−0093	−0098	0275
0100	−0094	−0093	0283
0105	−0092	−0086	0297
0110	−0088	−0079	0286
0115	−0083	−0073	0281
0120	−0078	−0070	0273
0125	−0075	−0071	0264
0130	−0074	−0075	0257
0135	−0076	−0080	0252
0140	−0079	−0087	0251
0145	−0083	−0093	0254
0150	−0088	−0098	0262
0155	−0092	−0099	0271
0160	−0094	−0096	0281

7. Numerical integration of the convection equations

To obtain numerical solutions of the convection equations, we must choose numerical values for the constants. Following Saltzman (1962), we shall let $\sigma=10$ and $a^2=\frac{1}{2}$, so that $b=8/3$. The critical Rayleigh number for instability of steady convection then occurs when $r=470/19=24.74$.

We shall choose the slightly supercritical value $r=28$. The states of steady convection are then represented by the points $(6\sqrt{2}, 6\sqrt{2}, 27)$ and $(-6\sqrt{2}, -6\sqrt{2}, 27)$ in phase space, while the state of no convection corresponds to the origin (0,0,0).

We have used the double-approximation procedure for numerical integration, defined by (9), (10), and (14). The value $\Delta\tau=0.01$ has been chosen for the dimensionless time increment. The computations have been performed on a Royal McBee LGP-30 electronic com-

TABLE 2. Numerical solution of the convection equations Values of X, Y, Z are given at every iteration N for which Z possesses a relative maximum, for the first 6000 iterations.

N	X	Y	Z	N	X	Y	Z
0045	0174	0055	0483	3029	0117	0075	0352
0107	−0091	−0083	0287	3098	0123	0076	0365
0168	−0092	−0084	0288	3171	0134	0082	0383
0230	−0092	−0084	0289	3268	0155	0069	0435
0292	−0092	−0083	0290	3333	−0114	−0079	0342
0354	−0093	−0083	0292	3400	−0117	−0077	0350
0416	−0093	−0083	0293	3468	−0125	−0083	0361
0478	−0094	−0082	0295	3541	−0129	−0073	0378
0540	−0094	−0082	0296	3625	−0146	−0074	0413
0602	−0095	−0082	0298	3695	0127	0079	0370
0664	−0096	−0083	0300	3772	0136	0072	0394
0726	−0097	−0083	0302	3853	−0144	−0077	0407
0789	−0097	−0081	0304	3926	0129	0072	0380
0851	−0099	−0083	0307	4014	0148	0068	0421
0914	−0100	−0081	0309	4082	−0120	−0074	0359
0977	−0100	−0080	0312	4153	−0129	−0078	0375
1040	−0102	−0080	0315	4233	−0144	−0082	0404
1103	−0104	−0081	0319	4307	0135	0081	0385
1167	−0105	−0079	0323	4417	−0162	−0069	0450
1231	−0107	−0079	0328	4480	0106	0081	0324
1295	−0111	−0082	0333	4544	0109	0082	0329
1361	−0111	−0077	0339	4609	0110	0080	0334
1427	−0116	−0079	0347	4675	0112	0076	0341
1495	−0120	−0077	0357	4741	0118	0081	0349
1566	−0125	−0072	0371	4810	0120	0074	0360
1643	−0139	−0077	0396	4881	0130	0081	0376
1722	0140	0075	0401	4963	0141	0068	0406
1798	−0135	−0072	0391	5035	−0133	−0081	0381
1882	0146	0074	0413	5124	−0151	−0076	0422
1952	−0127	−0078	0370	5192	0119	0075	0358
2029	−0135	−0070	0393	5262	0129	0083	0372
2110	0146	0083	0408	5340	0140	0079	0397
2183	−0128	−0070	0379	5419	−0137	−0067	0399
2268	−0144	−0066	0415	5495	0140	0081	0394
2337	0126	0079	0368	5576	−0141	−0072	0405
2412	0137	0081	0389	5649	0135	0082	0384
2501	−0153	−0080	0423	5752	0160	0074	0443
2569	0119	0076	0357	5816	−0110	−0081	0332
2639	0129	0082	0371	5881	−0113	−0082	0339
2717	0136	0070	0395	5948	−0114	−0075	0346
2796	−0143	−0079	0402				
2871	0134	0076	0388				
2962	−0152	−0072	0426				

puting machine. Approximately one second per iteration, aside from output time, is required.

For initial conditions we have chosen a slight departure from the state of no convection, namely (0,1,0). Table 1 has been prepared by the computer. It gives the values of N (the number of iterations), X, Y, and Z at every fifth iteration for the first 160 iterations. In the printed output (but not in the computations) the values of X, Y, and Z are multiplied by ten, and then only those figures to the left of the decimal point are printed. Thus the states of steady convection would appear as 0084, 0084, 0270 and −0084, −0084, 0270, while the state of no convection would appear as 0000, 0000, 0000.

The initial instability of the state of rest is evident. All three variables grow rapidly, as the sinking cold fluid is replaced by even colder fluid from above, and the rising warm fluid by warmer fluid from below, so that by step 35 the strength of the convection far exceeds that of steady convection. Then Y diminishes as the warm fluid is carried over the top of the convective cells, so that by step 50, when X and Y have opposite signs, warm fluid is descending and cold fluid is ascending. The motion thereupon ceases and reverses its direction, as indicated by the negative values of X following step 60. By step 85 the system has reached a state not far from that of steady convection. Between steps 85 and 150 it executes a complete oscillation in its intensity, the slight amplification being almost indetectable.

The subsequent behavior of the system is illustrated in Fig. 1, which shows the behavior of Y for the first 3000 iterations. After reaching its early peak near step 35 and then approaching equilibrium near step 85, it undergoes systematic amplified oscillations until near step 1650. At this point a critical state is reached, and thereafter Y changes sign at seemingly irregular intervals, reaching sometimes one, sometimes two, and sometimes three or more extremes of one sign before changing sign again.

Fig. 2 shows the projections on the X-Y- and Y-Z-planes in phase space of the portion of the trajectory corresponding to iterations 1400–1900. The states of steady convection are denoted by C and C'. The first portion of the trajectory spirals outward from the vicinity of C', as the oscillations about the state of steady convection, which have been occurring since step 85, continue to grow. Eventually, near step 1650, it crosses the X-Z-plane, and is then deflected toward the neighborhood of C. It temporarily spirals about C, but crosses the X-Z-plane after one circuit, and returns to the neighborhood of C', where it soon joins the spiral over which it has previously traveled. Thereafter it crosses from one spiral to the other at irregular intervals.

Fig. 3, in which the coordinates are Y and Z, is based upon the printed values of X, Y, and Z at every fifth iteration for the first 6000 iterations. These values determine X as a smooth single-valued function of Y and Z over much of the range of Y and Z; they determine X

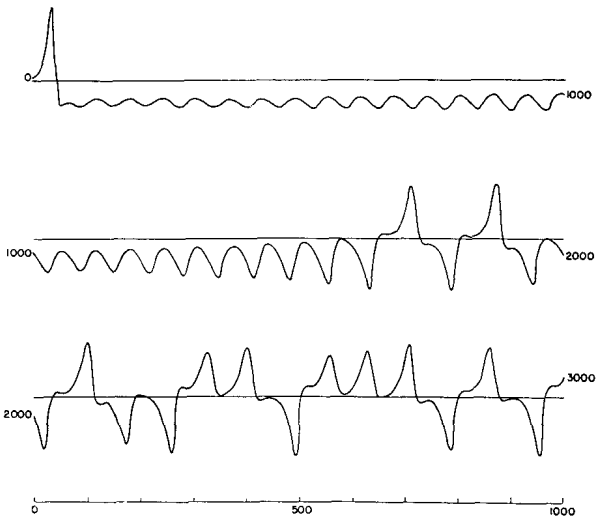

FIG. 1. Numerical solution of the convection equations. Graph of Y as a function of time for the first 1000 iterations (upper curve), second 1000 iterations (middle curve), and third 1000 iterations (lower curve).

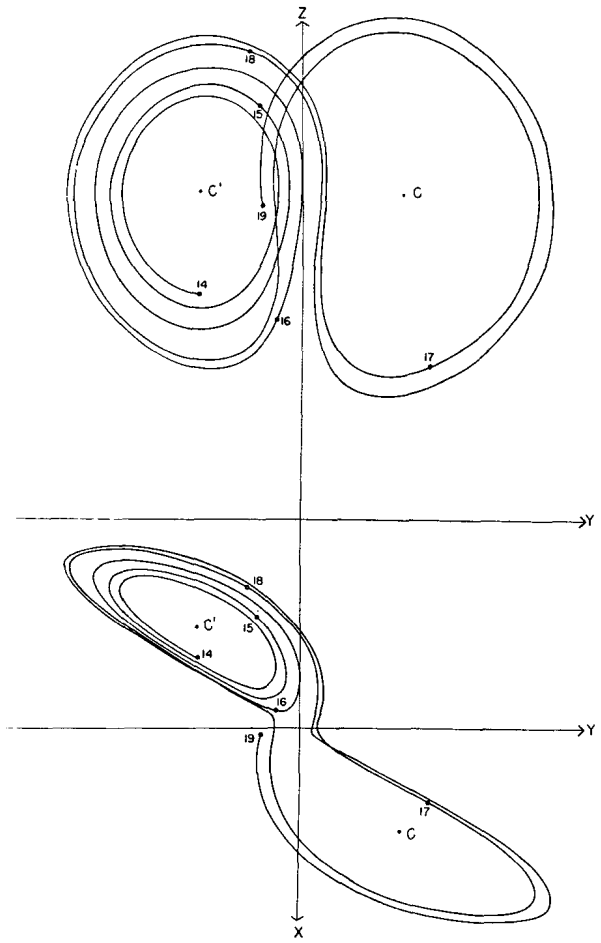

FIG. 2. Numerical solution of the convection equations. Projections on the X-Y-plane and the Y-Z-plane in phase space of the segment of the trajectory extending from iteration 1400 to iteration 1900. Numerals "14," "15," etc., denote positions at iterations 1400, 1500, etc. States of steady convection are denoted by C and C'.

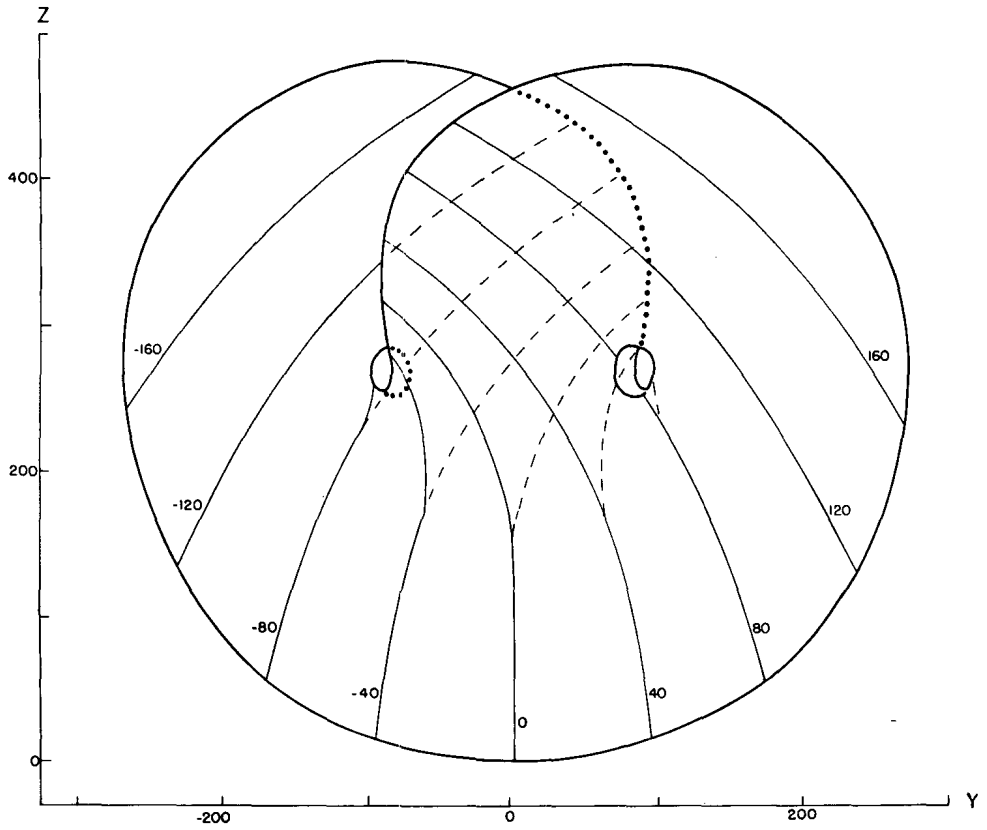

FIG. 3. Isopleths of X as a function of Y and Z (thin solid curves), and isopleths of the lower of two values of X, where two values occur (dashed curves), for approximate surfaces formed by all points on limiting trajectories. Heavy solid curve, and extensions as dotted curves, indicate natural boundaries of surfaces.

as one of two smooth single-valued functions over the remainder of the range. In Fig. 3 the thin solid lines are isopleths of X, and where two values of X exist, the dashed lines are isopleths of the lower value. Thus, within the limits of accuracy of the printed values, the trajectory is confined to a pair of surfaces which appear to merge in the lower portion of Fig. 3. The spiral about C lies in the upper surface, while the spiral about C' lies in the lower surface. Thus it is possible for the trajectory to pass back and forth from one spiral to the other without intersecting itself.

Additional numerical solutions indicate that other trajectories, originating at points well removed from these surfaces, soon meet these surfaces. The surfaces therefore appear to be composed of all points lying on limiting trajectories.

Because the origin represents a steady state, no trajectory can pass through it. However, two trajectories emanate from it, i.e., approach it asymptotically as $\tau \rightarrow -\infty$. The heavy solid curve in Fig. 3, and its extensions as dotted curves, are formed by these two trajectories. Trajectories passing close to the origin will tend to follow the heavy curve, but will not cross it, so that the heavy curve forms a natural boundary to the region which a trajectory can ultimately occupy. The holes near C and C' also represent regions which cannot be occupied after they have once been abandoned.

Returning to Fig. 2, we find that the trajectory apparently leaves one spiral only after exceeding some critical distance from the center. Moreover, the extent to which this distance is exceeded appears to determine the point at which the next spiral is entered; this in turn seems to determine the number of circuits to be executed before changing spirals again.

It therefore seems that some single feature of a given circuit should predict the same feature of the following circuit. A suitable feature of this sort is the maximum value of Z, which occurs when a circuit is nearly completed. Table 2 has again been prepared by the computer, and shows the values of X, Y, and Z at only those iterations N for which Z has a relative maximum. The succession of circuits about C and C' is indicated by the succession of positive and negative values of X and Y. Evidently X and Y change signs following a maximum which exceeds some critical value printed as about 385.

Fig. 4 has been prepared from Table 2. The abscissa is M_n, the value of the nth maximum of Z, while the ordinate is M_{n+1}, the value of the following maximum. Each point represents a pair of successive values of Z taken from Table 2. Within the limits of the round-off

in tabulating Z, there is a precise two-to-one relation between M_n and M_{n+1}. The initial maximum $M_1=483$ is shown as if it had followed a maximum $M_0=385$, since maxima near 385 are followed by close approaches to the origin, and then by exceptionally large maxima.

It follows that an investigator, unaware of the nature of the governing equations, could formulate an empirical prediction scheme from the "data" pictured in Figs. 2 and 4. From the value of the most recent maximum of Z, values at future maxima may be obtained by repeated applications of Fig. 4. Values of X, Y, and Z between maxima of Z may be found from Fig. 2, by interpolating between neighboring curves. Of course, the accuracy of predictions made by this method is limited by the exactness of Figs. 2 and 4, and, as we shall see, by the accuracy with which the initial values of X, Y, and Z are observed.

Some of the implications of Fig. 4 are revealed by considering an idealized two-to-one correspondence between successive members of sequences M_0, M_1, $\cdots$, consisting of numbers between zero and one. These sequences satisfy the relations

$$\begin{aligned} M_{n+1}&=2M_n && \text{if } M_n<\tfrac{1}{2} \\ M_{n+1}&\text{ is undefined} && \text{if } M_n=\tfrac{1}{2} \\ M_{n+1}&=2-2M_n && \text{if } M_n>\tfrac{1}{2}. \end{aligned} \tag{35}$$

The correspondence defined by (35) is shown in Fig. 5, which is an idealization of Fig. 4. It follows from repeated applications of (35) that in any particular sequence,

$$M_n=m_n\pm 2^nM_0, \tag{36}$$

where m_n is an even integer.

Consider first a sequence where $M_0=u/2^p$, where u is odd. In this case $M_{p-1}=\frac{1}{2}$, and the sequence terminates. These sequences form a denumerable set, and correspond to the trajectories which score direct hits upon the state of no convection.

Next consider a sequence where $M_0=u/2^pv$, where u and v are relatively prime odd numbers. Then if $k>0$, $M_{p+1+k}=u_k/v$, where u_k and v are relatively prime and u_k is even. Since for any v the number of proper fractions u_k/v is finite, repetitions must occur, and the sequence is periodic. These sequences also form a denumerable set, and correspond to periodic trajectories.

The periodic sequences having a given number of distinct values, or phases, are readily tabulated. In particular there are a single one-phase, a single two-phase, and two three-phase sequences, namely,

$$\begin{aligned} &2/3, \cdots, \\ &2/5, 4/5, \cdots, \\ &2/7, 4/7, 6/7, \cdots, \\ &2/9, 4/9, 8/9, \cdots. \end{aligned}$$

The two three-phase sequences differ qualitatively in that the former possesses two numbers, and the latter only one number, exceeding $\frac{1}{2}$. Thus the trajectory corresponding to the former makes two circuits about C, followed by one about C' (or vice versa). The trajectory corresponding to the latter makes three circuits about C, followed by three about C', so that actually only Z varies in three phases, while X and Y vary in six.

Now consider a sequence where M_0 is not a rational fraction. In this case (36) shows that M_{n+k} cannot equal

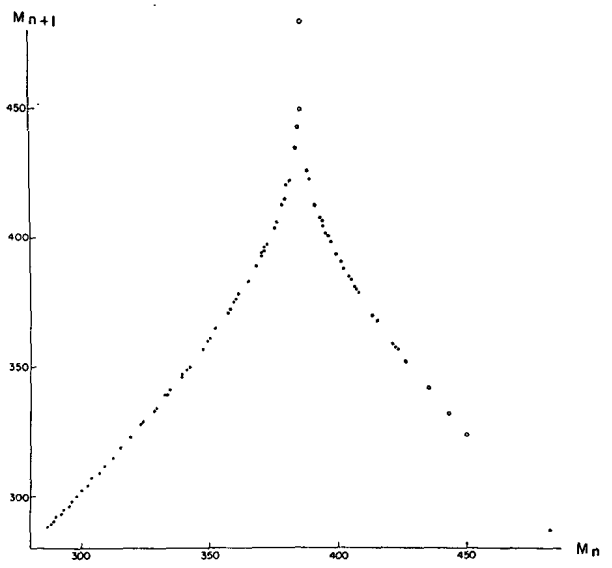

FIG. 4. Corresponding values of relative maximum of Z (abscissa) and subsequent relative maximum of Z (ordinate) occurring during the first 6000 iterations.

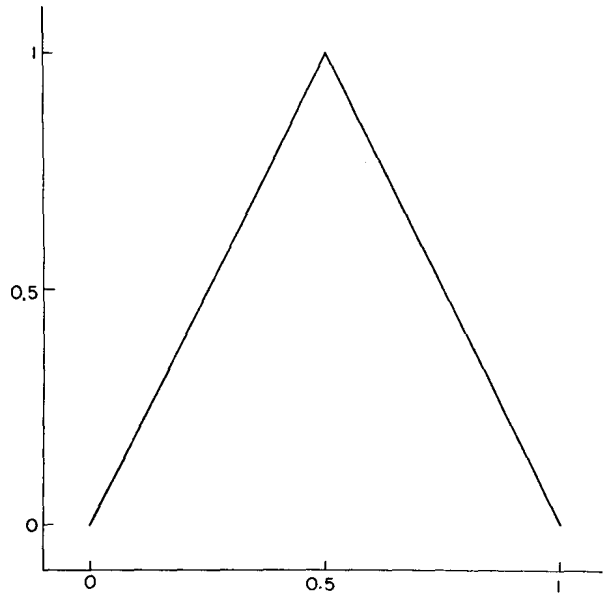

FIG. 5. The function $M_{n+1}=2M_n$ if $M_n<\frac{1}{2}$, $M_{n+1}=2-2M_n$ if $M_n>\frac{1}{2}$, serving as an idealization of the locus of points in Fig. 4.

M_n if $k>0$, so that no repetitions occur. These sequences, which form a nondenumerable set, may conceivably approach periodic sequences asymptotically and be quasi-periodic, or they may be nonperiodic.

Finally, consider two sequences M_0, M_1, $\cdots$ and M_0', M_1', $\cdots$, where $M_0'=M_0+\epsilon$. Then for a given k, if ϵ is sufficiently small, $M_k'=M_k\pm 2^k\epsilon$. All sequences are therefore unstable with respect to small modifications. In particular, all periodic sequences are unstable, and no other sequences can approach them asymptotically. All sequences except a set of measure zero are therefore nonperiodic, and correspond to nonperiodic trajectories.

Returning to Fig. 4, we see that periodic sequences analogous to those tabulated above can be found. They are given approximately by

$$398, \cdots,$$
$$377, 410, \cdots,$$
$$369, 391, 414, \cdots,$$
$$362, 380, 419, \cdots.$$

The trajectories possessing these or other periodic sequences of maxima are presumably periodic or quasi-periodic themselves.

The above sequences are temporarily approached in the numerical solution by sequences beginning at iterations 5340, 4881, 3625, and 3926. Since the numerical solution eventually departs from each of these sequences, each is presumably unstable.

More generally, if $M_n'=M_n+\epsilon$, and if ϵ is sufficiently small, $M_{n+k}'=M_{n+k}+\Lambda\epsilon$, where Λ is the product of the slopes of the curve in Fig. 4 at the points whose abscissas are M_n, $\cdots$, M_{n+k-1}. Since the curve apparently has a slope whose magnitude exceeds unity everywhere, all sequences of maxima, and hence all trajectories, are unstable. In particular, the periodic trajectories, whose sequences of maxima form a denumerable set, are unstable, and only exceptional trajectories, having the same sequences of maxima, can approach them asymptotically. The remaining trajectories, whose sequences of maxima form a nondenumerable set, therefore represent deterministic nonperiodic flow.

These conclusions have been based upon a finite segment of a numerically determined solution. They cannot be regarded as mathematically proven, even though the evidence for them is strong. One apparent contradiction requires further examination.

It is difficult to reconcile the merging of two surfaces, one containing each spiral, with the inability of two trajectories to merge. It is not difficult, however, to explain the *apparent* merging of the surfaces. At two times τ_0 and τ_1, the volumes occupied by a specified set of particles satisfy the relation

$$V_0(\tau_1)=e^{-(\sigma+b+1)(\tau_1-\tau_0)}V_0(\tau_0), \tag{37}$$

according to (30). A typical circuit about C or C' requires about 70 iterations, so that, for such a circuit, $\tau_2=\tau_1+0.7$, and, since $\sigma+b+1=41/3$,

$$V_0(\tau_1)=0.00007V_0(\tau_0). \tag{38}$$

Two particles separated from each other in a suitable direction can therefore come together very rapidly, and appear to merge.

It would seem, then, that the two surfaces merely appear to merge, and remain distinct surfaces. Following these surfaces along a path parallel to a trajectory, and circling C or C', we see that each surface is really a pair of surfaces, so that, where they appear to merge, there are really four surfaces. Continuing this process for another circuit, we see that there are really eight surfaces, etc., and we finally conclude that there is an infinite complex of surfaces, each extremely close to one or the other of two merging surfaces.

The infinite set of values at which a line parallel to the X-axis intersects these surfaces may be likened to the set of all numbers between zero and one whose decimal expansions (or some other expansions besides binary) contain only zeros and ones. This set is plainly nondenumerable, in view of its correspondence to the set of all numbers between zero and one, expressed in binary. Nevertheless it forms a set of measure zero. The sequence of ones and zeros corresponding to a particular surface contains a history of the trajectories lying in that surface, a one or zero immediately to the right of the decimal point indicating that the last circuit was about C or C', respectively, a one or zero in second place giving the same information about the next to the last circuit, etc. Repeating decimal expansions represent periodic or quasi-periodic trajectories, and, since they define rational fractions, they form a denumerable set.

If one first visualizes this infinite complex of surfaces, it should not be difficult to picture nonperiodic deterministic trajectories embedded in these surfaces.

8. Conclusion

Certain mechanically or thermally forced nonconservative hydrodynamical systems may exhibit either periodic or irregular behavior when there is no obviously related periodicity or irregularity in the forcing process. Both periodic and nonperiodic flow are observed in some experimental models when the forcing process is held constant, within the limits of experimental control. Some finite systems of ordinary differential equations designed to represent these hydrodynamical systems possess periodic analytic solutions when the forcing is strictly constant. Other such systems have yielded nonperiodic numerical solutions.

A finite system of ordinary differential equations representing forced dissipative flow often has the property that all of its solutions are ultimately confined within the same bounds. We have studied in detail the properties of solutions of systems of this sort. Our principal results concern the instability of nonperiodic solutions. A nonperiodic solution with no transient com-

ponent must be unstable, in the sense that solutions temporarily approximating it do not continue to do so. A nonperiodic solution with a transient component is sometimes stable, but in this case its stability is one of its transient properties, which tends to die out.

To verify the existence of deterministic nonperiodic flow, we have obtained numerical solutions of a system of three ordinary differential equations designed to represent a convective process. These equations possess three steady-state solutions and a denumerably infinite set of periodic solutions. All solutions, and in particular the periodic solutions, are found to be unstable. The remaining solutions therefore cannot in general approach the periodic solutions asymptotically, and so are nonperiodic.

When our results concerning the instability of nonperiodic flow are applied to the atmosphere, which is ostensibly nonperiodic, they indicate that prediction of the sufficiently distant future is impossible by any method, unless the present conditions are known exactly. In view of the inevitable inaccuracy and incompleteness of weather observations, precise very-long-range forecasting would seem to be non-existent.

There remains the question as to whether our results really apply to the atmosphere. One does not usually regard the atmosphere as either deterministic or finite, and the lack of periodicity is not a mathematical certainty, since the atmosphere has not been observed forever.

The foundation of our principal result is the eventual necessity for any bounded system of finite dimensionality to come arbitrarily close to acquiring a state which it has previously assumed. If the system is stable, its future development will then remain arbitrarily close to its past history, and it will be quasi-periodic.

In the case of the atmosphere, the crucial point is then whether analogues must have occurred since the state of the atmosphere was first observed. By analogues, we mean specifically two or more states of the atmosphere, together with its environment, which resemble each other so closely that the differences may be ascribed to errors in observation. Thus, to be analogues, two states must be closely alike in regions where observations are accurate and plentiful, while they need not be at all alike in regions where there are no observations at all, whether these be regions of the atmosphere or the environment. If, however, some unobserved features are implicit in a succession of observed states, two successions of states must be nearly alike in order to be analogues.

If it is true that two analogues have occurred since atmospheric observation first began, it follows, since the atmosphere has not been observed to be periodic, that the successions of states following these analogues must eventually have differed, and no forecasting scheme could have given correct results both times. If, instead, analogues have not occurred during this period, some accurate very-long-range prediction scheme, using observations at present available, may exist. But, if it does exist, the atmosphere will acquire a quasi-periodic behavior, never to be lost, once an analogue occurs. This quasi-periodic behavior need not be established, though, even if very-long-range forecasting is feasible, if the variety of possible atmospheric states is so immense that analogues need never occur. It should be noted that these conclusions do not depend upon whether or not the atmosphere is deterministic.

There remains the very important question as to how long is "very-long-range." Our results do not give the answer for the atmosphere; conceivably it could be a few days or a few centuries. In an idealized system, whether it be the simple convective model described here, or a complicated system designed to resemble the atmosphere as closely as possible, the answer may be obtained by comparing pairs of numerical solutions having nearly identical initial conditions. In the case of the real atmosphere, if all other methods fail, we can wait for an analogue.

Acknowledgments. The writer is indebted to Dr. Barry Saltzman for bringing to his attention the existence of nonperiodic solutions of the convection equations. Special thanks are due to Miss Ellen Fetter for handling the many numerical computations and preparing the graphical presentations of the numerical material.

REFERENCES

Birkhoff, G. O., 1927: *Dynamical systems.* New York, Amer. Math. Soc., Colloq. Publ., 295 pp.

Ford, L. R., 1933: *Differential equations.* New York, McGraw-Hill, 264 pp.

Fultz, D., R. R. Long, G. V. Owens, W. Bohan, R. Kaylor and J. Weil, 1959: Studies of thermal convection in a rotating cylinder with some implications for large-scale atmospheric motions. *Meteor. Monog,* 4(21), Amer. Meteor. Soc., 104 pp.

Gibbs, J. W., 1902: *Elementary principles in statistical mechanics.* New York, Scribner, 207 pp.

Hide, R., 1958: An experimental study of thermal convection in a rotating liquid. *Phil. Trans. Roy. Soc. London,* (A), **250,** 441–478.

Lorenz, E. N., 1960: Maximum simplification of the dynamic equations. *Tellus,* **12,** 243–254.

——, 1962a: Simplified dynamic equations applied to the rotating-basin experiments. *J. atmos. Sci.,* **19,** 39–51.

——, 1962b: The statistical prediction of solutions of dynamic equations. *Proc. Internat. Symposium Numerical Weather Prediction,* Tokyo, 629–635.

Nemytskii, V. V., and V. V. Stepanov, 1960: *Qualitative theory of differential equations.* Princeton, Princeton Univ. Press, 523 pp.

Poincaré, H., 1881: Mémoire sur les courbes définies par une équation différentielle. *J. de Math.,* **7,** 375–442.

Rayleigh, Lord, 1916: On convective currents in a horizontal layer of fluid when the higher temperature is on the under side. *Phil. Mag.,* **32,** 529–546.

Saltzman, B., 1962: Finite amplitude free convection as an initial value problem—I. *J. atmos. Sci.,* **19,** 329–341.

Appendix C

Bibliography on geomagnetic data assimilation

Here is (up to my knowledge) a list of references dealing with the application of data assimilation methods to geomagnetism, or more generally, magnetohydrodynamic systems.

Bibliography

Aubert, J. and A. Fournier, 2011: Inferring internal properties of Earth's core dynamics and their evolution from surface observations and a numerical geodynamo model. *Nonlinear Processes In Geophysics*, **18 (5)**, 657–674, doi:{10.5194/npg-18-657-2011}.

Beggan, C. and K. Whaler, 2010: Forecasting secular variation using core flows. *Earth Planets and Space*, **62 (10)**, 821–828, doi:{10.5047/eps.2010.07.004}.

Beggan, C. D. and K. A. Whaler, 2009: Forecasting change of the magnetic field using core surface flows and ensemble Kalman filtering. *Geophysical Research Letters*, **36**, doi:{10.1029/2009GL039927}.

Canet, E., 2009: Modèle dynamique et assimilation de données de la variation séculaire du champ magnétique terrestre. Ph.D. thesis, Université Joseph-Fourier, URL http://tel.archives-ouvertes.fr/tel-00521437.

Canet, E., A. Fournier, and D. Jault, 2009: Forward and adjoint quasi-geostrophic models of the geomagnetic secular variation. *Journal of Geophysical Research-Solid Earth*, **114**, doi:{10.1029/2008JB006189}.

Fournier, A., J. Aubert, and E. Thebault, 2011: Inference on core surface flow from observations and 3-D dynamo modelling. *Geophysical Journal International*, **186 (1)**, 118–136, doi:{10.1111/j.1365-246X.2011.05037.x}.

Fournier, A., C. Eymin, and T. Alboussiere, 2007: A case for variational geomagnetic data assimilation: insights from a one-dimensional, nonlinear, and sparsely observed MHD system. *Nonlinear Processes In Geophysics*, **14 (2)**, 163–180.

Fournier, A., et al., 2010: An Introduction to Data Assimilation and Predictability in Geomagnetism. *Space Science Reviews*, **155 (1-4)**, 247–291, doi:{10.1007/s11214-010-9669-4}.

Gillet, N., D. Jault, E. Canet, and A. Fournier, 2010: Fast torsional waves and strong magnetic field within the Earth's core. *Nature*, **465 (7294)**, 74–77, doi:{10.1038/nature09010}.

Jouve, L., A. S. Brun, and O. Talagrand, 2011: Assimilating data into an alpha Omega dynamo model of the sun: A variational approach. *Astrophysical Journal*, **735 (1)**, doi:{10.1088/0004-637X/735/1/31}.

Kuang, W., A. Tangborn, W. Jiang, D. Liu, Z. Sun, J. Bloxham, and Z. Wei, 2008: MoSST_DAS: The first generation geomagnetic data assimilation framework. *Communications in computational physics*, **3 (1)**, 85–108.

Kuang, W., A. Tangborn, Z. Wei, and T. Sabaka, 2009: Constraining a numerical geodynamo model with 100 years of surface observations. *Geophysical Journal International*, **179 (3)**, 1458–1468, doi:{10.1111/j.1365-246X.2009.04376.x}.

Kuang, W., Z. Wei, R. Holme, and A. Tangborn, 2010: Prediction of geomagnetic field with data assimilation: a candidate secular variation model for IGRF-11. *Earth Planets And Space*, **62 (10)**, 775–785, doi:{10.5047/eps.2010.07.008}.

Li, K., A. Jackson, and P. W. Livermore, 2011: Variational data assimilation for the initial-value dynamo problem. *Physical Review E*, **84 (5, Part 2)**, doi:{10.1103/PhysRevE.84.056321}.

Liu, D., A. Tangborn, and W. Kuang, 2007: Observing system simulation experiments in geomagnetic data assimilation. *Journal of Geophysical Research-Solid Earth*, **112 (B8)**, doi:{10.1029/2006JB004691}.

Morzfeld, M. and A. J. Chorin, 2012: Implicit particle filtering for models with partial noise, and an application to geomagnetic data assimilation. *Nonlinear Processes In Geophysics*, **19 (3)**, 365–382, doi:{10.5194/npg-19-365-2012}.

Sun, Z., A. Tangborn, and W. Kuang, 2007: Data assimilation in a sparsely observed one-dimensional modeled MHD system. *Nonlinear Processes In Geophysics*, **14 (2)**, 181–192.